DEVELOPMENT AND APPLICATION OF HYBRID FINITE METHODS FOR SOLUTION OF TIME DEPENDENT MAXWELL'S EQUATIONS

NEELAKANTAM VENKATARAYALU
B.E., Anna University, India
M.S., Ohio State University, USA

A THESIS SUBMITTED

FOR THE DEGREE OF DOCTOR OF PHILOSOPHY

DEPARTMENT OF ELECTRICAL AND COMPUTER ENGINEERING

NATIONAL UNIVERSITY OF SINGAPORE

2007

To my parents, *Varadarajulu* and *Nagama Devi*,

my brother, *Naren* and

my sister, *Meera*.

ACKNOWLEDGMENTS

I wish to thank Prof. Joshua Li Le-Wei and Prof. Robert Lee for their guidance, inspiration, encouragement and support throughout my course of study and research work. Their knowledge and experience have been of immense help. Especially, I wish to extend my appreciation to Prof. Robert Lee for agreeing to supervise my work from overseas and in helping me during my visits to the ElectroScience Laboratory, Ohio State University. I take this opportunity to express my special thanks to Prof. Jin-Fa Lee, Ohio State University, for the numerous stimulating discussions and suggestions on the topic. Furthermore, I would like to express my sincere appreciation to Mr. Gan Yeow Beng and Prof. Lim Hock of Temasek Laboratories, National University of Singapore for providing me the opportunity to pursue the doctoral program part-time at the Department of Electrical and Computer Engineering, National University of Singapore. I would like to thank Dr. Wang Chao Fu and Dr. Tapabrata Ray, for their support and encouragement.

I would like to express my deepest gratitude to my parents, Varadarajulu and Nagama Devi, and my siblings, Naren and Meera, for their love, understanding and support throughout my life.

TABLE OF CONTENTS

Page

Summary

In par with the progress in computer technology, is the demand for numerical modeling and simulation of physical phenomena. Simulation of electromagnetic effects using computers has become essential for understanding the physical behaviour and characterising the performance of complex radio frequency (RF) and microwave systems. Efficient computational electromagnetics (CEM) techniques and algorithms are evolving, harnessing both the physical and mathematical properties of electromagnetic fields and Maxwell's equations. Finite methods are numerical techniques which seek solution of Maxwell's equations in the differential form. The finite methods focused in this thesis are the finite difference time domain (FDTD), the finite element time domain (FETD) methods and the hybrid methods based on the two. Hybrid finite methods retain the advantages of a particular method and overcome its disadvantages by hybridising it with an alternate method. One such hybrid method is the hybrid FETD-FDTD method which retains the efficiency of FDTD method in modeling simple homogeneous shapes and overcomes stair-casing errors in modeling curved and intricate geometrical structures using the FETD method which, in general, is based on unstructured grids. In this thesis improvements to the FETD and the hybrid FETD-FDTD methods are proposed along with the successful application of the hybrid method for modeling and simulation of radiation from antennas.

Two kinds of numerical instability are observed in the hybrid method viz., a) weak-instability and b) severe numerical instability. The weak instability is inherent to the FETD method using edge element basis functions and manifests in the electric field solution as a gradient vector field which grows linearly with time. The problem of linear time growth is analogous to the problem of appearance of non-physical modes

in the eigenvalue modeling of electromagnetic resonators. The reason for the linear growth in the FETD solution is investigated and a novel method to eliminate the occurrence of such weak-instability using divergence-free constraint equations is proposed. The proposed constraint equations could directly be extended to eigenvalue problems as well. Efficient implementation of the constraint equations using tree-cotree decomposition of the finite element mesh is proposed. The success of the method in computing a divergence-free solution is demonstrated both in the context of FETD and the eigenvalue modeling of electromagnetic resonators.

The second kind of instability is inherent to the strategy adopted in hybridising the FETD and FDTD methods. This instability is severe and renders the hybrid method infeasible for practical applications. A detailed investigation on the numerical stability of the hybrid method with different hybridisation schemes available in literature based on the eigenvalues of the global iteration matrix is carried out. The equivalence between a particular case of FETD and the FDTD method which leads to symmetric coefficient matrices in the hybrid update equation of the stable FETD-FDTD method is demonstrated. The condition for numerical stability is then obtained by the von Neumann analysis of the hybrid time-marching scheme.

Another improvement proposed to the FETD method is the treatment of hanging variables specifically in the context of rectangular and hexahedral elements. Due to Galerkin-type treatment of the hanging variables, the resulting FETD method has the same conditions of stability as those of the regular FETD method. A novel method of FDTD subgridding with provable numerical stability can then be achieved by having the interface between coarse and fine grids of the subgridding mesh in the FETD region and treating the fine element unknowns on the interface as hanging variables. Numerical examples indicating the potential of the subgridding method with 1:2 and 1:4 refinements are demonstrated. Furthermore, the analytical lower bound on the level of numerical reflections due to the difference in numerical dispersion in fine and coarse grids, in a

general subgridding method is proposed. The level of numerical reflections introduced in the proposed method is compared with the analytical lower bound. The proposed subgridding method can reuse existing mesh generation tools available for the FDTD method and is suitable for modeling of geometrically fine features with a finer grid.

The FETD method on unstructured grids could be employed for modeling geometrically fine features as well. In this case, however, special requirements on the unstructured mesh generation exist. To have a conformal transition from unstructured to structured region pyramidal elements are used. A simple strategy for automatic hybrid mesh generation for the 3-D hybrid FETD-FDTD method is developed. The FETD solution in the unstructured region is further improved by using hierarchical higher order basis functions. The FETD method is extended to support modeling of ports with transverse electromagnetic mode of excitation. The developed numerical codes are successfully applied for the computation of the modal reflection coefficient, input impedance and radiation pattern of real world antennas and benchmark problems.

LIST OF TABLES

Table **Page**

LIST OF FIGURES

Figure **Page**

Referred Journal Publications

N. V. Venkatarayalu, Y. B. Gan, R. Lee, and L.-W. Li. Application of hybrid FETD-FDTD method in the modeling and analysis of antennas.*IEEE Transactions on Antennas and Propagation, Submitted.*

N. V. Venkatarayalu, R. Lee, Y. B. Gan, and L.-W. Li. A Stable FDTD Subgridding Method based on Finite Element Formulation with Hanging Variables. *IEEE Transactions on Antennas and Propagation*,55(3):907–915, Mar. 2007.

N. V. Venkatarayalu and Jin-Fa Lee. Removal of spurious dc modes in edge element solutions for modeling three-dimensional resonators. *IEEE Transactions on Microwave Theory and Techniques*, 54(7):3019–3025, July 2006.

N. V. Venkatarayalu, Y.-B. Gan, and L.-W. Li. Investigation of numerical stability of 2D FE/FDTD hybrid algorithm for different hybridization schemes. *IEICE Transactions on Communications*, E88-B(6):2341–2345, June 2005.

N. V. Venkatarayalu, Y. B. Gan, and L.-W. Li. On the numerical errors in the 2d FE/FDTD algorithm for different hybridization schemes. *IEEE Microwave and Wireless Components Letters*, 14(4):168–170, April 2004.

Conference Publications

N. V. Venkatarayalu, Y. B. Gan, R. Lee, and L.-W. Li. Antenna Modeling Using Stable Hybrid FETD-FDTD Method. Proceedings of 2007 IEEE International Symposium on Antennas and Propagation, pp. 3736-3739. Honolulu, Hawai'i, USA, June 10-15, 2007.

N. V. Venkatarayalu, Y. B. Gan, R. Lee, and L.-W. Li. Antenna Modeling Using 3D Hybrid Finite Element - Finite Difference Time Domain Method. Proceedings of 2006 International Symposium on Antennas and Propagation, ISAP 2006. Singapore, Nov 1-4, 2006.

N. V. Venkatarayalu, R. Lee, Y. B. Gan, and L.-W. Li. Hanging variables in Finite Element Time Domain Method with Hexahedral Edge Elements. Proceedings of 17th International Zurich Symposium on Electromagnetic Compatibility, EMC Zurich, pp. 184-187, Singapore, Feb 27- Mar 3, 2006.

Y. Srisukh, **N. V. Venkatarayalu**, R. Lee. Hybrid finite element/ finite difference methods in the time domain. Proceedings of 9th International Conference on Electromagnetics in Advanced Applications, Torino, Italy, Sep 12-16, 2005.

N. V. Venkatarayalu, M.N. Vouvakis, Yeow-Beng Gan, and Jin-Fa Lee. Suppressing linear time growth in edge element based finite element time domain solution using divergence free constraint equation. In *2005 IEEE Antennas and Propagation Society International Symposium*, volume 4B, pages 193–196vol.4B, 3-8 July 2005.

N. V. Venkatarayalu, R. Lee, Y. B. Gan, and L.-W. Li. Time Domain Finite Element Solution Using Hanging Variables on Rectangular Edge Elements. 2005 URSI North American Radio Science Meeting Digest, Washington DC, July 3-8, 2005.

N. V. Venkatarayalu, Y. B. Gan, and L.-W. Li. Investigation of Numerical Stability of 2D FE/FDTD Hybrid Algorithm for Different Hybridization Schemes. Proceedings of ISAP 2004, International Symposium on Antennas and Propagation, pp. 1113-1116, Sendai, Japan, August 17-21, 2004.

CHAPTER 1

INTRODUCTION

Maxwell's equations, unifying the laws of electricity and magnetism, accurately describe macroscopic electromagnetic field phenomena. The discipline of computational electromagnetics (CEM) deals with numerical methods for solving Maxwell's equations leading to the characterization of complex electromagnetic systems. Efficient numerical tools give engineers and designers an upper hand of assessing the performance of their design ahead of physical prototyping and measurement. Most common and popular numerical methods in CEM can broadly be classified into two classes viz., frequency domain and time domain methods. While frequency domain methods seek electromagnetic field solution under the time harmonic or steady state conditions, time domain methods capture the transient response of electromagnetic fields. Both classes have their own pros and cons. It is not possible to generalise the superiority of a particular method over the others. Major advantages of time domain methods over frequency domain methods are

a. A single simulation with appropriate input waveform is sufficient to characterize the electromagnetic behaviour of a system over a wideband of frequencies,

b. Transient field phenomena are well captured, and

c. Materials with non-linearity can be handled only using a time-domain based numerical method.

On the other hand, extra effort is needed in formulating time domain methods to model dispersive media where the material properties change with frequency. In summary, the applicability of the numerical method depends on the problem to be simulated. Of the two popular frequency domain techniques, the field formulation of finite element method (FEM) is based on seeking the solution of the vector Helmholtz equation with the physical electric (and/or magnetic) field as the unknown, while the method of moments (MoM) technique is based on seeking the solution of the electromagnetic fields by setting up an integral equation with the electric (and/or magnetic) current density as the physical unknown.

In the time domain regime, the finite difference time domain (FDTD) [1] is the most popular and established method and is based on seeking direct solution of Maxwell's two curl equations for electric and magnetic fields on a discretized grid. The simiplicity and the efficiency of this method has led to its popularity and several books have appeared on the topic [2–4]. The algorithm has the following key advantages viz., a) it is explicit in nature, i.e., the solution does not require any matrix inversion; b) mesh generation is relatively easy as compared to unstructured mesh generation; c) ability to handle material inhomogeneity is inherent; d) Courant condition for numerical stability is well established; and e) easier implementation of Perfectly Matched Layer (PML) to model unbounded problems. However, major limitation of the method lies with the staircasing errors due to the structured cartesian nature of the computational grid. The modeled geometry must conform to the grid which is in contrast to numerical methods based on unstructured grids, such as FEM. Over the past decade much effort has been put in extending FEM to the time domain regime [5–13]. Many possible formulations are possible and these techniques are collectively knowns as time domain finite element methods. Both FDTD and FEM along with other methods based on them, which seek solution to Maxwell's equations in the differential form, are called as finite methods.

The finite element time domain (FETD) method [8, 10] is a particular class of time domain finite element method having an advantage of unconditional numerical stability. The method is robust and most of the frequency domain concepts can be extended to the time domain. However, the method has not gained equal popularity as the FDTD method because of its two major disadvantages. The first is in the modeling of unbounded medium using PML which is complicated, inefficient and often numerically unstable with no rigorous condition for numerical stability. The second disadvantage, relatively less severe than the first, is the implicit time update equation which requires a sparse matrix solution during each time step. To overcome this loss in efficiency and to enable accurate modeling of geometries, a hybrid method in which the region in the vicinity of the geometry is meshed using unstructured grids conforming to the geometry, while the rest of the physical domain is modelled using traditional FDTD method with Cartesian grids, needs to be used. Such hybrid methods to overcome staircasing errors in FDTD using FETD were proposed in [14–17]. In [15], the 3-D FDTD method is hybridised with FETD on tetrahedral elements but the resulting algorithm is numerically unstable. In [18, 19], based on the equivalence of FDTD and a particular case of FETD method a stable hybrid 3-D FETD-FDTD method was proposed.

The focus of this thesis is in the development and subsequent applications of efficient hybrid time domain finite methods for the numerical solution of time dependent Maxwell's equations. The two finite methods focused are FDTD and FETD methods. The applications of the developed hybrid methods are targeted at, but not restricted to the modeling and simulation of radiation from antennas. The organisation of the thesis is as follows.

In Chapter 2, both FDTD and FETD methods are reviewed and the basic idea of hybridising FDTD with unstructured FETD method proposed earlier in literature is presented. Two kinds of numerical instability is possible in the hybrid method viz., a) weak-instability and b) severe numerical instability. The weak instability, where the

solution grows linearly with time is inherent to the FETD method using edge element basis functions. In Chapter 3, the reason for the linear growth in the solution and a novel method to eliminate the occurrence of such weak-instability using divergence-free constraint equations is proposed. It is found that the problem of linear time growth is analogous to the problem of appearance of non-physical modes in the eigenvalue modeling of electromagnetic resonators. The proposed method for suppressing weak instability in the FETD method can directly be applied to the problem of cavity modeling to suppress the occurrence of spurious modes in the eigenvalue solution. An efficient implementation of the constraint equation using tree-cotree decomposition of the finite element mesh is also presented.

It is possible to have different techniques to hybridise the FDTD and unstructured FETD methods. Often the resulting hybrid method is numerically unstable with the solution exhibiting severe instability rendering the hybrid method unfeasible for practical problems. In Chapter 4, a detailed investigation on the numerical stability of the hybrid method with different hybridisation schemes available in literature is presented. In particular, the stability of stable hybrid FETD-FDTD method is investigated in detail. The equivalence between a particular case of FETD and the FDTD method which leads to symmetric coefficient matrices in the hybrid update equation is demonstrated. The condition for numerical stability is then obtained by analysing the eigenvalues of the global iteration matrix of the hybrid time-marching scheme.

In Chapter 5, a novel method of FDTD subgridding with provable numerical stability is proposed. The subgridding formulation relies on a) having a stable hybrid FDTD-FETD method with structured rectangular or hexahedral elements in the FETD region and b) extending the concept of “hanging variables” to the FETD method. Due to Galerkin-type treatment of the hanging variables in the FETD method, the resulting FETD method has the same conditions of stability as those of regular FETD method. By having the interface between coarse and fine grids of the subgridding mesh in the

FETD region and treating the fine element unknowns on the interface as hanging variables, a stable FDTD subgridding method is achieved. Numerical reflections introduced in the subgridding method are investigated. A procedure for obtaining the analytical lower bound on the level of numerical reflections due to the difference in numerical dispersion in fine and coarse grids, in a general subgridding method is proposed. The proposed subgridding method can reuse the existing mesh generation tools available for the FDTD method and is suitable to model geometrically fine features with a finer grid.

Alternatively, for modeling geometries with fine details, the FETD method on unstructured grids could be employed. In Chapter 6, the application of the 3-D hybrid FETD-FDTD method with automatic hybrid mesh generation is presented. The numerical code developed is targeted for modeling and simulation of radiation from antennas. The application of the basic hybrid method is extended by modeling ports with transverse electromagnetic mode of excitation in the FETD method. Hierarchical higher order basis functions are used in the unstructured finite element region for better field representation and use of a coarser mesh. Computation of the modal reflection coefficient, input impedance and radiation pattern of real world antennas and the results obtained for benchmark problems are presented. Though examples of antenna modeling are considered, the application of the method can be extended to other areas of numerical modeling such as wave scattering and radar cross section (RCS) analysis, electromagnetic compatibility modeling, analysis of passive microwave circuits and studies in dosimetry and tissue interaction.

CHAPTER 2

TIME DOMAIN FINITE METHODS FOR SOLUTION OF MAXWELL'S EQUATIONS

2.1 Maxwell's Equations

The physics of time varying electric and magnetic fields are described by a collective set of equations known as Maxwell's equations [20]. The set of four equations that describe macroscopic electromagnetic phenomena in an arbitrary medium are

$$\nabla \times \vec{E} = -\frac{\partial \vec{B}}{\partial t} \tag{2.1}$$

$$\nabla \times \vec{H} = \frac{\partial \vec{D}}{\partial t} + \vec{J} \tag{2.2}$$

$$\nabla \cdot \vec{D} = \rho \tag{2.3}$$

$$\nabla \cdot \vec{B} = 0 \tag{2.4}$$

where $\vec{E} = \vec{E}(\vec{r}, t)$ is the electric field, $\vec{H}$ denotes the magnetic field, $\vec{D}$ denotes the electric flux density, $\vec{B}$ represents the magnetic flux density, $\vec{J}$ represents the electric current intensity, and ρ denotes the charge density. In above set of equations and in the rest of this thesis, the dependence of the physical quantities on space $\vec{r}$ and time t is implied and not shown explicitly. Eq. (2.1) is the Faraday's law and (2.2) is the Ampere's law. Eqs. (2.3) and (2.4) are Gauss' laws for electric flux and magnetic flux, respectively. The Gauss' laws can be derived from Eqs. (2.1) and (2.2) using continuity equation that relates ρ to $\vec{J}$ based on the conservation of charge [21] given as

$$\nabla \cdot \vec{J} + \frac{\partial \rho}{\partial t} = 0. \tag{2.5}$$

The electric (magnetic) flux and the electric (magnetic) field intensity are related by the constitutive relations. For a simple isotropic, non-dispersive, linear medium, the following constitutive relations hold good viz.,

$$\vec{D} = \varepsilon_0 \varepsilon_r \vec{E} \tag{2.6}$$

$$\vec{B} = \mu_0 \mu_r \vec{H} \tag{2.7}$$

where ε_r and μ_r are the dielectric constant and relative permeability of the medium, while ε_0 and μ_0 are the permittivity and permeability of vacuum or free space. In conductive media, the electric field gives rise to a conduction current $\vec{J_c}$ which leads to the following additional relationship

$$\vec{J_c} = \sigma \vec{E} \tag{2.8}$$

where σ is the electrical conductivity of the medium. In case of insulators, $\sigma = 0$ and for perfect electrical conductors (PEC), $\sigma = \infty$. Materials in general with $\varepsilon_r \neq 1$ and $\sigma \neq 0$ are called lossy dielectrics. In the case of lossy dielectrics, the current density $\vec{J}$ in (2.2) has two components viz.,

$$\vec{J} = \vec{J_c} + \vec{J_i} \tag{2.9}$$

where $\vec{J_i}$ is the impressed or excitation current density. It is this physical quantity that generates the time varying electric and magnetic fields governed by Eqs. (2.1)-(2.4).

There are many possible solutions which satisfy the Maxwell's equations and it is the boundary conditions which lead to a unique solution for a given problem. There are certain properties which the physical field quantities exhibit across material interfaces between regions with different ε_r and(or) μ_r. These properties can be summarised as

follows

$$\hat{n} \times (\vec{E}_1 - \vec{E}_2) = 0 \tag{2.10}$$

$$\hat{n} \times (\vec{H}_1 - \vec{H}_2) = 0 \tag{2.11}$$

$$\hat{n} \cdot (\vec{D}_1 - \vec{D}_2) = 0 \tag{2.12}$$

$$\hat{n} \cdot (\vec{B}_1 - \vec{B}_2) = 0 \tag{2.13}$$

which implies that the tangential component of the electric and magnetic fields is continuous across material interfaces. Similarly the normal component of the electric magnetic flux is continuous. $\hat{n}$ is a normal to the interface. Such physical properties dictate the choice of mathematical functions to be used to represent the particular field quantity.

A particular boundary condition, often used to model highly conductive media is the PEC boundary condition. In case of materials with high conductivity, the skin depth is so low that it is valid to approximate the skin depth to be zero i.e., the induced surface currents are restricted to the surface of the conductor. In this case no fields are sustained inside the medium and the boundary condition is

$$\hat{n} \times \vec{E} = 0 \tag{2.14}$$

meaning the tangential component of the electric field on PEC surface is zero.

Another boundary condition that the electric and magnetic fields satisfy at infinity is the Sommerfeld radiation condition, given by

$$\lim_{r \to \infty} r \left[\nabla \times \vec{E} + \frac{1}{c} \hat{r} \times \frac{\partial \vec{E}}{\partial t} \right] = 0. \tag{2.15}$$

Finally, initial conditions are required for a unique solution with respect to the time variable and this requires the electric and magnetic fields to be known at time $t = 0$.

The finite methods are a class of numerical techniques which seek solution of Maxwell's equations in differential form as in (2.1)-(2.4) subject to specific boundary conditions as dictated by the physical problem being simulated.

2.2 Finite Difference Time Domain Method

The finite-difference time-domain (FDTD) method is a powerful numerical electromagnetic method in solving real life problems in electromagnetics. Introduced by Kane Yee [1] in 1966, this method is a direct solution to the Maxwell's time dependent curl equations. Since then the method has been widely used to simulate and study different electromagnetic phenomena and several books have appeared on the topic [2–4]. The method treats the electric and magnetic field components sampled discretely both in space and time, in a finite volume of space as the physical unknown. The electric field grid is offset from the magnetic field grid both in space and time discretizations. On this discrete staggered grid, application of the central difference to approximate the spatial and temporal derivative that appear in the Maxwell's equations leads to a set of field equations which update the field components at any given time instant at any point in the grid in terms of the past field components. In other words the resulting time-update equations for the field components are explicit.

2.2.1 Field Update Equations

To derive the time update equation, we start from the Maxwell's two curl equations (2.1) and (2.2) coupled with the constitutive relationships for an isotropic lossy medium as

$$\nabla \times \vec{E} = -\mu \frac{\partial \vec{H}}{\partial t} \tag{2.16}$$

$$\nabla \times \vec{H} = \varepsilon \frac{\partial \vec{E}}{\partial t} + \sigma \vec{E} + \vec{J}_i \tag{2.17}$$

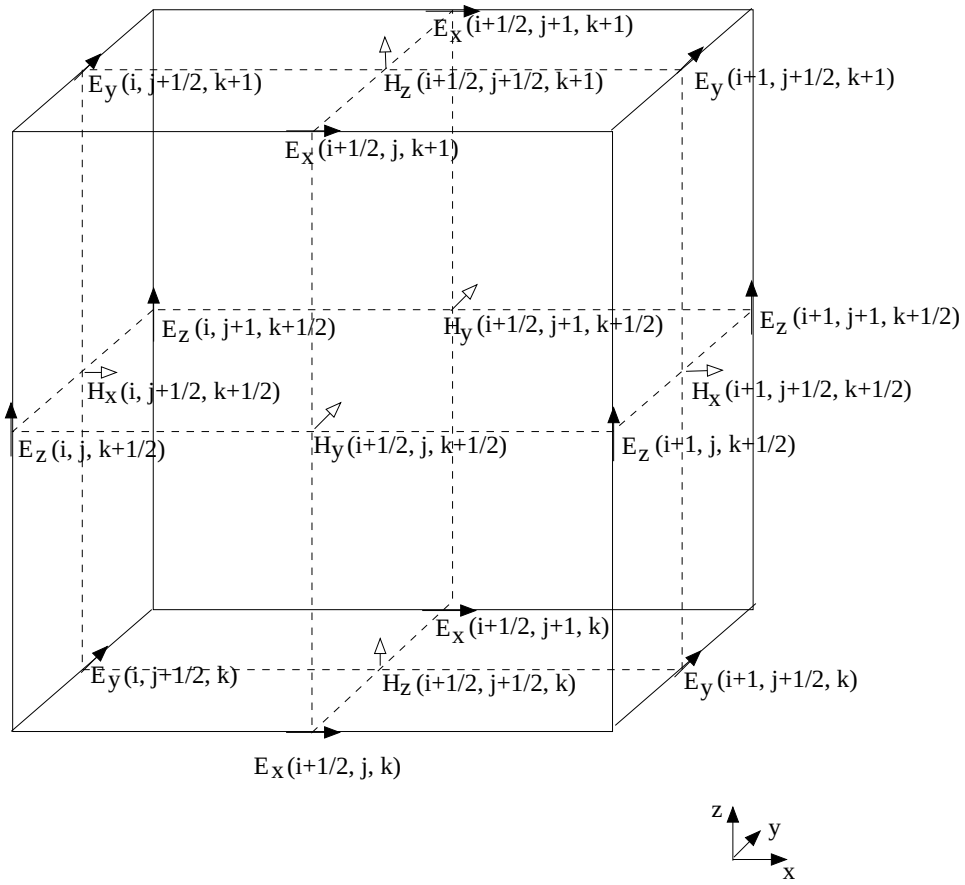

Figure 2.1: Yee cell showing the staggered E and H field unknowns.

The two equations represent a set of six scalar differential equations, which in a Cartesian coordinate system are given by

$$\begin{aligned}
\mu\frac{\partial H_x}{\partial t} &= \frac{\partial E_y}{\partial z} - \frac{\partial E_z}{\partial y} \\
\mu\frac{\partial H_y}{\partial t} &= \frac{\partial E_z}{\partial x} - \frac{\partial E_x}{\partial z} \\
\mu\frac{\partial H_z}{\partial t} &= \frac{\partial E_x}{\partial y} - \frac{\partial E_y}{\partial x} \\
\varepsilon\frac{\partial E_x}{\partial t} &= \frac{\partial H_z}{\partial y} - \frac{\partial H_y}{\partial z} - \sigma E_x - J_x \\
\varepsilon\frac{\partial E_y}{\partial t} &= \frac{\partial H_x}{\partial z} - \frac{\partial H_z}{\partial x} - \sigma E_y - J_y \\
\varepsilon\frac{\partial E_z}{\partial t} &= \frac{\partial H_y}{\partial x} - \frac{\partial H_x}{\partial y} - \sigma E_z - J_z.
\end{aligned} \tag{2.18}$$

The six field components and the six source components are continuous in space and time. To apply finite difference approximation to solve the above set of differential equations, both the unknown and the impressed current source are discretized both in space and time. Let the discrete time step be denoted as Δt and the space step along x, y and z be Δh. Given a continuous scalar function $f(x, y, z, t)$, we denote the discrete function $f^n_{i,j,k}$ as $f(i\Delta h, j\Delta h, k\Delta h, n\Delta t)$. The spatial and temporal derivative operators on the continuous function is approximated as

$$\left.\frac{\partial f}{\partial t}\right|_{(i\Delta h, j\Delta h, k\Delta h, n\Delta t)} \approx \frac{f^{n+1/2}_{i,j,k} - f^{n-1/2}_{i,j,k}}{\Delta t} \tag{2.19}$$

$$\left.\frac{\partial f}{\partial x}\right|_{(i\Delta h, j\Delta h, k\Delta h, n\Delta t)} \approx \frac{f^{n}_{i+1/2,j,k} - f^{n}_{i-1/2,j,k}}{\Delta h}. \tag{2.20}$$

Using the Taylor's series expansion, it can be shown that the above approximations are second order accurate, meaning that when either the time step or the space step is reduced by a factor of N, the error in the approximation decreases by a factor of N^2. Fig. 2.1 shows a unit cell of Yee's staggered grid. The fields are offset such that the a fully explicit finite difference scheme with second order accuracy can be achieved. Using the finite difference approximations for the derivative operators in (2.18), the

following update equations for H_x and E_x components are obtained:

$$H^{n+1/2}_{x(i,j+1/2,k+1/2)} = H^{n-1/2}_{x(i,j+1/2,k+1/2)} + \frac{\Delta t}{\mu \Delta h}\left[E^{n}_{y(i,j+1/2,k+1)} - E^{n}_{y(i,j+1/2,k)} - E^{n}_{z(i,j+1,k+1/2)} + E^{n}_{z(i,j,k+1/2)}\right]$$

$$\begin{aligned} E^{n+1}_{x(i+1/2,j,k)} = &\left[\frac{2\varepsilon - \sigma\Delta t}{2\varepsilon + \sigma\Delta t}\right] E^{n}_{x(i+1/2,j,k)} \\ &+ \frac{2\Delta t}{(2\varepsilon + \sigma\Delta t)\Delta h}\left[H^{n+1/2}_{z(i+1/2,j+1/2,k)} - H^{n+1/2}_{z(i+1/2,j-1/2,k)}\right. \\ &\left. - H^{n+1/2}_{y(i+1/2,j,k+1/2)} + H^{n+1/2}_{y(i+1/2,j,k-1/2)}\right] - \left[\frac{2\Delta t}{2\varepsilon + \sigma\Delta t}\right] J^{n+1}_{x(i+1/2,j,k)}. \end{aligned}$$

Similar updates for H_y, H_z, E_y and E_z components can be obtained. Thus the FDTD update equations reduce to a fully explicit time marching scheme in which the field component at the current time instant is a function of surrounding field components in the previous time step. For such an explicit time marching scheme, to ensure numerical stability, Δt is limited to Δh by the Courant-Friedrich-Lewy or CFL condition [22] given as

$$\Delta t \leq \frac{\Delta h}{v\sqrt{3}} \tag{2.21}$$

where v is the speed of light in the medium. The choice of Δh depends on the desired accuracy. To avoid significant dispersion errors, Δh is set between $\lambda_{min}/10 - \lambda_{min}/30$ where λ_{min} is the wavelength in the medium at the highest frequency of interest.

In a source free region with the absence of free electric charges and with zero electric and magnetic fields as the initial conditions, it can be shown that the FDTD update equations lead to a solution with net electric and magnetic flux leaving an Yee cell to be zero for all time steps. Thus, even though the Gauss' laws viz., (2.3) and (2.4) are not explicitly enforced in the FDTD algorithm, the resulting update equations implicitly ensure the electric and magnetic fluxes to be divergence-free.

2.2.2 Unbounded Media and Perfectly Matched Layer

In an unbounded medium, the radiated fields must satisfy the radiation boundary condition given in (2.15). Since the radiation boundary condition is imposed at $r \rightarrow \infty$, to implement this boundary condition, an infinite computational grid needs to be used which is impractical. The grid needs to be of finite size for implementation in a computer. In this case, the field components at the boundary of the finite grid need special treatment such that boundary conditions based on (2.15), called Absorbing Boundary Conditions (ABCs) are satisfied. ABCs of different orders of accuracy can be devised and implemented based on approximations of (2.15). However, depending on the order, such ABCs have perfect absorption of planewaves for only a limited number of angles of incidence and the levels of reflection at other angles could be significant. Hence, the applicability of such ABCs are limited. Berenger [23] proposed a lossy hypothetical material medium that has no reflection for any angle of incidence and appropriately called the perfectly matched layer (PML). PML could be used to truncate the computational grid. With the PML medium being lossy, all the absorbed waves are attenuated significantly with properly chosen electrical and magnetic conductivities. Berenger's PML is hypothetical and the solution satisfies modified Maxwell's equations based on the concept of "coordinate stretching" [24]. Alternatively, Sack et. al. [25] proposed a physical anisotropic medium with particular form of material tensor for perfect transmission properties. Though the PML was introduced for frequency domain FEM, the method has been adopted for FDTD [26] and extensively applied since. In [27] it was shown that the formulations for both Berenger's PML and anisotropic PML lead to the same modified Helmholtz equation. However, the solution for Berenger's PML is non-Maxwellian with non-zero divergence where as anisotropic PML leads to a solution with divergence condition satisfied as in the real physical solution. Moreover, the formulation of the PML could be easily extended to truncate domain boundary with inhomogeneity as in half space problems. Due to these reasons, the anisotropic PML is a good choice

to terminate FDTD grid. Consider an interface of free space and PML normal to the $z-$ axis. For a plane wave to be absorbed without any reflection, the material medium should be of the form

$$\bar{\bar{\varepsilon}} = \varepsilon_0 \begin{bmatrix} s_z & 0 & 0 \\ 0 & s_z & 0 \\ 0 & 0 & s_z^{-1} \end{bmatrix} \text{ and } \bar{\bar{\mu}} = \mu_0 \begin{bmatrix} s_z & 0 & 0 \\ 0 & s_z & 0 \\ 0 & 0 & s_z^{-1} \end{bmatrix} \tag{2.22}$$

where s_z is in general complex. For such a choice of material tensor, the reflectionless property is independent of the angle of incidence, frequency and polarization of the incident wave. When the computational grid is completely surrounded by PML, apart from PML termination on six sides, edge and corner PML regions exist. The material properties of an anisotropic PML is then given as

$$\bar{\bar{\varepsilon}} = \varepsilon_0 \begin{bmatrix} \frac{s_y s_z}{s_x} & 0 & 0 \\ 0 & \frac{s_x s_z}{s_y} & 0 \\ 0 & 0 & \frac{s_x s_y}{s_z} \end{bmatrix} \text{ and } \bar{\bar{\mu}} = \mu_0 \begin{bmatrix} \frac{s_y s_z}{s_x} & 0 & 0 \\ 0 & \frac{s_x s_z}{s_y} & 0 \\ 0 & 0 & \frac{s_x s_y}{s_z} \end{bmatrix}. \tag{2.23}$$

For the medium to absorb, the incident plane wave loss terms need to be introduced by choosing

$$s_\xi = 1 + \frac{\sigma_\xi}{j\omega\varepsilon_0}, \quad \xi = x, y, z \tag{2.24}$$

where σ_ξ is the conductivity along the ξ axis and is variant only with ξ. Different possible choices of s_ξ lead to different types of PML. For instance, in the case of the Complex Frequency Shifted PML, $s_\xi = k_\xi + \frac{\sigma_\xi}{\alpha_\xi + j\omega\varepsilon_0}$ with additional parameters k_ξ and α_ξ introduced, better absorption efficiency can be achieved. Even for the simplest choice as in (2.24), it is immediately observed that the PML is dispersive in nature. In FDTD, being a time domain method, special treatment is needed to handle such a dispersive media. Implementation of the PML in the FDTD method by introducing additional variables for the electric flux $\vec{D}$ and magnetic flux $\vec{B}$ is straight forward [26]. The key to the efficient implementation on PML in the FDTD method is to define constitutive

relationships such that the frequency dependent terms are decoupled making it easy to transform the resulting equations to the time domain. Specifically, defining

$$\vec{D} \equiv \begin{bmatrix} D_x \\ D_y \\ D_z \end{bmatrix} = \varepsilon_0 \begin{bmatrix} \frac{s_z}{s_x} & 0 & 0 \\ 0 & \frac{s_x}{s_y} & 0 \\ 0 & 0 & \frac{s_y}{s_z} \end{bmatrix} \begin{bmatrix} E_x \\ E_y \\ E_z \end{bmatrix}, \tag{2.25}$$

which leads to

$$\nabla \times \vec{H} \equiv \begin{bmatrix} \frac{\partial}{\partial y} H_z - \frac{\partial}{\partial z} H_y \\ \frac{\partial}{\partial z} H_x - \frac{\partial}{\partial x} H_z \\ \frac{\partial}{\partial x} H_y - \frac{\partial}{\partial y} H_x \end{bmatrix} = j\omega \begin{bmatrix} s_y & 0 & 0 \\ 0 & s_z & 0 \\ 0 & 0 & s_x \end{bmatrix} \begin{bmatrix} D_x \\ D_y \\ D_z \end{bmatrix}. \tag{2.26}$$

The transformation of (2.26) and (2.25) to time domain with s_ξ as in (2.24) and the subsequent discretization using central differencing lead to efficient explicit update equations for $\vec{D}$ and $\vec{E}$ [26]. The update equations for D_x and E_x components are

$$\begin{aligned} D^{n+1}_{x(i+1/2,j,k)} &= \frac{2\varepsilon_0 - \sigma_y \Delta t}{2\varepsilon_0 + \sigma_y \Delta t} D^n_{x(i+1/2,j,k)} \\ &\quad + \frac{2\varepsilon_0 \Delta t}{(2\varepsilon_0 + \sigma_y \Delta t)\Delta h} \Big[H^{n+1/2}_{z(i+1/2,j+1/2,k)} - H^{n+1/2}_{z(i+1/2,j-1/2,k)} \\ &\qquad - H^{n+1/2}_{y(i+1/2,j,k+1/2)} + H^{n+1/2}_{y(i+1/2,j,k-1/2)} \Big] \\ E^{n+1}_{x(i+1/2,j,k)} &= \frac{2\varepsilon_0 - \sigma_z \Delta t}{2\varepsilon_0 + \sigma_z \Delta t} E^n_{x(i+1/2,j,k)} \\ &\quad + \frac{2\varepsilon_0 \Delta t}{(2\varepsilon_0 + \sigma_z \Delta t)\varepsilon_0} \left[\left(1 + \frac{\sigma_x \Delta t}{2\varepsilon_0}\right) D^{n+1}_{x(i+1/2,j,k)} \right. \\ &\qquad \left. - \left(1 - \frac{\sigma_x \Delta t}{2\varepsilon_0}\right) D^n_{x(i+1/2,j,k)} \right]. \end{aligned}$$

Similar update equations for the magnetic field, with the magnetic flux defined appropriately, can be obtained.

2.2.3 Far-field Computation

The FDTD method being a finite method, is inherently a near-field technique which computes the fields within a finite region of interest. In radiation and scattering problems, it is necessary to know the far-zone fields to compute radiation pattern or radar

cross section (RCS) pattern. To extract the far-zone fields from the near field solution, near-field to far-field (NFFF) transformation based on the surface equivalence principle needs to be applied. It is possible to have two types of formulations viz., a) Time domain NFFF transformation and b) Frequency domain NFFF transformation. The time domain NFFF transformation is efficient to compute the far-field pattern over a band of frequencies at a specific direction, as in the case of monostatic RCS or antenna gain computation. The frequency domain NFFF transformation is efficient to compute the complete radiation or scattering pattern at a few discrete frequency points. Both the formulations involve a closed virtual surface S around the antenna or scatterer geometry. In case of radiation problems, the antenna with the excited source is enclosed by S. In the case of scattering problems, a total-field/scattered-field boundary condition is implemented which divides the computational region into a) total-field region enclosing the scatterer with both the incident and scattered fields and b) scattered-field region enclosing the total-field region where scattered field solution alone is present. The surface S is then placed in the scattered-field region to compute the far-zone scattered fields. From the tangential electric and magnetic fields on this surface, equivalent electric and magnetic currents are computed. With the equivalent currents as the source and using free space Green's function, the radiated or scattered electric field in the far-zone is computed. In the frequency domain NFFF transformation, the electric field in the far-zone is computed as

$$\vec{E}(\vec{r},\omega) = \frac{j\omega\mu_0}{4\pi r}\oint_S \left\{ \hat{r}\times\hat{r}\times\left[\hat{n}\times\vec{H}(\vec{r}',\omega)\right] - \frac{1}{\eta_0}\hat{r}\times\left[\hat{n}\times\vec{E}(\vec{r}',\omega)\right]\right\} \times \exp\left[-\frac{j\omega(r-\hat{r}\cdot\vec{r}')}{c}\right] ds' \tag{2.27}$$

where $\vec{r}$ is the observation point, $\vec{r}'$ is the source point on the virtual surface S and $\hat{n}$ is the unit outward normal to S. The tangential electric and magnetic fields on the surface S in (2.27) are in the frequency domain. In the discrete implementation of (2.27) with in the FDTD method, the closed surface S is chosen as a box conforming with the electric

field grid. Form the time domain fields on the center of each patch of the surface S, computed by a simple average of the neighbouring fields, the frequency domain fields at a particular frequency ω are obtained by a computationally efficient running-sum implementation of the discrete Fourier transform. Subsequently, the surface integral in (2.27), is carried out across all the patches on S.

In the time domain NFFF transformation, the time domain equivalent of (2.27) which involves the time domain Green's function is employed to extract the far-zone fields directly in the time domain. Specifically, by defining

$$\vec{W}(\vec{r},t) = \frac{1}{4\pi r c}\frac{\partial}{\partial t}\left[\oint_S \hat{n}\times\left[\vec{H}\left(\vec{r}',t-\tau_d\right)\right]dS'\right] \tag{2.28}$$

$$\vec{U}(\vec{r},t) = -\frac{1}{4\pi r c}\frac{\partial}{\partial t}\left[\oint_S \hat{n}\times\left[\vec{E}\left(\vec{r}',t-\tau_d\right)\right]dS'\right] \tag{2.29}$$

with the retardation time $\tau_d = \frac{r-\vec{r}'\cdot\hat{r}}{c}$, the far-zone electric field is computed as follows

$$E_\theta(\vec{r},t) \cong -\eta_0 W_\theta(\vec{r},t) - U_\phi(\vec{r},t) \tag{2.30}$$

$$E_\phi(\vec{r},t) \cong -\eta_0 W_\phi(\vec{r},t) + U_\theta(\vec{r},t). \tag{2.31}$$

Update equations based on the discretization of (2.28) and (2.29) with central differencing in time and with linear interpolation of temporal samples in the apportioning of time delayed electric and magnetic currents can be obtained [28].

2.3 Finite Element Time Domain Method

The finite element method (FEM) is a robust mathematical technique that has been extensively used for the numerical solutions to many kinds of boundary value problems often encountered in different areas of engineering and mathematical physics [29]. In computational electromagnetics, FEM was initially applied for the time-harmonic solution of Maxwell's equations [30], [31] and has been successful in modeling real world problems. These developments have lead to development of many commercial CEM

tools for full wave electromagnetic analysis. Over the past decade, the extension of FEM to the time domain has been explored by many researchers [5–12] and aspects of different techniques collectively referred to Time Domain Finite Element Methods (TDFEM) have been reviewed in [13]. The class of TDFEM formulated based on the second order vector Helmholtz equation with the electric field as physical quantity [8, 10] is referred to as finite element time domain (FETD) method . The underlying physical equation is similar to that of frequency domain based FEM formulation.

2.3.1 Vector Wave Equation

The vector wave equation or the vector Helmholtz equation can be obtained from Maxwell's equations by either eliminating the electric or the magnetic field. Eliminating the magnetic field in (2.1) and (2.2), we obtain

$$\nabla \times \frac{1}{\mu_r} \nabla \times \vec{E} + \varepsilon_r \frac{1}{c^2} \frac{\partial^2 \vec{E}}{\partial t^2} = -\mu_0 \frac{\partial \vec{J}_i}{\partial t} \quad , \text{in } \Omega. \tag{2.32}$$

For the sake of simplicity, only lossless media are considered. It is straight forward to extend the formulation to lossy media. For the time being it is assumed that the domain boundary is PEC. Hence the boundary conditions and initial conditions for the solution is

$$\hat{n} \times \vec{E} = 0 \quad \text{on } \Gamma \tag{2.33}$$

$$\vec{E}|_{t=0} = 0 \tag{2.34}$$

$$\left. \frac{\partial \vec{E}}{\partial t} \right|_{t=0} = 0. \tag{2.35}$$

2.3.2 Function Spaces and Galerkin's Method

We seek a solution of $\vec{E}$ with in a space of admissible vector functions $\mathcal{H}(\text{curl}, \Omega)$ such that the solution satisfies (2.32) . The physical properties of $\vec{E}$ are vital to choose the admissible function space. In order to have both $\vec{E}$ and $\vec{B}$ to have finite energy, it is necessary that any vector function $\vec{u} \in \mathcal{H}(\text{curl}, \Omega)$ and $\nabla \times \vec{u}$ to be square integrable, i.e.,

$$\vec{E} \in \mathcal{H}(\text{curl}, \Omega) = \left\{ \vec{u} | \int_{\Omega} \left[|\vec{u}|^2 + |\nabla \times \vec{u}|^2 \right] < \infty \right\}. \tag{2.36}$$

Moreover by the medium boundary interface condition on the tangential component of the electric field as in (2.10), $\vec{u} \in \mathcal{H}(\text{curl}, \Omega)$ must have tangentially continuity across material interfaces. Finally, the PEC boundary condition on Γ requires every vector function $\vec{u} \in \mathcal{H}(\text{curl}, \Omega)$ to have zero tangential component along the boundary Γ. For every trial vector $\vec{u} \in \mathcal{H}(\text{curl}, \Omega)$, there is a corresponding non-zero residual

$$\mathcal{R}(\vec{u}) = \nabla \times \frac{1}{\mu_r} \nabla \times \vec{u} + \varepsilon_r \frac{1}{c^2} \frac{\partial^2 \vec{u}}{\partial t^2} + \mu_0 \frac{\partial \vec{J}_i}{\partial t} \tag{2.37}$$

By testing the residual with testing functions in a suitable testing function space, which in this case is $\mathcal{H}(\text{curl}, \Omega)$, the Galerkin statement is obtained as follows :

Seek $\vec{u}(t) \in \mathcal{H}(\text{curl}, \Omega)$ such that

$$\begin{aligned} \mathcal{B}(\vec{v}, \vec{u}) = \int_{\Omega} \vec{v} \cdot \left[\nabla \times \frac{1}{\mu_r} \nabla \times \vec{u} + \varepsilon_r \frac{1}{c^2} \frac{\partial^2 \vec{u}}{\partial t^2} + \mu_0 \frac{\partial \vec{J}_i}{\partial t} \right] d\Omega = 0 \\ \forall \vec{v} \in \mathcal{H}(\text{curl}, \Omega) \text{ and } t \in (0, T). \end{aligned} \tag{2.38}$$

Using vector Green's theorem in (2.38), the following weak form is obtained as

Seek $\vec{u}(t) \in \mathcal{H}(\text{curl}, \Omega)$ such that

$$\begin{aligned} \mathcal{B}(\vec{v}, \vec{u}) = \int_{\Omega} \left[\nabla \times \vec{v} \cdot \frac{1}{\mu_r} \nabla \times \vec{u} + \varepsilon_r \frac{1}{c^2} \vec{v} \cdot \frac{\partial^2 \vec{u}}{\partial t^2} + \mu_0 \vec{v} \cdot \frac{\partial \vec{J}_i}{\partial t} \right] d\Omega \\ - \int_{\Gamma} \vec{v} \cdot \frac{1}{\mu_r} (\nabla \times \vec{u}) \times \hat{n} \, ds = 0, \\ \forall \vec{v} \in \mathcal{H}(\text{curl}, \Omega) \text{ and } t \in (0, T). \end{aligned} \tag{2.39}$$

The surface integral term in (2.39) is a consequence of the Green's theorem and vanishes because $\hat{n} \times \vec{v} = 0$ along Γ. The finite element procedure is then to generate a finite dimensional subspace $\mathcal{V}^h \subset \mathcal{H}(\text{curl}, \Omega)$ by partitioning or discretizing Ω into a finite set of elements. Such a discretization of Ω is denoted as Ω^h. The superscript h denotes the maximum edge length of the finite element discretization. The discrete equivalent of (2.39) is then

Seek $\vec{u}_h(t) \in \mathcal{V}^h$ such that

$$\int_\Omega \left[\nabla \times \vec{v}_h \cdot \frac{1}{\mu_r} \nabla \times \vec{u}_h + \varepsilon_r \frac{1}{c^2} \vec{v}_h \cdot \frac{\partial^2 \vec{u}_h}{\partial t^2} + \mu_0 \vec{v}_h \cdot \frac{\partial \vec{J}_i}{\partial t} \right] d\Omega = 0, \quad \forall \vec{v}_h \in \mathcal{V}^h \text{ and } t \in (0, T). \tag{2.40}$$

The next step is to choose appropriate and suitable spatial vector basis functions that span the finite dimensional subspace $\mathcal{V}^h$ defined on the discretization Ω^h. The vector basis functions are denoted as $\vec{W}_i$ ($i = 1 \cdots N$ with N being the degrees of freedom). The trial and testing functions in (2.40) are expanded using these basis functions as

$$\vec{u}_h(t) = \sum_{i=1}^{N} u_i(t) \vec{W}_i \,, \qquad \vec{v}_h = \sum_{i=1}^{N} v_i \vec{W}_i$$

where $u_i(t)$ is the time varying coefficient of the basis function $\vec{W}_i$ in the expansion of $u_h(t)$. The condition that (2.40) holds true for all $\vec{v}_h \in \mathcal{V}^h$ leads to the following system of semi-discrete ordinary differential equations which is still continuous in time viz.,

$$\mathbf{T} \frac{1}{c^2} \frac{d^2 \mathbf{u}}{dt^2} + \mathbf{S}\mathbf{u} + \mathbf{f} = 0 \tag{2.41}$$

where $\mathbf{u} = [u_1(t) u_2(t) \cdots u_N(t)]^t$ is a vector of time dependent coefficients and

$$S_{ij} = \int_{\Omega} \nabla \times \vec{W}_i \cdot \frac{1}{\mu_r} \nabla \times \vec{W}_j \; d\Omega \tag{2.42}$$

$$T_{ij} = \int_{\Omega} \vec{W}_i \cdot \varepsilon_r \vec{W}_j \; d\Omega \tag{2.43}$$

$$f_i = \mu_0 \int_{\Omega} \vec{W}_i \cdot \frac{\partial \vec{J}}{\partial t} \; d\Omega. \tag{2.44}$$

$\mathbf{S}$ is the stiffness matrix and $\mathbf{T}$ the mass matrix. It is easy to see from definition of $\mathbf{T}$ that it is a positive definite matrix. However, $\mathbf{S}$ matrix is positive semi-definite. The zero eigenvalues are due to the non-zero null space of the curl ($\nabla\times$) operator. The vector $\mathbf{f}$ is called the source or the excitation vector with the impressed electric current as the source term.

2.3.3 Spatial Discretisation and Vector Finite Element Basis Functions

In the FEM formulation, the domain Ω is discretized into finite elements. Triangular and rectangular finite elements are widely used in 2-D and similarly tetrahedral and rectangular brick elements are popular choices in 3-D. Unstructured mesh generators, using triangular and tetrahedral elements, can represent the modeled geometry accurately. Rectangular and brick elements, similar to the FDTD Yee cell, are used in structured Cartesian mesh generators which apply stair-case approximations on the modeled geometry. The robustness of FEM is that it is not essential that only a particular finite element should be used in the discretization of Ω. Hybrid meshes with two or more kinds of finite elements can be used, as long as the basis functions (which span $\mathcal{V}^h \subset \mathcal{H}(\text{curl}, \Omega)$) are well defined. The lowest order basis functions which span $\mathcal{V}^h$ are termed as edge vector basis functions or edge elements [32], [33]. These basis functions are the same as Whitney 1-form elements, useful in interpolating vector fields using the circulation of the field along the edges of the element [34, 35]. These vector basis functions are associated with each edge of the finite element mesh and have a constant

tangential component along that edge. The tangential component across other edges is zero. This property of the basis function ensures the tangential continuity of the vector field it represents and hence makes it a suitable choice for representing the electric field. Another important property of this basis function is to be able to span a gradient space. When nodal basis functions are used in seeking FEM solution for the Helmholtz equation, spurious modes occur and corrupt the approximate numerical solution. When tangential vector finite elements, which span a the gradient vector field are used, the frequencies of the spurious modes are at zero or DC [36].

In the case of triangular and tetrahedral elements, edge element basis functions are defined as

$$\vec{W}_{ij} = \xi_i \nabla \xi_j - \xi_j \nabla \xi_i \tag{2.45}$$

where ξ_i is the scalar linear Lagrange interpolation polynomial associated with node i i.e., ξ_i is a linear function being unity at node i and zero at the other nodes of the triangle or tetrahedron. $\vec{W}_{ij}$ is the basis function associated with the edge formed by the nodes i and j. The plot of the 3 basis functions of a particular triangular element is shown in Fig. 2.2. It is seen that each basis function, as desired, has tangential component across its associated edge alone and only normal component along the other edges. Moreover, edge elements have the property of

$$\int_i^j \vec{W}_{ij} \cdot \vec{dl} = 1. \tag{2.46}$$

For this reason, the coefficient of the edge basis function is simply the circulation of the electric field along its associated edge. To have the coefficient of basis functions which represent directly the electric field along its associated edge, the basis function defined in (2.45) is simply scaled as

$$\vec{N}_{ij} = l_{ij} \vec{W}_{ij} = l_{ij} \left[\xi_i \nabla \xi_j - \xi_j \nabla \xi_i \right] \tag{2.47}$$

where l_{ij} is the length of the associated edge. Another property of the edge element

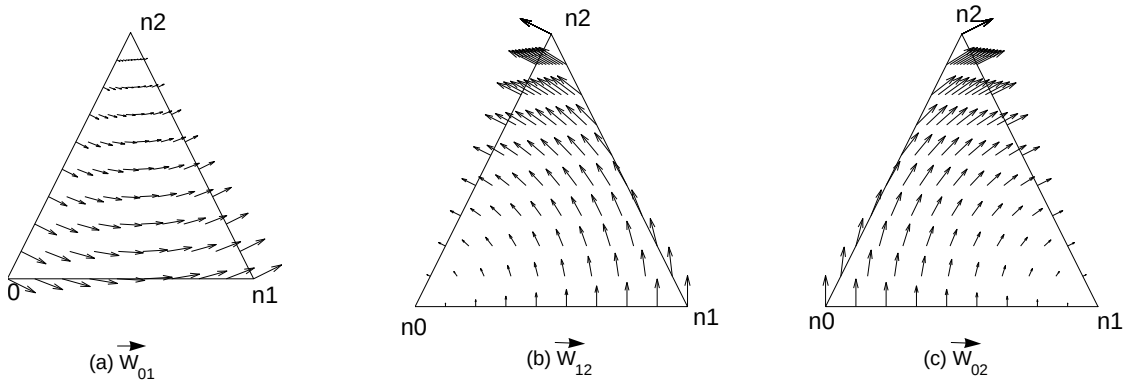

Figure 2.2: Edge element basis functions on a triangular element.

basis functions is that the divergence of each basis function within an element is zero. However, within a tetrahedral element, vector functions with non-zero divergence i.e., those vector functions which are gradients of scalar fields, can be represented using these basis functions. In fact, it is because of these gradient fields, which span the null space of the curl operator, that the frequency of the spurious modes is reduced to zero frequency [36]. Edge element basis functions can similarly be defined on rectangular and hexahedral elements. In the case of rectangular elements, the basis functions are defined as

$$\begin{aligned} \vec{W}_{ij} &= \xi_i \nabla(\xi_j + \xi_k) - \xi_j \nabla(\xi_i + \xi_l) \\ &= \hat{e}_{ij} \left(\xi_i + \xi_j\right) \end{aligned} \tag{2.48}$$

where $\hat{e}_{ij}$ is a unit vector along the nodes i and j. ξ_i is a linear scalar function with unity at node i and zero at other three nodes of the rectangle. The plot of the vector basis functions on a 2-D rectangular element is shown in Fig. 2.3. These basis functions have finite support, basically in the two elements sharing the associated edge. Such local finite support of the basis function, typical in FEM, leads to system matrices which are sparse.

Vector basis functions are complete to order p when any vector function in their function space and the curl of the function are polynomials of utmost degree p. In the

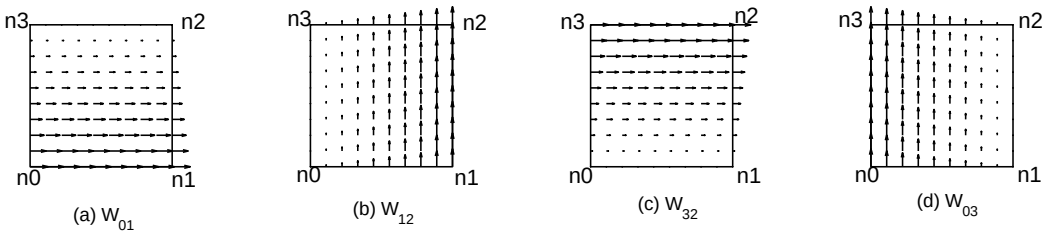

Figure 2.3: Edge element basis functions on a rectangular element.

case of the edge elements it is easy to see that the curl of the basis function is a constant. Hence, edge element basis functions are complete to order zero and are called the zeroth order basis functions. In terms of convergence, they exhibit second order accuracy with respect to the mesh size i.e., the error in the numerical solution is $O(h^2)$. It is possible to construct higher order basis functions which are of two types viz., a) hierarchical basis functions [37] and b) interpolatory basis functions [38]. With hierarchical basis functions, it is possible to have a finite element mesh with different orders of basis functions for different elements. For this reason, hierarchical basis functions are suitable for $p-$ adaptive mesh refinement. The advantage of interpolatory basis functions over hierarchical is that such basis functions have high linear independence leading to a well-conditioned mass matrix. This is not generally the case in hierarchical basis functions even though it is possible to construct higher order basis functions with good linear independence [39].

With respect to the assembly of finite element mass and stiffness matrices in a computer implementation, there are many possible approaches. For edge elements on rectangular and hexahedral elements the matrices can be computed analytically [31]. Similar closed form representation of the matrices for edge elements, in terms of the coordinates of the three nodes of an arbitrary triangle or four nodes of an arbitrary tetrahedron is possible. Alternatively, assembling the matrices using numerical integration rules such as Gaussian quadrature rules for triangular and tetrahedral elements can be adopted, but

seldom used as this approach is more CPU intensive. However, computing the elemental matrices using appropriate numerical integration rules can offer other advantages such as improvements in the condition of the matrices. For instance in [40], GaussLobattoLegendre quadrature rules are used resulting in a block diagonal mass matrix which is trivial to invert. The most efficient way to compute element matrices, especially for hierarchical higher order basis functions, is by having universal matrices as described in [37] which are independent of the triangular or tetrahedral element. For arbitrary elements, the matrices can be obtained from the universal matrices. The method of having universal matrices is easy to extend to higher order hierarchical basis functions.

2.3.4 Temporal Discretization

Many possible time integration schemes are possible for the temporal discretization of the second order ordinary differential equations in (2.41) [8, 10]. In particular, the Newmark-beta formulation is attractive since it leads to a scheme which is unconditionally stable and has second order accuracy in the discrete approximation [41]. By applying Newmark-beta scheme, (2.41) is approximated as

$$\begin{aligned}\mathbf{T}\frac{1}{c^2\Delta t^2}\left[\mathbf{u}^{n+1}-2\mathbf{u}^{n}+\mathbf{u}^{n-1}\right]+\mathbf{S}\left[\beta\mathbf{u}^{n+1}+(1-2\beta)\mathbf{u}^{n}+\beta\mathbf{u}^{n-1}\right]\\ +\left[\beta\mathbf{f}^{n+1}+(1-2\beta)\mathbf{f}^{n}+\beta\mathbf{f}^{n-1}\right]=0\end{aligned} \tag{2.49}$$

where β is a constant and Δt is the time step size and n indicates the time index i.e., $\mathbf{u}^n = [u_1(n\Delta t)\, u_2(n\Delta t)\, \cdots\, u_N(n\Delta t)]^t$. The above discretization leads to the following update equation for the unknown coefficients at time step $n+1$

$$\begin{aligned}\left[\mathbf{T}+\beta c^2\Delta t^2\mathbf{S}\right]\mathbf{u}^{n+1}=\left[2\mathbf{T}-(1-2\beta)c^2\Delta t^2\mathbf{S}\right]\mathbf{u}^{n}\\ -\left[\mathbf{T}+\beta c^2\Delta t^2\mathbf{S}\right]\mathbf{u}^{n-1}\\ -c^2\Delta t^2\left[\beta\mathbf{f}^{n+1}+(1-2\beta)\mathbf{f}^{n}+\beta\mathbf{f}^{n-1}\right]\end{aligned} \tag{2.50}$$

In [10] it is shown that (2.50) is numerically stable for $\beta \geq \frac{1}{4}$. The Newmark-beta method is a particular case of general implicit two-step recurrence algorithms discussed in [13] with parameter $\Theta_1 = 0$ and $\Theta_2 = \frac{\beta}{2}$. A truncation error of $O(\Delta t^2)$ is achieved when $\beta = \frac{1}{4}$.

Based on the respective positive definite and positive semi-definite properties of $\mathbf{T}$ and $\mathbf{S}$ matrix, the proof for the unconditional stability of the implicit update equation (2.50) was shown in [10] using an eigenvalue analysis of the iteration matrix. Similar proof for unconditional stability using modal decomposition can be obtained [13]. Unconditional stability implies that there is no upper bound for Δt dictated by the spatial discretization size, unlike the FDTD method which is conditionally stable. The choice of Δt is based on the accuracy requirement and based on heuristic assumptions is often set as $\frac{0.1}{f_{max}}$ where f_{max} is the highest frequency of interest. Such a time step corresponds to one-tenth the time period of a signal with frequency f_{max}.

2.3.5 Matrix Solution Techniques

The FETD update equation (2.50) being implicit in nature requires a solution of a matrix equation of the form

$$\mathbf{A}\mathbf{x} = \mathbf{b} \tag{2.51}$$

where $\mathbf{A} = \mathbf{T} + \beta c^2 \Delta t^2 \mathbf{S}$, $\mathbf{x}$ is the unknown basis function coefficients at the current time step, and $\mathbf{b}$ is the excitation vector containing the source term and the solution at the previous time steps. Either a direct solver or an iterative solver could be used for the matrix solution. The fact that the matrix $\mathbf{A}$ is symmetric positive definite (s.p.d) guarantees a Cholesky factorization of the form

$$\mathbf{A} = \mathbf{L}\mathbf{L}^t \tag{2.52}$$

to exist. $\mathbf{L}$ is the Cholesky factor of $\mathbf{A}$. In case of a direct solver, the complete Cholesky factor is computed and the matrix solution is subsequently obtained in two steps viz.,

a forward substitution and a backward substitution. The computational complexity of Cholesky factorization in terms of floating point operations is $O(N^2)$ and the memory requirement is $O(N^{\frac{3}{2}})$. Each forward or backward substitution requires $O(N^{\frac{3}{2}})$ flops. As the number of unknowns increases it is expensive both in terms of storage of the complete Cholesky factor and flops involved in a matrix solution step. In such a case, it is efficient to use an iterative solver such as Conjugate Gradient solver. Such a Krylov subspace based solver requires a matrix-vector multiplication to be performed during each iteration till a specified convergence criteria is met. The storage requirement in this case is the storage requirement of the original matrix $\mathbf{A}$ which is $O(N)$ and the number of flops required is $O(n_{CG}N)$ where n_{CG} is the number of iterations in conjugate gradient method for the solution to converge. The convergence criteria is set on the relative residual defined as

$$res = \frac{\|\mathbf{b} - \mathbf{A}\mathbf{x}_n\|}{\|\mathbf{b}\|} \tag{2.53}$$

where $\mathbf{x}_n$ is the solution at the nth iteration of the conjugate gradient method. When the relative residual is below certain specified tolerance δ, the iterative solver is said to have converged. The matrix $\mathbf{A}$ being s.p.d. in nature, the CG iterations are guaranteed to converge. n_{CG} depends on the condition number of $\mathbf{A}$ denoted as $\kappa(\mathbf{A})$ which in turn is dependent on the electrical size of the elements and the quality of the mesh. As $\mathbf{A}$ is a normal matrix, the condition number is defined as the ratio of the maximal and minimal eigenvalues of $\mathbf{A}$. The stiffness matrix, $\mathbf{S}$ being positive semi-definite, the minimal eigenvalue of $\mathbf{A}$ is bounded by the minimal eigenvalue of the mass matrix $\mathbf{T}$. The matrix $\mathbf{T}$ in general, is well conditioned for a good quality mesh and $\kappa(\mathbf{T})$ is bounded for a uniform finite element mesh. However, in the case of the stiffness matrix $\mathbf{S}$, its condition number is inversely proportional to the finite element mesh size h as $\kappa(\mathbf{S}) \propto \frac{1}{h^2}$. To illustrate this fact, an example of 1 cm$\times$1 cm$\times$1 cm PEC cavity, discretized with tetrahedral elements is considered. Fig. 2.4 shows the dependence of

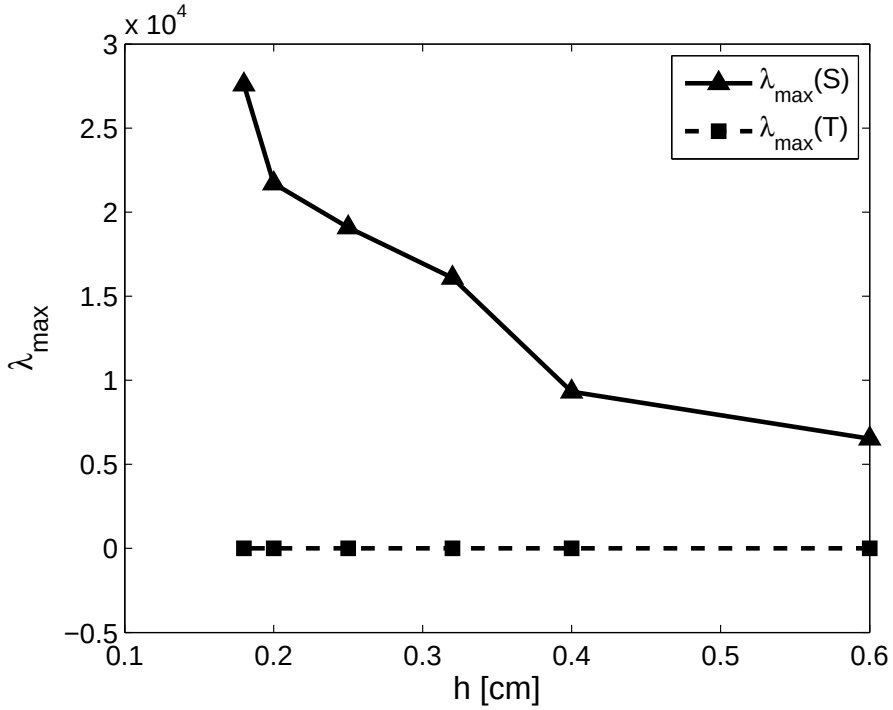

Figure 2.4: Maximum eigenvalues of $\mathbf{S}$ and $\mathbf{T}$ matrices of simple rectangular PEC cavity.

the maximum eigenvalues of $\mathbf{S}$ and $\mathbf{T}$ matrices for the cavity under different discretization sizes h. Also, the number of zero eigenvalues of $\mathbf{S}$ increases when the mesh size h is decreased. Thus, the condition number of $\mathbf{S}$ and hence of $\mathbf{A}$ deteriorates when the mesh is refined, with Δt being fixed by the maximum frequency of interest. For large $\kappa(\mathbf{A})$, $n_{CG} \propto \sqrt{\kappa(\mathbf{A})}$ [9], [42] and hence the number of iterations for the CG method to converge increases when the mesh size is electrically small. This problem can be mitigated to a degree by having Δt bound to Δh i.e., with $\frac{c\Delta t}{\Delta h} = C$ where C is a constant. However, such a condition limits the full potential of the unconditional stability of FETD. An alternate solution is to use a preconditioned conjugate gradient (PCG) solver to overcome, to a certain extent, the problems of high condition number of the system matrix. This method is based on constructing an effective preconditioner $\mathbf{M}$ and applying the CG method on a modified problem of the form

$$\mathbf{M}^{-1}\mathbf{A}\mathbf{x} = \mathbf{M}^{-1}\mathbf{b}. \tag{2.54}$$

When the preconditioner $\mathbf{M}$ approximates the original matrix $\mathbf{A}$ and its inverse is easier to compute, then the conjugate gradient method on the modified system is highly efficient compared to the original system of equations. An incomplete Cholesky factor of $\mathbf{A}$ which essentially is computed by Guassian elimination but modified based on strategies such as "drop tolerance" and (or) "levels of fill" with benefits of reduced memory requirements and flops at the cost of a crude approximation to $\mathbf{A}$, often performs well as a highly efficient preconditioner. In this case, the preconditioner $\mathbf{M} = \mathbf{R}\mathbf{R}^t \approx \mathbf{A}$ is never explicitly constructed; instead the incomplete Cholesky factor $\mathbf{R}$ is computed. The matrix-vector multiplication operations of the form $\mathbf{M}^{-1}\mathbf{z}$ is simply performed by forward and backward substitutions using $\mathbf{R}$. An efficient preconditioner is one for which $\kappa(\mathbf{M}^{-1}\mathbf{A})$ is bounded and independent of the mesh size h. The ideal pre-conditioner, constructed using the complete Cholesky factorization of $\mathbf{A}$, requires only one iteration in the PCG solver irrespective of the mesh size h. However, this comes under the cost of high memory requirement, as mentioned earlier. Incomplete factorization on the other hand decreases the memory requirement in storing the preconditioner but at the cost of increased CG iterations. Thus, in choosing a preconditioner, there is a trade off between memory requirement and CPU time. In the decomposition of $\mathbf{A}$, re-ordering of the unknown indexes results in significant improvements in the sparsity of resulting $\mathbf{R}$. Many reordering schemes such as minimal degree ordering or nested dissection are available. Sparse matrix solver packages such as TAUCS [43] have built in interfaces to different reordering algorithms. One such powerful re-ordering routine is METIS which is based on nested-dissection/minimum-degree re-ordering [44].

Fig. 2.5 and Fig. 2.6 illustrate the advantages of matrix re-ordering in improving the sparsity of the Cholesky factor. Fig. 2.5(a) shows the sparsity pattern of the typical system matrix $\mathbf{A}$ for a finite element mesh with arbitrary ordering of edges. Fig. 2.5(b) shows the sparsity of the complete Cholesky factor, $\mathbf{L}$, which is a lower triangular matrix. It is observed that the number of non-zero entries is 464,082. Fig. 2.6(a) shows

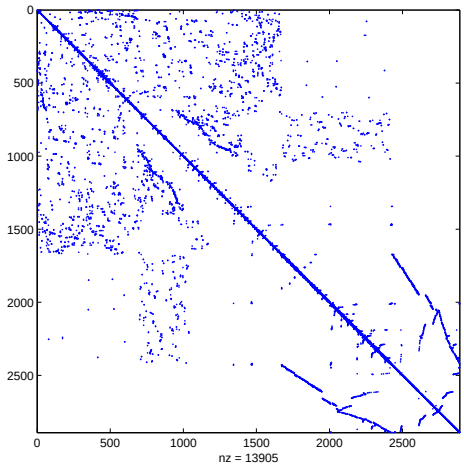

(a) **A** matrix

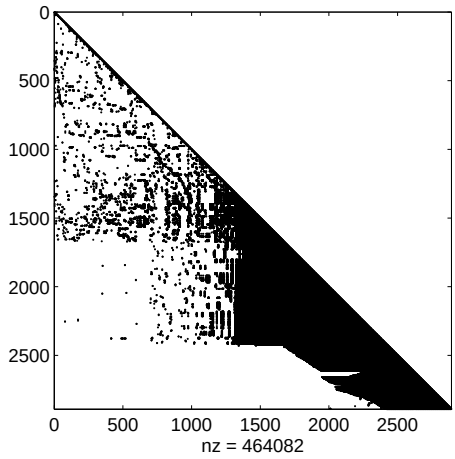

(b) **L** matrix

Figure 2.5: System matrix **A** with arbitrary ordering and its corresponding Cholesky factor.

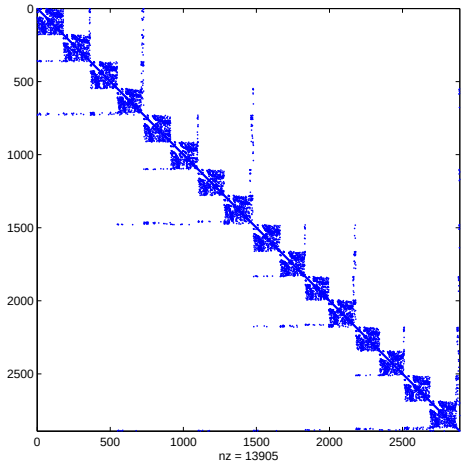

(a) Re-ordered **A** matrix

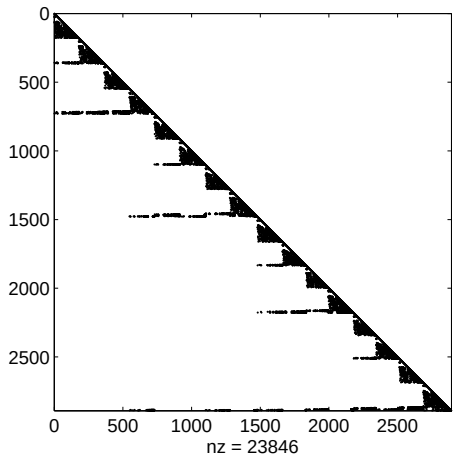

(b) **L** matrix

Figure 2.6: Re-ordered matrix **A** using nested dissection/minimum-degree re-ordering and its corresponding Cholesky factor.

the sparsity pattern of the re-ordered $\mathbf{A}$ matrix using the METIS package. Fig. 2.6(b) shows the Cholesky factor of the re-ordered $\mathbf{A}$ matrix. It is observed that the number of non-zero entries is 23,846, nearly 20 times lesser non-zero entries than the case without re-ordering. Such significant improvements in the sparsity can be observed even in the case of incomplete Cholesky factorization. Matrix re-ordering not only reduces memory requirement in storing $\mathbf{L}$ or $\mathbf{R}$ but also reduces CPU time in the PCG solution, since the number of flops for each matrix-vector multiplication is reduced with increase in sparsity. The system matrix $\mathbf{A}$ being independent of time needs to be assembled only once. The construction of the pre-conditioner with the matrix re-ordering and factorization steps needs to be performed only once after the assembly of $\mathbf{A}$ and before the starting of the time-stepping procedure. Usually the number of time steps is large. Hence the computational requirements in setting up the matrix pre-conditioner is negligible compared to the time-stepping procedure and significant reduction in CPU time and memory requirements can be achieved.

It is possible to formulate a TDFEM based technique starting from the two first order Maxwell's curl equations (2.1) and (2.2) [6, 45], similar to the FDTD method. Such a formulation can lead to an explicit time marching alleviating the need for matrix inversion at each time step. However, the resulting algorithm is conditionally stable with the conditions of stability dictated by the lowest edge length in the unstructured mesh. The choice a time-step cannot be generalized in this case and the maximum time step allowed is dependent on the problem to be simulated and the finite element mesh used.

2.3.6 Absorbing Boundary Condition

To model unbounded problems, similar to the case in FDTD method, ABCs or PML are two possible approaches which can be adopted. The first order ABC, frequently

used in frequency domain FEM [46], is given by

$$\hat{n} \times \nabla \times \vec{E} = jk_0\gamma_t\vec{E} \tag{2.55}$$

where $k_0 = \frac{j\omega/}{c}$ is the free space wave-number and $\gamma_t\vec{u} = \hat{n} \times \vec{u} \times \hat{n}$ is the tangential trace operator. In other words, $\gamma_t\vec{u}$ is the tangential component of $\vec{u}$ along the surface. The corresponding first order ABC in the time domain is

$$\hat{n} \times \nabla \times \vec{E} = \frac{1}{c}\frac{\partial}{\partial t}\gamma_t\vec{E}. \tag{2.56}$$

It is fairly simple to incorporate the first order ABC in (2.56) with in the FETD formulation. For trial vector functions $\vec{u}$ which satisfy (2.56), the surface integral term which appears in the Galerkin testing, as in (2.39), can be written as

$$\begin{aligned}\int_{\Gamma_{abc}} \vec{v} \cdot (\nabla \times \vec{u}) \times \hat{n}\, ds &= -\int_{\Gamma_{abc}} \vec{v} \cdot (\hat{n} \times \nabla \times \vec{u})\, ds \\ &= -\frac{1}{c}\frac{\partial}{\partial t}\int_{\Gamma_{abc}} (\hat{n} \times \vec{v}) \cdot (\hat{n} \times \vec{u})\, ds.\end{aligned} \tag{2.57}$$

The discrete Galerkin statement in this case is then

Seek $\vec{u}_h(t) \in \mathcal{V}^h \subset \mathcal{H}(\text{curl}, \Omega)$ such that

$$\begin{aligned}\int_\Omega \left[\nabla \times \vec{v}_h \cdot \frac{1}{\mu_r}\nabla \times \vec{u}_h + \varepsilon_r\frac{1}{c^2}\vec{v}_h \cdot \frac{\partial^2\vec{u}_h}{\partial t^2} + \mu_0\vec{v}_h \cdot \frac{\partial\vec{J}_i}{\partial t}\right] d\Omega \\ + \frac{1}{c}\frac{\partial}{\partial t}\int_{\Gamma_{abc}} (\hat{n} \times \vec{v}_h) \cdot (\hat{n} \times \vec{u}_h)\, ds = 0,\end{aligned} \tag{2.58}$$

$\forall\vec{v}_h \in \mathcal{V}^h$ and $t \in (0, T)$.

After expanding the trial and testing functions using basis functions and following a similar procedure as in Sec. 2.3.2, the following system of ordinary differential equations is obtained,

$$\mathbf{T}\frac{1}{c^2}\frac{d^2\mathbf{u}}{dt^2} + \mathbf{R}\frac{1}{c}\frac{d\mathbf{u}}{dt} + \mathbf{S}\mathbf{u} + \mathbf{f} = 0 \tag{2.59}$$

where $\mathbf{S}, \mathbf{T}$ and $\mathbf{f}$ are defined in (2.42),(2.43) and (2.44), respectively; and $\mathbf{R}$ is defined as

$$R_{ij} = \int_{\Gamma_{abc}} \hat{n} \times \vec{W}_i \cdot \hat{n} \times \vec{W}_j\ ds. \tag{2.60}$$

The Newmark-beta scheme for temporal discretization can be extended to the general case of the second-order ordinary differential equations [10]. Applying the scheme to (2.59) results in the following implicit update equation

$$\begin{aligned}\left[\mathbf{T}+\frac{1}{2}c\Delta t\mathbf{R}+\beta c^2\Delta t^2\mathbf{S}\right]\mathbf{u}^{n+1} = &\left[2\mathbf{T}-(1-2\beta)c^2\Delta t^2\mathbf{S}\right]\mathbf{u}^{n}\\ &-\left[\mathbf{T}-\frac{1}{2}c\Delta t\mathbf{R}+\beta c^2\Delta t^2\mathbf{S}\right]\mathbf{u}^{n-1}\\ &-c^2\Delta t^2\left[\beta\mathbf{f}^{n+1}+(1-2\beta)\mathbf{f}^{n}+\beta\mathbf{f}^{n-1}\right].\end{aligned} \tag{2.61}$$

It is possible to derive, in general the mth order ABC [46]; and its implementation within the FETD method involves deriving the time domain equivalent of the ABC and devising a suitable temporal discretization schemes for deriving the update equations. The property of unconditional stability is not necessarily maintained for the resulting update equations. The second order ABC was implemented in FETD method in [11] with only a marginal improvement in performance compared to the first-order ABC [47]. For this reason, the implementation of PML as in FDTD methods within the FETD framework has been investigated.

2.3.7 Perfectly Matched Layer

Implementation of PML in the FETD method has not attracted as much attention as the FDTD counterpart. In general the PML medium is a dispersive anisotropic tensor. To reduce the complexity in time domain analog of the constitutive relationship, either non-dispersive case [48] or approximation of the frequency dependence [49] has been considered. The dispersive nature of the PML has been modeled accurately in [50, 51] using recursive convolutions evaluated with assumption that the field is a piece-wise constant [50] or piece-wise linear [51] with time. The implementation, though offers a good absorption efficiency than ABCs, no rigorous proof of stability exists and often suffers from numerical instability [51]. In [52], a novel method of implementing the

anisotropic PML by using modifying basis functions was proposed. Common to all the different implementations is the increased computational complexity and lack of theoretical proof of numerical stability.

2.4 Hybridising FDTD with FETD

The implementation of PML in FETD method is not trivial and straight forward unlike the case with the FDTD method. Moreover, it is shown in [9] that, the computational complexity of the 3-D FETD algorithm in terms of CPU time with a fixed physical simulation time is $O(N^{\frac{3}{2}})$ and is slightly less efficient than FDTD which has complexity $O(N^{\frac{4}{3}})$ where the number of unknowns $N \propto \frac{1}{\Delta h}^3$. Though FETD has marginally higher complexeity than FDTD, the method has an inherent advantage that the fundamental source of errors in FDTD viz., the stair-stepping approximations of the modelled geometry is eliminated. This issue of stair-casing errors has been a subject of research for more than a decade and many algorithms such as the Finite-Volume Time-Domain (FVTD), FDTD methods for non-orthogonal grids [53] and conformal FDTD methods for curved PEC structures [54,55] have been proposed. The disadvantage of these methods is that the computational efficiency of the FDTD method for Cartesian grids is lost, requiring substantially more CPU time and memory to solve a problem and are often restrictive to a particular class of problems. Improvements to FDTD for large problems by hybridizing with higher-order techniques such as pseudospectral time-domain (PSTD) [56] have recently been proposed. Hybrid methods to overcome staircasing errors in FDTD using FETD were initially proposed in [14–17]. For such algorithms, efficient unstructured mesh generation tool is a fundamental requirement. In [15], the 3-D FDTD algorithm is hybridized by modelling curved boundaries with tetrahedral edge elements. A second order accurate interpolation is performed to obtain the unknowns on the Finite element domain boundaries, which do not conform to the finite difference

grid. In this section, the 2-D FETD-FDTD hybrid algorithm for the TE case is reviewed. The hybridization procedure and the linkage between the finite element and the finite difference domains are detailed. As will be seen later, the discussed method is numerically unstable. However, it will be shown in Chapter 4 that the implementation of the stable hybrid FETD-FDTD method proposed in [18], is similar in procedure to the one discussed in the following section.

2.4.1 Formulation: 2-D TE$_z$ Case

The physical space is split into two domains viz., the FD domain, Ω_{FD} and the FE domain, Ω_{FE}. Ω_{FD} has both electric field E^{FD} and magnetic field H^{FD} unknowns while Ω_{FE} has only electric field unknowns E^{FE}. The boundary of Ω_{FE}, Γ^e_{FE} conforms to the electric field grid of Ω_{FD} and the corresponding electric field unknowns on it are denoted as $E^{FD}_{\Gamma} \subset E^{FD}$. E^{FD}_{Γ} are the boundary values for the solution in Ω_{FE}. Ω_{FE} is triangulated in such a way so that, Γ^e_{FD} conforms with the mesh in Ω_{FE} and has the electric field unknowns on it denoted as $E^{FE}_{\Gamma} \subset E^{FE}$. The magnetic field unknowns in Ω_{FD} that require E^{FE}_{Γ} and E^{FD}_{Γ} for updating, are denoted as $H^{FD}_{\Gamma} \subset H^{FD}$. A sample discretization and domain boundaries with the corresponding unknowns are shown in Fig. 2.7.

As in traditional FDTD formulation, the Maxwell's two curl equations are used in Ω_{FD} and the second order vector wave equation is used in Ω_{FE} to arrive at the update equations for the unknowns in the respective domains. For the sake of simplicity, both domains are considered to be lossless, non-dispersive, isotropic and homogeneous. In

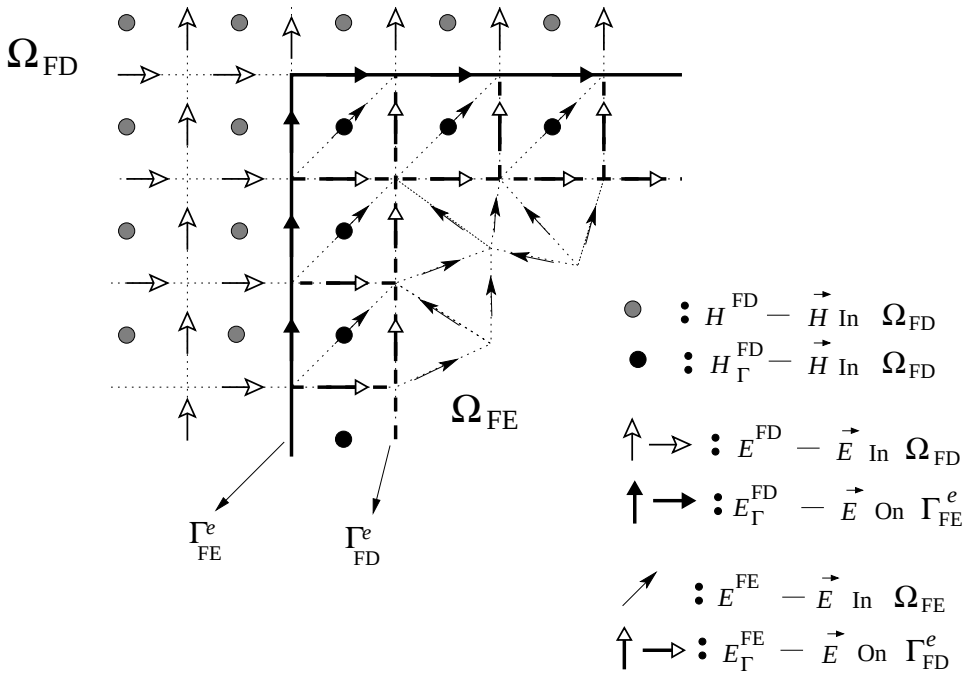

Figure 2.7: Boundaries of the FE and FD domains and the corresponding notations used for unknowns.

Ω_{FD}, for the 2-D TE$_z$ case (with E_x, E_y and H_z components) the FDTD update equations are given as

$$H^{n+1/2}_{z(i+1/2,j+1/2)} = H^{n-1/2}_{z(i+1/2,j+1/2)} - \frac{\Delta t}{\mu_0 \Delta h}\begin{bmatrix} E^n_{y(i+1,j+1/2)} - E^n_{y(i,j+1/2)} \\ -E^n_{x(i+1/2,j+1)} + E^n_{x(i+1/2,j-1)} \end{bmatrix} \tag{2.62}$$

$$E^{n+1}_{x(i+1/2,j)} = E^n_{x(i+1/2,j)} + \frac{\Delta t}{\varepsilon_0 \Delta h}\left[H^{n+1/2}_{z(i+1/2,j+1/2)} - H^{n+1/2}_{z(i+1/2,j-1/2)}\right] - \frac{\Delta t}{\varepsilon_0} J^{n+1}_{x(i+1/2,j)} \tag{2.63}$$

$$E^{n+1}_{y(i,j+1/2)} = E^n_{y(i,j+1/2)} + \frac{\Delta t}{\varepsilon_0 \Delta h}\left[H^{n+1/2}_{z(i+1/2,j+1/2)} - H^{n+1/2}_{z(i-1/2,j+1/2)}\right] - \frac{\Delta t}{\varepsilon_0} J^{n+1}_{y(i,j+1/2)}. \tag{2.64}$$

In (2.62), for the update of $H_z \in H^{FD}_{\Gamma}$, the electric field unknowns $(E_x, E_y) \in E^{FD}_{\Gamma} \cup E^{FE}_{\Gamma}$ are used. In Ω_{FE} we proceed from the second order vector wave equation as in (2.32) with the source term $\vec{J}_i = 0$ and the following Dirichlet boundary condition viz.,

$$\hat{n} \times \vec{E} \times \hat{n} = E^{FD}_{\Gamma}, \qquad \text{on } \Gamma^e_{FE}. \tag{2.65}$$

In (2.65), E_{Γ}^{FD}, the FDTD solution on Γ_{FE}^{e} is time varying. Hence, (2.65) represents a time varying Dirichlet boundary condition. Using edge element basis functions to span the electric field in Ω_{FE} and applying the Faedo-Galerkin process discussed in Sec. 2.3.2, results in a system of o.d.e given as in (2.41) with the finite element matrices $\mathbf{S}$ and $\mathbf{T}$ defined as in (2.42) and (2.43), respectively. In this case, the excitation vector $\mathbf{f}$ has contributions due to the boundary condition in (2.65) and unlike the definition in (2.44), is given as

$$f_i = \sum_{e_j \in \Gamma_{FE}^{e}} \left[T_{ij} \frac{1}{c^2} \frac{d^2 E_{\Gamma(j)}^{FD}}{dt^2} + S_{ij} E_{\Gamma(j)}^{FD} \right] \tag{2.66}$$

where $E_{\Gamma(j)}^{FD}$ is the finite difference unknown associated with the edge e_j on Γ_{FE}^{e}.

Using the Newmark-beta method as in Sec.2.3.4 for the temporal discretization and with $\mathbf{f}$ given by (2.66), an implicit update equation of the electric field unknowns in Ω_{FE} is obtained as

$$\mathbf{A}\,\mathbf{e}^{n+1} = \mathbf{B}\,\mathbf{e}^{n} - \mathbf{A}\,\mathbf{e}^{n-1} - c^2 \Delta t^2 \mathbf{f}^{n+1} \tag{2.67}$$

with

$$\mathbf{A} = \mathbf{T} + c^2 \Delta t^2 \beta \mathbf{S}$$

$$\mathbf{B} = \mathbf{2T} - c^2 \Delta t^2 (1 - 2\beta) \mathbf{S};$$

and $\mathbf{f}^{n+1}$ evaluated using the temporal discretization of (2.66) and given as

$$f_i^{n+1} = \sum_{e_j \in \Gamma_{FE}^{e}} \left\{ \begin{array}{l} \dfrac{T_{ij}}{c^2 \Delta t^2} \left[E_{\Gamma}^{FD} \big|_{(j)}^{n+1} - 2\, E_{\Gamma}^{FD} \big|_{(j)}^{n} + E_{\Gamma}^{FD} \big|_{(j)}^{n-1} \right] \\ \qquad + S_{ij} \left[\beta\, E_{\Gamma}^{FD} \big|_{(j)}^{n+1} + (1 - 2\beta)\, E_{\Gamma}^{FD} \big|_{(j)}^{n} + \beta\, E_{\Gamma}^{FD} \big|_{(j)}^{n-1} \right] \end{array} \right\}. \tag{2.68}$$

Eq. (2.67) is the required matrix equation to be solved during each time step to obtain the electric field solution in Ω_{FE}, subject to the time varying boundary condition (2.65) appearing in the excitation vector $\mathbf{f}$ as in (2.68). The steps involved during each time step in the hybrid FETD-FDTD algorithm can be summarized as

1. $H^{FD}\big|^{\,n+1/2}$ are updated using (2.62), with $H_\Gamma^{FD}\big|^{\,n+1/2}$ updated using $E_\Gamma^{FD}\big|^{\,n}$ and $E_\Gamma^{FE}\big|^{\,n}$.

2. PMC boundary conditions in Ω_{FD}, if any, are enforced on $H^{FD}\big|^{\,n+1/2}$.

3. $E^{FD}\big|^{\,n+1}$, which include $E_\Gamma^{FD}\big|^{\,n+1}$ are updated using (2.63) and (2.64).

4. PEC boundary conditions in Ω_{FD}, if any, are enforced on $E^{FD}\big|^{\,n+1}$.

5. $E_\Gamma^{FD}\big|^{\,n+1}$ being the boundary values of Ω_{FE}, are integrated into the finite element update equation using (2.68).

6. Matrix equation (2.67) is solved to update $E^{FE}\big|^{\,n+1}$.

7. $E_\Gamma^{FE}\big|^{\,n+1} \subset E^{FE}\big|^{\,n+1}$ is made available for the next update of H_Γ^{FD}.

In step 1 of the time-stepping procedure, the solution in Ω_{FE} penetrates into Ω_{FD}, and in step 5, the solution in Ω_{FD} penetrates into Ω_{FE}. Steps 1-4 are the traditional FDTD time marching procedure. With regard to implementation, the basic code to implement the field updating procedure can be used as such without any modification, provided that in step 7, the unknowns $E_\Gamma^{\mathrm{FE}}\big|^{\,n+1}$ are mapped onto the corresponding unknowns in the electric field grid in Ω_{FD}. It should be noted that while linking the unknowns between the two domains, the directions of the unknowns have to match globally. This can be easily ensured by using the direction of the unknown in Ω_{FD} as the reference. If the edge associated to the particular unknown is opposite in direction in Ω_{FE}, then its associated unknown is multiplied by -1 while mapping onto the corresponding unknown in Ω_{FD}.

2.4.2 Numerical Examples and Results

In order to highlight the efficiency and accuracy of the hybrid algorithm, the solutions for scattering by a circular PEC cylinder for TE$_z$ incidence obtained using FDTD

and the hybrid algorithm are compared with the analytical results. The scattered H_z component by a PEC cylinder can be evaluated analytically [57] in cylindrical coordinates in terms of Bessel and Hankel functions as

$$H_z^s(\omega,\rho,\phi) = -H_0 \sum_{n=-\infty}^{+\infty} j^{-n} \frac{J_n'(\beta a)}{H_n^{(2)'}(\beta a)} H_n^{(2)}(\beta\rho) e^{jn\phi} \tag{2.69}$$

where $\beta = \omega\sqrt{\mu_0\varepsilon_0}$ and a is the radius of the circular cross-section. For a given waveform $p(t)$ of the incident plane wave which, in this example, is a differentiated Gaussian pulse, let $P(\omega)$ be its Fourier transform. To obtain the corresponding time domain scattered waveform, the scattered field computed in the frequency domain using (2.69) is weighted with $P(\omega)$ and an inverse Fourier transform is applied subsequently. The radius of the circular cylinder in this example is arbitrarily chosen as 0.125m. The frequency band of interest is $800 - 2000$ MHz. Three different cell sizes viz., $\lambda_{min}/20 = 7.5$mm, $\lambda_{min}/30 = 5$mm and $\lambda_{min}/40 = 3.75$mm are chosen. Total Field/ Scattered field formulation is implemented to solve for the scattered field directly in a single FDTD simulation. For the FDTD simulations, the cylinder geometry is approximated to conform to the Cartesian grid using stair-casing, as shown in Fig. 2.8. The time domain scattered H_z^s component at ($\rho = 0.18$m,$\phi = 180°$) for the various cases is shown in Fig. 2.9(a) along with the analytical solution. In Fig. 2.9(b), the error in the solution as compared to the analytical solution is shown. The 20 cells/λ case has an error as high as -12 dB. For the hybrid case, the physical dimension of Ω_{FE} is chosen to be a box of 0.3 m$\times$0.3 m and the hybrid geometry for $\Delta h = \lambda_{min}/20$ is shown in Fig. 2.10. The average length of each edge in the triangulation of Ω_{FE} is close to the FDTD cell size in all cases. Also, since the geometry is PEC, no unknowns are required for the space inside the geometry. The hybrid mesh generator developed uses the Triangle [58] code for triangular mesh generation. The hybrid mesh generator ensures that the requirements on the interface between Ω_{FE} and Ω_{FD} are maintained. The solution obtained using the hybrid algorithm is shown in Fig. 2.11. The insets in Fig. 2.9(a) and Fig. 2.11(a) magnify the tail of the first reflection from the PEC cylinder. It is seen that

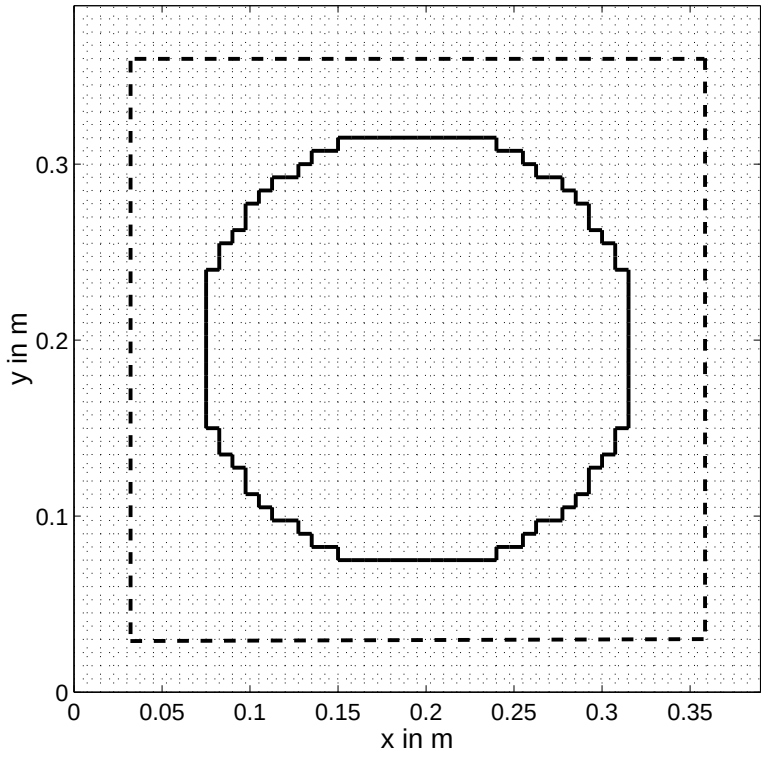

Figure 2.8: FDTD mesh for the circular PEC cylinder geometry with the total field/ scattered field regions.

significant ripple is observed in the FDTD solution and its level decreases with finer mesh. Even in the case with $\Delta h = \lambda_{min}/40$ the ripple is noticeable. Clearly, this ripple is due to the stair-case approximation of the curved geometry, and is totally absent in the hybrid case. On observing Fig. 2.9(b) and Fig. 2.11(b), it is noticed that an improvement of at least 15dB in the solution error is seen in all cases when compared to the corresponding FDTD results. The performance of the hybrid algorithm with $\Delta h = \lambda_{min}/20$ is much better than the FDTD solution with $\Delta h = \lambda_{min}/40$.

To better illustrate the advantages of the FETD-FDTD method, a comparison of the efficiency of the hybrid method with regular FDTD is shown in Fig. 2.12. The dependence of error in the solution with the number of unknowns and the corresponding CPU time is shown. The root mean square error in the scattered time domain H_z component

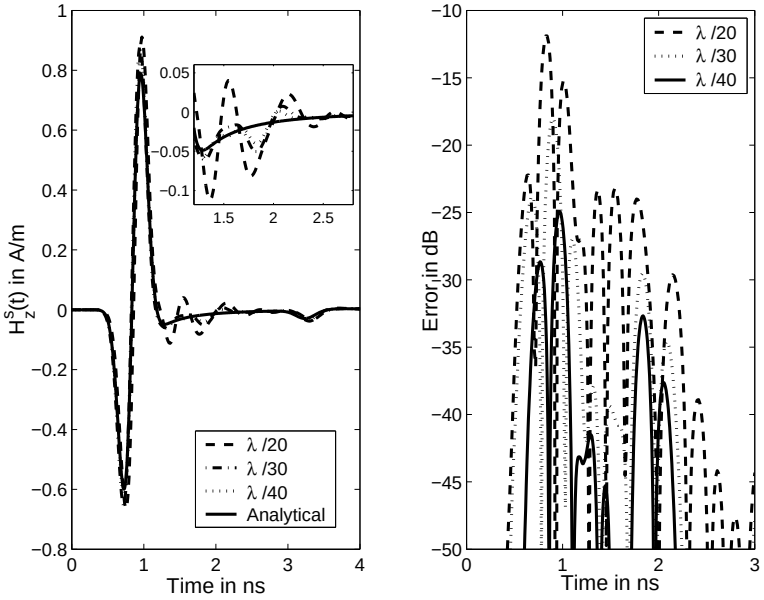

Figure 2.9: Time domain H_z solution using FDTD method for various cell sizes compared to the analytical solution.

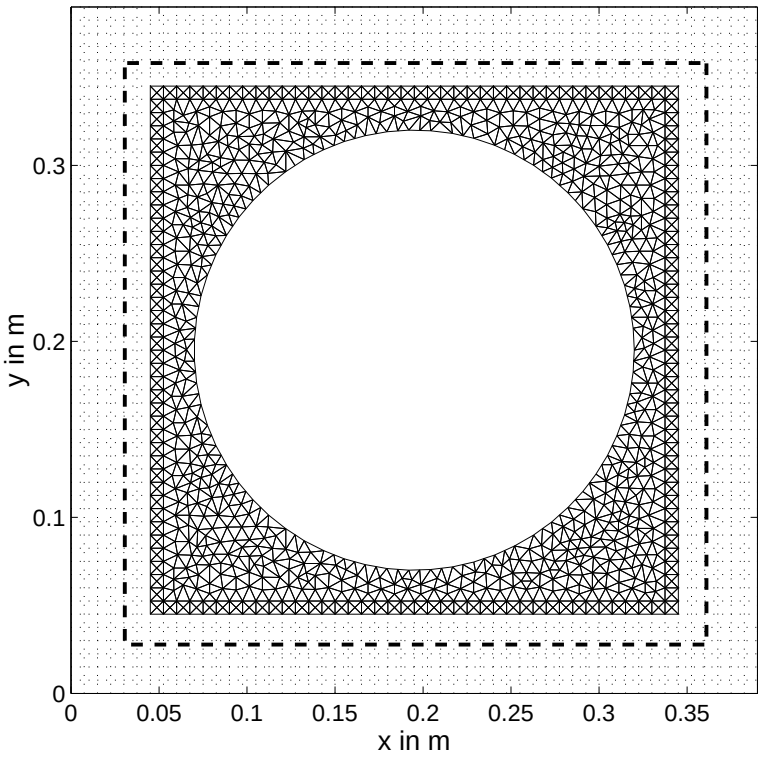

Figure 2.10: Hybrid mesh for the circular PEC cylinder geometry with the total field/ scattered field regions.

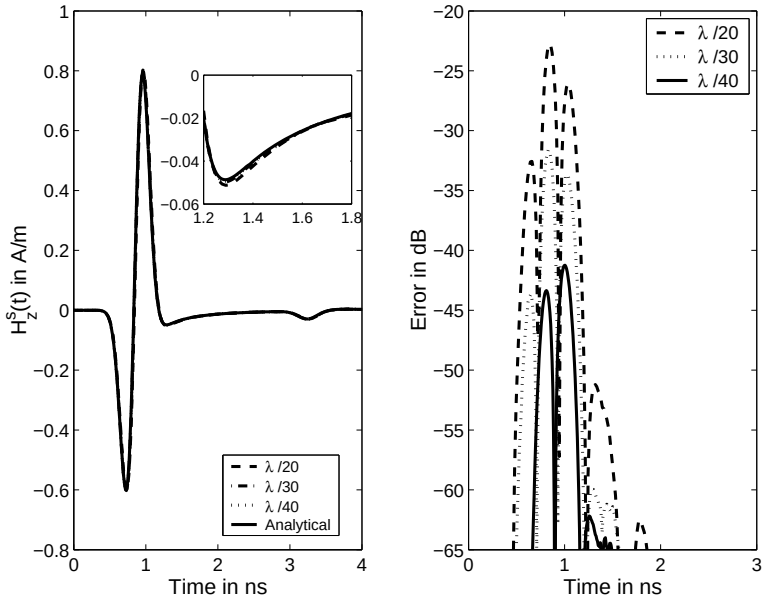

Figure 2.11: Time domain H_z solution using hybrid FETD-FDTD method for various cell sizes compared to the analytical solution.

in the backscattered direction, defined by

$$e_{rms} = \left[\frac{1}{N_t} \sum_{n=0}^{N_t} \left| H_z^n - H_z^{anal}(n\Delta t) \right|^2 \right]^{\frac{1}{2}} \tag{2.70}$$

is used as the performance index in terms of error in the solution. N_t is the total number of time steps. These results are for a square Ω_{FE} as shown in Fig. 2.10. It is much desired to have Ω_{FE} as closely bounded to the curved geometry as possible, in which case much better performance in terms of CPU time than the results shown in Fig. 2.12 can be achieved. However, even for the current example, it is observed from Fig. 2.12(a), that firstly, for a given number of unknowns, the error in the FDTD solution is higher than the error in the hybrid solution. Secondly, the rate at which the error in the FETD-FDTD hybrid solution reduces with increase in the number of unknowns is higher than the FDTD solution. In the circular cylinder geometry, the errors due to stair-case approximations in the FDTD method are significant even at the levels of refinements of $\lambda/40$. In Fig. 2.12(b) the CPU time required for a certain level of error in the solution is

shown. The hybrid method with PCG solver using incomplete Cholesky factor as pre-conditioner requires lower CPU time than the hybrid case with just a CG solver without any pre-conditioner. The FDTD method in general requires lower CPU time. However, with the error in the solution as the criteria, it is observed that the FDTD method requires finer mesh size, would need much more CPU time than the hybrid case to generate a solution with similar error. Moreover, by confining Ω_{FE} closely to the curved regions would reduce the CPU time for the hybrid method significantly.

In the previous example of scattering by a circular PEC cylinder, comparisons of near-field solutions among the FDTD, Hybrid and analytical methods were made. In the next example, monostatic RCS of a PEC cylinder with square cross-section is considered. Two different angles of incidence viz., $\phi_i = 45^\circ$ and $\phi_i = 30^\circ$ are considered. The hybrid mesh used for the two cases is shown in Fig. 2.13. Although it is possible to have the same geometry for the two cases and changing the angle of the incident plane wave in the total-field / scattered-field formulation, for convenience ϕ_i is set as 0° for both cases and the geometry is rotated. The diagonal of the square cross-section is 0.25 m. A 2-D time domain NFFF transformation [59] is applied on a virtual surface in the scattered field region to obtain the scattered far-zone H_z component in the back-scattered direction. Subsequently, the backscattered RCS is computed over the frequency band of interest, which in this example is $800 - 2000$ MHz. In Fig. 2.14, the results for monostatic RCS obtained using the hybrid method is compared with the FDTD and method of moments solutions. Δh is set as $\lambda_{min}/40$ for both the FDTD and the hybrid methods. As expected, the hybrid results are in better agreement with the method of moment solution [60]. In Fig. 2.15, a good agreement with MoM results in the case of $\phi_i = 30^\circ$ is observed.

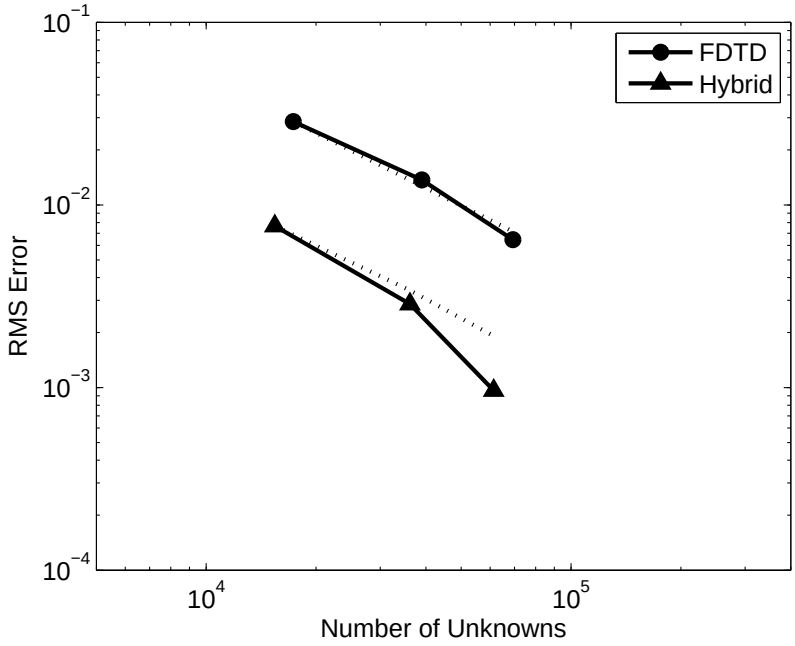

(a) Number of Unknowns vs RMS Error

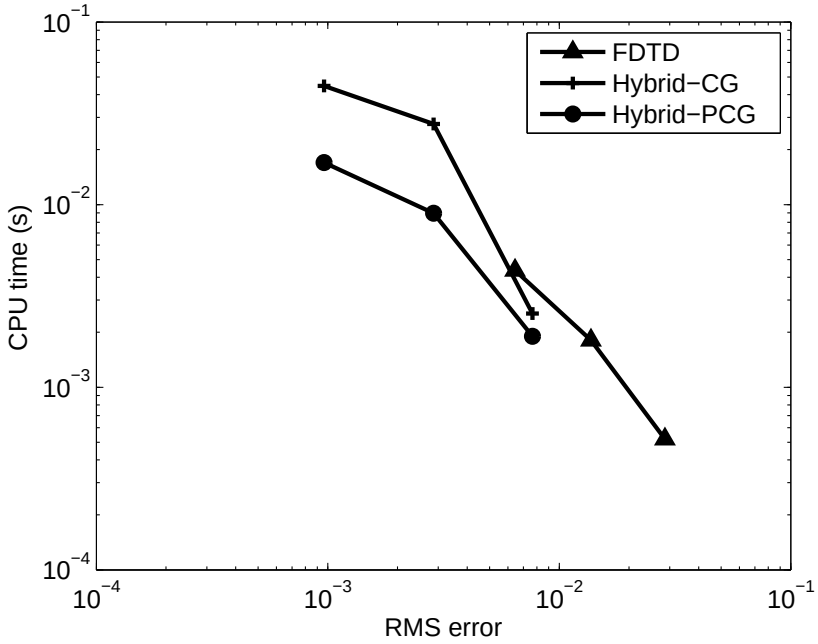

(b) RMS Error vs CPU Time

Figure 2.12: Comparison of efficiency of hybrid FETD-FDTD method with FDTD method.

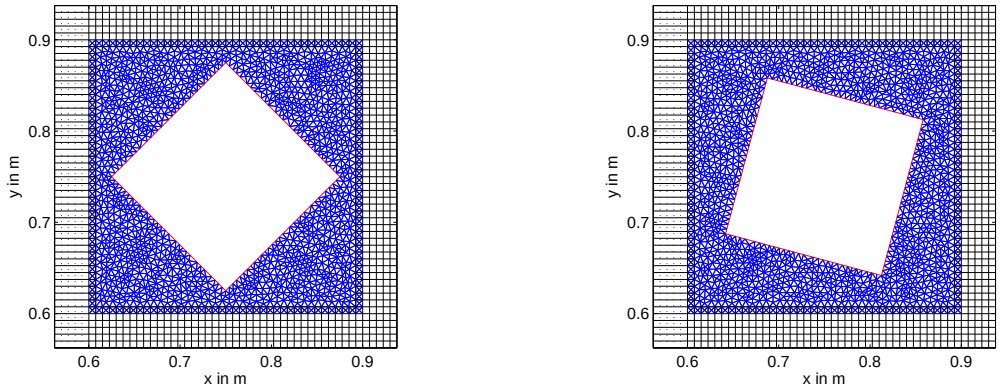

(a) $\phi_i = 45°$ (b) $\phi_i = 30°$

Figure 2.13: Hybrid mesh for computation of monostatic RCS from a rectangular PEC cylinder.

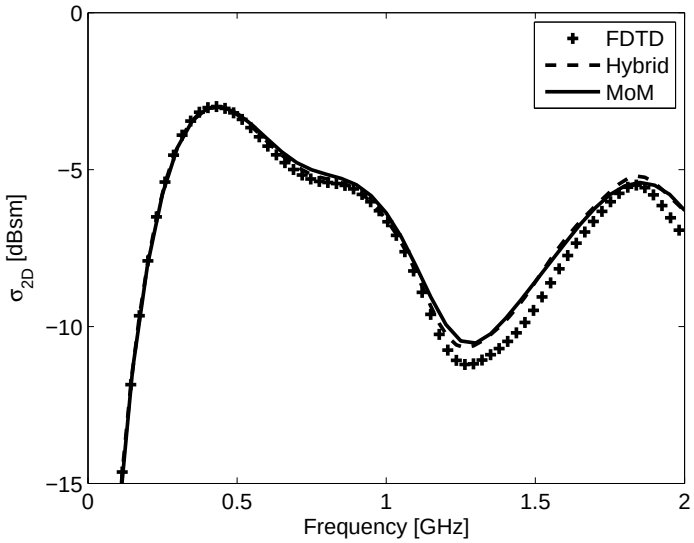

Figure 2.14: Comparison of monostatic RCS with $\phi_i = 45°$ obtained using FDTD method, hybrid FETD-FDTD method and method of moments.

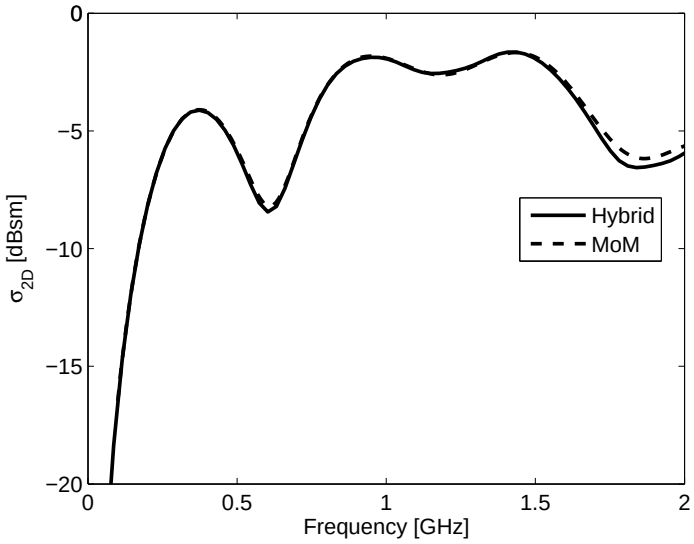

Figure 2.15: Comparison of monostatic RCS with $\phi_i = 30^\circ$ obtained using the hybrid FETD-FDTD method and method of moments.

2.4.3 Numerical Instability

Temporal instabilities arise in the hybrid FETD-FDTD algorithm [14], [61]. It is very interesting to note that the Newmark-β scheme is unconditionally stable for $\beta \geq 0.25$. The FDTD algorithm by itself is conditionally stable. However, the hybrid algorithm is unstable. Two kinds of numerical instability are observed in hybrid FETD-FDTD methods. One is the severe numerical instability and the other is the relatively weak-instability where the solution grows linearly with ti me. The reason for linear growth is the appearance of spurious modes in the form of solenoidal fields in the electric field solution. A novel method for suppressing the occurrence of these spurious modes is proposed and discussed in detail in Chapter 3.

The late time instability is inherently due to the hybridization of FETD and FETD methods. In Fig. 2.16, the effect of late time instability in the hybrid method presented in the previous section is illustrated. The time history of the scattered H_z component by a PEC cylinder is shown. Though the computations in the previous section were based on terminating the simulation before the onset of the numerical instability, in general, it

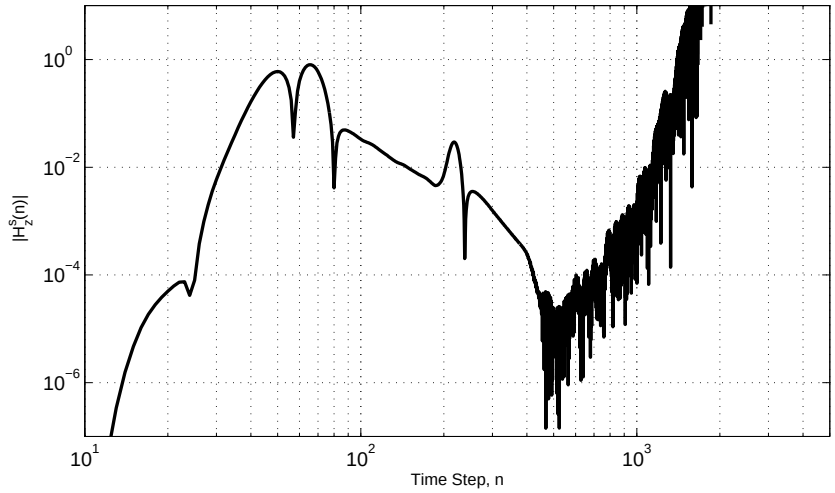

Figure 2.16: Time domain scattered H_z component showing numerical instability.

is not trivial to predict when the instability will appear. In [62] filtering techniques are proposed to control the stability of the algorithm. However, a need to have a numerically stable hybridization scheme with well defined conditions of stability is of importance for the successful extensive application of the method for modeling real life problems. A detailed analysis of the stability of the hybrid algorithm for different hybridization and the ability to achieve conditional stability will be left as the topic for Chapter 4.

2.5 Concluding Remarks

The two fundamental finite methods viz., the FDTD method and the FETD method having advantages over each other with regard to efficiency and errors in numerical modeling can be combined to achieve a robust time domain hybrid method. Applying FETD method to model structures with intricate geometric details and FDTD method for solution in relatively simple regions, stair-casing errors can be completely eliminated at a reasonable increase in computational cost. The hybrid method was shown to have better accuracy for a given number of unknowns and computational time. The problem

of weak and severe instability encountered in the hybrid method is the topic discussed in Chapters 3 and 4.

CHAPTER 3

DIVERGENCE-FREE SOLUTION WITH EDGE ELEMENTS USING CONSTRAINT EQUATIONS

3.1 Introduction

In the FEM formulation, the second order vector Helmholtz equation is the governing equation. As seen in the Sec. 2.3, Maxwell's two curl equations are combined to arrive at the vector Helmholtz equation and the divergence-free conditions in (2.3) and (2.4) are not explicitly enforced. A vector field solution for Helmholtz equation need not necessarily satisfy the divergence-free conditions. In general, irrotational vector fields, which are gradient of scalar fields, form a solution to the Helmholtz equation but fail to satisfy the divergence-free conditions of Maxwell's equations. In the FEM formulation, the divergence-free condition is neither implicitly enforced unlike the FDTD method, nor is explicitly enforced. As long as the vector function space spanned by the vector finite element basis functions span such gradient fields, the numerical solution is corrupted with non-physical modes which satisfy Helmholtz equation. Such non-physical modes are termed as "spurious modes". Edge element basis functions span a discrete gradient space and hence the FEM solution obtained with edge element basis functions are corrupted with spurious modes. However unlike the case of spurious modes in nodal finite elements, these spurious modes occur only at zero frequency [36]. In case of higher order vector basis functions [32], the basis functions are explicitly decoupled into irrotational and solenoidal spaces. When the irrotational basis functions are not employed, spurious modes do not appear. However, in the case of edge elements, such

explicit discrete Helmholtz decomposition is not possible. In this case, to eliminate the appearance of spurious modes, special formulation typically by imposing additional constraints are necessary.

In this chapter, the manifestation of the problem of spurious modes in two contexts viz., a) as zero eigenvalues in the modeling of electromagnetic resonators and b) as linear time growth in the FETD solution, is presented. A novel method of imposing constraint equations to eliminate the appearance of the spurious modes is proposed and to demonstrate the technique, cavity resonator modeling is considered. Further more, the constraint equations can be efficiently imposed by the tree-cotree decomposition of the finite element mesh. Successful application of the technique in eliminating the zero eigenvalues and in eliminating late time linear time growth in FETD solution using edge elements, both in the context of cavity modeling is presented. The contents of this chapter with the examples shown were published in [63] and [64].

3.2 Manifestation of Spurious Modes

3.2.1 DC Modes of Electromagnetic Resonators

FEM is well established in modeling of electromagnetic cavity resonators to identify the resonant frequencies and the corresponding modal field distribution. While exploring new avenues in FEM, modeling of such problems is handy and informative. These problems involve modeling of a bounded region where typically the walls of the resonator are PECs. The resonant frequencies of resonators with simple shapes such as rectangular or cylindrical resonators can be computed analytically. This enables one to compare the FEM solution with analytical results and identify potential drawbacks such as appearance of spurious modes.

Consider Maxwell's equations in a source-free and lossless region Ω, as shown in Fig. 3.1. If the boundary, $\partial\Omega$, is formed entirely by either perfect electric conductors

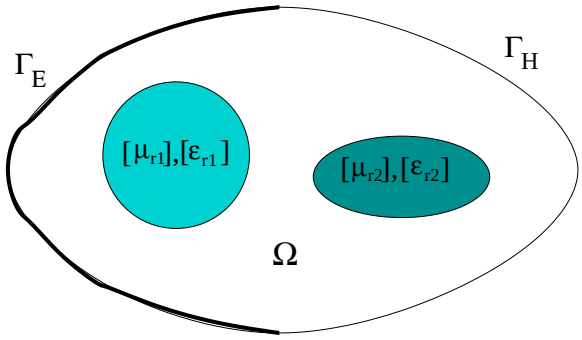

Figure 3.1: A lossless resonator with inhomogeneous materials included within. The boundary of the resonator is assumed to be either perfect electric or perfect magnetic conductors.

(PECs) or perfect magnetic conductors (PMCs), the electric and magnetic fields in Ω satisfy:

$$\left.\begin{array}{ll} \nabla \times \vec{E} = -j\omega\mu_0 \left[\mu_r\right] \vec{H}; & \nabla \times \vec{H} = j\omega\varepsilon_0 \left[\varepsilon_r\right] \vec{E} \\ \nabla \cdot \left(\left[\mu_r\right] \vec{H}\right) = 0 & \nabla \cdot \left(\left[\varepsilon_r\right] \vec{E}\right) = 0 \end{array}\right\} \text{ in } \Omega$$
$$\gamma_t \vec{E}\,|_{\Gamma_E} = 0 \quad \gamma_t \vec{H}\,|_{\Gamma_H} = 0 \tag{3.1}$$

where the tangential trace operator is defined by $\gamma_t \vec{u}\,|_{\Gamma} = \hat{n} \times \vec{u} \times \hat{n}$, with $\hat{n}$ as the unit outward surface normal from Ω. Note that in (3.1), the PEC and the PMC boundaries are denoted by Γ_E and Γ_H, respectively. In the next section, the application of edge elements in solving for the resonant modes of the lossless cavity is presented.

By eliminating the magnetic field, $\vec{H}$, from Maxwell's two curl equations in (3.1), the following transformed eigenvalue problem is obtained:

$$\begin{aligned} &\nabla \times \left[\mu_r\right]^{-1} \nabla \times \vec{E} - k^2 \left[\varepsilon_r\right] \vec{E} = 0 \text{ in } \Omega, \\ &\gamma_t \vec{E}\,|_{\Gamma_E} = 0; \quad \left(\left[\mu_r\right]^{-1} \nabla \times \vec{E}\right) \times \hat{n}\,|_{\Gamma_H} = 0. \end{aligned} \tag{3.2}$$

where $k^2 = \frac{\omega^2}{c^2}$. For $k^2 \neq 0$, equation (3.2) does imply the divergence free condition,$\nabla \cdot \left(\left[\varepsilon_r\right] \vec{E}\right) = 0$. However, in the case of $\vec{E} = \nabla\phi$, we have $k^2 = 0$. Subsequently, the

divergence-free condition may no longer hold. The variational statement for (3.2) is

$$\begin{gathered}\text{Seek } \vec{E} \in \mathcal{H}_0\left(curl;\Omega\right) \text{ and } k^2 \in \mathbb{R} \text{ such that} \\ a\left(\vec{v},\vec{E}\right) - k^2\left(\vec{v},\left[\varepsilon_r\right]\vec{E}\right)_\Omega = 0 \\ \forall \vec{v} \in \mathcal{H}_0\left(curl;\Omega\right).\end{gathered} \tag{3.3}$$

The admissible function space for the trial and testing function space $\mathcal{H}_0\left(curl;\Omega\right)$ is defined by $\mathcal{H}_0\left(curl;\Omega\right) = \left\{\vec{v}\,\middle|\int_\Omega\left(\left|\vec{v}\right|^2 + \left|\nabla\times\vec{v}\right|^2\right)d\Omega < \infty;\ \gamma_t\vec{v}\,|_{\Gamma_E} = 0\right\}$. Moreover, the bilinear form $a\left(\vec{v},\vec{u}\right)$ and the inner product $\left(\vec{v},\vec{u}\right)_\Omega$ are:

$$\begin{gathered}a\left(\vec{v},\vec{u}\right) = \int_\Omega\left(\nabla\times\vec{v}\bullet\frac{1}{\left[\mu_r\right]}\nabla\times\vec{u}\right)d\Omega, \\ \left(\vec{v},\vec{u}\right)_\Omega = \int_\Omega\left(\vec{v}\bullet\vec{u}\right)d\Omega.\end{gathered} \tag{3.4}$$

However, as discussed in [65], there are three groups of eigen-pairs for the eigenvalue problem stated in (3.3), as follows:

$$\begin{aligned}&\text{group 1:}\quad k^2 \neq 0,\quad \nabla\cdot\left(\left[\varepsilon_r\right]\vec{E}\right) = 0 \\ &\text{group 2:}\quad k^2 = 0,\quad \nabla\cdot\left(\left[\varepsilon_r\right]\vec{E}\right) = 0 \\ &\text{group 3:}\quad k^2 = 0,\quad \nabla\cdot\left(\left[\varepsilon_r\right]\vec{E}\right) \neq 0.\end{aligned} \tag{3.5}$$

Both groups 1 and 2 are physical eigenmodes of the resonators. The number of eigenmodes in group 2 is one less than the number of separated PECs. Eigenmodes in group 3 do not satisfy completely the Maxwell's equations, specifically the divergence-free condition of electric field as in (2.3), and we refer to them as DC spurious modes. In employing edge elements to approximate the eigenmodes of (3.3), the number of DC spurious modes is the same as the number of "free nodes". The free nodes are referred to as the vertex nodes that are not on PECs. In the case of a resonator without PEC, the nodes that are not designated as the reference grounding nodes are the free nodes. To suppress these DC spurious modes, we modify (3.2) into a constrained eigenvalue problem as:

$$\begin{gathered}\nabla\times\left[\mu_{\mathrm{r}}\right]^{-1}\nabla\times\vec{E} - k^2\left[\varepsilon_r\right]\vec{E} = 0 \text{ in } \Omega \\ \gamma_t\vec{E}\,|_{\Gamma_E} = 0;\quad \left(\left[\mu_r\right]^{-1}\nabla\times\vec{E}\right)\times\hat{n}\,|_{\Gamma_H} = 0 \\ \text{with } \nabla\bullet\left(\left[\varepsilon_r\right]\vec{E}\right) = 0 \text{ in } \Omega.\end{gathered} \tag{3.6}$$

Moreover, the corresponding variational statement becomes:

$$\begin{gathered}\text{Seek } \vec{E} \in \mathcal{H}_0\left(curl;\Omega\right) \text{ and } k^2 \in \mathbb{R} \text{ such that} \\ a\left(\vec{v},\vec{E}\right) - k^2\left(\vec{v},\left[\varepsilon_r\right]\vec{E}\right)_\Omega = 0 \\ \forall \vec{v} \in \mathcal{H}_0\left(curl;\Omega\right) \\ \text{subject to } \left(\nabla\phi,\left[\varepsilon_r\right]\vec{E}\right)_\Omega = 0 \; \forall \phi \in \mathcal{H}_0^1\left(\Omega\right)\end{gathered} \tag{3.7}$$

where

$$\mathcal{H}_0^1\left(\Omega\right) = \left\{ u \left| \int_\Omega \left(|u|^2 + |\nabla u|^2\right) d\Omega < \infty; u\,|_{\Gamma_E} = 0 \right. \right\}. \tag{3.8}$$

The constrained equation $\left(\nabla\phi,\left[\varepsilon_r\right]\vec{E}\right)_\Omega = 0, \forall\phi \in \mathcal{H}_0^1\left(\Omega\right)$, used to enforce the divergence-free condition, ensures $\nabla \bullet \left(\left[\varepsilon_r\right]\vec{E}\right) = 0$ in a distributional (or weak) sense.

In the FEM, the resulting generalized eigenvalue problem involves sparse symmetric matrices and the Lanczos algorithm is an efficient technique for computing its eigenvalues and eigenvectors [66]. In the context of cavity modeling without spurious modes, a constrained Lanczos algorithm was introduced in [65]. The method was based on restricting the Krylov subspace of the Lanczos algorithm and hence the resulting eigenvectors, by enforcing the divergence-free (solenoidal) condition of electric flux in a weak sense. This restriction was carried out by devising a projection operator which removes gradient fields in the Ritz vector obtained in each iteration of the Lanczos algorithm. The use of projection operator would involve the construction of finite element matrices corresponding to nodal basis functions and necessitate the solution of a Poisson problem in each iteration of the Lanczos algorithm. In [67], to harness the use of readily available scalable sparse eigenvalue solvers such as ARnoldi PACKage (ARPACK), a spectral shift method was proposed. In this technique, the original eigenvalue problem is modified such that the non-physical eigenvalues are shifted to the middle of the spectrum. The shift is such that the solenoidal eigenmodes are unaffected. This method involves construction of mixed finite element matrices using nodal and edge elements

in solving the Poisson equation. Constraint equations proposed in this Chapter alleviate the need to construct matrices other than those required in the original eigenvalue problem. No new basis functions other than the edge elements are involved in the current formulation. The idea is similar to that in [65] in that it relies on the fact that the solution is orthogonal to the null space of the curl operator. However, instead of restricting each Ritz vector using the projection operator, a method of applying constraint equations directly on the Krylov vector involved in the matrix solution of the Ritz vector is developed. The resulting Ritz vector is such that its corresponding field solution is orthogonal to the null space of the curl operator. As will be seen in the sections to follow, the proposed constraint equations can be efficiently imposed by the Tree-Cotree splitting of the finite element mesh, and operating on the tree variables alone. Moreover, since the occurrence of non-physical zero eigenvalues are completely suppressed, a shift-and-invert strategy with negative shift results in a positive definite system matrix, which can be solved efficiently using the preconditioned conjugate gradient algorithm. Also, the proposed constraint equations can be directly integrated along with ARPACK via the "reverse communication interface" [68].

3.2.2 Linear Time Growth in FETD

The problem of field solution with non-zero divergence arising when using edge elements, manifests as a linear time growth in the FETD method [62]. Similar to the eigenvalue problem, in the FETD method we seek the solution of the time dependent vector Helmholtz equations as in (2.32). Eq. (2.32) has a non-trivial solution of the form $\vec{E} = t\,\nabla\phi$ which grows linearly with time. Analogous to the eigenvalue problem, it is the gradient field supported by the edge element basis functions which introduce a linear time growth. Subsequently, the divergence-free condition of the electric flux no longer holds.

The number of spurious modes that contribute to the linear time growth is the same as the number of the "free nodes". To suppress the appearance of the spurious modes and hence suppress the linear time growth, the governing equation (2.32) is modified as

$$\begin{gathered}\nabla \times \frac{1}{\mu_r}\nabla \times \vec{E} + \varepsilon_r \frac{1}{c^2}\frac{\partial^2 \vec{E}}{\partial t^2}\vec{E} = 0 \text{ in } \Omega \\ \gamma_t \vec{E}\,|_{\Gamma_E} = 0; \quad \left(\tfrac{1}{\mu_r}\nabla \times \vec{E}\right) \times \hat{n}\,|_{\Gamma_H} \;\; = 0 \\ \text{with } \nabla \bullet \left([\varepsilon_r]\,\vec{E}\right) = 0 \text{ in } \Omega.\end{gathered} \tag{3.9}$$

The corresponding variational statement of the modified governing equation in (3.9) is

$$\begin{gathered}\text{Seek } \vec{E} \in \mathcal{H}_0\,(curl;\Omega) \text{ such that} \\ \int_\Omega \left[\nabla \times \vec{v} \cdot \frac{1}{\mu_r}\nabla \times \vec{u} + \varepsilon_r \frac{1}{c^2}\vec{v} \cdot \frac{\partial^2 \vec{u}}{\partial t^2}\right] d\Omega = -\int_\Omega \mu_0 \vec{v} \cdot \frac{\partial \vec{J}_i}{\partial t} d\Omega \\ \forall \vec{v} \in \mathcal{H}_0(curl,\Omega) \text{ and } t \in (0,T) \\ \text{subject to } \left(\nabla\phi, \varepsilon_r \vec{E}\right)_\Omega = 0 \; \forall \phi \in \mathcal{H}_0^1\,(\Omega)\,.\end{gathered} \tag{3.10}$$

In [62], instead of applying an additional constraint on the electric field solution, the governing equation was modified as

$$\left(\nabla \times \frac{1}{\mu_r}\nabla \times + \delta\right)\vec{E} + \frac{\varepsilon_r}{c^2}\frac{\partial^2}{\partial t^2}\vec{E} = 0 \tag{3.11}$$

such that the non-trivial solution, which is $\vec{E} = \nabla\phi\cos(\omega_\delta t)$ with $\omega_\delta = c\sqrt{\delta/\mu_r\varepsilon_r}$, does not grow with time. The choice of δ is based on numerical experiments. In the current approach, instead of modifying the governing equation, the divergence free condition in (3.10) is applied as a constraint equation while seeking the field solution.

3.3 Discrete Divergence-Free Condition

3.3.1 Implementation Using Edge Elements

Following the finite element discretization procedure of Sec. 2.3.3, the trial and test vector functions are sought within a finite dimensional subspace $\mathbf{V}^h \subset \mathcal{H}_0(curl;\Omega)$, which is the span of the well-adopted edge element basis functions. Subsequently, we have a finite dimensional approximation to the variational statement in (3.7) :

$$\begin{gathered}\text{Seek } \vec{E}^h \in \mathbf{V}^h \subset \mathbf{H}_0\left(curl;\Omega\right) \text{ and } k^h \in \mathbb{R} \text{ such that} \\ a\left(\vec{v}^h, \vec{E}^h\right) - \left(k^h\right)^2 \left(\vec{v}^h, \left[\varepsilon_r\right]\vec{E}^h\right)_{\Omega^h} = 0 \\ \forall \vec{v}^h \in \mathbf{V}^h \\ \text{subject to } \left(\nabla\phi^h, \left[\varepsilon_r\right]\vec{E}^h\right)_{\Omega^h} = 0 \; \forall \phi^h \in \Pi^h \left(\subset \mathcal{H}_0^1\left(\Omega\right)\right).\end{gathered} \tag{3.12}$$

Moreover, it is evident that $\Pi^h = \left\{u^h \in \mathcal{H}_0^1\left(\Omega^h\right), u^h\,|_K \in P_K^1\right\}$. The notation $u^h\,|_K$ means the restriction of function u^h in a tetrahedral element $K \in \Omega^h$; whereas P_K^1 denotes all linear polynomials within element $K \in \Omega^h$. According to the deRham-complex [35], it can be shown that $\nabla\Pi^h \subset \mathbf{V}^h$ - the so-called "inclusion condition" [69]. The first part of Eq. (3.12) is well-documented and corresponds to a generalized eigenmatrix equation:

$$\mathbf{Se} = k^2\mathbf{Te} \tag{3.13}$$

where $\mathbf{S}$ and $\mathbf{T}$ are defined in (2.42) and (2.43), respectively.

Similarly, for the FETD method, the finite dimensional approximation of the variational statement (3.10) is

$$\begin{gathered}\text{Seek } \vec{E}^h \in \mathbf{V}^h \in \mathcal{H}_0\left(curl;\Omega\right) \text{ such that} \\ \int_\Omega \left[\nabla\times\vec{v}^h \cdot \frac{1}{\mu_r}\nabla\times\vec{u}^h + \varepsilon_r\frac{1}{c^2}\vec{v}^h\cdot\frac{\partial^2\vec{u}^h}{\partial t^2}\right]d\Omega = -\int_\Omega \mu_0\vec{v}^h\cdot\frac{\partial\vec{J}_i}{\partial t}d\Omega \\ \forall\vec{v}\in\mathbf{V}^h \text{ and } t\in(0,T) \\ \text{subject to } \left(\nabla\phi^h, \left[\varepsilon_r\right]\vec{E}^h\right)_{\Omega^h} = 0 \; \forall \phi^h \in \Pi^h \left(\subset \mathcal{H}_0^1\left(\Omega\right)\right).\end{gathered} \tag{3.14}$$

The first part of (3.14) leads to the same matrix equation as in (2.41) and time update equations as in (2.50) can be obtained. The matrix structure of the constraint equation, i.e., the second part of (3.12) and (3.14), will be discussed in the next section.

It is to be noted that in discrete finite dimensional applications, the discrete Helmholtz decomposition [70] is analogous to the continuous version for any vector-valued functions. Specifically, for the finite dimensional space, $\mathbf{V}^h$, which is the span of edge

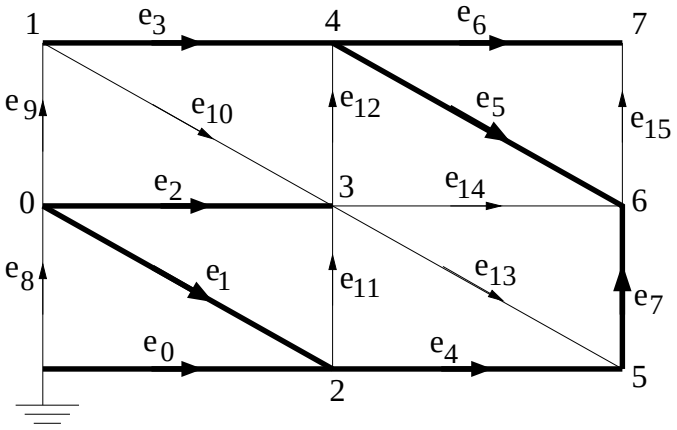

Figure 3.2: A sample triangular finite element mesh in 2-D with an arbitrary tree-cotree partitioning of the mesh.

element basis functions, we have $\mathbf{V}^h = \nabla\Pi^h \oplus \mathbf{R}^h$ where

$$\nabla\Pi^h = \{\nabla\phi | \phi \in \mathcal{H}_0^1(\Omega^h), \phi\,|_K \in P_K^1\} \tag{3.15}$$

and $\mathbf{R}^h \equiv \left(\nabla\Pi^h\right)^\perp$ is the space of discrete divergence-free finite elements [71]. The function space $(\mathcal{F})^\perp$ denotes the orthogonal complement of $\mathcal{F}$. In general, the eigenvalue solution of (3.13) leads to exactly $N_n \left(= \dim(\nabla\Pi^h)\right)$ number of spurious solutions with zero eigenvalues. In the eigenvalue problem, to suppress the occurrence of these spurious DC solutions, when using the Lanczos/Arnoldi algorithm, we need to impose constraint equations in addition to the generalized eigenmatrix equation in (3.13). Similarly, in the FETD method in addition to the implicit update equation in (2.50) additional constraint equation needs to be imposed to suppress the linear time growth. Before presenting the implementation of the constraint equation, the discrete gradient and integration matrix forms are introduced in the following section.

3.3.2 Discrete Gradient and Integration Matrix Forms

Resonators without PECs ($\Gamma_E = \emptyset$)

The procedure to construct the discrete gradient operator, expressed in matrix form, and its inverse, the discrete integration operator will be described. For simplicity, we shall illustrate the construction through a two-dimensional example, as shown in Fig. 3.2. Fig. 3.2 shows a simple triangular finite element mesh with a total of 16 edges. The FEM mesh can also be viewed as a graph. The edges are divided into two groups, tree and cotree edges, via the minimum spanning tree algorithm [72]. For example, in Fig. 3.2, the tree edges are the thicker and darker edges, whereas the cotree edges are the lighter ones. A tree is a set of connected edges which do not form a loop. It is not coincidental that the number of tree edges is the same as the number of free vertex nodes [73] (in Fig. 3.2, there are 8 tree edges and 8 free vertex nodes). Notice that in Fig. 3.2, we have arbitrarily assigned the left-lowest node to be the reference node, which corresponds to ground (zero potential). In general cases where perfect electric conductors (PECs) are present, it is customary to assign ground to all PECs. Note that the tree-cotree decomposition in Fig. 3.2 is not unique and other forms of decomposition are also possible.

Consider $\vec{u}^h \in \nabla\Pi^h \subset \mathbf{V}^h$, then

$$\sum_{i=0}^{N_e-1} u_i \vec{W}_i = \sum_{m=0}^{N_n-1} \phi_m \nabla\varsigma_m. \tag{3.16}$$

Equation (3.16) provides the basis to construct the discrete gradient operator. It is observed that

$$\begin{aligned} \int_{\text{edge } i=\{j,k\}} \sum_{l=0}^{N_e-1} u_l \vec{W}_l \cdot d\vec{l} &= \int_{\text{edge } i=\{j,k\}} \sum_{m=0}^{N_n-1} \phi_m \nabla\varsigma_m \cdot d\vec{l} \\ \Rightarrow u_i &= \phi_k - \phi_j. \end{aligned} \tag{3.17}$$

From the property of edge elements in (2.46), it is seen that the coefficient u_i of the edge element basis can be interpreted physically as circulation, namely,

$$u_i = \int_{\text{edge } i=\{j,k\}} \vec{u} \bullet d\vec{l}. \tag{3.18}$$

Hence, referring to Fig. 3.2, the relation between the circulation and the potential values can be expressed as

$$\begin{bmatrix} e_0 \\ e_1 \\ \vdots \\ e_{15} \end{bmatrix} = \begin{bmatrix} 0 & 0 & 1 & 0 & 0 & 0 & 0 & 0 \\ -1 & 0 & 1 & 0 & 0 & 0 & 0 & 0 \\ & \ddots & \ddots & \ddots & \ddots & & & \\ 0 & 0 & 0 & 0 & 0 & 0 & -1 & 1 \end{bmatrix} \begin{bmatrix} \phi_0 \\ \phi_1 \\ \vdots \\ \phi_7 \end{bmatrix}$$

$$\text{or} \qquad \mathbf{e} = \mathbf{G}\phi \tag{3.19}$$

Note that the discrete gradient matrix $\mathbf{G}$ is very sparse, with every row having at most two non-zero entries, which are either 1 or -1. In analogy to the continuous case the following properties hold true, viz.,

$$\begin{aligned} \ker(\nabla\times) = \text{range}(\nabla) &\Rightarrow \mathbf{SG} = 0 \\ \ker(\nabla\cdot) = \text{range}(\nabla\times) &\Rightarrow \mathbf{G}^T\mathbf{S} = 0 \end{aligned} \tag{3.20}$$

where $\ker(\bullet)$ and range $(\bullet)$ are the respective null and range spaces of the operator $\bullet$. As can be seen from (3.19), the dimension of the discrete gradient matrix is $N_e \times N_n$ and is not invertible. However, if we focus on the portion of the gradient matrix, which relates the tree edges to the nodal potential values, we have

$$\mathbf{G}_t = \begin{bmatrix} 0 & 0 & 1 & 0 & 0 & 0 & 0 & 0 \\ -1 & 0 & 1 & 0 & 0 & 0 & 0 & 0 \\ -1 & 0 & 0 & 1 & 0 & 0 & 0 & 0 \\ 0 & -1 & 0 & 0 & 1 & 0 & 0 & 0 \\ 0 & 0 & -1 & 0 & 0 & 1 & 0 & 0 \\ 0 & 0 & 0 & 0 & -1 & 0 & 1 & 0 \\ 0 & 0 & 0 & 0 & -1 & 0 & 0 & 1 \\ 0 & 0 & 0 & 0 & 0 & -1 & 1 & 0 \end{bmatrix} \tag{3.21}$$

where the subscript t represents the tree partition. The inverse of $\mathbf{G}_t$ is defined as the discrete integration matrix Σ. To compute the discrete integration matrix $\mathbf{\Sigma}$, we can

simply invert $\mathbf{G}_t$. Alternatively it can be assembled from the fact that each nodal potential value, ϕ_m, can be obtained by collecting the circulation along the tree path starting from the reference node to the vertex m. The rows and columns of $\mathbf{\Sigma}$ correspond to the free nodes and tree edges, respectively. In the ith row of $\mathbf{\Sigma}$, every non-zero column entry corresponds to an edge which is in the path along the tree to the ith node from the reference node. These entries are either +1 or -1, depending on the direction of the tree edge (whether the edge is in the same or opposite direction along the path from the reference node). Considering ϕ_3, by inspection of Fig. 3.2, we have $\phi_3 = e_0 - e_1 + e_2$. Through similar procedures, the following result can be obtained:

$$\begin{bmatrix} \phi_0 & \phi_1 & \phi_2 & \phi_3 & \phi_4 & \phi_5 & \phi_6 & \phi_7 \end{bmatrix}^T = \begin{bmatrix} 1 & -1 & 0 & 0 & 0 & 0 & 0 & 0 \\ 1 & 0 & 0 & -1 & 1 & -1 & 0 & 1 \\ 1 & 0 & 0 & 0 & 0 & 0 & 0 & 0 \\ 1 & -1 & 1 & 0 & 0 & 0 & 0 & 0 \\ 1 & 0 & 0 & 0 & 1 & -1 & 0 & 1 \\ 1 & 0 & 0 & 0 & 1 & 0 & 0 & 0 \\ 1 & 0 & 0 & 0 & 1 & 0 & 0 & 1 \\ 1 & 0 & 0 & 0 & 1 & -1 & 1 & 1 \end{bmatrix} \begin{bmatrix} e_0 \\ e_1 \\ e_2 \\ e_3 \\ e_4 \\ e_5 \\ e_6 \\ e_7 \end{bmatrix}$$

or

$$\boldsymbol{\phi} = \mathbf{\Sigma} \mathbf{e}_t \tag{3.22}$$

Notice that indeed $\mathbf{\Sigma}\mathbf{G}_t = \mathbf{I}$ as we expected. Moreover, by (3.20) and (3.19), the dimension of the null space of $\mathbf{S}$ is the same as the number of free nodes, N_n.

Resonator with Multiple PECs

In Fig. 3.3, we show a resonator with two separate PECs together with a finite element triangulation. Note that a common ground for both PECs needs to be assigned and the tree-cotree partition is built accordingly. Since all spurious DC modes correspond to gradient fields with all PECs having the same potential values, there are only three free vertexes and hence only three non-physical spurious DC modes. The corresponding tree-cotree markings of the edge elements are also shown in Fig. 3.3. The three spurious DC modes can be completely determined through three independent potential values by

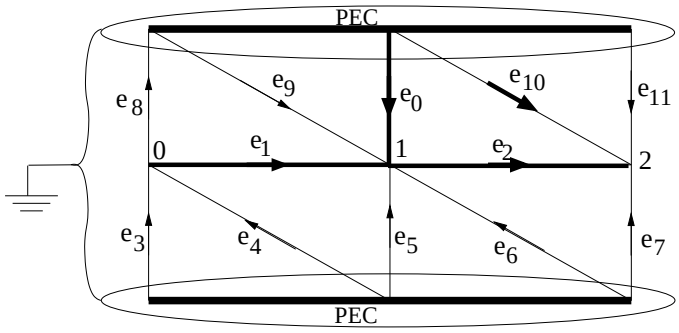

Figure 3.3: Tree-cotree marking for the non-physical DC modes for a resonator with two separate PECs.

(see Fig. 3.3)

$$\begin{bmatrix} e_0 \\ e_1 \\ e_2 \\ e_3 \\ \vdots \\ e_{11} \end{bmatrix} = \begin{bmatrix} 0 & 1 & 0 \\ -1 & 1 & 0 \\ 0 & -1 & 1 \\ 1 & 0 & 0 \\ \vdots & \vdots & \vdots \\ 0 & 0 & 1 \end{bmatrix} \begin{bmatrix} \phi_0 \\ \phi_1 \\ \phi_2 \end{bmatrix} \Rightarrow \mathbf{e} = \mathbf{G}\boldsymbol{\phi}$$

and

$$\mathbf{e}_t = \begin{bmatrix} 0 & 1 & 0 \\ -1 & 1 & 0 \\ 0 & -1 & 1 \end{bmatrix} \begin{bmatrix} \phi_0 \\ \phi_1 \\ \phi_2 \end{bmatrix} = \mathbf{G}_t\boldsymbol{\phi}. \tag{3.23}$$

Moreover, the corresponding integration matrix is

$$\boldsymbol{\Sigma} = \mathbf{G}_t^{-1} = \begin{bmatrix} 1 & -1 & 0 \\ 1 & 0 & 0 \\ 1 & 0 & 1 \end{bmatrix}. \tag{3.24}$$

3.3.3 Discrete Constraint Equations

The discrete constrained equations for the edge elements are described in this section. It can be formally stated as: An edge element vector $\vec{u}_c \left(= \mathbf{u}_c^T \mathbf{W}\right) \in \mathbf{V}^h$ is called a constrained vector if and only if:

$$(\vec{g}, [\varepsilon_r]\, \vec{u}_c)_\Omega = \mathbf{g}^T \mathbf{T} \mathbf{u}_c = 0, \qquad \forall \vec{g} \left(= \mathbf{g}^T \mathbf{W}\right) \in \nabla \Pi^h. \tag{3.25}$$

Since $\vec{g} \in \nabla\Pi^h$, according to (3.19), there exists a $\phi \left(= \boldsymbol{\phi}^T \boldsymbol{\varsigma}\right) \in \Pi^h$, such that $\mathbf{g} = \mathbf{G}\boldsymbol{\phi}$. Therefore, the constrained equation (3.25) becomes

$$\boldsymbol{\phi}^T \mathbf{G}^T \mathbf{T} \mathbf{u}_c = 0 \quad \forall \boldsymbol{\phi} \in \mathbb{R}^{N_n}. \tag{3.26}$$

Hence, from Eq. (3.26), we conclude that an edge element vector $\vec{u}_c \left(= \mathbf{u}_c^T \mathbf{W}\right) \in \mathbf{V}^h$ is a constrained vector iff

$$\mathbf{G}^T \mathbf{T} \mathbf{u}_c = 0. \tag{3.27}$$

In practice, the constrained equations can be enforced through any of the following forms

$$\mathbf{G}^T \left(a\mathbf{S} + b\mathbf{T}\right) \mathbf{u}_c = 0,\ a, b \in \mathbb{R},\ b \neq 0. \tag{3.28}$$

Equation (3.28) can be established through (3.27) and (3.20).

3.3.4 Efficient Implementation Using Tree-Cotree Splitting

Typically, a matrix solution is necessary to compute an edge element solution vector. This is true both in the eigenvalue problem when Lanczos algorithm is used to compute the eigenvalues and in the FETD method with an implicit update at each time-step. The general system of equation to be solved is of the form

$$(a\mathbf{S} + b\mathbf{T})\mathbf{e} = \mathbf{f}. \tag{3.29}$$

As long as the electric field solution vector computed from (3.29) satisfies (3.28), the solution is constrained and is free from contamination by the spurious modes or gradient fields. There are many possible ways of implementing the constraint such that the solution of (3.29) satisfies (3.27) or (3.28). Here we discuss three approaches.

The first procedure would be to operate on the solution vector $\mathbf{e}$ after seeking the solution of (3.29). The constraint equation to remove the gradient terms in this case is

$$\begin{gathered} \mathbf{e} = (a\mathbf{S} + b\mathbf{T})^{-1}\mathbf{f} \\ \mathbf{e} \leftarrow \mathbf{e} - \mathbf{G}(\mathbf{G}^T\mathbf{T}\mathbf{G})^{-1}\mathbf{G}^t\mathbf{T}\mathbf{e}. \end{gathered} \tag{3.30}$$

The implementation of (3.30) requires the inversion of $(\mathbf{G}^t\mathbf{T}\mathbf{G})$ which is positive definite.

The second procedure would be to operate on the excitation vector $\mathbf{f}$ instead of the solution vector $\mathbf{e}$. In the following, we devise a constraint equation to be imposed on $\mathbf{f}$ such that $\mathbf{e}$ satisfies (3.28). For this, consider $\mathbf{e}$ that satisfies (3.28), i.e.,

$$\mathbf{G}^T\left(a\mathbf{S}+b\mathbf{T}\right)\mathbf{e}=0 \Leftrightarrow \mathbf{G}^T\mathbf{f}=0. \tag{3.31}$$

Equation (3.31) is the necessary constraint equation to be imposed on $\mathbf{f}$ such that the solution of (3.29) leads to $\mathbf{e}$ being constrained and free from contamination by gradient fields. A possible approach to impose the constraint in (3.31) on $\mathbf{f}$ is to apply the following transformation to $\mathbf{f}$ before seeking the matrix solution viz.,

$$\begin{aligned}\mathbf{f} &\leftarrow \mathbf{f}-\mathbf{G}(\mathbf{G}^T\mathbf{G})^{-1}\mathbf{G}^t\mathbf{f}\\ \mathbf{e} &= (a\mathbf{S}+b\mathbf{T})^{-1}\mathbf{f}.\end{aligned} \tag{3.32}$$

The implementation in (3.32) requires solution of the matrix system $(\mathbf{G}^T\mathbf{G})$. Note that $\mathbf{G}^T\mathbf{G}$ is invertible.

For an efficient implementation of the constraint in (3.31) without the need for additional matrix solution is the third approach, based on the tree-cotree splitting of the finite element mesh. Once the tree-cotree partitioning is performed, the constraint in (3.31) can be rewritten as

$$\left[\begin{array}{cc}\mathbf{G}_t^T & \mathbf{G}_c^T\end{array}\right]\left[\begin{array}{c}\mathbf{f}_t\\ \mathbf{f}_c\end{array}\right]=\mathbf{0} \tag{3.33}$$

where the subscripts t and c represent tree and cotree edges, respectively. As shown in previous section, $\mathbf{G}_t$ is a $N_n \times N_n$ square matrix and is invertible with its inverse given by the integrator operator, i.e., $\mathbf{\Sigma}=\mathbf{G}_t^{-1}$. Given any $\mathbf{f}$, it can be constrained to satisfy (3.33) by simply setting the tree variables in $\mathbf{f}$, i.e., $\mathbf{f}_t$ in terms of the cotree variables $\mathbf{f}_c$, and results in a modified/constrained $\mathbf{f}'$ as

$$\mathbf{f}=\left[\begin{array}{c}\mathbf{f}_t\\ \mathbf{f}_c\end{array}\right] \Rightarrow \mathbf{f}'=\left[\begin{array}{c}\mathbf{f'}_t=-\Sigma^T\mathbf{G}_c^T\mathbf{f}_c\\ \mathbf{f}_c\end{array}\right]. \tag{3.34}$$

Note that in (3.34), $\mathbf{G}_c^T \mathbf{f}_c$ involves only addition and subtraction operations. Also, when Σ is explicitly constructed, multiplication by Σ involves once again only addition and subtraction operations. Moreover, imposing the constraint in (3.34) by the tree-cotree splitting involves the tree variables only. For a typical Delaunay Tessellation, the number of edges averages about 7.3 times the number of nodes [74]. Since the number of tree variables is one less than the number of nodes, the operation in (3.34) involves only approximately 14% of the total number of edges variables. Therefore, the extra cost in performing the constraint equations is minimal, while it completely suppresses the occurrence the gradient fields or DC spurious modes in the field solution.

3.4 Eigenvalue Problem

3.4.1 Constraint Equations with Lanczos Algorithm

The shift-and-invert Lanczos algorithm for the generalized eigenvalue problem of (3.13) with a shift of σ computes the eigenvalues around σ and their corresponding eigenvectors. In each iteration of the algorithm, the Ritz vector $\mathbf{r}$ is generated as a solution of a system

$$(\mathbf{S} - \sigma\mathbf{T})\mathbf{r} = \mathbf{q}. \tag{3.35}$$

As long as the Ritz vectors computed from (3.35) satisfy (3.28), the resulting eigenvector (spanned by the Ritz vectors) is constrained and is free from contamination by the DC spurious modes. Note that (3.35) is in the same form as (3.29) with $a = 1$ and $b = -\sigma$. The ARPACK package is a popular and extensively used implementation of the shift-and-invert Lanczos algorithm. The numerical results obtained for the cavity problems with and without physical DC modes are presented in the next section. The eigenvalue solver used to generate the results is based on ARPACK, and its "reverse

communication interface" feature [68] is utilized. This feature allows the user to provide matrix-dependent operations. The shift-and-invert mode operation of ARPACK for solution of (3.35) needs the user to provide two operations, viz.,

(a) Matrix vector multiplication of the form $\mathbf{q} \leftarrow \mathbf{T}\bar{\mathbf{r}}$, and

(b) Matrix solution of a linear system of the form

$\mathbf{r} \leftarrow (\mathbf{S} - \sigma\mathbf{T})^{-1}\bar{\mathbf{q}}$;

where $\bar{\mathbf{r}}$ and $\bar{\mathbf{q}}$ are computed by scaling $\mathbf{r}$ and $\mathbf{q}$ respectively, and are handled by the ARPACK code. The Ritz vector lies in the Krylov subspace constructed using $\bar{\mathbf{r}}$. By operation (b), for $\bar{\mathbf{r}}$ and hence $\mathbf{r}$ to be constrained, we need to enforce (3.34) on $\mathbf{q}$. Consequently, the operation (a) is followed by constraining the tree variables of $\mathbf{q}$ as in (3.34). This is the additional operation involved in the eigenvalue solver, as compared to that of the normal unconstrained case. Moreover, the initial guess vector, typically generated randomly, has to be constrained as well. For the shift σ in operation (b), when σ is positive, $(\mathbf{S} - \sigma\mathbf{T})$ is indefinite. However, since the constraint equations eliminate non-physical zero eigenvalues, setting σ to be negative would still result in the computation of positive eigenvalues (and physical zero eigenvalues, if any). When σ is negative, $(\mathbf{S}-\sigma\mathbf{T})$ is positive definite. The matrix solution in operation (b) can then be performed efficiently using a preconditioned conjugate gradient (PCG) algorithm with incomplete Cholesky factor as a preconditioner. A good value of σ would be $\sigma = -\alpha\bar{k}_{\min}^2$ (we have chosen $\alpha = 0.1$ in our computations). $\bar{k}_{\min}$ is the estimated wavenumber of lowest mode (excluding the physical DC modes), whose wavelength corresponds to twice the maximum dimension of the cavity. Seeking a matrix solution of a positive definite system instead of the traditional need to solve for an indefinite system is the fundamental advantage of the proposed method. Though an iterative solver could be employed for the matrix solution, the results reported in this thesis are obtained using a direct solver for the matrix solution in operation (b). It is to be noted that in the case of an iterative

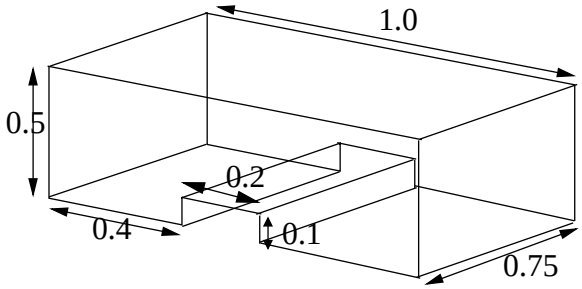

Figure 3.4: Geometry of ridged cavity. All dimensions are in cm.

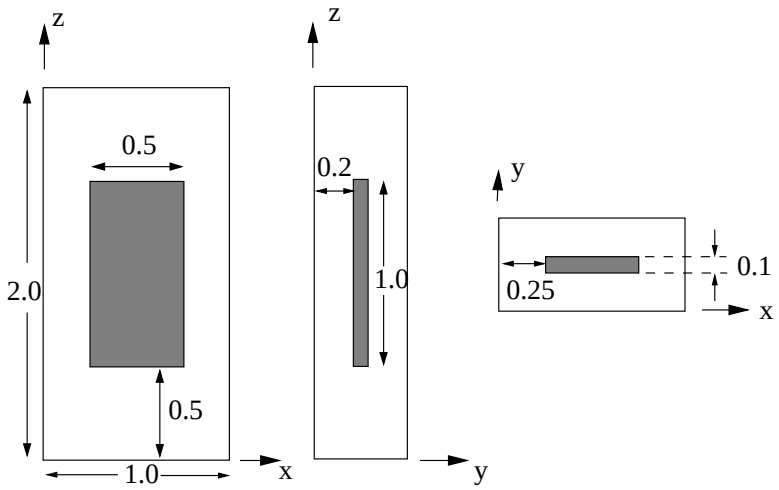

Figure 3.5: Geometry of rectangular resonator enclosing a PEC box (shaded). All dimension are in cm.

solver like PCG, the residual for convergence must be much smaller than the tolerance specified for the ARPACK code. With a tolerance of 1e-6 for the ARPACK code, a residual of 1e-8 for the convergence of the CG solver is sufficient to suppress the occurrence of spurious DC modes.

3.4.2 Numerical Results

The first example considered is a typical ridged cavity [31] shown in Fig. 3.4. The maximum dimension of the cavity is $l_{\max} = \sqrt{1^2 + 0.75^2 + 0.5^2} = 1.3463$ cm. Therefore, the lowest wavenumber is estimated to be $\bar{k}_{\min} = \frac{2\pi}{2l_{\max}} = 2.3335$. Subsequently, the shift is $\sigma = -0.1\bar{k}^2_{\min} = -0.54453$. The finite element mesh has 549 tetrahedral elements and the number of edge unknowns is 495 out of which 56 correspond to tree edges. The first 8 eigenvalues obtained, both with and without constraint equations, are shown in Table 3.1. It is observed that the constraint equations completely eliminate the occurrences of zero eigenvalues, whereas the unconstrained case shows 6 spurious modes with zero eigenvalues. A good measure of the irrotational components in the eigenvector solution $\mathbf{e}$ is $\text{err}(\mathbf{e}) = \left\|\mathbf{G}^T\mathbf{T}\mathbf{e}\right\|$. By (3.27), when $\mathbf{e}$ corresponds to a divergence-free solution, $\text{err}(\mathbf{e}) = 0$. This measure is also shown in Table 3.1, where it is observed that in the constrained case, $\text{err}(\mathbf{e}) = 0$ is negligible for all eigenvectors. However, for the unconstrained case, this measure is significant even for the eigenmodes with non-zero eigenvalues. This is because the solution for the physical modes are obtained from the Ritz vectors contaminated by the solution of non-physical DC modes. The number of iterations for the ARPACK code to converge for the unconstrained case (with randomly generated initial vector) was 132; and for the constraint case (with randomly generated divergence-free initial vector) was 149. The reason for more iterations in the constrained case is simply due to the higher resonant modes, which are farther away from the shift and therefore require more Krylov vectors to converge.

Cavity with Physical DC Mode

In some cavities, physical DC modes are present. The number of such modes is always one less than the number of perfect electric conductors (PECs). To highlight the fact that the constraint equations eliminate only the spurious and not the physical DC solution, an example of a 3-D rectangular resonator with a PEC box enclosed within

is presented. The geometry is shown in Fig. 3.5. The outer PEC box has a dimension of 1 cm $\times$ 0.5 cm $\times$ 2 cm, and the inner PEC box has a dimension of 0.5 cm $\times$ 0.1 cm $\times$ 1 cm. Thus, there are two PEC conductors and hence one physical DC mode is present. The volume between the two conductors is discretized into 723 tetrahedral elements. The number of edge unknowns is 593 out of which 43 correspond to tree edges. The results of the eigenvalue solver without and with constraint equations are given in Table 3.2. The measure curl($\mathbf{e}$) in Table 3.1 is the L2-norm of the curl of the eigenvector i.e, curl($\mathbf{e}$)$= \|\mathbf{Se}\|$. The unconstrained solver computes five eigenvectors with zero eigenvalues. Since all five eigenvectors lie in the null space of the curl operator (observed from the measure, curl($\mathbf{e}$)), it is not possible to detect the physical eigenmode. However, in the case of the eigensolver with constraint equations, the spurious modes are eliminated and only one physical eigenmode with zero eigenvalue is obtained. This mode, like the rest of the modes has no irrotational component, as verified by err($\mathbf{e}$) tabulated in Table 3.2. With a tolerance of 1e-6 and for a total of 8 eigenmodes, the ARPACK code converged in 105 iterations for the unconstrained case and 112 iterations for the constrained case.

3.5 Suppressing Linear Time Growth in FETD

3.5.1 Constraint Equations with Conjugate Gradient Solver

In the FETD method, the implicit update equation from (2.50) is of the form

$$\left[\mathbf{T} + \beta c^2 \Delta t^2 \mathbf{S}\right] \mathbf{u}^{n+1} = \mathbf{f}. \tag{3.36}$$

As long as $\mathbf{u}^{n+1}$ computed from (3.36) satisfies (3.28), the resulting electric flux is divergence-free. Note that (3.36) is in the same form as (3.29) with $a = 1$ and $b = \beta c^2 \Delta t^2$. Thus the constraint (3.34) needs to be applied on $\mathbf{f}$ before seeking the matrix solution in (3.36). The constraint on $\mathbf{f}$ is sufficient to obtain a divergence free solution when a direct solver is used for matrix solution. When iterative solvers are used,

Table 3.1: First 8 lowest eigenvalues of ridged cavity computed without and with constraint equations

Mode	**Ref. [31]**	**Unconstrained**		**Constrained**	
No.		k(cm^{-1})	err($\mathbf{e}$)	k(cm^{-1})	err($\mathbf{e}$)
1	4.999	0.000	1.281	4.987	0.248e-12
2	7.354	0.000	1.068	7.292	0.227e-12
3	7.832	0.000	1.180	7.833	0.264e-12
4	7.942	0.000	1.056	7.863	0.205e-12
5	7.959	0.000	1.092	7.960	0.260e-12
6	8.650	0.000	1.077	8.606	0.166e-12
7	8.916	4.987	0.034	9.083	0.181e-12
8	9.103	7.292	0.002	9.154	0.187e-12

Table 3.2: First 8 lowest eigenvalues of rectangular resonator enclosing a PEC box computed without and with constraint equations

Mode No.	**Unconstrained**			**Constrained**		
	k(cm^{-1})	err($\mathbf{e}$)	curl($\mathbf{e}$)	k(cm^{-1})	err($\mathbf{e}$)	curl($\mathbf{e}$)
1	0.000	1.214	0.000	0.000	0.145e-12	0.000
2	0.000	1.463	0.000	2.179	0.153e-12	1.422
3	0.000	1.169	0.000	3.165	0.167e-12	3.053
4	0.000	1.578	0.000	3.317	0.136e-12	3.257
5	0.000	1.475	0.000	3.959	0.130e-12	4.637
6	2.179	0.005	1.423	4.129	0.180e-12	5.324
7	3.165	0.011	3.053	4.274	0.162e-12	5.285
8	3.317	0.030	3.257	5.313	0.152e-12	8.232

only in the ideal case with no rounding-off errors, applying the constraint equation on the Krylov vector would lead to a divergence-free solution. Due to the finite precision representation of real numbers, gradient fields could be introduced during the Krylov iterations of the CG solver. When preconditioned CG solvers are used with a good preconditioner such as the incomplete Cholesky factor, only few Krylov iterations are required for convergence and applying the constraint equation on the Krylov vector would suffice for a divergence-free solution. When a CG solver without any preconditioner is used, an implementation of divergence-free condition as in (3.30) can be employed once in a few time steps to remove any gradient terms introduced due to round-off error in the Krylov iterations. The proposed constraint equations have been derived from the case of discrete-space continuous-time framework, allowing its extension to both eigenvalue problems and FETD method. In [75], the discrete origin of linear time growth based on the eigenvalues and eigenvectors of the amplification matrix of the FETD method under the case of discrete-space discrete-time is demonstrated. Constraint equations, similar in principle to the proposed method, have been derived in [75].

3.5.2 Numerical Results

To illustrate the suppression of the linear time growth using constraint equations, we consider the case of a ridged cavity, the same as the one considered in Sec. 3.4.2 and as shown in Fig. 3.4. The cavity is excited by a divergence-free electric current with a Gaussian pulse waveform located at an arbitrary edge of the tetrahedral mesh. When creating the tree-cotree edges of the mesh, the source edges must be part of the co-tree set. Preconditioned CG solver is used with a preset tolerance of 1e-6. The incomplete Cholesky factor has a drop tolerance of 1e-2. The iterative solver takes 4 iterations to converge. The time history of the electric field at an arbitrary location is recorded. The discrete Fourier transform of this time domain signal reveals the resonant frequencies of the cavity as spectral peaks. In Fig. 3.6, the spectra of the electric fields within the cavity

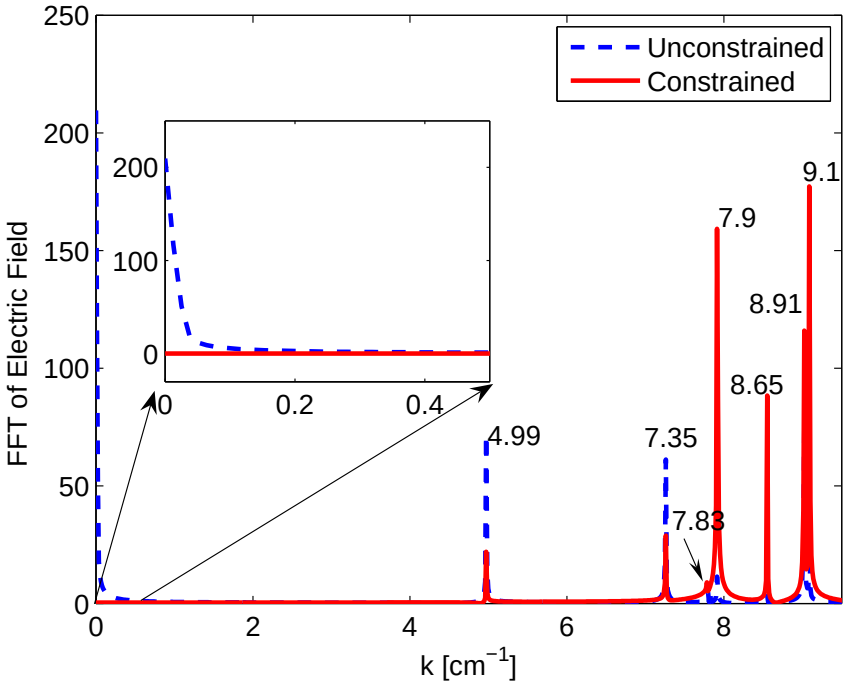

Figure 3.6: Spectrum of electric field showing different resonant modes for the solution without and with divergence-free constraint equations.

for both cases, viz. without constraint and with divergence free constraint equation are compared. The inset magnifies the low frequency region, where it is observed that the unconstrained case is corrupted by the gradient vector functions with linear time dependence.

Note that the linear time growth reflects as $\frac{1}{k^2}$ in the spectral domain (see inset of Fig. 3.6). Also the spectral peaks indicating the resonant frequencies are in agreement with the results from the eigenvalue solver in Table. 3.1. In Fig. 3.7, the power content of the DC terms ($k = 0$) in the electric field solution with respect to time is shown. The DC power increases with time in the case of the unconstrained solution. For the constrained case, there is no DC power as the spurious modes are completely suppressed by the constraint equations.

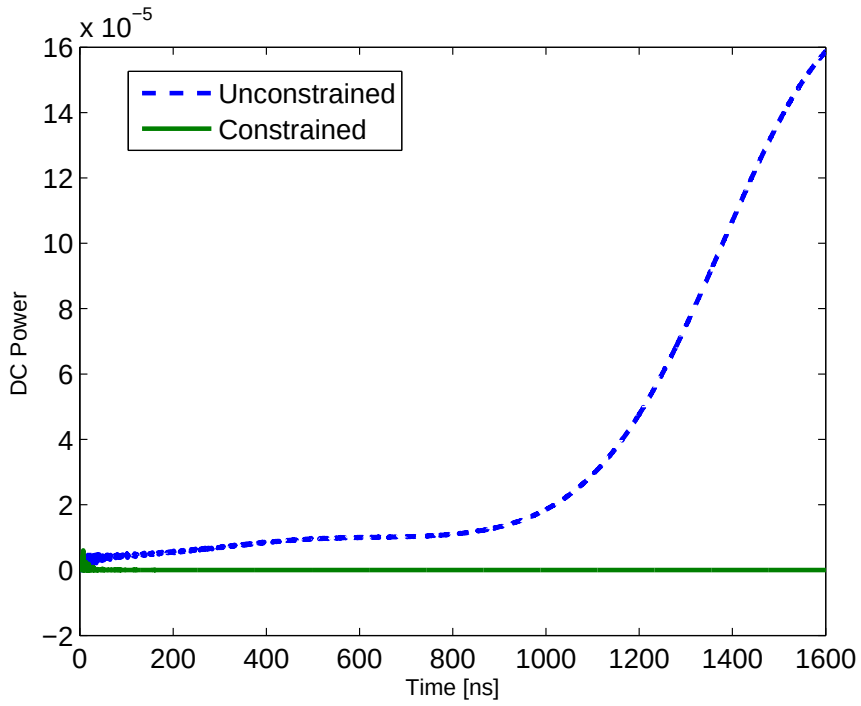

Figure 3.7: Power content of DC terms in the electric field solution without and with divergence-free constraints.

3.6 Conclusions

Gradient vector fields satisfy vector Helmholtz equations but they fail to satisfy the divergence-free condition of electric flux, required by Maxwell's equations. When edge element basis functions, which span a discrete gradient space, are employed for the finite element solution, gradient vector field appears as spurious modes. Such spurious modes manifest as unphysical DC modes in eigenvalue problems. In FETD method, such spurious modes give rise to a linear time growth, a form of weak-instability. A novel method to eliminate such spurious modes using "divergence-free" constraint equations is developed. This method of imposing constraint such that the computed electric flux solution is divergence-free does not involve any other basis functions other than the edge elements. The weak form of the divergence-free nature of the electric flux translates to the corresponding constraint equations imposed on the Krylov vector that either generates

the Ritz vector in the Lanczos/Arnoldi algorithm in the context of eigenvalue problems or electric field solution in the CG solver in the context of FETD method. The method to impose the constraint equations efficiently using the tree-cotree partitioning of the finite element mesh has been presented. In eigenvalue problems, an added advantage achieved is the ability to use negative shift in the Lanczos algorithm with shift-and-invert strategy. This results in solving a positive definite matrix which otherwise is indefinite. Numerical examples verify conclusively the elimination of spurious modes in the solution of the eigenvalue problem.

CHAPTER 4

STABILITY OF HYBRID FETD-FDTD METHOD

4.1 Introduction

A fundamental requirement of a numerical method for solution of partial differential equations is convergence. By convergence, when the time step and spatial step sizes are reduced to zero in a particular relative rate, the numerical solution should converge to the exact solution. To have a convergent scheme, it is necessary that the approximations of the differential operators in arriving at the numerical scheme are consistent. The truncation errors in the approximation of the differential operators must vanish in the limit as the step size tends to zero. For initial value problems, however, consistency alone does not guarantee convergence. By the Lax Equivalence theorem [76], which states that a consistent finite difference approximation for a well-posed initial value problem is convergent if and only if it is stable. Thus numerical stability is of paramount importance in devising a convergent numerical method for solution of initial value problems. Apart from being necessary for a convergent numerical method, numerical stability of a time marching method is vital for wider applications of such methods for real world problems. Explicit schemes in general exhibit conditional stability whereas in the case of implicit schemes such as the Newmark-beta scheme, unconditional stability can be achieved under specific choice of parameters. To arrive at conditions for numerical stability of a particular finite method, the Fourier analysis or more popularly called von Neumann analysis [77] based on the eigenvalues of the amplification matrix of the time marching scheme can be applied. An alternate procedure, without the need of explicitly

constructing the amplification matrix, is based on the modal decomposition of the update scheme and subsequent use of $z-$transform and the Routh-Hurwitz criteria [29] to arrive at conditions for numerical stability. The procedure of investigating the numerical stability and some of the results obtained in this chapter have been published in [78].

4.2 Investigation of Stability

To investigate the stability of the hybrid FETD-FDTD method, the update equations of the unknowns in Ω_{FD} and Ω_{FE} are combined and a single two-step time update equation is obtained. Based on the update equation a global iteration or amplification matrix for the hybrid algorithm can be obtained. Subsequent study of the eigenvalues of the amplification matrix reveals the behaviour of numerical stability. In this Chapter, several different hybridization schemes are considered. The effect of each scheme on the coefficient matrices of the update equation is seen. The von Neumann condition that the magnitude of the largest eigenvalue, also called as the spectral radius, of the amplification matrix is less than or equal to one, is the necessary and sufficient condition for stability of finite difference schemes with normal amplification matrix [77]. A real matrix $\mathbf{A}$ is normal if $\mathbf{A}^T\mathbf{A} = \mathbf{A}\mathbf{A}^T$. When the amplification matrix is not normal as in the FETD method and the hybrid method, the condition for stability is necessary but not sufficient [76]. The additional condition for stability in this case is that the eigenvalues with multiplicity greater than one have magnitude strictly less than one [41]. However, when the magnitude of the largest eigenvalue, also called the spectral radius of the amplification matrix is greater than one, the scheme is numerically unstable. The stability investigation for different hybridization schemes, performed in this Chapter helps in the identification of such numerically unstable schemes.

4.2.1 Hybrid Update Equation

The numerical stability of a time-marching algorithm represented by

$$\mathbf{v}^{n+1} = \mathbf{G}(\Delta t, \Delta h)\mathbf{v}^{n} \tag{4.1}$$

where $\mathbf{v}^n$ is the unknown at time $n\Delta t$ can be investigated by analyzing the eigenvalues of the global iteration or amplification matrix $\mathbf{G}$. The necessary condition for stability is $\rho(\mathbf{G}) \leq 1$, where $\rho(\mathbf{G}) = |\lambda_G^{\max}|$ is the spectral radius of the matrix $\mathbf{G}$ [76].

The hybrid FETD-FDTD method, as discussed in Sec.2.4 decomposes the computational domain into Ω_{FD} and Ω_{FE}. The electric field unknowns are distributed in Ω_{FD} and Ω_{FE}. The notations for the variables used in arriving at the hybrid update equation are shown in Table. 4.2.1. To obtain the global iteration matrix $\mathbf{G}$ for the hybrid algorithm, the update equations for the unknowns in Ω_{FD} and Ω_{FE} have to be combined. Typically, in the case of finite difference method on uniform Cartesian grid such as the FDTD method, the eigenvalues of the global iteration matrix can be computed analytically by representing the solution in the spectral domain. In the case of finite element method with unstructured mesh, it is not possible to compute the eigenvalues of $\mathbf{G}$ analytically. In the investigation of stability of different schemes, the eigenvalues of $\mathbf{G}$ are computed for a particular case of sample hybrid mesh. However, for certain schemes, based on the spectral properties of update coefficient matrices, rigorous conditions for stability can be obtained. The analysis to follow is for the 2-D TE$_z$ case and can be extended to 3-D case with out any limitation.

The magnetic and electric field FDTD update equations for the unknowns in Ω_{FD}, given by (2.62), (2.63) and (2.64) can be written in a matrix form as follows

$$\mathbf{h}_{FD}^{n+1/2} = \mathbf{h}_{FD}^{n-1/2} - \mathbf{A}_{FD}^{e} \begin{pmatrix} \mathbf{e}_{FD} \\ \mathbf{e}_{\overline{FE}} \\ \mathbf{e}_{\overline{FD}} \end{pmatrix}^{n} \tag{4.2}$$

$$\begin{pmatrix} \mathbf{e}_{FD} \\ \mathbf{e}_{\overline{FE}} \\ \mathbf{e}_{\overline{FD}} \end{pmatrix}^{n+1} = \begin{pmatrix} \mathbf{e}_{FD} \\ \mathbf{e}_{\overline{FE}} \\ \mathbf{e}_{\overline{FD}} \end{pmatrix}^{n} + \mathbf{A}_{FD}^{h}\mathbf{h}_{FD}^{n+1/2}. \tag{4.3}$$

Table 4.1: Notations used for stability analysis.

Variable	Description
$\mathbf{h}_{FD}$	Magnetic field unknowns in Ω_{FD}
$\mathbf{e}_{FD}$	Electric field unknowns in Ω_{FD}
$\mathbf{e}_{FE}$	Electric field unknowns in Ω_{FE}
$\mathbf{e}_{\overline{FD}}$	Electric field unknowns on the boundary of Ω_{FD}
$\mathbf{e}_{\overline{FE}}$	Electric field unknowns on the boundary of Ω_{FE}

In general, the matrix $\mathbf{A}_{FD}^{h}$ and $\mathbf{A}_{FD}^{e}$ are sparse. For Maxwell's equations in the lossless case, the non-zero entries of $\mathbf{A}_{FD}^{h}$ are $\pm\Delta t/(\mu_0\Delta h)$ and those of $\mathbf{A}_{FD}^{e}$ are $\pm\Delta t/(\epsilon_0\Delta h)$. Here, Δt is the time step size and Δh is the space step size. The matrix $\mathbf{A}_{FD} = \mathbf{A}_{FD}^{h}\mathbf{A}_{FD}^{e}$ can be viewed as the discrete $\nabla \times \nabla\times$ operator scaled by $(c^2\Delta t^2)$. By eliminating $\mathbf{h}_{FD}$ from the FDTD update equations, the electric field update equation in Ω_{FD} is

$$\begin{pmatrix}\mathbf{e}_{FD}\\ \mathbf{e}_{\overline{FE}}\\ \mathbf{e}_{\overline{FD}}\end{pmatrix}^{n+1} = \begin{pmatrix}2\mathbf{I}-\mathbf{A}_{11} & -\mathbf{A}_{12} & \mathbf{0}\\ -\mathbf{A}_{12}^{t} & 2\mathbf{I}-\mathbf{A}_{22} & -\mathbf{A}_{23}\\ \mathbf{0} & -\mathbf{A}_{23}^{t} & 2\mathbf{I}-\mathbf{A}_{33}\end{pmatrix}\begin{pmatrix}\mathbf{e}_{FD}\\ \mathbf{e}_{\overline{FE}}\\ \mathbf{e}_{\overline{FD}}\end{pmatrix}^{n} - \begin{pmatrix}\mathbf{e}_{FD}\\ \mathbf{e}_{\overline{FE}}\\ \mathbf{e}_{\overline{FD}}\end{pmatrix}^{n-1} \tag{4.4}$$

where

$$\mathbf{A}_{FD} = \begin{pmatrix}\mathbf{A}_{11} & \mathbf{A}_{12} & \mathbf{0}\\ \mathbf{A}_{12}^{t} & \mathbf{A}_{22} & \mathbf{A}_{23}\\ \mathbf{0} & \mathbf{A}_{23}^{t} & \mathbf{A}_{33}\end{pmatrix} = \mathbf{A}_{FD}^{h}\mathbf{A}_{FD}^{e}.$$

From the FETD update equation as in (2.50), the implicit update equation for the unknowns in Ω_{FE} is written as

$$\begin{pmatrix}\mathbf{M}_{22} & \mathbf{M}_{23} & \mathbf{M}_{24}\\ \mathbf{M}_{23}^{t} & \mathbf{M}_{33} & \mathbf{M}_{34}\\ \mathbf{M}_{24}^{t} & \mathbf{M}_{34}^{t} & \mathbf{M}_{44}\end{pmatrix}\begin{pmatrix}\mathbf{e}_{\overline{FE}}\\ \mathbf{e}_{\overline{FD}}\\ \mathbf{e}_{FE}\end{pmatrix}^{n+1} = \begin{pmatrix}\mathbf{N}_{22} & \mathbf{N}_{23} & \mathbf{N}_{24}\\ \mathbf{N}_{23}^{t} & \mathbf{N}_{33} & \mathbf{N}_{34}\\ \mathbf{N}_{24}^{t} & \mathbf{N}_{34}^{t} & \mathbf{N}_{44}\end{pmatrix}\begin{pmatrix}\mathbf{e}_{\overline{FE}}\\ \mathbf{e}_{\overline{FD}}\\ \mathbf{e}_{FE}\end{pmatrix}^{n} - \begin{pmatrix}\mathbf{M}_{22} & \mathbf{M}_{23} & \mathbf{M}_{24}\\ \mathbf{M}_{23}^{t} & \mathbf{M}_{33} & \mathbf{M}_{34}\\ \mathbf{M}_{24}^{t} & \mathbf{M}_{34}^{t} & \mathbf{M}_{44}\end{pmatrix}\begin{pmatrix}\mathbf{e}_{\overline{FE}}\\ \mathbf{e}_{\overline{FD}}\\ \mathbf{e}_{FE}\end{pmatrix}^{n-1} \tag{4.5}$$

The matrices $\mathbf{M}$ and $\mathbf{N}$ are given as

$$\begin{aligned}\mathbf{M} &= \begin{pmatrix}\mathbf{M}_{22} & \mathbf{M}_{23} & \mathbf{M}_{24}\\ \mathbf{M}_{23}^t & \mathbf{M}_{33} & \mathbf{M}_{34}\\ \mathbf{M}_{24}^t & \mathbf{M}_{34}^t & \mathbf{M}_{44}\end{pmatrix} = \mathbf{T} + \beta c^2 \Delta t^2 \mathbf{S}\\ \mathbf{N} &= \begin{pmatrix}\mathbf{N}_{22} & \mathbf{N}_{23} & \mathbf{N}_{24}\\ \mathbf{N}_{23}^t & \mathbf{N}_{33} & \mathbf{N}_{34}\\ \mathbf{N}_{24}^t & \mathbf{N}_{34}^t & \mathbf{N}_{44}\end{pmatrix} = 2\mathbf{T} - (1-2\beta) c^2 \Delta t^2 \mathbf{S}\end{aligned}$$

where $\mathbf{T}$ and $\mathbf{S}$ are the mass and stiffness matrices for the electric field basis functions as defined in (2.47).

In the hybrid method, $\mathbf{e}_{\overline{FD}}$ is updated using (4.5) and $\mathbf{e}_{\overline{FE}}$ is update using (4.4). The update equation for the hybrid algorithm can then be written by combining Eqs. (4.4) and (4.5) as

$$\mathbf{Q}_1 \mathbf{e}^{n+1} = \mathbf{Q}_0 \mathbf{e}^n - \mathbf{Q}_1 \mathbf{e}^{n-1} \tag{4.6}$$

where

$$\mathbf{Q}_1 = \begin{pmatrix}\mathbf{I} & \mathbf{0} & \mathbf{0} & \mathbf{0}\\ \mathbf{0} & \mathbf{I} & \mathbf{0} & \mathbf{0}\\ \mathbf{0} & \mathbf{M}_{23}^t & \mathbf{M}_{33} & \mathbf{M}_{34}\\ \mathbf{0} & \mathbf{M}_{24}^t & \mathbf{M}_{34}^t & \mathbf{M}_{44}\end{pmatrix} \tag{4.7}$$

$$\mathbf{Q}_0 = \begin{pmatrix}2\mathbf{I} - \mathbf{A}_{11} & -\mathbf{A}_{12} & \mathbf{0} & \mathbf{0}\\ -\mathbf{A}_{12}^t & 2\mathbf{I} - \mathbf{A}_{22} & -\mathbf{A}_{23} & \mathbf{0}\\ \mathbf{0} & \mathbf{N}_{23}^t & \mathbf{N}_{33} & \mathbf{N}_{34}\\ \mathbf{0} & \mathbf{N}_{24}^t & \mathbf{N}_{34}^t & \mathbf{N}_{44}\end{pmatrix} \tag{4.8}$$

and

$$\mathbf{e} = \begin{pmatrix}\mathbf{e}_{FD}\\ \mathbf{e}_{\overline{FE}}\\ \mathbf{e}_{\overline{FD}}\\ \mathbf{e}_{FE}\end{pmatrix}.$$

The two-step hybrid update equation in (4.6) can be written in the form of (4.1) using the following substitution

$$\mathbf{v}^n = \begin{pmatrix}\mathbf{e}^n\\ \mathbf{e}^{n-1}\end{pmatrix}; \tag{4.9}$$

which results in the following iteration matrix,

$$\mathbf{G} = \begin{pmatrix}\mathbf{Q}_1^{-1}\mathbf{Q}_0 & -\mathbf{I}\\ \mathbf{I} & \mathbf{0}\end{pmatrix}. \tag{4.10}$$

The eigenvalues of $\mathbf{G}$, λ_G, can be computed efficiently by computing the eigenvalues of a lower order matrix $\mathbf{Q}_1^{-1}\mathbf{Q}_0$, say λ_Q. It can be shown that λ_G can be computed from λ_Q as

$$\lambda_G = \frac{\lambda_Q}{2} \pm \sqrt{\left(\frac{\lambda_Q}{2}\right)^2 - 1}. \tag{4.11}$$

Upon assembling the matrices $\mathbf{Q}_0$ and $\mathbf{Q}_1$ for a given hybrid mesh, the eigen values of the iteration matrix λ_G and hence $\rho(\mathbf{G})$ can be computed. $\rho(\mathbf{G}) \leq 1$ is a necessary condition for stability, though not sufficient, since $\mathbf{G}$ is not a normal matrix.

4.2.2 Hybridization Schemes

Depending on the hybridization of FDTD method with FETD, the matrix structure of the hybrid update equation in (4.6) varies. The first scheme considered is based on the initial formulation proposed in [14, 16, 61] and discussed in Sec. 2.4. This method is referred to as Scheme I. For this scheme all the entries in the update coefficient matrices $\mathbf{Q}_0$ and $\mathbf{Q}_1$ are non-zero and sparse. A sample mesh for this scheme is shown in Fig. 4.1(a). An alternate scheme based on the same principle as Scheme I is to discretise the overlapping region at the interface of Ω_{FD} and Ω_{FE} with a particular triangulation as shown in Fig. 4.1(b). For this scheme, referred to as Scheme II, $\mathbf{M}_{23} = \mathbf{N}_{23} = \mathbf{0}$ in (4.7) and (4.8). Note that there is no coupling between $\mathbf{e}_{\overline{FD}}$ and $\mathbf{e}_{\overline{FE}}$ under the special case of triangulation.

Scheme III follows the strategy proposed in [79] and the hybrid mesh for this case is shown in Fig. 4.2. Hybrid mesh generation for this scheme is relatively simple since the scheme only requires the boundary of Ω_{FE} to conform with the electric field grid of Ω_{FD}, unlike Schemes I and II where the interior boundary elements of the finite element triangulation in Ω_{FE} need to be constrained such that they overlap with the electric field grid of Ω_{FD}. However, Scheme III would require the magnetic field (H_z component)

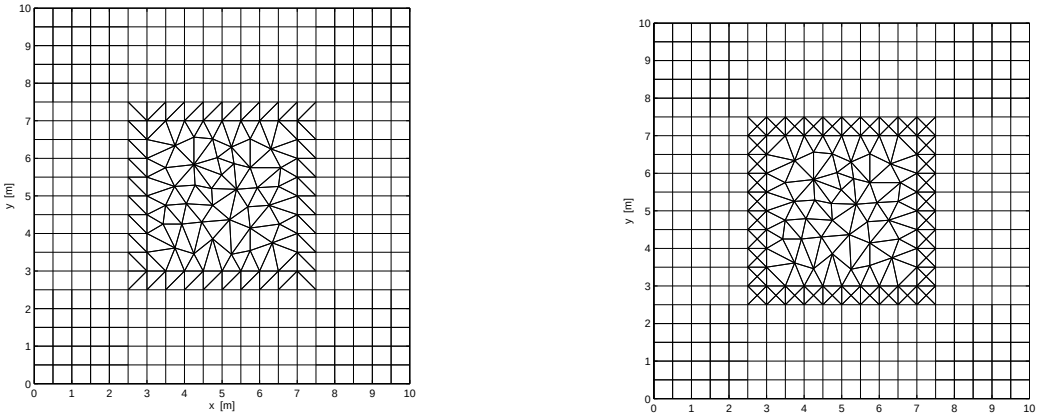

(a) Scheme I (b) Scheme II

Figure 4.1: Hybrid mesh for Schemes I and II.

inside the FE region, to be updated as

$$H^{n+1/2}_{z(i+1/2,j+1/2)} = H^{n-1/2}_{z(i+1/2,j+1/2)} - \frac{\Delta t}{\mu_0 A_k} \sum_{i=0}^{2} l_i^k e_i^k \tag{4.12}$$

where A_k is the area of the kth triangular element which contains the point $((i + 1/2)\Delta h, (j + 1/2)\Delta h)$. l_i^k is the length of the ith edge and e_i^k is the corresponding unknown edge vector in the clockwise direction obtained from the solution in Ω_{FE}. Eq. (4.12) is obtained by applying $\nabla\times$ operator on the triangular finite element with linear edge vector basis functions. Note that (4.12) can also be obtained starting from the integral form of Faradays law, assuming H_z to be constant within the element. This scheme is different from the other schemes considered and does not have the same form of update coefficients as in (4.7) and (4.8). The eigenvalue analysis is not performed for this scheme though an implementation of the scheme is carried out to compare its performance in terms of stability with the other schemes studied. In [80], Scheme II was shown to introduce less unphysical reflections in the numerical solution and hence to have better accuracy compared to Schemes I and III.

Schemes IV and V are different from Schemes I and II in that instead of triangular elements, rectangular elements are used in the interface region of Ω_{FD} and Ω_{FE}.

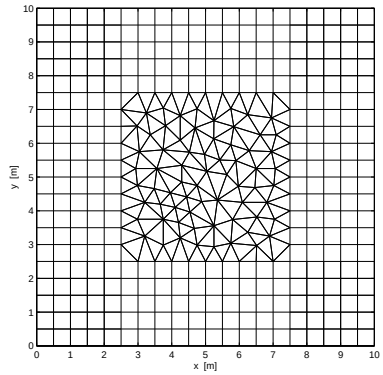

Figure 4.2: Hybrid mesh for Scheme III

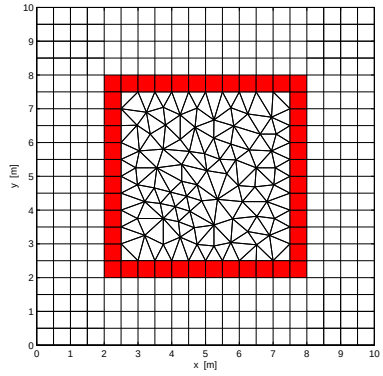

Figure 4.3: Hybrid mesh for Schemes IV and V

It immediately follows that $\mathbf{M}_{24} = \mathbf{N}_{24} = \mathbf{0}$ in (4.7) and (4.8) for this particular choice of discretization where there is no coupling between the basis functions associated with $\mathbf{e}_{\overline{FE}}$ and $\mathbf{e}_{FE}$. The hybrid mesh for this case is shown in Fig. 4.3 where the shaded region is the interface of Ω_{FD} and Ω_{FE} discretized using rectangular finite elements. Thus Ω_{FE} is discretized with both triangular and rectangular elements. The finite element mass and stiffness matrices for both triangular and rectangular elements can be computed analytically. For Scheme IV, the exact mass and stiffness matrices for the rectangular elements are used. In the case of Scheme V, the integration over rectangular elements is performed using trapezoidal rule of numerical integration. This

scheme is the 2-D equivalent of the scheme proposed in [18]. The use of trapezoidal integration leads to a diagonal mass matrix, as will be seen in Sec. 4.4. This leads to $\mathbf{M}_{23} = \beta c^2 \Delta t^2 \mathbf{S}_{23}$ in (4.7) and $\mathbf{N}_{23} = -(1-2\beta) c^2 \Delta t^2 \mathbf{S}_{23}$ in (4.8). Further more, for the time integration using the Newmark-beta method, the parameter β is set as zero for the rectangular elements resulting in $\mathbf{M}_{23} = \mathbf{0}$ and $\mathbf{N}_{23} = -c^2 \Delta t^2 \mathbf{S}_{23}$ in (4.8). When $\beta = 0$, the temporal discretization is the same as the second order accurate central differencing. In fact, following this procedure on rectangular elements results in a update scheme which is equivalent to FDTD method and is the key for a stable hybridization of FETD method with FDTD method.

4.3 Numerical Experiments

To investigate the eigenvalues of the global iteration matrix for the different hybridization schemes, the sample hybrid meshes in Figs. 4.1 (a), and 4.1(b) and Fig. 4.3 are considered. In all the cases, the hybrid mesh is truncated by a PEC. The update coefficient matrices $\mathbf{Q}_0$ and $\mathbf{Q}_1$ are assembled for the different schemes with $\Delta t = \frac{\Delta h}{c\sqrt{2}}$. The eigenvalues of $\mathbf{Q}_1^{-1}\mathbf{Q}_0$ is computed initially followed by computation of λ_G using (4.11). The distributions of eigenvalues in the complex plane, for Schemes I, II, IV and V are shown in Figs. 4.4, 4.5, 4.6 and 4.7 respectively.

Ideally, all eigenvalues should lie on the unit circle in the complex plane. If any of the eigenvalue is inside the unit circle, then the numerical scheme is dissipative (which should not be the case when dealing with Maxwell's equations in lossless media). If any of the eigenvalue is outside the unit circle, then the scheme is numerically unstable. In Table 4.3, the spectral radius and the percentage of eigenvalues lying outside the unit circle for the four schemes are compared. It is seen that the spectral radius of the iteration matrix for Scheme V is unity, while for the other schemes it exceeds unity.

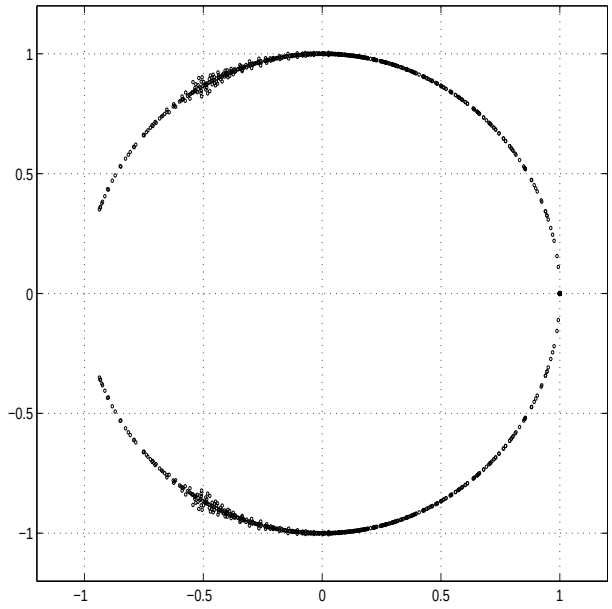

Figure 4.4: Distribution of eigenvalues of the iteration matrix in Scheme I for the mesh shown in Fig. 4.1(a)

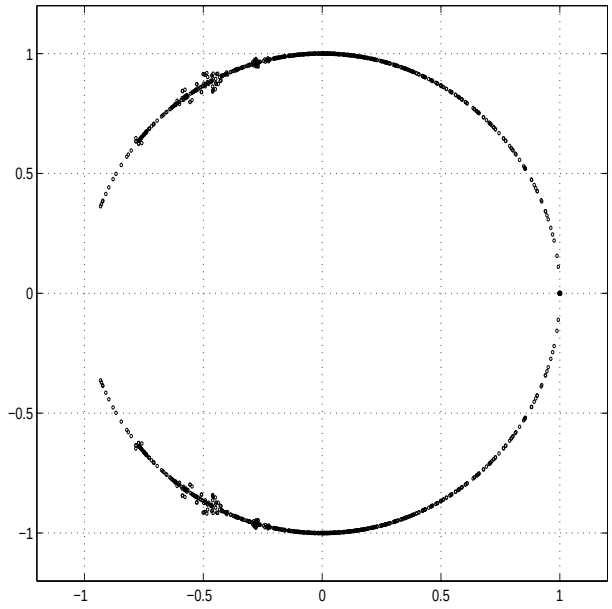

Figure 4.5: Distribution of eigenvalues of the iteration matrix in Scheme II for the mesh shown in Fig. 4.1(b)

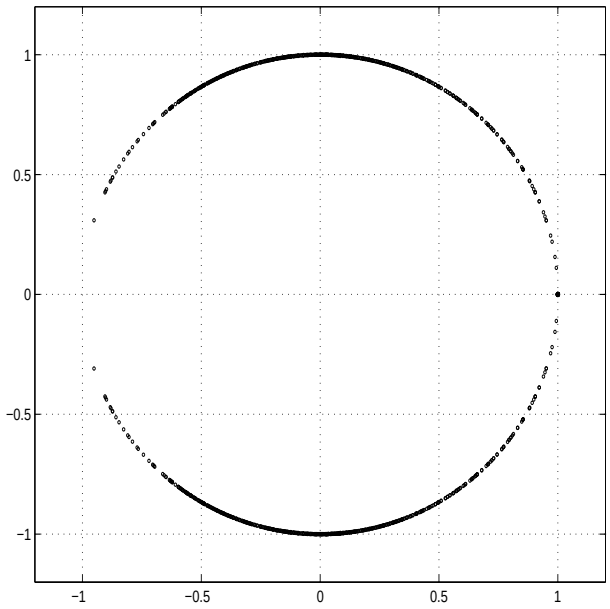

Figure 4.6: Distribution of eigenvalues of the iteration matrix in Scheme IV for the mesh shown in Fig. 4.3

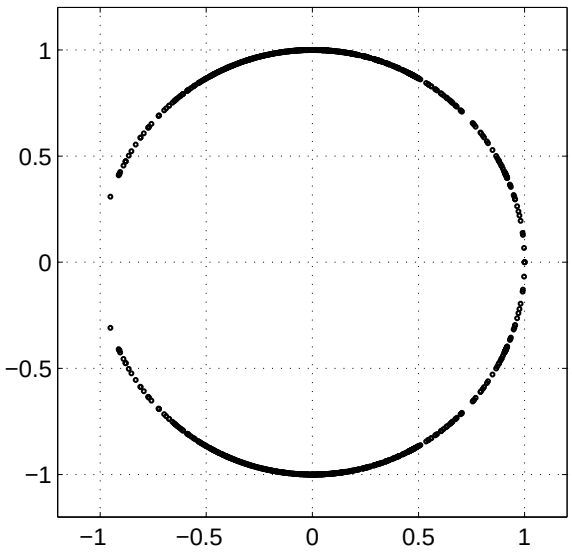

Figure 4.7: Distribution of eigenvalues of the iteration matrix in Scheme V for the mesh shown in Fig. 4.3

Table 4.2: Eigenvalue statistics of the iteration matrix in different schemes.

	Scheme I	Scheme II	Scheme IV	Scheme V
$\rho(\mathbf{G})$	1.04423	1.030587	1.000703	1
% of $\lvert\lambda_G\rvert > 1$	12.54	8.07	1	0

Thus Schemes I, II and IV are numerically unstable. Scheme V on the other hand satisfies the von Neumann stability condition.

To further verify the conclusions on stability based on the above analysis, the time domain field solution for each of the hybrid schemes is computed. The problem is modeled as a square cavity excited by a differentiated Gaussian pulse shaped electric current, positioned at the same location for all the schemes. The $H_z(t)$ component at a particular location inside the 2-D cavity, for the different schemes including Scheme III, is shown in Fig. 4.8. It is clearly observed that instabilities arise within 1000 time steps for Schemes I, II and III, and for Scheme IV, it starts to appear around 60,000 time steps. Scheme V does not exhibit any numerical instability, being consistent with the eigenvalue analysis.

4.4 Stability of Scheme V

In Scheme V, instead of analytically evaluating the exact elemental $\mathbf{S}_e$ and $\mathbf{T}_e$ matrices of the rectangular elements, numerical integration is used. Specifically, the trapezoidal integration is used. When numerical integration is employed, additional errors are introduced in the finite element matrices. However, any numerical integration rule with a particular order of accuracy is acceptable as long as the order of convergence achieved if exact integration were to be used, is preserved [81]. In the case of second order hyperbolic equations such as the vector Helmholtz equation, $O(h^{2p})$ convergence is achieved with basis functions of order p with the integrals in the Galerkin framework

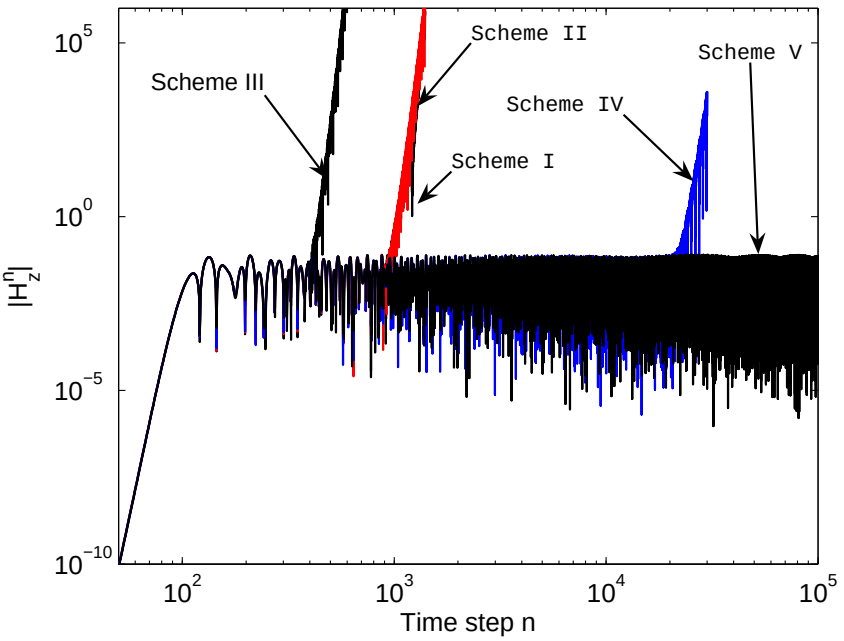

Figure 4.8: Solution of H_z^n component inside a 2-D square cavity obtained using different hybridization schemes.

evaluated exactly to the order of $2(p-1)$ [82]. In the case of linear basis functions, with $p = 1$ to maintain the order of convergence of $O(h^2)$, it is sufficient for the numerical integration to have an order $O(h)$ accuracy. The two point trapezoidal rule has accuracy of order $O(h^3)$ and hence can be employed for evaluating the mass and stiffness matrices without any loss in the order of convergence achieved with exact integration when edge element basis functions are used. With the trapezoidal rule, the elements of $\mathbf{T}_e$ and $\mathbf{S}_e$ are evaluated as

$$T_{ij}^e = \frac{\Delta h^2}{4} \sum_{k=0}^{3} \vec{N}_i|_{n_k} \cdot \varepsilon_r \vec{N}_j|_{n_k} \tag{4.13}$$

$$S_{ij}^e = \frac{\Delta h^2}{4} \sum_{k=0}^{3} \nabla \times \vec{N}_i|_{n_k} \cdot \frac{1}{\mu_r} \nabla \times \vec{N}_j|_{n_k} \tag{4.14}$$

where the basis functions and their curls are evaluated only at the 4 nodes of the rectangular element. The elemental matrices of a reference rectangular element with edge

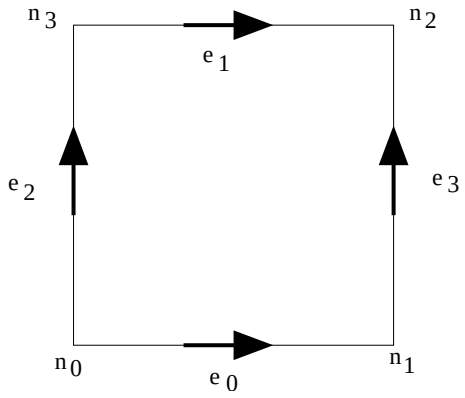

Figure 4.9: Reference node and edge numbering on a rectangular element.

and node numbering as in Fig. 4.9 are given in [83] as

$$\mathbf{T}^e = \frac{\Delta h^2}{2}\mathbf{I} \tag{4.15a}$$

$$\mathbf{S}^e = \begin{bmatrix} 1 & -1 & -1 & 1 \\ -1 & 1 & 1 & -1 \\ -1 & 1 & 1 & -1 \\ 1 & -1 & -1 & 1 \end{bmatrix} \tag{4.15b}$$

where $\mathbf{I}$ is an identity matrix of dimension four. In the case of the mass matrix, the use of trapezoidal integration rule is equivalent to "mass-lumping" where the resulting matrix is diagonal, while the $\mathbf{S}^e$ is the same as the one with exact integration [84]. The stiffness matrix is unaffected since the curl of the basis function is constant in the 2-D case and hence trapezoidal rule and exact integration lead to the same stiffness matrix. However, this is not true with hexahedral element in 3-D as will be seen in Sec. 4.6.

The four eigenvalues of the single rectangular element i.e., the eigenvalues of the generalized system $\mathbf{S}^e\mathbf{e} = \lambda_e\mathbf{T}^e\mathbf{e}$, are obtained using a symbolic computation tool as $\left[0, 0, 0, \frac{8}{\Delta h^2}\right]$. The zero eigenvalues correspond to the gradient field or the null space of $\mathbf{S}^e$ and there are three modes consistent with the number of free nodes. The maximum eigenvalue is $\lambda_e^{\max} = \frac{8}{\Delta h^2}$, by which the following identity

$$\mathbf{e}^t\mathbf{S}^e\mathbf{e} \leq \frac{8}{\Delta h^2}\mathbf{e}^t\mathbf{T}^e\mathbf{e} \tag{4.16}$$

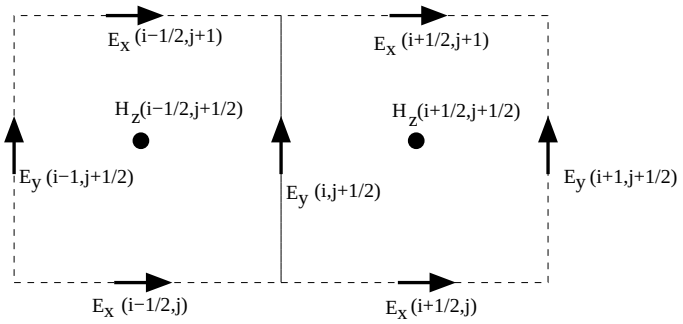

Figure 4.10: 2-D FDTD stencil with electric field as unknown

hold good for any vector $\mathbf{e}$.

4.4.1 Equivalence between FETD and FDTD Methods

To illustrate the equivalence of the FDTD and FETD methods in the special case of Scheme V, consider two adjacent Yee cells as shown in Fig. 4.10. With the magnetic field unknown eliminated, Fig. 4.10is essentially the finite difference stencil for the update of $E^{n+1}_{y(i,j+1/2)}$. From (2.64), the regular FDTD update for $E^{n}_{y(i,j+1/2)}$ in the absence of electric current is

$$E^{n}_{y(i,j+1/2)} = E^{n-1}_{y(i,j+1/2)} + \frac{\Delta t}{\varepsilon_0 \Delta h}\left[H^{n-1/2}_{z(i+1/2,j+1/2)} - H^{n-1/2}_{z(i-1/2,j+1/2)}\right]. \tag{4.17}$$

Subtracting (4.17) from the update for $E^{n+1}_{y(i,j+1/2)}$ leads to

$$E^{n+1}_{y(i,j+1/2)} - 2E^{n}_{y(i,j+1/2)} + E^{n-1}_{y(i,j+1/2)} = \frac{\Delta t}{\varepsilon_0 \Delta h}\left[(H^{n+1/2}_{(i+1/2,j+1/2)} - H^{n-1/2}_{(i+1/2,j+1/2)}) - (H^{n+1/2}_{(i-1/2,j+1/2)} - H^{n-1/2}_{(i-1/2,j+1/2)})\right]. \tag{4.18}$$

Using the magnetic field update equation of (2.62) in (4.18), the update of $E^{n+1}_{y(i,j+1/2)}$ is given as

$$\begin{aligned} E^{n+1}_{y(i,j+1/2)} &= 2E^{n}_{y(i,j+1/2)} \\ &\quad - \frac{c^2\Delta t^2}{\Delta h^2}\begin{pmatrix} 1 & -1 & -1 & 2 & -1 & 1 & -1 \end{pmatrix}\begin{pmatrix} E^n_{x(i-1/2,j)} \\ E^n_{x(i-1/2,j+1)} \\ E^n_{y(i-1,j+1/2)} \\ E^n_{y(i,j+1/2)} \\ E^n_{x(i+1/2,j)} \\ E^n_{x(i+1/2,j+1)} \\ E^n_{y(i+1,j+1/2)} \end{pmatrix} \\ &\quad - E^{n-1}_{y(i,j+1/2)} \end{aligned} \tag{4.19}$$

which is in a form similar to (4.4).

The implicit FETD update equation in (2.50) with $\beta = 0$ is given as

$$\mathbf{T}\mathbf{e}^{n+1} = \left[2\mathbf{T} - c^2\Delta t^2\mathbf{S}\right]\mathbf{e}^{n} - \mathbf{T}\mathbf{e}^{n-1}. \tag{4.20}$$

Note that with mass lumping, $\mathbf{T}$ is diagonal, so (4.20) leads to an explicit update equation. Treating the stencil in Fig. 4.10 as two rectangular finite elements and using the elemental matrices in (4.15), the FETD update equation in (4.20) leads to the following update equation for $E^{n+1}_{y(i,j+1/2)}$

$$\begin{aligned} \Delta h^2 E^{n+1}_{y(i,j+1/2)} &= 2\Delta h^2 E^{n}_{y(i,j+1/2)} \\ &\quad - c^2\Delta t^2\begin{pmatrix} 1 & -1 & -1 & 2 & -1 & 1 & -1 \end{pmatrix}\begin{pmatrix} E^n_{x(i-1/2,j)} \\ E^n_{x(i-1/2,j+1)} \\ E^n_{y(i-1,j+1/2)} \\ E^n_{y(i,j+1/2)} \\ E^n_{x(i+1/2,j)} \\ E^n_{x(i+1/2,j+1)} \\ E^n_{y(i+1,j+1/2)} \end{pmatrix} \\ &\quad - \Delta h^2 E^{n-1}_{y(i,j+1/2)}. \end{aligned} \tag{4.21}$$

Equation (4.19), scaled by Δh^2 is the same as the FETD update in (4.21). Thus it is seen that FETD on rectangular elements with trapezoidal rule for evaluating element matrices and using central differencing for temporal discretization $(\beta = 0)$ leads to an

update scheme that is equivalent to the FDTD scheme with magnetic field eliminated.

4.4.2 Condition for Stability

With the equivalence of the FDTD method and FETD method established, it is easy to see the following equivalence between the sub-matrices in (4.24) viz.,

$$\Delta h^2 \mathbf{A}_{23} = c^2 \Delta t^2 \mathbf{S}_{23}^T. \tag{4.22}$$

After the scaling of the FDTD update equation with Δh^2, we can express the coefficient matrices of the hybrid update equation as

$$\begin{aligned}
\mathbf{Q}_1 &= \begin{pmatrix} \Delta h^2\mathbf{I} & \mathbf{0} & \mathbf{0} & \mathbf{0} \\ \mathbf{0} & \Delta h^2\mathbf{I} & \mathbf{0} & \mathbf{0} \\ \mathbf{0} & \mathbf{0} & \mathbf{M}_{33} & \mathbf{M}_{34} \\ \mathbf{0} & \mathbf{0} & \mathbf{M}_{34}^t & \mathbf{M}_{44} \end{pmatrix} \\
&= \begin{pmatrix} \mathbf{T}_{11} & \mathbf{0} & \mathbf{0} & \mathbf{0} \\ \mathbf{0} & \mathbf{T}_{22} & \mathbf{0} & \mathbf{0} \\ \mathbf{0} & \mathbf{0} & \mathbf{T}_{33} & \mathbf{T}_{34} + \frac{c^2\Delta t^2}{4}\mathbf{S}_{34} \\ \mathbf{0} & \mathbf{0} & \mathbf{T}_{34}^t + \frac{c^2\Delta t^2}{4}\mathbf{S}_{34}^t & \mathbf{T}_{44} + \frac{c^2\Delta t^2}{4}\mathbf{S}_{44} \end{pmatrix}
\end{aligned} \tag{4.23}$$

$$\begin{aligned}
\mathbf{Q}_0 &= \begin{pmatrix} \Delta h^2(2\mathbf{I} - \mathbf{A}_{11}) & -\Delta h^2\mathbf{A}_{12} & \mathbf{0} & \mathbf{0} \\ -\Delta h^2\mathbf{A}_{12}^t & \Delta h^2(2\mathbf{I} - \mathbf{A}_{22}) & -\Delta h^2\mathbf{A}_{23} & \mathbf{0} \\ \mathbf{0} & \mathbf{N}_{23}^t & \mathbf{N}_{33} & \mathbf{N}_{34} \\ \mathbf{0} & \mathbf{0} & \mathbf{N}_{34}^t & \mathbf{N}_{44} \end{pmatrix} \\
&= \begin{pmatrix} 2\mathbf{T}_{11} - c^2\Delta t^2\mathbf{S}_{11} & -c^2\Delta t^2\mathbf{S}_{12} & \mathbf{0} & \mathbf{0} \\ -c^2\Delta t^2\mathbf{S}_{12}^t & 2\mathbf{T}_{22} - c^2\Delta t^2\mathbf{S}_{22} & -c^2\Delta t^2\mathbf{S}_{23} & \mathbf{0} \\ \mathbf{0} & -c^2\Delta t^2\mathbf{S}_{23}^t & 2\mathbf{T}_{33} - c^2\Delta t^2\mathbf{S}_{33} & -\frac{c^2\Delta t^2}{2}\mathbf{S}_{34} \\ \mathbf{0} & \mathbf{0} & -\frac{c^2\Delta t^2}{2}\mathbf{S}_{34}^t & 2\mathbf{T}_{44} - \frac{c^2\Delta t^2}{2}\mathbf{S}_{44} \end{pmatrix}
\end{aligned} \tag{4.24}$$

Both $\mathbf{Q}_0$ and $\mathbf{Q}_1$ are symmetric matrices with real eigenvalues. Hence, λ_Q, the eigenvalue of $\mathbf{Q}_1^{-1}\mathbf{Q}_o$ is real. Using the fact that λ_Q is real in (4.11), the condition $|\lambda_G| \leq 1$ is equivalent to $|\lambda_Q| \leq 2$.

In what is to follow, the condition on Δt such that $|\lambda_Q| \leq 2$ is satisfied is derived. Consider the generalized eigenvalue problem of the form

$$\mathbf{S}\mathbf{e} = \zeta \mathbf{T}\mathbf{e} \tag{4.25}$$

where $\mathbf{T}$ and $\mathbf{S}$ are the mass and stiffness matrices assembled over triangular and rectangular elements. With $\mathbf{S}$ being positive semi-definite and $\mathbf{T}$ being positive definite, $\zeta \geq 0$. From the generalized eigenvalue equation $\mathbf{Q}_0\mathbf{e} = \lambda_Q \mathbf{Q}_1\mathbf{e}$, written in the form

$$\left[2\mathbf{T} - c^2\Delta t^2(1-2\beta)\mathbf{S}\right]\mathbf{e} = \lambda_Q \left[\mathbf{T} + c^2\Delta t^2 \beta \mathbf{S}\right]\mathbf{e} \tag{4.26}$$

one can establish the relation between ζ and λ_Q as

$$\lambda_Q = \frac{2 + 2\zeta\beta c^2\Delta t^2 - \zeta c^2 \Delta t^2}{1 + \zeta\beta c^2 \Delta t^2} \tag{4.27}$$

For the implicit case with $\beta = 1/4$ in (4.27), it can be shown that λ_Q decreases monotonically with ζ i.e., $\frac{\partial \lambda_Q}{\partial \zeta} \leq 0, \forall \zeta \geq 0$ which leads to the bounds of λ_Q as $|\lambda_Q| \leq 2, \forall \zeta \geq 0$. Thus, implicit FETD with $\beta = \frac{1}{4}$ satisfies the von Neumann condition for stability and leads to unconditionally stability. The result is in agreement with the conditions for stability of the Newmark-beta scheme derived in [10].

For the explicit case with $\beta = 0$ in (4.27) , we have

$$\lambda_Q = 2 - \zeta c^2 \Delta t^2. \tag{4.28}$$

From (4.28), $\lambda_Q^{\max} = 2$ since $\zeta \geq 0$. Thus $\lambda_Q^{\max} = 2$ for any choice of Δt, for both implicit and explicit FETD. However, for the explicit case, the condition that $\lambda_Q^{\min} = -2$ in (4.28) leads to the condition that

$$\zeta \leq \frac{4}{c^2\Delta t^2}. \tag{4.29}$$

Based on the fact that the assembly of matrices $\mathbf{T}$ and $\mathbf{S}$ is over K finite elements which are either explicit (rectangular) or implicit (triangular) elements, the following inequality hold true viz.,

$$\sum_{k=1}^{K} \mathbf{e}^t \mathbf{S}_k \mathbf{e} \leq \zeta^{\max} \sum_{k=1}^{K} \mathbf{e}^t \mathbf{T}_k \mathbf{e} \tag{4.30}$$

where $\zeta^{\max}$ is the maximum eigenvalue of the generalized system (4.25). $\mathbf{T}_k$ and $\mathbf{S}_k$ are the elemental mass and stiffness matrices of the kth element. Considering the above inequality for the case of expicit rectangular elements alone along with the condition in (4.29) for $\lambda_Q^{\min} \geq -2$ leads to condition

$$\sum_{k=1}^{K} \mathbf{e}^t \mathbf{S}_k \mathbf{e} \leq \frac{4}{c^2 \Delta t^2} \sum_{k=1}^{K} \mathbf{e}^t \mathbf{T}_k \mathbf{e}. \tag{4.31}$$

Based on the identity in (4.16) for each explicit rectangular element, equation (4.31) is satisfied under the condition that

$$\lambda_e^{\max} = \frac{8}{\Delta h^2} \leq \frac{4}{c^2 \Delta t^2} \tag{4.32}$$

which leads to the condition on Δt as

$$\Delta t \leq \frac{\Delta h}{c\sqrt{2}}. \tag{4.33}$$

With the choice of Δt as in (4.33), the resulting eigenvalues of $\mathbf{Q}_1^{-1}\mathbf{Q}_0$ is bounded as $|\lambda_Q| \leq 2$ resulting in $|\lambda_G| \leq 1$. Thus (4.33) is the necessary condition for numerical stability and the condition is the same as the Courant criteria for stability of the FDTD method in 2-D. The same condition for stability as FDTD case is expected due to the equivalence between the FDTD method and the special case of FETD method on rectangular elements. The hybridization of FETD and FDTD methods using Scheme V, leading to well defined condition for stability, is referred to as the stable FETD-FDTD method.

In the numerical experiments in the previous section, Δt was set such that (4.33) is satisfied. The above derivation of condition of stability explains the reason why the eigenvalues of the amplification matrix were right on the unit circle in the complex plane for Scheme V as shown in Fig. 4.7. Similar procedure to arrive at the condition of stability based on the assembly of the system matrices over finite elements using the modal decomposition technique is shown in [18]. Note that the implementation of the hybrid FETD-FDTD method remains the same as discussed in Sec. 2.4.1.

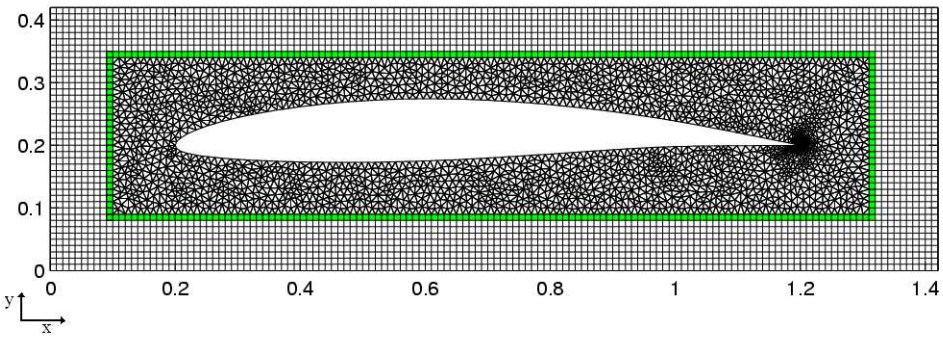

Figure 4.11: Hybrid mesh used in computation of scattering by NACA64A410 Airfoil

The amplification matrix of the stable FETD-FDTD method is not normal and is not unitarily diagonalizable. When the amplification matrix is non-diagonalizable, in spite of having all eigenvalues with unit magnitude, the solution can permit polynomial growth with respect to time [85]. In [75], the spectral properties of the amplification matrix of the FETD method is investigated and the discrete origin of the linear time growth, discussed in the previous Chapter is demonstrated. The same procedure can be extended to the hybrid FETD-FDTD method and we can conclude that the condition for stability in (4.33) can permit a linear time growth (due to accumulation of numerical round off errors) and the technique of constraint equations developed in Chapter 3, to mitigate the problem in FETD method can be extended to the hybrid method as well.

4.5 Example and Results

To highlight the application of the stable FETD-FDTD method, the computation of 2-D TE$_z$ scattering from an NACA64a410 Airfoil is considered. The length of the airfoil is 1m which corresponds to 5λ at 1.5 GHz. The hybrid mesh used in this computation is shown in Fig. 4.11 where the fine triangular discretization along the trailing edge of the airfoil can be observed. For triangulation in Ω_{FE}, the Triangle code [58] has been used. The incident plane wave is an $\hat{x}$- directed differentiated Gaussian pulse with

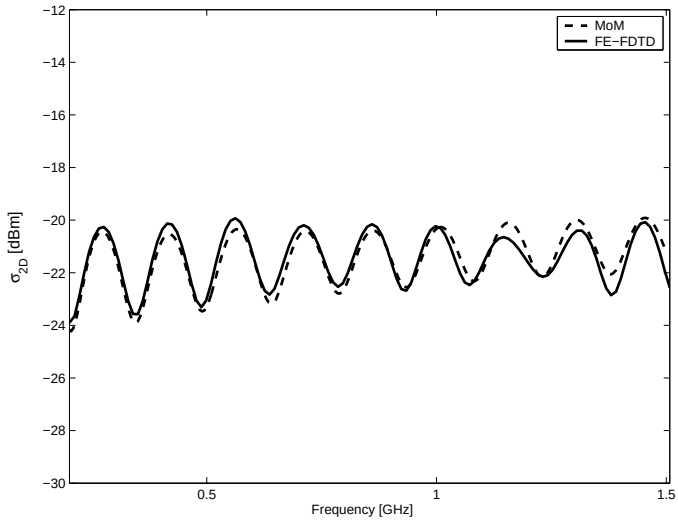

Figure 4.12: Comparison of backscattered RCS over the frequency range 0.2 GHz - 1.5 GHz

significant spectral content in the band of 0.2 GHz - 1.5 GHz. The FDTD grid size is set as $\Delta x = \Delta y = 0.01$ m. A Total-Field/Scattered-Field boundary is implemented in Ω_{FD} and time domain NFFF transformation [2] is performed to obtain far zone scattered electric field components. A direct solver using a complete Cholesky factorization of the implicit matrix is employed for the update of unknowns in Ω_{FE}.

The 2-D backscattered RCS over the frequency range of 0.2 GHz-1.5 GHz is shown in Fig. 4.12. The results are compared with the frequency domain based method of moments solution [60]. A good agreement is observed across the entire band. In Fig. 4.13 the bistatic RCS pattern at 1.5 GHz, obtained using the stable hybrid FETD-FDTD algorithm, is compared with the results obtained using method of moments. Deviations in the solution could be attributed to the relatively coarse cell size of $\lambda/20$ at 1.5 GHz used in Ω_{FD} as compared to the $\lambda/80$ mesh size used in the MoM computation and the inherent dispersion errors in the finite methods.

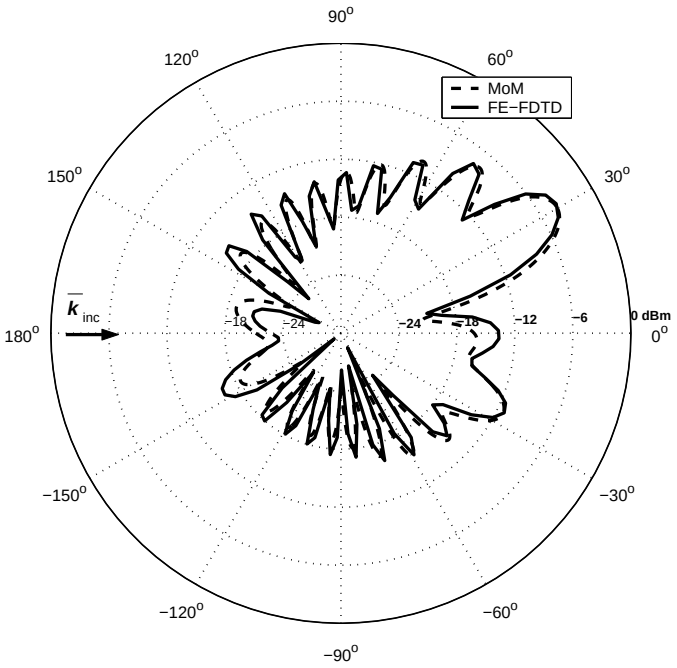

Figure 4.13: Comparison of bistatic RCS of the airfoil at 1.5 GHz

4.6 Extension to 3-D

It is seen in the 2-D case that for a stable hybrid algorithm, the finite element region must have both triangular and rectangular elements. Extending to the 3-D case, both tetrahedral and hexahedral elements are needed in the finite element region. While generating a hybrid mesh with both hexahedral elements and tetrahedral elements, two possible interfaces between the structured and unstructured regions can be considered as in Figs. 4.14(a) and (b). While the case in Fig. 4.14(b) requires the need for the introduction of additional pyramidal elements and the need for the construction of vector basis functions on pyramids, the case of Fig. 4.14(a) alleviates the need for using pyramidal elements. The case of Fig. 4.14(a) has non-conforming unknowns (shown in dashed-line) on the interface along the diagonal of the rectangular faces. In [14], a second order accurate interpolation was used to update these diagonal unknowns using the FDTD solution on the four edges of the rectangular face. The method is similar

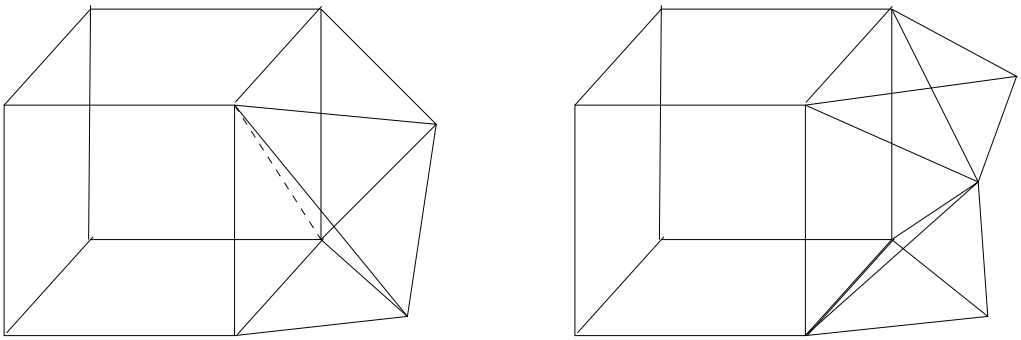

(a) Non-matching interface

(b) Matching interface with pyramidal element

Figure 4.14: Interface between structured finite difference and unstructured finite element regions in 3-D

to Schemes I and II in the aspect that the FDTD solution is used as the time varying Dirichlet boundary condition for the FETD solution. As seen in the earlier analysis, the resulting algorithm is numerically unstable. Numerical instability can be suppressed using filtering techniques [62] but often limits the application of the method [80]. On the other hand, the case in Fig. 4.14(b) with the availability of vector basis functions on pyramids, is similar to the 2-D FETD-FDTD case. A stable hybrid method can be achieved, provided that similar to the 2-D case, FETD scheme on hexahedral elements equivalent to FDTD scheme in 3-D exists. Following the same procedure as in the 2-D case viz., by using trapezoidal rule for evaluation of mass and stiffness matrices of a hexahedral element and using central differencing for temporal discretization, the resulting FETD update equations are the same as the 3-D FDTD update equations. Based on this fact, the FETD method and FDTD method can be hybridised [86], similar to the 2-D case with the mesh transition from the unstructured to structured region as in Fig. 4.14(b). Consider an arbitrary hexahedral element with dimensions l_x, l_y and l_z along the respective coordinate directions. Using the trapezoidal rule for integration,

the elemental matrices are evaluated as

$$T_{ij}^e = \frac{l_x l_y l_z}{8} \sum_{k=0}^{8} \vec{N}_i|_{n_k} \cdot \varepsilon_r \vec{N}_j|_{n_k} \tag{4.34}$$

$$S_{ij}^e = \frac{l_x l_y l_z}{8} \sum_{k=0}^{8} \nabla \times \vec{N}_i|_{n_k} \cdot \frac{1}{\mu_r} \nabla \times \vec{N}_j|_{n_k}. \tag{4.35}$$

The basis function and its curl are evaluated only at the nodes of the hexahedral element. With the edge and node numbering of the reference element as in [31], the elemental matrices are given as

$$\mathbf{T}^e = \frac{l_x l_y l_z}{4} \begin{bmatrix} \mathbf{I} & & \\ & \mathbf{I} & \\ & & \mathbf{I} \end{bmatrix} \tag{4.36a}$$

$$\mathbf{S}^e = \begin{bmatrix} \mathbf{S}_{xx} & \mathbf{S}_{xy} & \mathbf{S}_{xz} \\ \mathbf{S}_{yx} & \mathbf{S}_{yy} & \mathbf{S}_{yz} \\ \mathbf{S}_{zx} & \mathbf{S}_{zy} & \mathbf{S}_{zz} \end{bmatrix} \tag{4.36b}$$

where

$$\mathbf{S}_{\xi\xi} = \frac{l_\xi}{2} \left[\frac{l_\eta}{l_\zeta} \mathbf{K}_1 + \frac{l_\zeta}{l_\eta} \mathbf{K}_2 \right]$$

$$\mathbf{S}_{\xi\eta} = \mathbf{S}_{\xi\eta}^T = -\frac{l_\zeta}{2} \mathbf{K}_3$$

with

$$\mathbf{K}_1 = \begin{bmatrix} 1 & 0 & -1 & 0 \\ 0 & 1 & 0 & -1 \\ -1 & 0 & 1 & 0 \\ 0 & -1 & 0 & 1 \end{bmatrix}$$

$$\mathbf{K}_2 = \begin{bmatrix} 1 & -1 & 0 & 0 \\ -1 & 1 & 0 & 0 \\ 0 & 0 & 1 & -1 \\ 0 & 0 & -1 & 1 \end{bmatrix}$$

$$\mathbf{K}_3 = \begin{bmatrix} 1 & 0 & -1 & 0 \\ -1 & 0 & 1 & 0 \\ 0 & 1 & 0 & 1 \\ 0 & -1 & 0 & -1 \end{bmatrix};$$

and ξ, η and ζ being cyclic permutation of the coordinates x, y and z respectively. It is seen that unlike the 2-D case, $\mathbf{S}^e$ with trapezoidal integration is different from the matrix obtained using exact integration given in [31]. Note that unlike the 2-D case, the curl of the basis function varies within the volume of the hexahedral element. As an

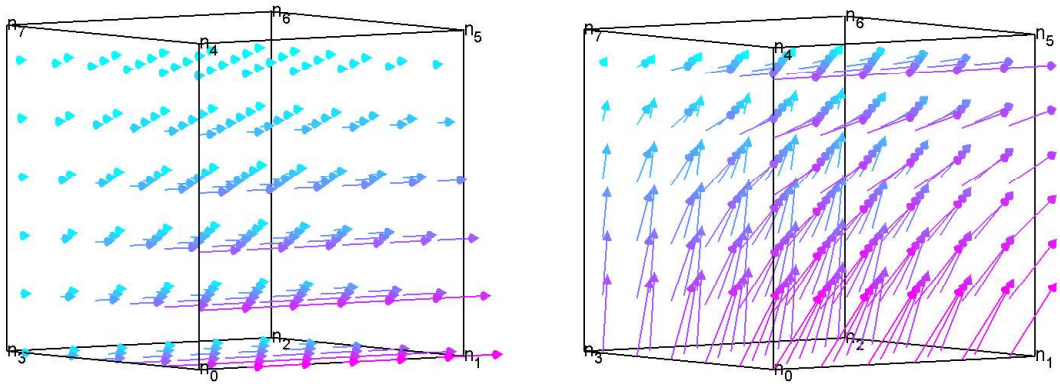

(a) $\vec{W}_{01}$ (b) $\nabla \times \vec{W}_{01}$

Figure 4.15: An edge element basis function and its curl on a hexahedral element.

illustrative example, an edge element $\vec{W}_{01}$ and its curl $\nabla \times \vec{W}_{01}$ are shown in Fig. 4.15 where it can be seen that $\vec{W}_{01}$ has component along edge $\{0,1\}$. In Fig. 4.16, the finite difference stencil to update an electric field unknown is shown. Fig. 4.16(a) shows the FDTD stencil with the dual grid having the magnetic field. The electric field unknown of interest is updated using the surrounding magnetic fields (Ampere's law) while those magnetic field unknowns are updated using the surrounding electric field (Faraday's law) resulting in a final stencil as shown in Fig. 4.16(a). In the FETD method, all the four hexahedral elements having the electric field unknown of interest as the common edge are considered as in Fig. 4.16(b). Using the elemental matrices obtained using the trapezoidal integration, for all the four hexahedral elements, the resulting stencil is the same as the one for the FDTD method. The update coefficients of both FDTD and FETD can be shown to be the same, following the same procedure as in the 2-D case.

The eigenvalues of the generalized system $\mathbf{S}^e\mathbf{x} - \lambda\mathbf{T}^e\mathbf{x} = 0$ for the case of a hexahedral element with elemental matrices obtained using trapezoidal integration are computed using Mathematica and the unique eigenvalues are obtained as

$$\left[0, 4\left(\frac{1}{l_x^2}+\frac{1}{l_y^2}\right), 4\left(\frac{1}{l_y^2}+\frac{1}{l_z^2}\right), 4\left(\frac{1}{l_z^2}+\frac{1}{l_x^2}\right), 4\left(\frac{1}{l_x^2}+\frac{1}{l_y^2},+\frac{1}{l_z^2}\right)\right].$$

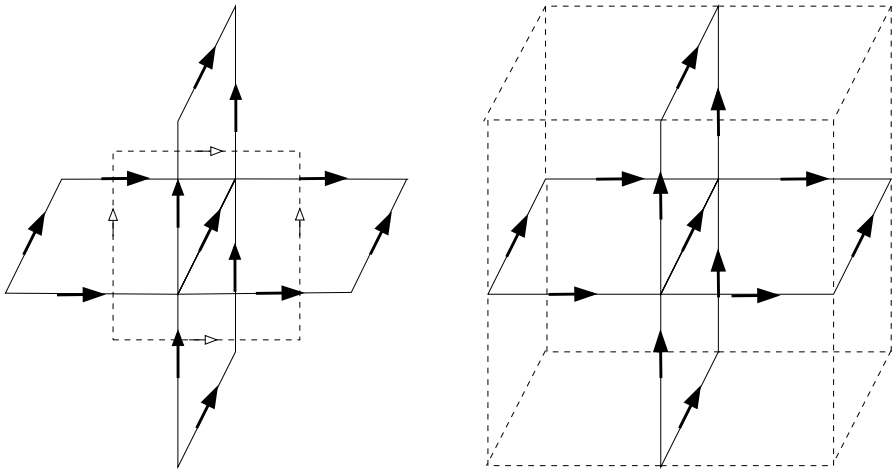

(a) FDTD (b) FETD

Figure 4.16: Stencil to update electric field unknown using FDTD and FETD methods.

There are seven zero eigenvalues, consistent with the number of free nodes. The maximum eigenvalue is $\lambda_e^{\max} = 4\left(\frac{1}{l_x^2} + \frac{1}{l_y^2}, + \frac{1}{l_z^2}\right)$ with multiplicity 2. When $l_x = l_y = l_z = \Delta h$, $\lambda_e^{\max} = \frac{12}{\Delta h^2}$. Following the same stability analysis procedure for the 2-D case discussed in Sec. 4.4, the stability condition similar to (4.32) is obtained in the 3-D case as follows

$$\lambda_e^{\max} = \frac{12}{\Delta h^2} \leq \frac{4}{c^2 \Delta t^2} \tag{4.37}$$

which leads to the condition on Δt as

$$\Delta t \leq \frac{\Delta h}{c\sqrt{3}}. \tag{4.38}$$

This result can be obtained following the same procedure of the 2-D analysis, since the 3-D FETD-FETD method with transition of mesh from the unstructured to the structured region as in Fig. 4.14(b) results in the hybrid update equation in the same form as that of the 2-D case. Condition in (4.38) is again the same as Courant criteria for numerical stability of FDTD method in 3-D a consequence of the equivalence between

the special case of FETD method and the FDTD method. Thus the hybrid 3-D FETD-FDTD method has the same conditions of numerical stability as the 3-D FDTD method.

4.7 Concluding Remarks

A framework based on the eigenvalue analysis to study the numerical stability of hybrid FETD-FDTD algorithm is developed. Construction of global iterative matrix for the hybrid algorithm is presented. Numerical experiments based on the eigenvalue analysis of the iteration matrix for different hybridization schemes on sample hybrid meshes revealed that Scheme V satisfies the von Neumann stability condition. The stability of Scheme V is due to the equivalence between FETD and FDTD methods. The derivation of the stability condition for the hybrid FETD-FDTD method shows the method to have the same conditions of stability as the FDTD method both in 2-D and 3-D.

CHAPTER 5

HANGING VARIABLES AND FETD BASED FDTD SUBGRIDDING METHOD

5.1 Introduction

The finite element method provides a rigorous framework for *a priori* error estimation and hence a robust error control using adaptive mesh refinement. h-adaptive mesh refinement involves reducing the size of the elements with relatively high estimated error. The process of refinement by merely splitting an element into smaller elements could lead to a mesh with bad quality resulting in the manifestation of problems due to low frequency instability such as poor rate of convergence of iterative solvers. On the contrary, when nesting of elements is used for mesh refinement, good mesh quality is guaranteed. However, in this case, hanging variables are introduced and they require special treatment. Recently, the concept of hanging variables in the context of vector basis functions was introduced in frequency domain FEM to handle nested triangular and tetrahedral elements [87], leading to an efficient mesh refinement in h-adaptive finite element solvers [88]. In this Chapter, the formulation of hanging variables to the FETD method with linear rectangular and hexahedral edge elements is presented. Inspired by [87], the edge element basis functions associated with the hanging variables are constrained to ensure proper field continuity resulting in the construction of so-called intergrid boundary operator. The mass and stiffness matrices are then obtained by a *Galerkin*-type operation using the intergrid boundary operator. As a result, the final mass and stiffness matrices have spectral properties similar to traditional finite element

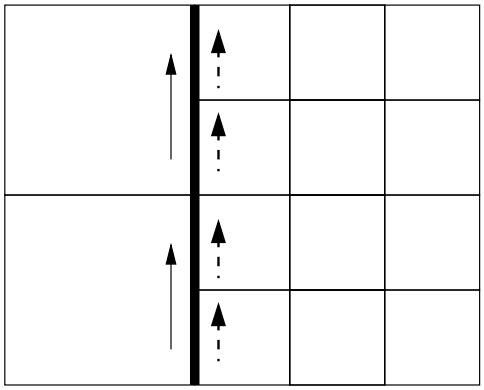

Figure 5.1: Rectangular elements with hanging edges (dashed) across the interface between coarse and fine elements

matrices. Based on these spectral properties, the conditions for numerical stability of both implicit and explicit FETD methods with hanging variables can be established. Moreover, with a successful procedure for the treatment of hanging variables in FETD method, it is possible to develop an FDTD subgridding method with the interface region between the coarse and fine grids, handled by the FETD method with hanging variables. The resulting FDTD subgridding algorithm is guaranteed to be numerically stable with well defined condition for numerical stability. The development and application of such a subgridding method is presented in this Chapter. The contents of this Chapter with the examples shown were published in [83].

5.2 Hanging Variables in FETD

Consider the 2-D case of rectangular elements as shown in Fig. 5.1 showing single level of nesting of the coarse element. Hanging variables, associated with edges shown in dashed arrow are present at the interface between the coarse element and the fine elements. The treatment of hanging variables applied in this section is very general. It allows transitions from a coarse element to a fine element with more than one level of nesting. However, for the purposes of describing the method and demonstrating the

approach, the case with single level of nesting where the edge length of the coarse element is twice the edge length of the fine element is considered.

Let $\mathbf{c}^h$ be the coefficients associated with the fine elements and $\mathbf{c}^{2h}$ be that associated with the coarse elements, i.e.,

$$\mathbf{c}^h = \begin{bmatrix} \mathbf{c}_i^h \\ \mathbf{c}_b^h \end{bmatrix} \text{ and } \quad \mathbf{c}^{2h} = \begin{bmatrix} \mathbf{c}_i^{2h} \\ \mathbf{c}_b^{2h} \end{bmatrix} \tag{5.1}$$

where subscript i corresponds to the interior unknowns and subscript b corresponds to the boundary unknowns on the coarse-fine grid interface. Thus, with reference to Fig. 5.1, $\mathbf{c}_b^h$ corresponds to the dashed arrows and $\mathbf{c}_b^{2h}$ to the solid arrows. $\mathbf{c}_b^h$ represent the hanging variables. The continuity conditions across the boundary are imposed by restricting the fine boundary unknowns (hanging variables) in terms of the coarse boundary unknowns, as follows

$$\mathbf{c}_b^h = \mathbf{I}_b \mathbf{c}_b^{2h} \tag{5.2}$$

where $\mathbf{I}_b$ is the intergrid boundary operator. To have a valid intergrid boundary operator, certain conditions need to be satisfied by the basis functions on the coarse and the fine elements [87]. The fine elements with hanging variables must be equipped with proper basis functions such that condition of tangential continuity of the field can be satisfied across the interface. Violation of this condition would lead to appearance of spurious modes, similar to the one encountered when nodal finite element basis functions are used to represent the electric field. In the current case, with the coarse and fine elements being topologically similar, retaining the original edge element basis functions for a rectangular element should suffice to ensure continuity of the fields across the interface.

To construct $\mathbf{I}_b$ for 2-D rectangular elements, with reference to Fig. 5.2(a), the coarse element basis function associated with edge $\{0,1\}$ is given in terms of the fine element basis functions, as follows.

$$\vec{W}_{0,1}^{2h} = \vec{W}_{0,4}^{h} + \vec{W}_{4,1}^{h} + \frac{1}{2}\left(\vec{W}_{7,8}^{h} + \vec{W}_{8,5}^{h}\right). \tag{5.3}$$

Let $c^h_{wi,j}$ be the coefficient associated with basis function $\vec{W}^h_{i,j}$. By (5.3), continuity is ensured along the edge $\{0,1\}$, if the coefficient of the coarse element basis is the same as that of the two finite element basis functions associated with edge $\{0,4\}$, and edge $\{4,1\}$, i.e., when

$$c^h_{w0,4} = c^{2h}_{w0,1} \tag{5.4a}$$

$$c^h_{w4,1} = c^{2h}_{w0,1}. \tag{5.4b}$$

From this relationship, $\mathbf{I}_b$ can be constructed.

For the case of 3-D hexahedral element, with reference to Fig. 5.2(b), let face $\{0,1,5,4\}$ be on the interface of coarse and fine elements. Thus, edges $\{0,8\}$, $\{8,1\}$, $\{13,14\}$, $\{14,15\}$, $\{4,22\}$ and $\{22,5\}$ form a set of 6 x-directed hanging variables and edges $\{0,13\}$,$\{13,4\}$, $\{8,14\}$, $\{14,22\}$, $\{1,15\}$ and $\{15,5\}$ form a set of z-directed hanging variables. The coarse element basis function associated with x-directed edges viz., edges $\{0,1\}$ and $\{4,5\}$ are given in terms of the fine element basis functions, as follows

$$\begin{aligned}\vec{W}^{2h}_{0,1} =& \vec{W}^h_{0,8} + \vec{W}^h_{8,1} \\ &+ \frac{1}{2}\left(\vec{W}^h_{11,12} + \vec{W}^h_{12,9} + \vec{W}^h_{13,14} + \vec{W}^h_{14,15}\right) \\ &+ \frac{1}{4}\left(\vec{W}^h_{20,21} + \vec{W}^h_{21,16}\right)\end{aligned} \tag{5.5a}$$

$$\begin{aligned}\vec{W}^{2h}_{4,5} =& \vec{W}^h_{4,22} + \vec{W}^h_{22,5} \\ &+ \frac{1}{2}\left(\vec{W}^h_{25,26} + \vec{W}^h_{26,23} + \vec{W}^h_{13,14} + \vec{W}^h_{14,15}\right) \\ &+ \frac{1}{4}\left(\vec{W}^h_{20,21} + \vec{W}^h_{21,16}\right).\end{aligned} \tag{5.5b}$$

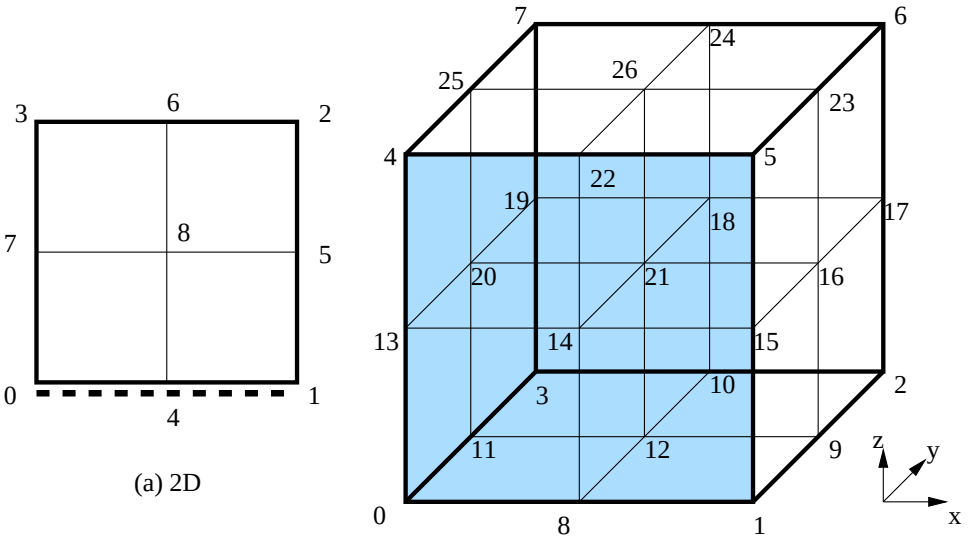

(a) 2D

(b) 3D

Figure 5.2: Reference rectangle and hexahedral element subdivision with node numbering and the intergrid boundary.

From (5.5), the relationships between the coefficients of x-directed fine and coarse boundary basis functions are given by

$$c^h_{w0,8} = c^{2h}_{w0,1} \tag{5.6a}$$

$$c^h_{w8,1} = c^{2h}_{w0,1} \tag{5.6b}$$

$$c^h_{w13,14} = \frac{1}{2}c^{2h}_{w0,1} + \frac{1}{2}c^{2h}_{w4,5} \tag{5.6c}$$

$$c^h_{w14,15} = \frac{1}{2}c^{2h}_{w0,1} + \frac{1}{2}c^{2h}_{w4,5} \tag{5.6d}$$

$$c^h_{w4,22} = c^{2h}_{w4,5} \tag{5.6e}$$

$$c^h_{w22,5} = c^{2h}_{w4,5}. \tag{5.6f}$$

Similarly, another 6 relationships between the coefficients of the z-directed fine and coarse boundary basis functions can be derived. Subsequently, $\mathbf{I}_b$ can be constructed for the hanging variables on the face $\{0,1,5,4\}$.

In the FETD formulation, we start from the time-dependent vector Helmholtz equation. Applying the Faedo-Galerkin process and assembling the finite element matrices

over all the rectangular elements, a system of equations is obtained as follows:

$$\mathbf{T}_{\text{raw}}\frac{1}{c^2}\frac{d^2\mathbf{c}_{\text{raw}}}{dt^2}+\mathbf{S}_{\text{raw}}\mathbf{c}_{\text{raw}}=0 \tag{5.7}$$

where

$$\mathbf{T}_{\text{raw}}=\begin{bmatrix} \mathbf{T}_{ii}^{2h} & \mathbf{T}_{ib}^{2h} & & \\ \mathbf{T}_{ib}^{2h\,T} & \mathbf{T}_{bb}^{2h} & & \\ & & \mathbf{T}_{bb}^{h} & \mathbf{T}_{bi}^{h} \\ & & \mathbf{T}_{bi}^{h\,T} & \mathbf{T}_{ii}^{h} \end{bmatrix},$$

$$\mathbf{S}_{\text{raw}}=\begin{bmatrix} \mathbf{S}_{ii}^{2h} & \mathbf{S}_{ib}^{2h} & & \\ \mathbf{S}_{ib}^{2h\,T} & \mathbf{S}_{bb}^{2h} & & \\ & & \mathbf{S}_{bb}^{h} & \mathbf{S}_{bi}^{h} \\ & & \mathbf{S}_{bi}^{h\,T} & \mathbf{S}_{ii}^{h} \end{bmatrix},$$

$$\mathbf{c}_{\text{raw}}=\begin{bmatrix} \mathbf{c}_{i}^{2h} \\ \mathbf{c}_{b}^{2h} \\ \mathbf{c}_{i}^{h} \\ \mathbf{c}_{b}^{h} \end{bmatrix};$$

and the unknowns $\mathbf{c}_{\text{raw}}$ include the hanging variables and the assembly of $\mathbf{S}_{\text{raw}}$ and $\mathbf{T}_{\text{raw}}$ is over all elements treating the hanging variables as unknowns without applying the constraint in (5.2).

To obtain a valid system with proper field continuity satisfied across the interface, the constraint in (5.2) is imposed in the form of a restriction operator $\mathbf{R}$ that involves the intergrid boundary operator $\mathbf{I}_b$. The restriction operator is given by

$$\mathbf{R}=\begin{bmatrix} \mathbf{I} & 0 & 0 & 0 \\ 0 & \mathbf{I} & \mathbf{I}_b{}^T & 0 \\ 0 & 0 & 0 & \mathbf{I} \end{bmatrix}. \tag{5.8}$$

The resulting system is

$$\mathbf{T}_{\text{valid}}\frac{1}{c^2}\frac{d^2\mathbf{c}}{dt^2}+\mathbf{S}_{\text{valid}}\mathbf{c}=0 \tag{5.9}$$

where

$$\begin{aligned} \mathbf{S}_{\text{valid}} &= \mathbf{R}\mathbf{S}_{\text{raw}}\mathbf{R}^T && \text{(5.10a)} \\ &= \begin{bmatrix} \mathbf{S}_{ii}^{2h} & \mathbf{S}_{ib}^{2h} & \\ \mathbf{S}_{ib}^{2h\,T} & \mathbf{S}_{bb}^{2h}+\mathbf{I}_b^T\mathbf{S}_{bb}^{h}\mathbf{I}_b & \mathbf{I}_b^T\mathbf{S}_{bi}^{h} \\ & \mathbf{S}_{bi}^{h\,T}\mathbf{I}_b & \mathbf{S}_{ii}^{h} \end{bmatrix} \\ \mathbf{T}_{\text{valid}} &= \mathbf{R}\mathbf{T}_{\text{raw}}\mathbf{R}^T && \text{(5.10b)} \\ &= \begin{bmatrix} \mathbf{T}_{ii}^{2h} & \mathbf{T}_{ib}^{2h} & \\ \mathbf{T}_{ib}^{2h\,T} & \mathbf{T}_{bb}^{2h}+\mathbf{I}_b^T\mathbf{T}_{bb}^{h}\mathbf{I}_b & \mathbf{I}_b^T\mathbf{T}_{bi}^{h} \\ & \mathbf{T}_{bi}^{h\,T}\mathbf{I}_b & \mathbf{T}_{ii}^{h} \end{bmatrix} \end{aligned}$$

and

$$\mathbf{c} = \begin{bmatrix} \mathbf{c}_i^{2h} \\ \mathbf{c}_b^{2h} \\ \mathbf{c}_i^{h} \end{bmatrix}.$$

The final assembled system does not involve any hanging variables or unknowns on the fine grid interface boundary. The operation in (5.10) can be viewed as a consequence of restricting both the trial and testing finite element function spaces such that the constraint on the hanging variables given by (5.2) is satisfied and there by the vector functions in both the trial and testing function spaces have tangential continuity along the interface of coarse and fine elements. In this regard, the current treatment of hanging variables is based on a *Galerkin*-type operation.

5.2.1 Time Stepping and Stability

In this section the numerical stability of implicit and explicit temporal discretizations of (5.9) is analysed. As in regular FETD, the Newmark-beta scheme can be used to discretise (5.9). From the definition of the restriction matrix $\mathbf{R}$ in (5.8), it is obvious that

$$\mathbf{R}^T\mathbf{x} \neq 0 \quad \forall \mathbf{x} \neq 0. \tag{5.11}$$

To investigate the spectral properties of $\mathbf{T}_{\text{valid}}$, for any $\mathbf{x} \neq 0$, consider,

$$\begin{aligned} \mathbf{x}^T\mathbf{T}_{\text{valid}}\mathbf{x} &= \mathbf{x}^T(\mathbf{R}\mathbf{T}_{\text{raw}}\mathbf{R}^T)\mathbf{x} \\ &= (\mathbf{R}^T\mathbf{x})^T\mathbf{T}_{\text{raw}}(\mathbf{R}^\mathbf{T}\mathbf{x}) \\ &> 0. \end{aligned} \tag{5.12}$$

Therefore, $\mathbf{T}_{\text{valid}}$ is positive definite. Note that (5.11) and the fact that $\mathbf{T}_{\text{raw}}$ is positive definite, i.e., $\mathbf{x}^T\mathbf{T}_{\text{raw}}\mathbf{x} > 0, \forall \mathbf{x} \neq 0$, are used in arriving at (5.12). Similarly, $\mathbf{S}_{\text{valid}}$ is positive semi-definite. Hence, the conditions of stability for the Newmark-beta method apply to the current FETD with hanging variables. Unconditionally stable 2nd order

accurate time stepping is achieved by setting $\beta = \frac{1}{4}$.

In the case of explicit FETD (central differencing for time), a special case of Newmark -beta method with $\beta = 0$, the condition for stability as in [13] is

$$\Delta t \leq \frac{2}{\sqrt{\lambda_m^v}} \tag{5.13}$$

where λ_m^v is the maximum eigenvalue of the system $\mathbf{S}_{\text{valid}}\mathbf{x} = \lambda \mathbf{T}_{\text{valid}}\mathbf{x}$, or equivalently the spectral radius of $\mathbf{T}_{\text{valid}}^{-1}\mathbf{S}_{\text{valid}}$. Let $\mathbf{x}_m$ be the corresponding eigenvector $\mathbf{x}_m$, i.e.,

$$\mathbf{x}_m^T \mathbf{S}_{\text{valid}} \mathbf{x}_m = \lambda_m^v \mathbf{x}_m^T \mathbf{T}_{\text{valid}} \mathbf{x}_m. \tag{5.14}$$

Similarly, let λ_m^r be the spectral radius of $\mathbf{T}_{\text{raw}}^{-1}\mathbf{S}_{\text{raw}}$. Then, for any $\bar{\mathbf{x}}$

$$\bar{\mathbf{x}}^T \mathbf{S}_{\text{raw}} \bar{\mathbf{x}} \leq \lambda_m^r \bar{\mathbf{x}}^T \mathbf{T}_{\text{raw}} \bar{\mathbf{x}}. \tag{5.15}$$

By following the same procedure in (5.12) with $\bar{\mathbf{x}}_m = \mathbf{R}^T \mathbf{x}_m$, (5.14) leads to

$$\bar{\mathbf{x}}_m^T \mathbf{S}_{\text{raw}} \bar{\mathbf{x}}_m = \lambda_m^v \bar{\mathbf{x}}_m^T \mathbf{T}_{\text{raw}} \bar{\mathbf{x}}_m. \tag{5.16}$$

After using (5.16) and setting $\bar{\mathbf{x}} = \bar{\mathbf{x}}_m$, (5.15) leads to the following inequality

$$\lambda_m^v \leq \lambda_m^r. \tag{5.17}$$

Eq. (5.17) gives the upper bound of λ_m^v by which, a more stringent condition for stability can be obtained from (5.13) as follows

$$\Delta t \leq \frac{2}{\sqrt{\lambda_m^r}}. \tag{5.18}$$

From the generalized eigenvalues of mass and stiffness matrices of hexahedral elements obtained using trapezoidal integration rule, shown in Sec. 4.6, we have

$$\lambda_m^r = 4c^2 \sqrt{\frac{1}{\Delta x_f^2} + \frac{1}{\Delta y_f^2} + \frac{1}{\Delta z_f^2}} \tag{5.19}$$

leading to the condition for stability as

$$\Delta t \leq \frac{1}{c} \left[\sqrt{\frac{1}{\Delta x_f^2} + \frac{1}{\Delta y_f^2} + \frac{1}{\Delta z_f^2}} \right]^{-1} \tag{5.20}$$

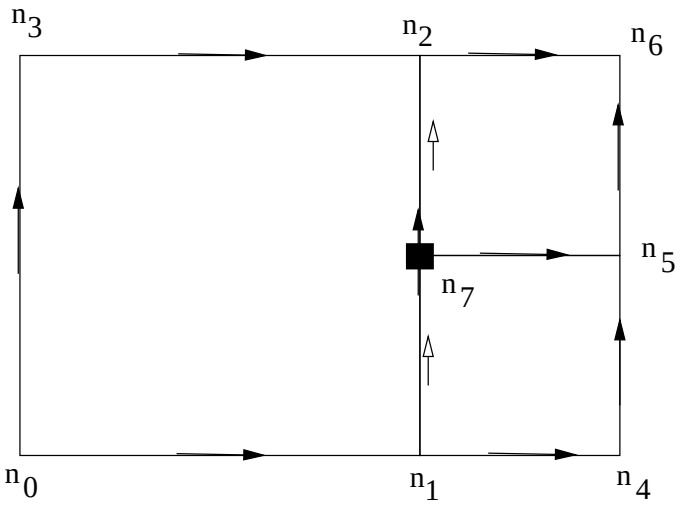

Figure 5.3: Sample mesh with hanging variables for computing the number of zero eigenvalues.

where $\Delta x_f, \Delta y_f$ and Δz_f are the dimensions of the hexahedral elements in the fine region. Eq. (5.20) is the same Courant-Friedrichs-Levy (CFL) condition for FDTD in the fine region. Thus, a time-step satisfying the CFL limit ensures the stability of the explicit FETD algorithm with hanging variables. The result is expected since the explicit FETD is equivalent to the FDTD method. However, it is verified that the treatment of hanging variables following the Galerkin principles does guarantee numerical stability.

5.2.2 Dimension of Gradient Space

To illustrate the dimension of the gradient space embedded in the constrained finite element space, by the current treatment of hanging variables, a simple mesh as shown in Fig. 5.3 is considered. The edge length of the fine element is Δh_f. The valid mass and stiffness matrices for the nine edge element unknowns are constructed. The nine eigenvalues of the generalized system are then computed to be

$$\left[0, 0, 0, 0, 0, 0, \frac{39 \pm \sqrt{321}}{12\Delta h_f^2}, \frac{6}{\Delta h_f^2}\right].$$

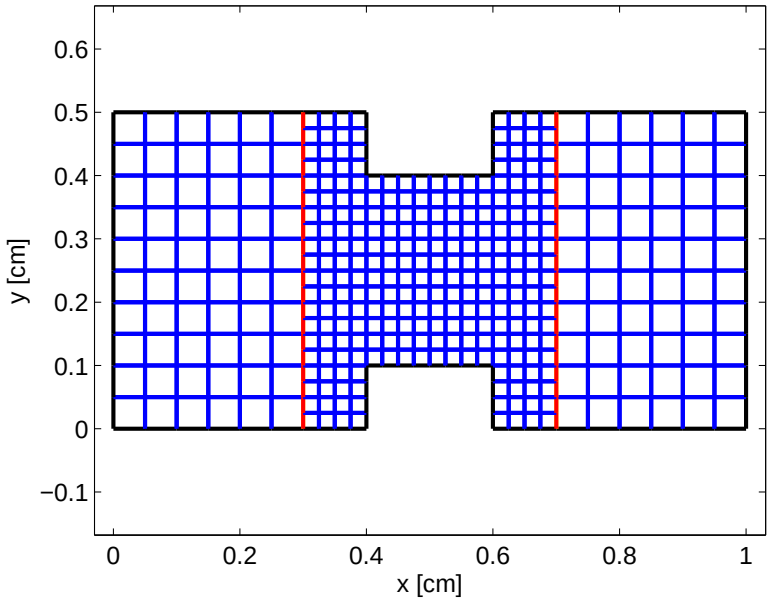

Figure 5.4: Mesh of ridged waveguide with rectangular elements and hanging variables.

It is seen that the dimension of the gradient space or equivalently the number of zero eigenvalues is six. The total number of nodes is eight. With one reference node for zero potential, the number of free nodes is seven. However, with respect to Fig. 5.3 the gradient function $\nabla\xi_7$ is not present in the constrained finite element space. Hence the number of free nodes is six with each node i having a corresponding gradient field spanned by the constrained edge element basis functions. The maximum eigenvalue is $\lambda_m^v = \frac{6}{\Delta h_f^2}$. In the case of the raw system with the unconstrained hanging variables as unknowns, $\lambda_m^r = \frac{8}{\Delta h_f^2}$ as established in Sec. 4.6. It is seen that the result is consistent with (5.17).

5.2.3 Implementation

In the 2-D case with rectangular elements, Eq (5.4) shows that each hanging variable maps only to its corresponding coarse element unknown. In other words, each row of $\mathbf{I}_b$ has exactly a non-zero entry that is equal to 1 (at the column corresponding to the coarse

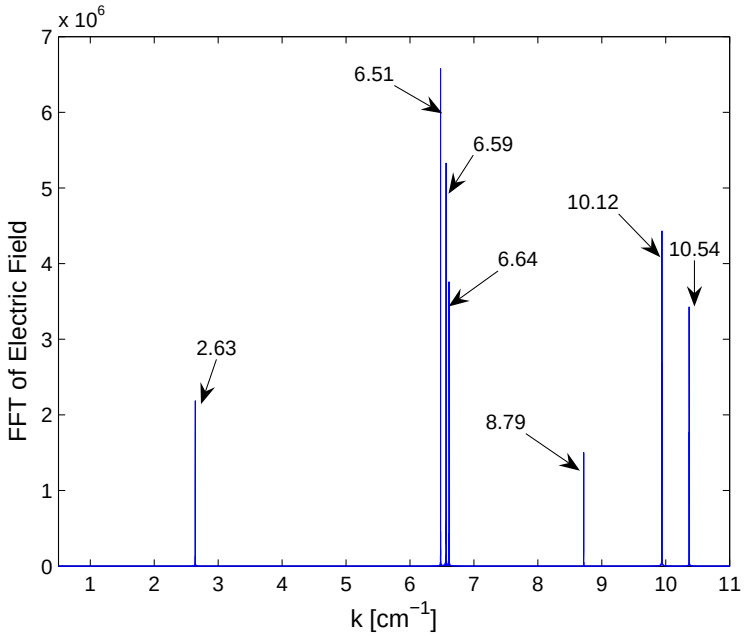

Figure 5.5: Resonant frequencies of the ridged waveguide.

element unknown). In this case, $\mathbf{T}_{\text{valid}}$ and $\mathbf{S}_{\text{valid}}$ can be constructed directly in the implementation. In the conventional finite element assembly procedure, edges of the fine elements that constitute a hanging variable are numbered as their corresponding coarse edges. Thus, the final mass and stiffness matrices ($\mathbf{T}_{\text{valid}}$, $\mathbf{S}_{\text{valid}}$) can be assembled directly without the need to compute $\mathbf{S}_{\text{raw}}$, $\mathbf{T}_{\text{raw}}$ and $\mathbf{R}$. Moreover, if $\mathbf{T}_{\text{raw}}$ is diagonal, then $\mathbf{T}_{\text{valid}}$ is also diagonal. Hence the FETD update remains explicit.

However, in the 3-D case, two types of hanging variables exist viz.,

- Hanging edges with only one corresponding coarse edge which contributes a single non-zero entry to the corresponding column of $\mathbf{I}_b$. Edge $\{0,8\}$ in Fig. 5.2 is an example.

- Hanging edges with two corresponding coarse edges which contribute entries of $\frac{1}{2}$ to each corresponding column of $\mathbf{I}_b$. Edge $\{13,14\}$ in Fig. 5.2 is an example.

This is observed from the relationship between coefficients of the fine edges and the corresponding coarse edge as given in (5.6). As in the 2-D case, explicit construction

of $\mathbf{R}$ can still be avoided. In this case, the restriction operator is generated for each element, and the element matrices associated with $\mathbf{T}_{\text{valid}}$ and $\mathbf{S}_{\text{valid}}$ are computed from (5.10) during the assembly of the global mass and stiffness matrices on all elements. Thus, as compared to conventional finite element assembly procedure, the necessary additional operations are the matrix multiplications in (5.10) for each fine element that has a hanging variable. However, though $\mathbf{T}_{\text{raw}}$ can be diagonalized via the process of mass lumping, the resulting $\mathbf{T}_{\text{valid}}$ is not diagonal, due to the nature of $\mathbf{I}_b$. This means that the update equations associated with the unknowns on the grid boundary are implicit. The dimension of this implicit block is equal to the number of coarse edges on the coarse-fine grid interface, which is less than the total number of unknowns in the FETD region. These unknowns require a sparse matrix solution, which can be performed efficiently by Cholesky factorization of the implicit block. Note that the implicit block is symmetric positive definite and its complete Cholesky factor exists. It should be noted that the factorization of this matrix does not increase the complexity of the method. One can assume that the number of unknowns at the coarse-fine interface is proportional to $N^{2/3}$, where N is the number of volume unknowns. The computational cost of the sparse factorization is proportional to N, and the additional storage costs of the factorized matrix is $N^{2/3} \log N$. Thus, the overall complexity of the method is the same as the traditional FDTD.

5.2.4 Ridged Waveguide Example

To validate the treatment of hanging variables in FETD method, a sample problem of computing the cutoff frequencies of a ridged waveguide is considered. The cross-section of the waveguide and the 2-D mesh is shown in Fig. 5.4. The area in the vicinity of the ridge, chosen arbitrarily, has fine elements. For this 2-D case, when explicit FETD is employed, in spite of the restriction operation, the time update is explicit requiring

only matrix-vector multiplications during each time step. The time step is chosen such that the Courant criteria with the edge length of fine element is satisfied. The waveguide is excited by a differentiated Gaussian pulse. Fourier transform of the electric field sampled at an arbitrarily chosen location is shown in Fig. 5.5. The resonant peaks obtained using the FETD method is in a good agreement with the cutoff frequencies of the same structure obtained from a generalized eigenvalue problem on a triangular mesh with edge element basis functions. The time domain solution does not have any spurious modes which are inconsistent with the eigenvalue solution indicating that the treatment of hanging variables does not corrupt the numerical solution with unphysical modes. Though not shown, no signs of numerical instability were observed in the time domain response.

5.2.5 Rectangular Resonator Example

The second example is a 3-D case of rectangular resonant cavity structure. In this example, though explicit FETD is used, the interface unknowns form an implicit block and matrix solution is obtained using complete factorization. The dimensions of the cavity is 1 cm$\times$1 cm$\times$2 cm. The computational domain is split into two regions, as shown in the inset of Fig. 5.6. The coarse element size is 0.2 cm and the fine element size is 0.1 cm. Hanging variables are present in the interface surface on the $z = 1$ cm plane. The spectrum of the electric field at a point inside the cavity is shown in Fig. 5.6. In Table 5.1, the first five cutoff wavenumbers are compared to the analytical solution. It is observed that the error in the numerical solution is less than 2%. The simulation was carried out for half a million times steps with a CFL number of 0.9999. No signs of numerical instabilities were observed.

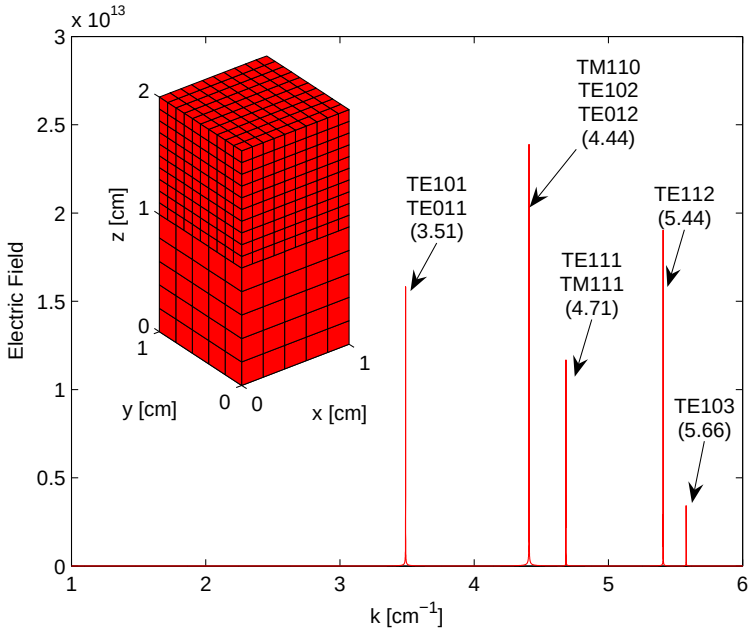

Figure 5.6: Spectrum of electric field inside the rectangular resonant cavity.

Table 5.1: First 5 cutoff wavenumbers for rectangular resonant cavity

Mode	**Analytical**	**Numerical**	**%Error**
TE_{101}, TE_{011}	3.51	3.49	0.57
TE_{110}, TE_{102},TE_{012}	4.44	4.41	0.68
TE_{111}, TM_{111}	4.71	4.68	0.64
TE_{112}	5.44	5.41	0.55
TE_{103}	5.66	5.58	1.41

5.3 FETD Based FDTD Subgridding

The FDTD method has errors due to stair-casing involved in the modeling of non-rectilinear geometry, as well as errors due to poor modeling of the field variation. A possible way to overcome these errors is to use fine meshing, in which case the number of unknowns increases significantly. An immediate alternative would be to use fine mesh for regions with intricate details, and model the rest of the domain with coarse grids. The basic idea behind FDTD subgridding algorithms is that the computational domain is split into coarse and fine regions as desired, with a suitable communication between the unknowns at the boundary of the two regions. There have been numerous attempts to develop subgridding schemes [81, 89–91]; however, all of these approaches suffer from late time instability. Monk [92] presents a stable method, but it is only valid for 2-D and only along a single interface (no corner region). All of these schemes assume that there is a single time step used throughout the computational domain. Depending on the conditions on the time step in the coarse region, there are two possible subgridding schemes viz., a) Same Time Step (STS) scheme in which the time step in the coarse region is the same as that of the fine region (obeying the Courant condition for stability); and b) Multiple Time Step (MTS) scheme in which the time step in the coarse and fine grids are not necessarily the same, but both satisfy the Courant condition for the respective grids. Obviously, MTS is more desirable, but it is more difficult to develop a stable method based on this scheme. The method proposed here will concern only the STS scheme.

In the proposed work we handle the coarse-fine grid unknowns by introducing an interface region between the coarse and fine grids, where the solution is based on FETD method. The coarse-fine interface is present in the FETD interface region with both coarse and fine cells or elements. The treatment of hanging variable presented in the previous section is employed to handle the interface between coarse and fine elements.

Subsequently, by using the stable hybridization scheme to couple the finite element and finite difference grids, a stable FDTD subgridding scheme is achieved.

5.3.1 Hybrid FETD-FDTD

The illustration of the use of FETD method with hanging variables to handle the interface between the coarse and fine regions of the FDTD subgridding method for the 2-D case is shown in Fig. 5.7. Note that the FETD region is structured and hence interface between FETD and FDTD methods does not require to adopt any special strategies in terms of mesh generation, such as insertion of pyramidal elements. The stable hybrid FETD-FDTD method discussed in previous Chapter can be employed in both the 2-D and 3-D cases. Moreover, since the treatment of hanging variables in the FETD method allows higher levels of refinement of the finite elements, the resulting subgridding method allows transitions from a coarse grid to fine grid so long as the coarse grid size is a multiple of the fine grid spacing. However, suitable restriction operators, depending on the level of nesting, need to be obtained. In the case of 2-D, it is trivial to obtain the restriction operator unlike the 3-D case.

5.3.2 Equivalent FDTD-like Update Equations

Instead of introducing an FETD based region for the interface of coarse and fine grids, it is possible to arrive at update equations for the electric and magnetic field unknowns directly based on the FETD method for treatment of hanging variables. In this way, the resulting update equations are similar to the regular FDTD update equations. Such explicitly derived update equations offer an advantage in the implementation point of view eliminating the need to implement a code for the FETD framework to handle the interface region. To illustrate the procedure to arrive at such update equations, consider a 2-D FDTD stencil shown in Fig. 5.8. The update for $H_{z(i,j)}$ is the same as regular

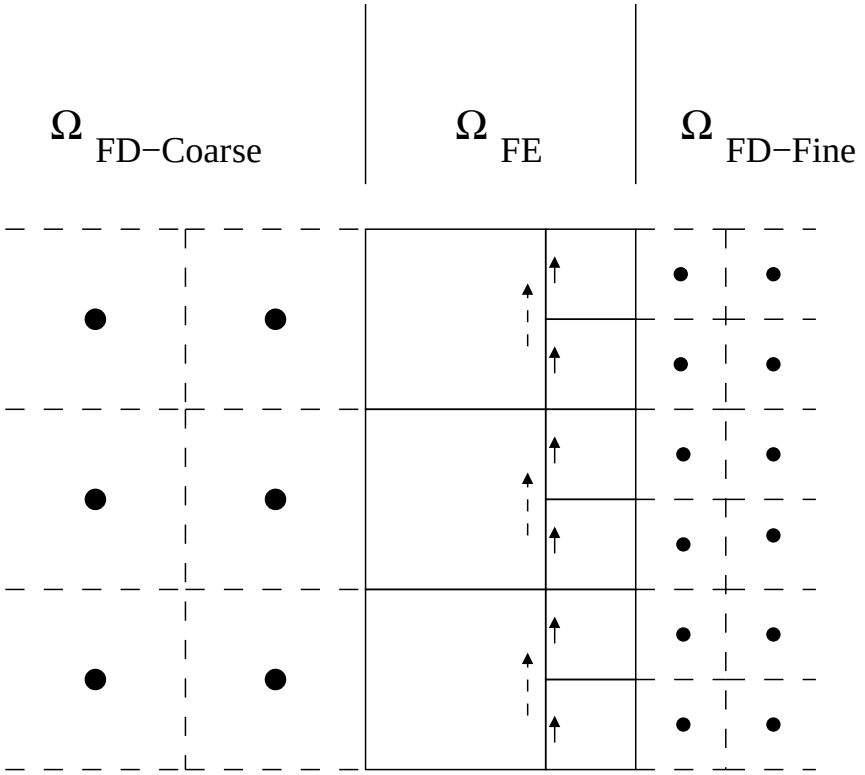

Figure 5.7: FDTD subgridding mesh with hanging variables in FETD based interface mesh.

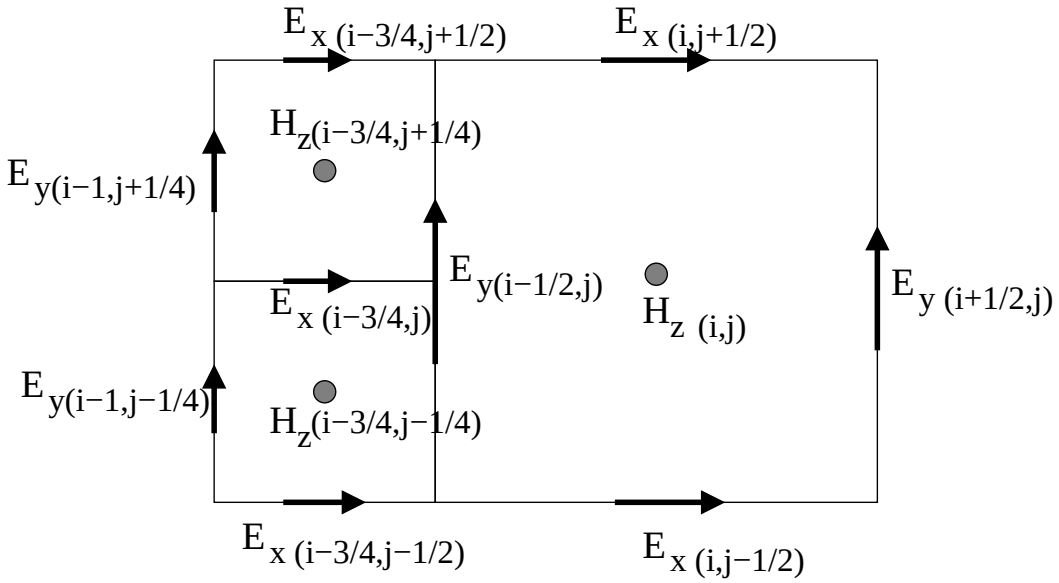

Figure 5.8: 2-D stencil for update of unknown on the interface of coarse and fine grid.

FDTD. Since the hanging variables $E_{y(i-1/2,j+1/2)}$ and $E_{y(i-1/2,j-1/2)}$ are represented by $E_{y(i-1/2,j)}$, the magnetic field unknowns on the fine side of the interface need to be modified as follows

$$\begin{aligned}
H^{n+1/2}_{z(i-3/4,j+1/4)} &= H^{n-1/2}_{z(i-3/4,j+1/2)} \\
&\quad - \frac{2\Delta t}{\mu_0 \Delta h}\left[E^n_{y(i-1/2,j)} - E^n_{y(i-1,j+1/4)}\right. \\
&\quad \left. + E^n_{x(i-3/4,j)} - E^n_{x(i-3/4,j+1/2)}\right] \\
H^{n+1/2}_{z(i-3/4,j-1/4)} &= H^{n-1/2}_{z(i-3/4,j-1/4)} \\
&\quad - \frac{2\Delta t}{\mu_0 \Delta h}\left[E^n_{y(i-1/2,j)} - E^n_{y(i-1,j-1/4)}\right. \\
&\quad \left. + E^n_{x(i-3/4,j-1/2)} - E^n_{x(i-3/4,j)}\right]
\end{aligned} \tag{5.21}$$

where Δh is the coarse mesh size and $\Delta h/2$ is the fine mesh size. Based on the finite element mass and stiffness matrices (shown in Sec. 4.4), and using explicit FETD for the temporal discretization of (5.9), it leads to the following update equation for the electric field unknowns on the interface across coarse and fine regions viz.,

$$\begin{aligned}
E^{n+1}_{y(i-1/2,j)} &= 2E^n_{y(i-1/2,j)} - \frac{c^2\Delta t^2}{\Delta h^2}\left\{2E^n_{y(i-1/2,j)}\right. \\
&\quad - \left[E^n_{y(i+1/2,j)} + \frac{1}{2}(E^n_{y(i-1,j+1/4)} + E^n_{y(i-1,j-1/4)})\right] \\
&\quad + E^n_{x(i,j+1/2)} - E^n_{x(i,j-1/2)} \\
&\quad \left. - E^n_{x(i-3/4,j+1/2)} + E^n_{x(i-3/4,j-1/2)}\right\} \\
&\quad - E^{n-1}_{y(i-1/2,j)}.
\end{aligned} \tag{5.22}$$

The update equation for the rest of the unknowns remain the same as that of regular FDTD corresponding to either the coarse or the fine region. The equivalent FDTD-like update equations shown here provide an alternate method for the implementation of the proposed subgridding method and is straight forward to extended the procedure for level of refinement greater than 1:2. A similar procedure can be applied for the 3-D case with the corresponding mass and stiffness matrices for hexahedral elements.

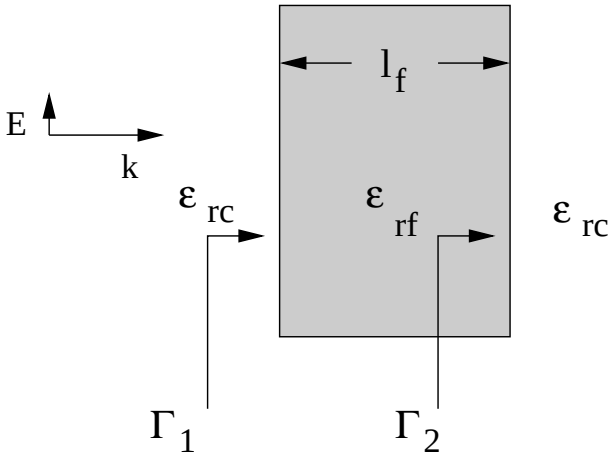

Figure 5.9: Dispersive dielectric slab analogy to capture numerical grid dispersion behaviour in coarse and fine FDTD regions.

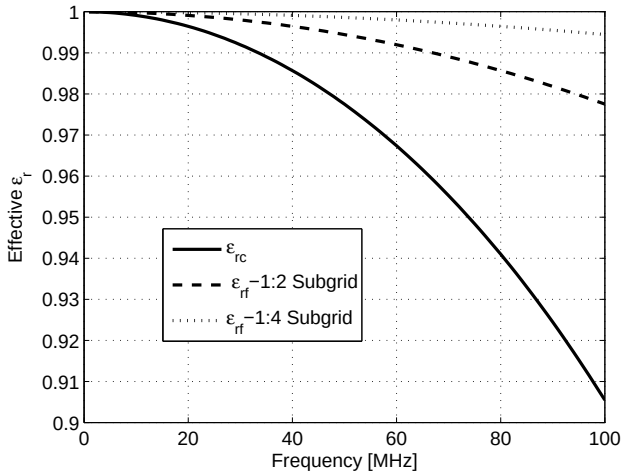

Figure 5.10: Dispersive effective relative permittivity for coarse mesh, 1:2 subgrid and 1:4 subgrid.

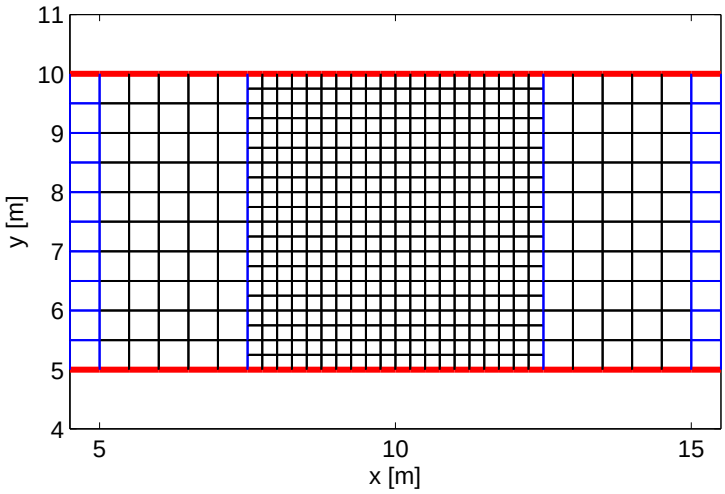

(a) 1:2 Subgrid

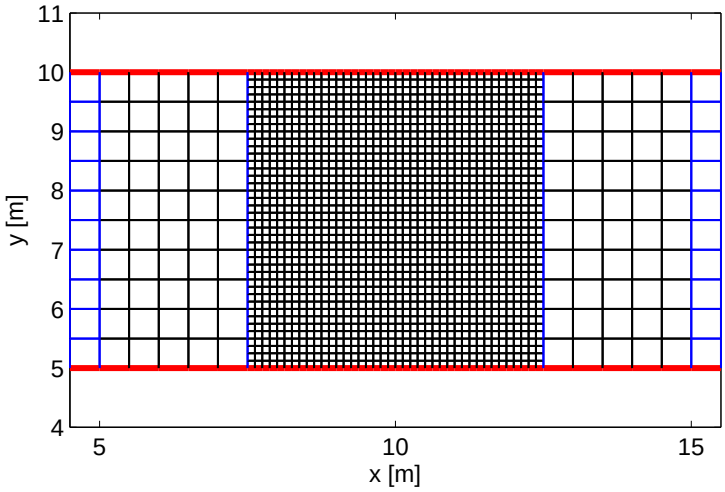

(b) 1:4 Subgrid

Figure 5.11: Numerical experiment of subgridding mesh inside a parallel plate waveguide.

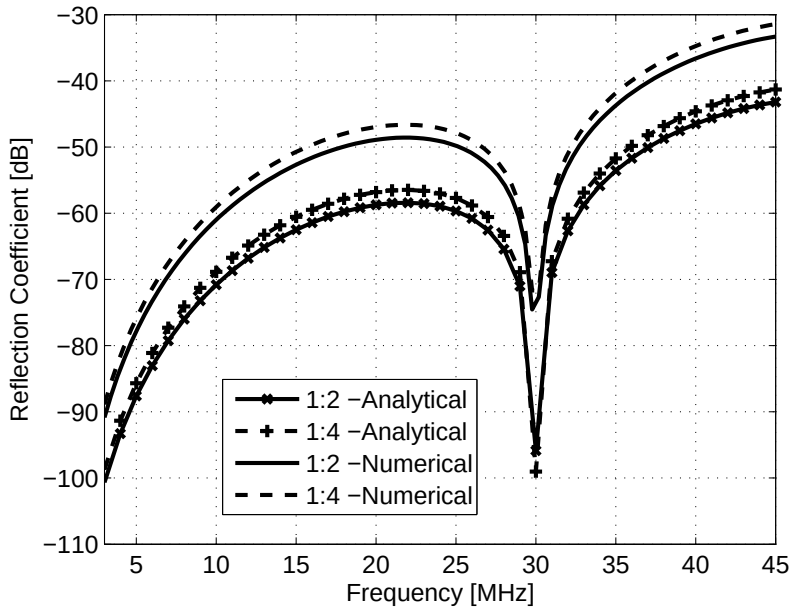

Figure 5.12: Level of unphysical reflections introduced by the treatment of hanging variable.

5.4 Investigation of Spurious Errors

Solution obtained using FDTD inherently suffers from unphysical dispersion errors arising due to the second order accurate approximation of the spatial and temporal derivative operators. The phase velocity of the numerical wave solution is lesser than the speed of light in vacuum and is dependent on the spatial and temporal resolutions. Therefore, in subgridding schemes, the numerical dispersion characteristics are different in the coarse and fine regions of the computational grid. This difference in numerical dispersion behaviour is a major source of spurious errors. In this section we quantify the errors introduced due to the difference in numerical phase velocity in the coarse and fine grids analytically and compare with the numerical solution obtained using the proposed technique. For the FDTD method in the 2-D case, the following numerical dispersion

relationship holds good viz.,

$$\left(\frac{\Delta h}{c\Delta t}\right)^2 \sin^2\left(\frac{\omega\Delta t}{2}\right) = \sin^2\left(\frac{\Delta h}{2}\tilde{k}\cos\alpha\right) + \sin^2\left(\frac{\Delta h}{2}\tilde{k}\sin\alpha\right) \tag{5.23}$$

where $\tilde{k}$ is the numerical wavenumber and α is the angle of wave propagation. $\tilde{k}$ can be computed by the Newton's method for a given problem with a particular spatial and temporal resolution. It is immediately seen that the numerical wave number for the coarse mesh, $\tilde{k}_c$ and fine mesh, $\tilde{k}_f$ are different. To analytically compute the reflections due to difference in $\tilde{k}_c$ and $\tilde{k}_f$ we draw an analogy to the case of reflections from a dielectric slab with different relative permittivities viz., ε_{rc} and ε_{rf} as shown in Fig. 5.9. The relative permittivities are related to the numerical wavenumbers as $\varepsilon_{rc} = \tilde{k}_c^2/k_0^2$ and $\varepsilon_{rf} = \tilde{k}_f^2/k_0^2$ where k_0 is the free space wavenumber. In Fig. 5.10 we compare the relative permittivity in each region for a test example with a coarse mesh size of $\Delta h = 0.5$ m and $\Delta t = 0.294$ ns. Note that $\tilde{k}_c$ and $\tilde{k}_f$ are obtained by solving (5.23) with appropriate parameters and choosing $\alpha = 0^\circ$. The reflection coefficient, Γ_1 due to a dielectric slab for the transverse electric case, is given by

$$\Gamma_1 = \frac{\rho_1(1 - e^{-2j\tilde{k}_f l_f})}{1 - \rho_1^2 e^{-2j\tilde{k}_f l_f}} \tag{5.24}$$

where

$$\rho_1 = \frac{\sqrt{\varepsilon_{rc}} - \sqrt{\varepsilon_{rf}}}{\sqrt{\varepsilon_{rc}} + \sqrt{\varepsilon_{rf}}} = \frac{\tilde{k}_c - \tilde{k}_f}{\tilde{k}_c + \tilde{k}_f} \tag{5.25}$$

and l_f is the length of the slab (or equivalently the fine region). To compare the analytical reflection coefficient with the numerical results, we consider the case of a parallel plate waveguide with the fine region embedded inside. The size of the fine region is 5 m$\times$5 m corresponding to $1\lambda \times 1\lambda$ at 30 MHz. Two cases of fine region viz., 1) with 1:2 refinement and 2) with 1:4 refinement, are considered and shown in Figs. 5.11(a) and 5.11(b). Note that the parallel plate waveguide is filled with free space, both in the fine and coarse regions. Both the coarse ends of the waveguide are terminated by perfectly

match layer (PML). The numerical reflection coefficient is computed as

$$\Gamma(f)(\text{dB}) = 20\log\left|\frac{\mathcal{F}(H_z(t) - H_z^{inc}(t))}{\mathcal{F}(H_z^{inc}(t))}\right| \tag{5.26}$$

where $H_z(t)$ is the time signal recorded with the fine mesh, at a physical observation point which is the same as that for recording $H_z^{inc}(t)$ without the fine mesh. $\mathcal{F}(u)$ denotes the Fourier transform of u. The reflection coefficient computed using (5.26) gives the errors introduced in the solution due to embedding of the fine region with in the coarse grid. Both analytical and numerical results thus obtained are shown in Fig. 5.12. The trend of the numerical errors follow the analytical prediction well, and the level of reflection is higher than the analytical prediction by about 10 dB. We conclude that the major source of errors introduced is primarily the difference in the dispersion behaviour in the coarse and fine regions. The additional errors are attributed to the method of handling hanging variables at the interface across the coarse and fine regions. The truncation error in the update of unknowns on the interface of coarse and fine region is $O(h)$ where as for the interior unknowns the truncation error is $O(h^2)$. Also observed is that the error levels for the 1:4 refinement case is slightly more than the 1:2 refinement case. In both the cases, the reflection errors are less than 30 dB in the desired band of interest.

5.5 Numerical Results

The first example is a 2-D problem of the scattering by a PEC cylinder with circular cross-section. The radius of the cylinder is 5 m. For plane wave excitation, a differentiated Gaussian pulse with significant spectral content in the frequency range of 3-30 MHz is used. The cell size for the coarse FDTD grid is $\Delta x_c = \Delta y_c = \Delta h_c = 0.5$ m, corresponding to $\lambda/20$ at 30 MHz. Both 1:2 and 1:4 refinement cases are considered with the fine grid size being $\Delta h_f = 0.25$ m and $\Delta h_f = 0.125$ m respectively. The mesh with 1:4 subgridding employed in this example is shown in the inset of Fig. 5.13. The

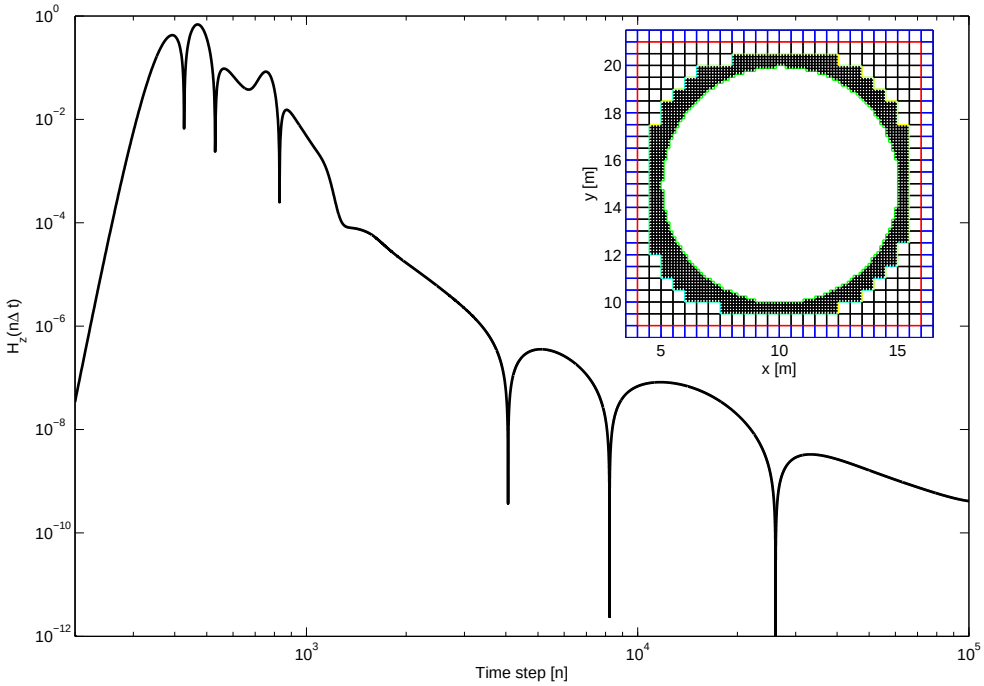

Figure 5.13: Time history of $H_z(n\Delta t)$ component obtained in the solution for scattering by PEC cylinder. Inset shows the 1:4 subgridding mesh used.

Table 5.2: Computational statistics for scattering by PEC cylinder

Case	**FDTD**	**1:2 Subgrid**	**1:4 Subgrid**
Solution Time (s)	47.13	50.22	61.21
Memory (KB)	621	836	1720
Error at 30MHz	6.0%	2.8%	1.5%
Maximum error	11.8%	6.5%	3.4%

coarse FDTD region has a total-scattered field boundary, to extract the scattered field solution. Fig. 5.13 shows the scattered $H_z(t)$ component in the backscattered direction for sufficiently long number of time steps and no signs of numerical instability are observed. For the radar-cross-section (RCS) computation, a time domain NFFF transformation is applied to obtain the far zone solution from the near field solution. The backscattered RCS of the PEC cylinder over the frequency band is obtained using a) the subgridding method with 1:2 and 1:4 refinements, b) regular FDTD with cell size $\Delta h = 0.5$ m and c) analytical solution, all of which are compared in Fig. 5.14. The relative errors in the 2-D bistatic RCS for the different cases are shown in Fig. 5.15. As expected, the solution using the subgridding method is closer to the analytical solution, in comparison with regular FDTD solution. In Table 5.2 the details of computation time, memory requirement and error in solution for the different cases is tabulated. The memory requirement reported here does not include the memory required by the RCS computation routines. The memory requirement for the storage of far-zone vector potential in the near-to-far transformation is the same for all the three cases and hence not included. The 1:4 refinement case has the least relative error due to the more accurate representation of the geometry and hence much less staircasing errors. If levels of accuracy as obtained by the 1:4 subgrid case are desired while using the traditional FDTD method, then a fine mesh has to be used all throughout the computational domain leading to a highly inefficient method compared to the proposed subgridding method.

The next example is the case of 2-D scattering by the NACA64a410 Airfoil which is the same as the one discussed in Sec. 4.5. The incident plane wave is in the band of 0.2-1.5 GHz. The coarse grid size is 0.5 cm. The length of the airfoil is 1 m, corresponding to 5λ at 1.5 GHz. Here again both 1:2 and 1:4 refinement cases with fine grid size of 0.25 cm and 0.125 cm, respectively, are considered. The geometry of the airfoil and the subgridding mesh of the nose section with 1:4 transition is shown in Fig. 5.16. The results for the backscattered RCS are compared to that obtained using

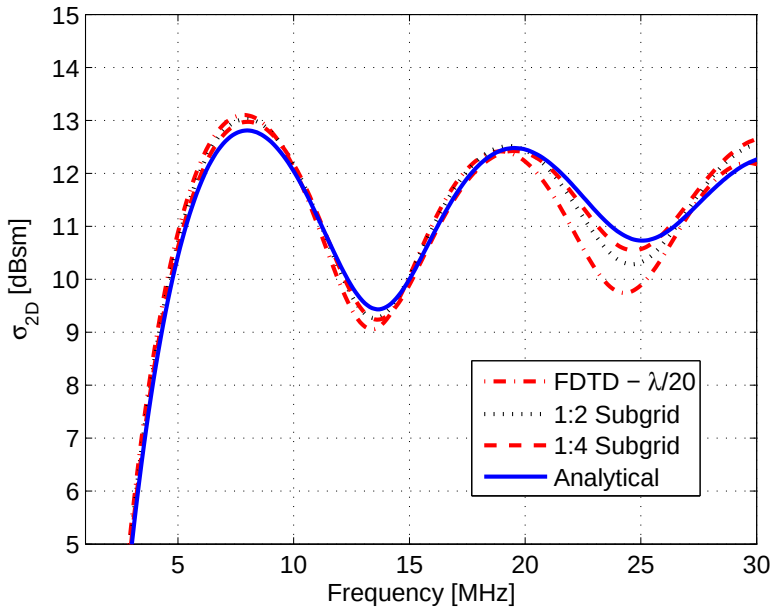

Figure 5.14: 2-D backscattered RCS compared with FDTD (with and without subgridding) and analytical results.

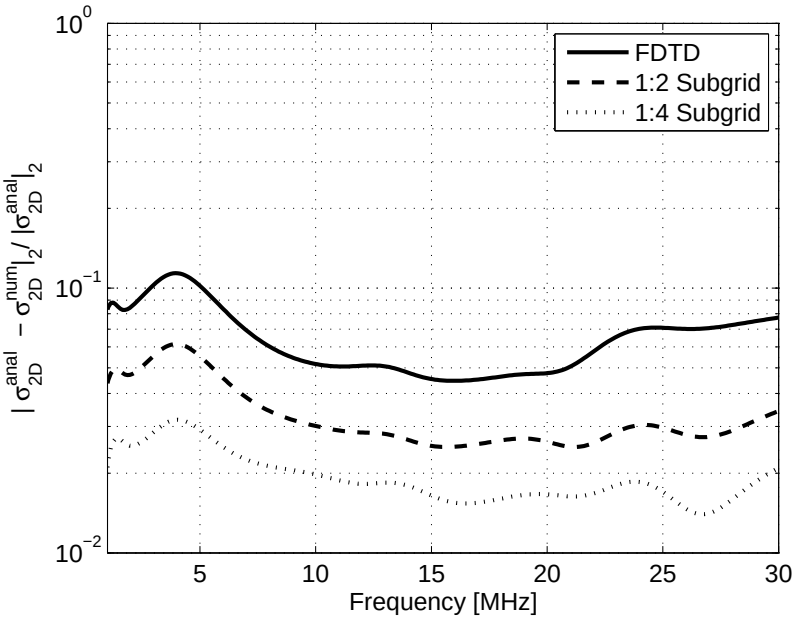

Figure 5.15: Relative error in the computed 2-D bistatic RCS using FDTD (with and without subgridding).

method of moments (MoM) in Fig. 5.17. Also shown in Fig. 5.17 is the result obtained using traditional FDTD with cell size of 0.5 cm, which is the same as the coarse grid size used in the subgridding case. Both FDTD with subgridding and regular FDTD agree with the MoM in computational results in the low frequency end of the band. At the high frequency end, as expected, the subgridding case performs better than the FDTD solution. The primary reason is the errors introduced due to the stair-case approximation of the airfoil. This is further verified by comparison of MoM results with the result obtained using stable hybrid FETD-FDTD method, where unstructured triangular elements are used to mesh the airfoil more accurately. In comparison with the FETD-FDTD method, the current subgridding method does not require a matrix solution for updates in 2-D case and in the 3-D case, the implicit matrix is confined to the unknowns on the coarse-fine interface. This is because while using rectangular (hexahedral) elements, mass-lumping can be performed leading to an explicit update equation. Whereas, in FETD-FDTD method, the update of finite element unknowns during each time step requires a matrix solution. For a given geometry, the number of unknowns in the unstructured case is often lower than those in the subgridding case. However, the number of unknowns can be significantly controlled in the subgridding method by confining the fine region to those regions where a fine grid is necessary. Another advantage of the proposed method is that the mesh generation requirement is the same as that of the traditional FDTD method and already available tools for FDTD mesh generation could be re-used. FETD-FDTD method has very stringent mesh generation requirements. The bistatic RCS of the airfoil at 1.5 GHz using the 1:2-subgrid case is compared to MoM results in Fig. 5.18. A good agreement is observed in all directions.

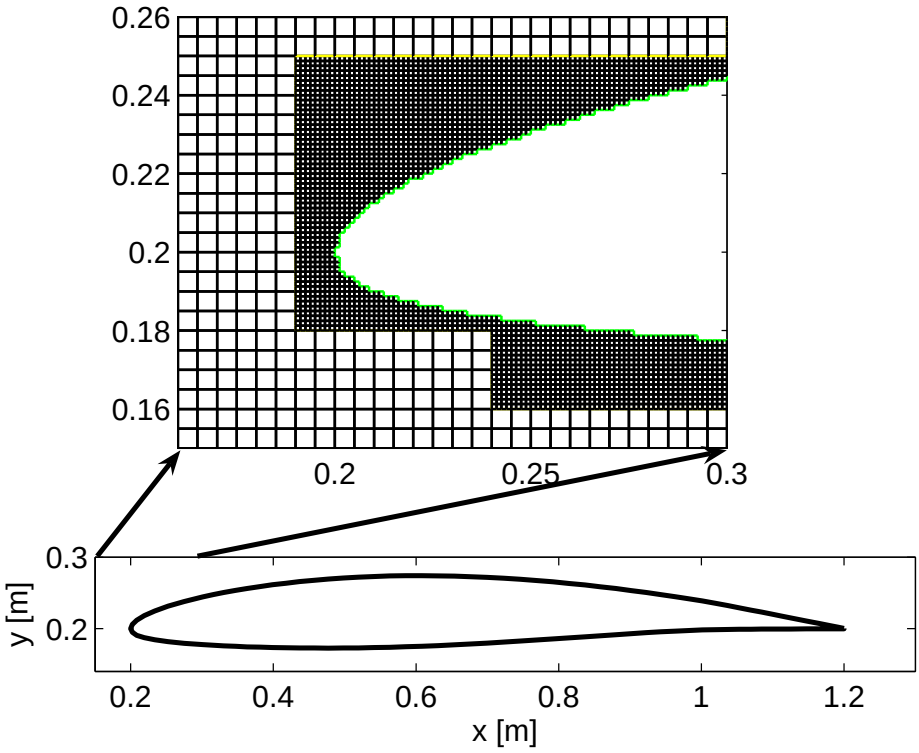

Figure 5.16: Subgridding mesh for scattering by NACA64a410 Airfoil

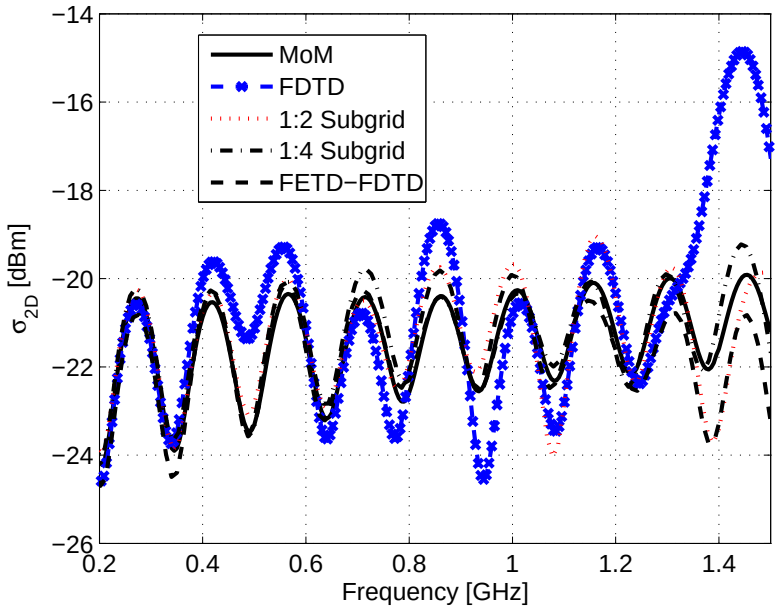

Figure 5.17: Comparison of 2-D backscattered RCS of NACA64a410 airfoil in the band 0.2-1.5 GHz

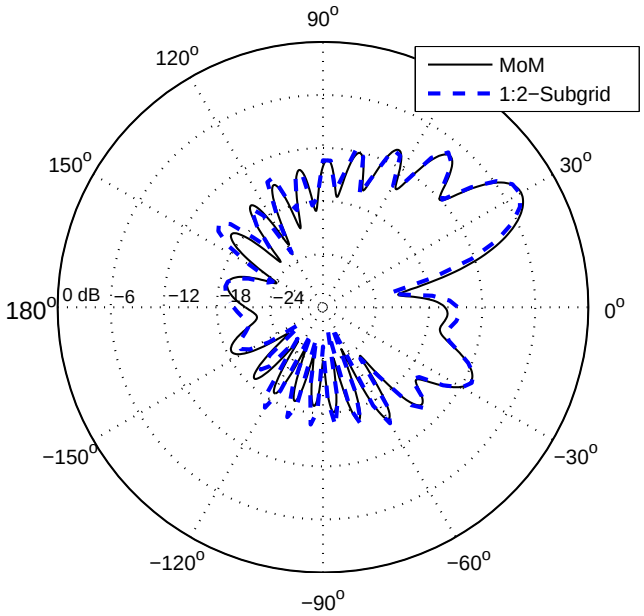

Figure 5.18: Bistatic RCS of NACA64a410 airfoil at 1.5GHz compared with MoM results

5.6 Interfacing Hexahedral and Tetrahedral Elements

For hybridizing the unstructured FETD method and the FDTD method, two different interface strategies were shown in Fig. 4.14. The case in Fig. 4.14(a) alleviates the need for using pyramidal elements. The use of interpolation to update the diagonal unknowns using the FDTD solution, proposed in [14] can be viewed as applying interpolation operation on the trial functions instead of the testing function resulting in a non-Galerkin procedure leading to numerical instability. In the case of treatment with hanging variables, the Galerkin-type procedure leads to stable FETD formulation. It is tempting to attempt the extension of the concept of hanging variables to the case of interface between tetrahedral and hexahedral elements which could lead to stable hybridization of the FETD and FDTD methods without requiring pyramidal elements. However, unlike the case of hanging variables with two similar elements discussed in the previous section, the current case involves two dissimilar elements across the interface. To have a

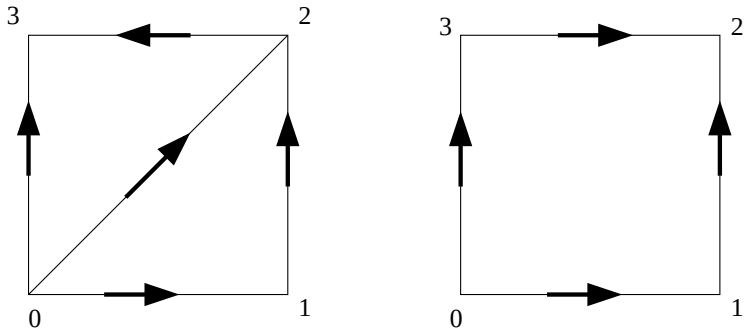

(a) Triangular Elements (b) Rectangular Element

Figure 5.19: Reference triangular and rectangular edge elements

valid intergrid boundary operator, one of the conditions is that the basis functions on either side of the interface must be able to ensure tangential continuity across. This condition is violated in the case of interfacing tetrahedral and hexahedral elements as the elements are topologically dissimilar. The finite element space of 2-D edge elements on the two triangles on a rectangular face does not contain the finite element space of edge elements of the parent rectangular face. However, with the idea of treating the intergrid boundary operator as a projection operator, an attempt is made to interface unstructured and structured elements as in Fig. 4.14(a). The intergrid boundary operator with reference to Fig. 5.19 is then

$$\begin{bmatrix} c^t_{01} \\ c^t_{23} \\ c^t_{03} \\ c^t_{12} \\ c^t_{02} \end{bmatrix} = \begin{bmatrix} 1 & & & \\ & -1 & & \\ & & 1 & \\ & & & 1 \\ 1/2 & 1/2 & 1/2 & 1/2 \end{bmatrix} \begin{bmatrix} c^r_{01} \\ c^r_{32} \\ c^r_{03} \\ c^r_{12} \end{bmatrix} \tag{5.27}$$

where c^t_{ij} is the coefficient of the basis function associated with edge $\{i, j\}$ of the triangular element and c^r_{ij} is the coefficient of the basis function associated with edge $\{i, j\}$ of the rectangular element. A 3-D implementation based on the projection operator in (5.27) for interfacing rectangular and triangular elements was preformed and used to compute the eigenvalues of a rectangular cavity. Using the projection operator in 5.27, valid mass and stiffness matrices are obtained for a hybrid mesh with both tetrahedral

and hexahedral elements as shown in Fig. 5.20(a). In Fig. 5.21 the computed resonant wave numbers using an eigenvalues solver are shown for the case of a mesh with tetrahedral elements (dots) and the hybrid mesh (crosses). It is noted that the number of zero eigenvalues for the case with tetrahedral elements is 63 which agrees with the number of internal nodes in the tetrahedral mesh. However, in the case of the hybrid mesh, the number of zero eigenvalues is 54. There are 9 non-zero eigenvalues introduced in the hybrid case which are referred to as non-physical modes. The number of these non-physical modes is in agreement with the number of internal nodes on the interface between the tetrahedral and hexahedral meshes, shown in Fig. 5.20(b). The fact that across the interface the triangular elements and rectangular elements are topologically different and the finite element space of 2-D edge elements on the two triangles on a rectangular face does not contain the finite element space of edge elements of the parent rectangular face contributes to these non-physical modes. The occurrence of such troublesome spurious modes guides us to adopt a strategy shown in Fig. 4.14(b), of introducing pyramidal elements to avoid any non-conforming edges for the hybrid 3-D FETD-FDTD method.

5.7 Concluding Remarks

Treatment of hanging variables, recently introduced for triangular and tetrahedral nested meshes, has been extended to rectangular and hexahedral linear finite elements. The Galerkin treatment of the hanging variable retains the symmetry and spectral property of the resulting finite element mass and stiffness matrices. This leads to numerically stable time-stepping schemes within the FETD framework. A numerically stable FDTD subgridding method is achieved by introducing an interface region based on FETD to link the coarse and fine grid regions. The new method retains the same requirement on mesh generation as in the FDTD subgridding method. By using explicit time-stepping

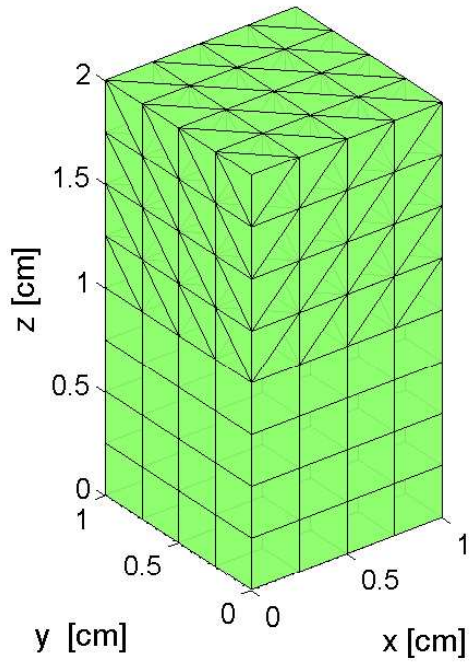

(a) Hybrid Mesh

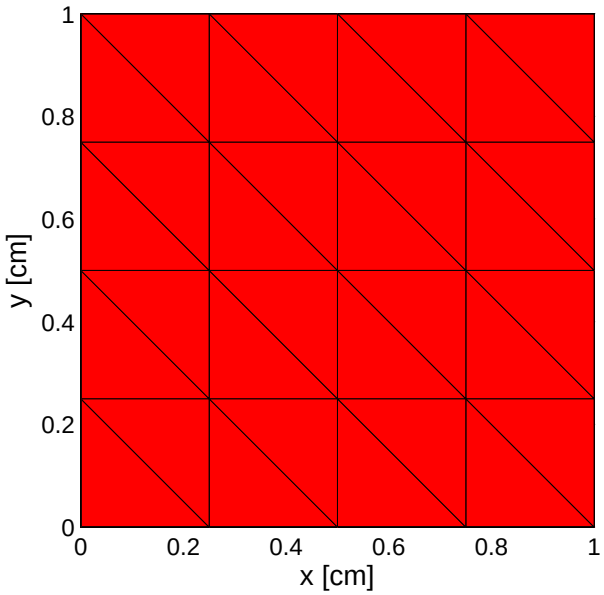

(b) Interface Triangulation

Figure 5.20: Hybrid mesh of rectangular cavity with tetrahedral and hexahedral elements.

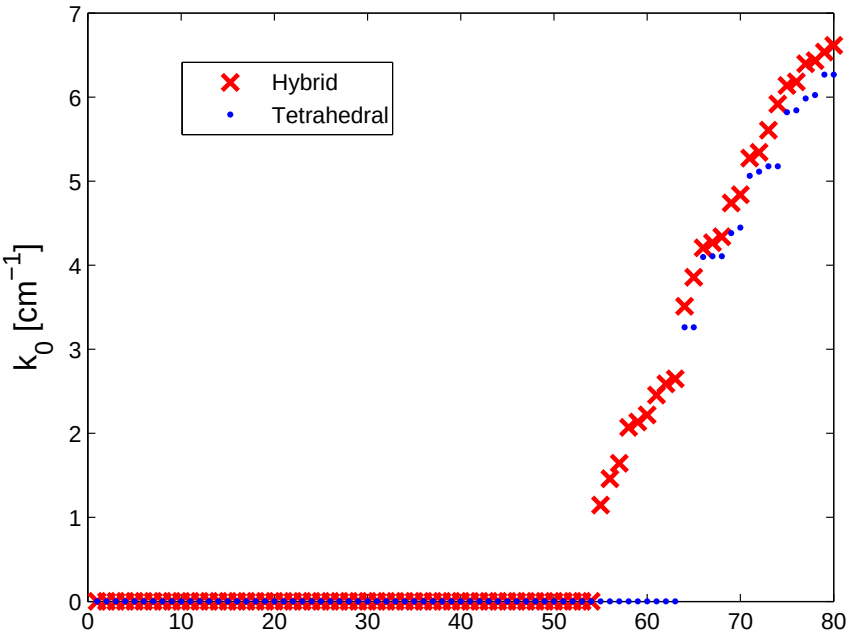

Figure 5.21: Computed resonant wave numbers indicating the appearance of non-physical modes in the hybrid case.

for the unknowns in the interface region, the computational complexity is the same as that of FDTD subgridding method for both 2-D and 3-D. It is also demonstrated that to device a valid intergrid boundary operator across two different elements, the basis functions on the either side of the interface must be able to ensure tangential continuity. Violation of this condition leads to appearance of spurious modes. Thus extending the concept of hanging variables to handle the interface between tetrahedral and hexahedral elements is not viable.

CHAPTER 6

ANTENNA MODELING USING 3-D HYBRID FETD-FDTD METHOD

6.1 Introduction

With requirements on antenna characteristics becoming more complex due to pervasive use of wireless communication devices, numerical modeling of antennas becomes an integral and vital step in antenna design. Efficient numerical techniques for more accurate modeling of complex antennas and their radiation phenomena are desirable, more than before. With increasing number of wireless applications demanding higher data transmission rates, products based on broadband and ultrawideband technologies have become a commonplace. Such technologies need wideband antenna elements for optimal transfer of radio-frequency energy to the wireless channel. Numerical tools based on time domain methods are most efficient for the design and analysis of such broadband and ultrawide band antennas. The hybrid FETD-FDTD method with the ability to model complex geometries accurately using unstructured grids and efficiently model relatively simple homogeneous regions using structured Cartesian grids is well suited for numerical modeling of broadband and ultrawide band antennas.

In this Chapter, the application of stable 3-D hybrid FETD-FDTD method for analysis of antennas in general is presented. A simple hybrid mesh generation strategy, which can be readily applied in the modeling of antennas is presented. The use of hierarchical higher order basis functions defined on tetrahedral elements in the FETD region is presented. Accurate modeling of antenna ports in the FETD method, using transverse

electromagnetic (TEM) mode of excitation and subsequent computation of the modal reflection coefficient and input impedance of antenna is presented. Successful application of the hybrid method in the numerical modeling and computation of reflection coefficient and radiation pattern of different antenna structures are presented. Even though only the radiation problems are considered, the extension of the method for scattering problems could be achieved by implementing the well established Total Field/Scattered Field boundary condition in the FDTD region, as in the case of the 2-D examples discussed in Chapters 2 and 5. The discussion and the results in this Chapter have been communicated for publication [93].

6.2 3-D Hybrid FETD-FDTD Method

The antenna structure is enclosed in the FETD region which is surrounded by the structured FDTD region, similar to the 2-D case discussed in Sec. 2.4. In the 3-D case however, the non-conformal edges are avoided in the transition between tetrahedral and hexahedral elements by introducing pyramidal elements as shown in Sec. 4.6. The resulting hybrid method is conditionally stable as was shown in [18]. The computational grid is truncated in the FDTD region using anisotropic PML. The FETD method with ABC to model unbounded problems is accurate enough only for few simple antenna geometries [94] and PML is necessary for improved accuracy in the solution. In the hybrid method, as the FDTD region encloses the FETD region, the need to model PML in the FETD region is alleviated. However, the success in applying the hybrid method for real-life antenna structures relies on the ability to obtain hybrid mesh with tetrahedral, pyramidal and hexahedral elements.

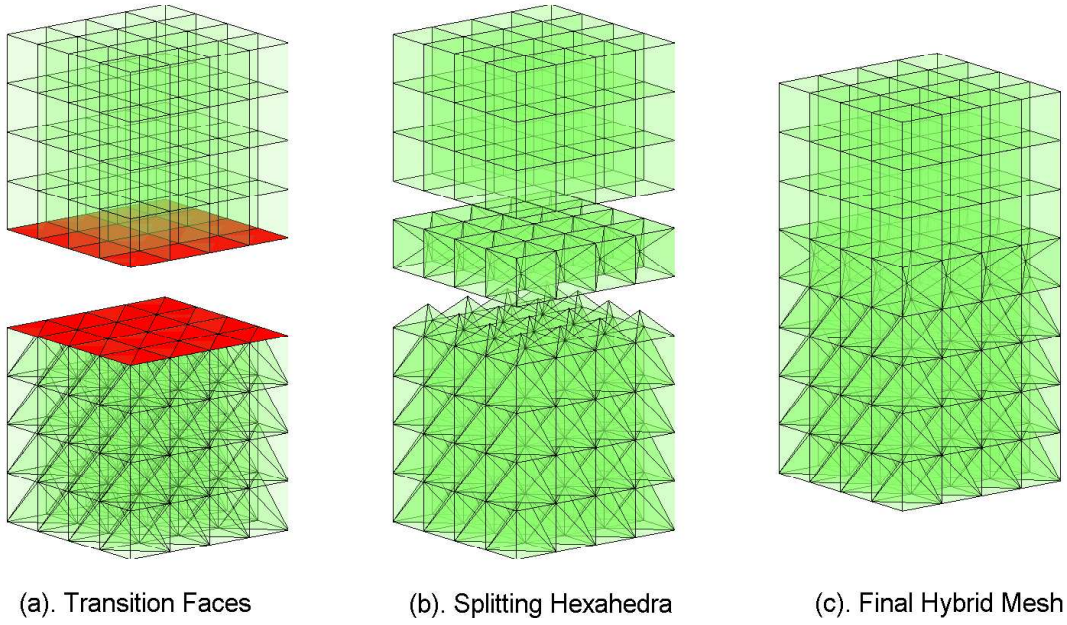

Figure 6.1: Steps involved in hybrid mesh generation.

6.2.1 Hybrid Mesh Generation

The first step in the hybrid mesh generation involves basic unstructured tetrahedral mesh generation of the antenna structure. Outer boundary of the tetrahedral mesh must have a surface triangulation consistent with the FDTD cell size, Δh. Layer of hexahedral elements with edge length Δh is then added around the tetrahedral mesh. In the interface between tetrahedral and hexahedral elements, the only non-conforming edges (tetrahedral) must form the diagonals of the hexahedral faces on the interface. The fact that this requirement is not guaranteed in general by most of the available unstructured mesh generators remains a major hurdle in the application of the hybrid algorithm. Fig. 6.1(a) shows the hexahedral and tetrahedral regions of the mesh, separated to show the rectangular and triangular faces on their interface. The number of nodes on the interface from the tetrahedral mesh and the hexahedral mesh are the same. The number of edges on the tetrahedral interface is greater than the number of edges on the hexahedral interface by the number of rectangular faces on the interface. Once such a mesh is generated, hexahedral elements with a face on the interface is split into two tetrahedra and five pyramidal elements, as shown in Fig. 6.1(b), leading to the final hybrid mesh shown in Fig. 6.1(c).

6.2.2 Pyramidal Edge Elements

Edge vector basis functions have been used extensively on tetrahedral and hexahedral elements. For the 3-D Hybrid FETD-FDTD method, similar basis functions need to be defined for pyramidal elements. Edge vector basis functions on pyramidal elements were designed in [95]. Each basis function is associated with a particular edge of the pyramidal element, similar to edge vector basis functions on tetrahedral elements. Thus, each pyramidal element has eight degrees of freedom, corresponding to the number of edges. With reference to Fig. 6.2, the edge basis functions of a pyramidal element are

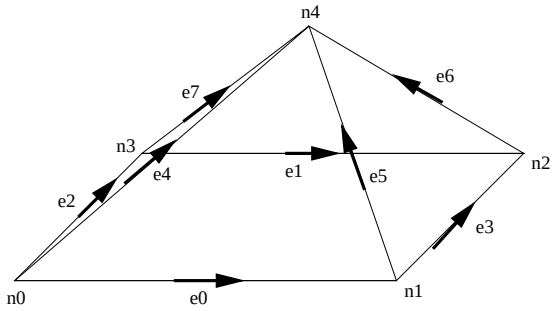

Figure 6.2: Pyramidal element with reference node and edge numbering.

of two types. The first type is the basis functions associated with the four edges on the base of the pyramid i.e., edges $\{e_0, e_1, e_2, e_3\}$ and are given as

$$\vec{W}_{ij} = \xi_i \nabla(\xi_j + \xi_k) - \xi_j \nabla(\xi_i + \xi_l) \tag{6.1}$$

where i, j, k, l are the four nodes forming the base of the pyramid and ξ_i is a scalar function with unity on node i and zero at the other four nodes of the pyramidal element. A plot of these basis functions is shown in Fig. 6.3. It is noted that the form of these basis functions is the same as edge element basis for rectangular elements given in (2.48), indicating that the base of the pyramidal element can be a face of an adjacent hexahedral element. The second type of basis functions are associated with the four oblique edges connecting the base nodes to the apex of the pyramidal element i.e., edges $\{e_4, e_5, e_6, e_7\}$. These basis functions are given as

$$\vec{W}_{ij} = \xi_i \nabla \xi_j - \xi_j \nabla \xi_i \tag{6.2}$$

which is in similar form to the edge element basis functions defined on triangular element in (2.45). Thus, an oblique face of the pyramidal element can be a face of an adjacent tetrahedral element. A plot of these basis functions is shown in Fig. 6.4.

In the transition from tetrahedral to hexahedral elements with edge length Δh, only a particular class of pyramidal elements of height $\Delta h/2$ and a square base of side-length Δh are generated. Once the basis functions for such pyramids are defined, their mass

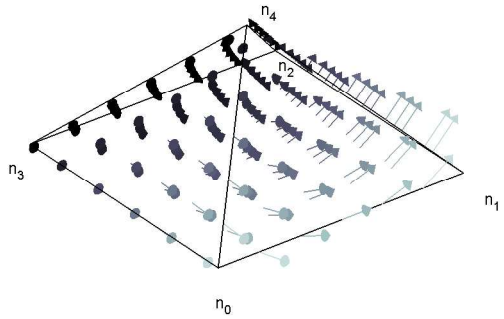

(a) $\vec{W}_{01}$

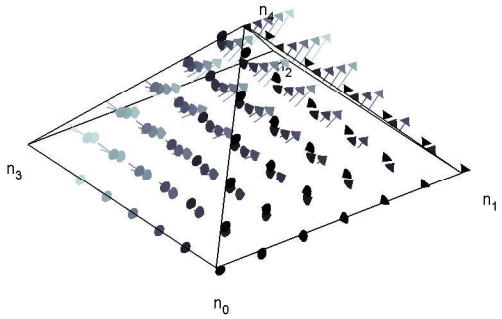

(b) $\vec{W}_{32}$

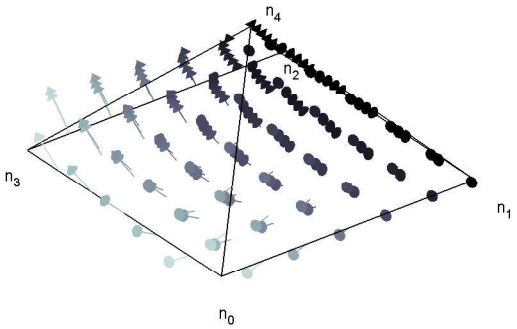

(c) $\vec{W}_{03}$

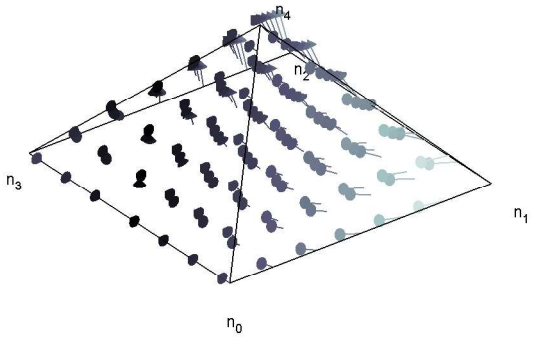

(d) $\vec{W}_{12}$

Figure 6.3: Pyramidal edge element basis functions - Type 1

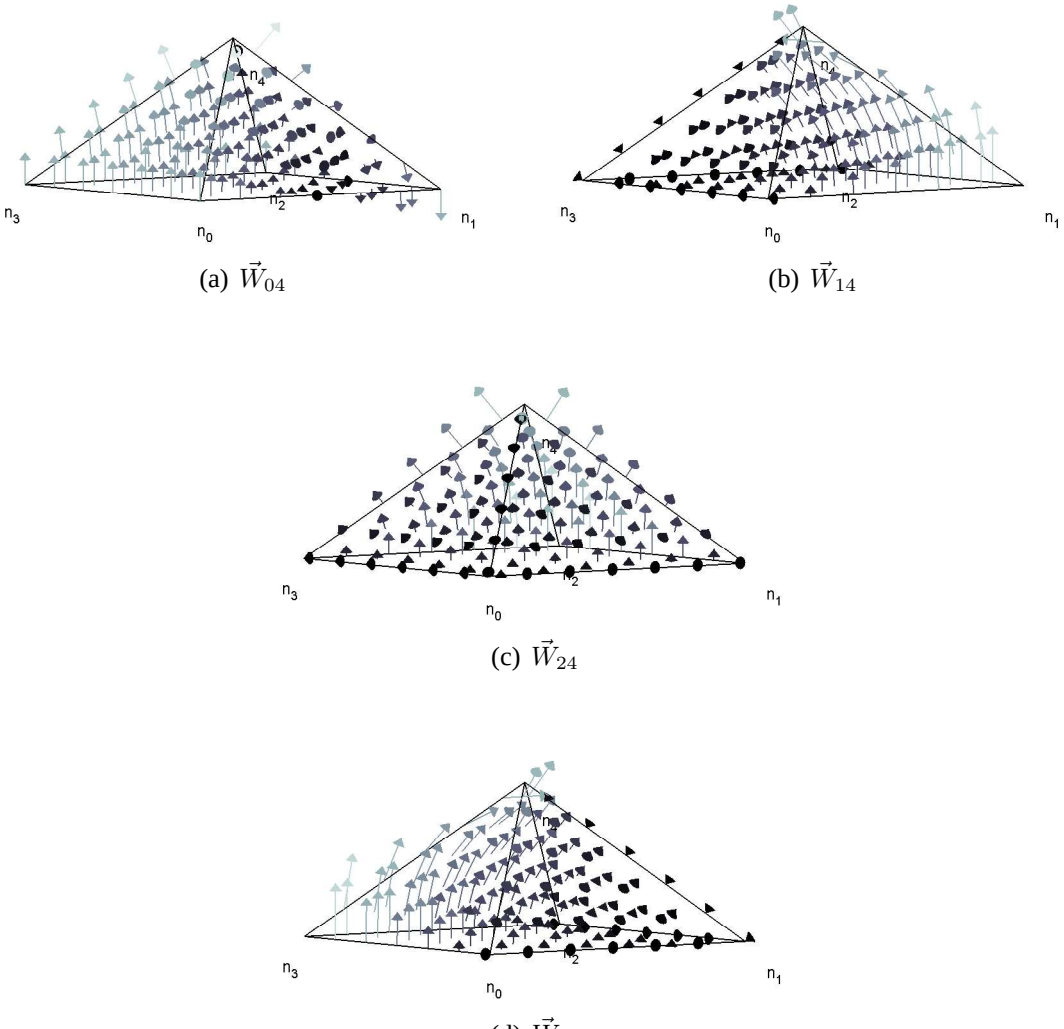

(a) $\vec{W}_{04}$ (b) $\vec{W}_{14}$

(c) $\vec{W}_{24}$

(d) $\vec{W}_{34}$

Figure 6.4: Pyramidal edge element basis functions - Type 2

and stiffness matrices can be evaluated using a symbolic computation tool such as Mathematica, and is obtained as

$$\mathbf{T}^e = \frac{\Delta h}{4320}\begin{pmatrix} 192 & 96 & 12 & -12 & -9 & 9 & 9 & -9 \\ 96 & 192 & -12 & 12 & -9 & 9 & 9 & -9 \\ 12 & -12 & 192 & 96 & -9 & -9 & 9 & 9 \\ -12 & 12 & 96 & 192 & -9 & -9 & 9 & 9 \\ -9 & -9 & -9 & -9 & 308 & 160 & 92 & 160 \\ 9 & 9 & -9 & -9 & 160 & 308 & 160 & 92 \\ 9 & 9 & 9 & 9 & 92 & 160 & 308 & 160 \\ -9 & -9 & 9 & 9 & 160 & 92 & 160 & 308 \end{pmatrix} \tag{6.3}$$

and

$$\mathbf{S}^e = \frac{1}{18\Delta h}\begin{pmatrix} 17 & 7 & -1 & 1 & -16 & 16 & 8 & -8 \\ 7 & 17 & 1 & -1 & -8 & 8 & 16 & -16 \\ -1 & 1 & 17 & 7 & -16 & -8 & 8 & 16 \\ 1 & -1 & 7 & 17 & -8 & -16 & 16 & 8 \\ -16 & -8 & -16 & -8 & 32 & -8 & -16 & -8 \\ 16 & 8 & -8 & -16 & -8 & 32 & -8 & -16 \\ 8 & 16 & 8 & 16 & -16 & -8 & 32 & -8 \\ -8 & -16 & 16 & 8 & -8 & -16 & -8 & 32 \end{pmatrix} \tag{6.4}$$

for a pyramidal element with reference edge numbering as in Fig. 6.2.

In general, there are six possible orientations for the pyramidal elements in the hybrid mesh with each orientation having one of the six faces of an adjacent hexahedral element as the base of the pyramidal element. The mass and stiffness matrices are independent of its orientation and depend only on the edge length of hexahedral element which is the same as the FDTD cell size, Δh. The eigenvalues of the generalized system $\mathbf{S}^e\mathbf{x} - \lambda\mathbf{T}^e\mathbf{x} = 0$ for the pyramidal element are obtained as

$$\left[0, 0, 0, 0, \frac{40}{\Delta h^2}, \frac{1280}{19\Delta h^2}, \frac{1280}{19\Delta h^2}, \frac{112}{\Delta h^2}\right].$$

The number of zero eigenvalues corresponding to the static gradient fields are four, consistent with the number of free nodes. The fundamental property of the $\mathcal{H}(\text{curl}; \Omega)$ basis functions, to include the null space of curl operator, is satisfied by the above edge element basis functions defined on pyramidal elements.

6.2.3 Hierarchical Higher-Order Vector Basis Functions

Higher order vector basis functions provide an advantage of improved resolution of the field solution along with the benefit of having coarser elements in the finite element mesh. Hierarchical higher order vector basis functions [37] provide an added advantage of locally resolving the fields by using basis functions of different orders within a computational domain. The edge element basis functions are the lowest order tangential vector finite elements incomplete to order 1. They are also referred to as having a mixed-order of 0.5 [96]. Edge elements span the space $\mathcal{H}^0(\text{curl}; \Omega)$ where superscript 0 refers to the highest degree of polynomial of the curl of the basis function. The curl of the edge element on a tetrahedron is a constant vector function, the highest degree of the polynomial being zero. The next set of higher-order basis functions with the corresponding curl being piecewise-linear vector functions, excluding the gradient fields [74], are called tangential vector finite elements. They span the space $\mathcal{H}^1(\text{curl}; \Omega)$. Note that the explicit Helmholtz decomposition of the higher order vector basis functions is possible and the higher order gradient basis functions are ignored, reducing the dimensionality of the vector function space and eliminating the occurrence of field solutions with non-zero divergence. With the gradient basis functions eliminated, these basis functions are incomplete to order 2 [37] and also referred to as having a mixed-order of 1.5 [96]. For a tetrahedral element, these basis functions are given in Table. 6.1 where ξ_i is the scalar linear Lagrange interpolation polynomial. It is noted that the facial basis functions in Table. 6.1 are not unique and it is possible and valid to employ them in other forms as proposed in [37, 96]. The choices of basis functions in Table. 6.1 were used in [97]. Tangential Vector basis functions are the same as $p = 2$, the 1st-type Nedelec curl conforming elements [32, 98]. With the higher order basis functions, each edge of the tetrahedron has two basis functions associated with it, one of them being the lower order edge element basis function. Similarly each face of the tetrahedron has two basis functions associated with it. For a given tetrahedron, there are in total 20 basis functions.

Table 6.1: Tangential vector basis functions, their associated topology and dimensions on a tetrahedral element.

Order	**Topology**	**Basis Function**	**Dimension**
0.5	Edge{ij}	$\xi_i \nabla \xi_j - \xi_j \nabla \xi_i$	6
	Edge{ij}	$4\nabla(\xi_i \xi_j)$	6
	Face{ijk}	$4\xi_j(\xi_i \nabla \xi_k - \xi_i \nabla \xi_k)$	4
1.5	Face{ijk}	$4\xi_k(\xi_i \nabla \xi_j - \xi_j \nabla \xi_i)$	4

Each basis function has tangential component only along its associated topology listed in Table. 6.1 and has zero tangential component along other non-associated edges and faces. The evaluation and assembly of mass and stiffness matrices for arbitrary tetrahedral elements can be performed analytically and efficiently by constructing universal matrices following the procedure discussed in [73] or [37].

6.2.4 Hybridization with Hierarchical Higher Order Elements

In the hybrid FETD-FDTD method, it is possible to use hierarchical higher order basis functions throughout the FETD mesh, on all hexahedral, pyramidal and tetrahedral elements. However, the FDTD region surrounding the unstructured FETD region has the lower order edge elements, demanding a typical FDTD grid size of $\lambda_{min}/20$. Due to the conformal nature of the FDTD grid and FETD mesh, the hexahedral and pyramidal elements adjacent to the FDTD region have the same size as the FDTD grid size. Often, for lower order, edge element basis functions, the grids size should be around $\lambda_{min}/20$ and it is inefficient and unnecessary to have higher order basis functions on such elements. Due to this fact, the use of higher order basis functions is restricted to tetrahedral elements alone. The hierarchical nature of the basis functions, enables the use of higher

order bases on the tetrahedral elements while lower order edge elements are used in the pyramidal and hexahedral elements. It is noted that the tetrahedral elements adjacent to the pyramidal elements share a common face and three common edges. No degree of freedom is assigned to the faces shared by pyramidal and tetrahedral elements. Similarly no degree of freedom corresponding to the higher order basis functions associated with edge is assigned to the edges shared by pyramidal and tetrahedral elements. In the corner regions of the FETD mesh, hexahedral elements sharing a common edge with tetrahedral elements are present. For such edges again, higher order unknowns are not assigned. This way, vector basis functions of different orders can be used within one finite element mesh. In Fig. 6.5, the basis functions associated with a tetrahedral element sharing a face with a pyramidal element and an edge with a hexahedral element are shown. There are six facial basis functions associated with the three faces not shared by the adjacent pyramidal element and six higher order edge basis functions associated with the three edges not shared by the adjacent pyramidal and hexahedral elements. There are three edge element basis functions associated with the three edges shared by the adjacent pyramidal elements. In total, the degrees of freedom for this tetrahedron is 15 with the other five higher order degrees of freedom un-assigned due to the interface with pyramidal and hexahedral elements.

6.3 TEM Port Modeling

In the hybrid mesh, the antenna structure requiring accurate modeling is located in the finite element region. Hence, the FETD formulation must include the excitation of antennas using ports. The boundary condition for ports and the subsequent implementation in the FETD method, presented in this section, can be used to model the excitation of antenna structures fed by coaxial line or stripline ports. Such feeding structures are

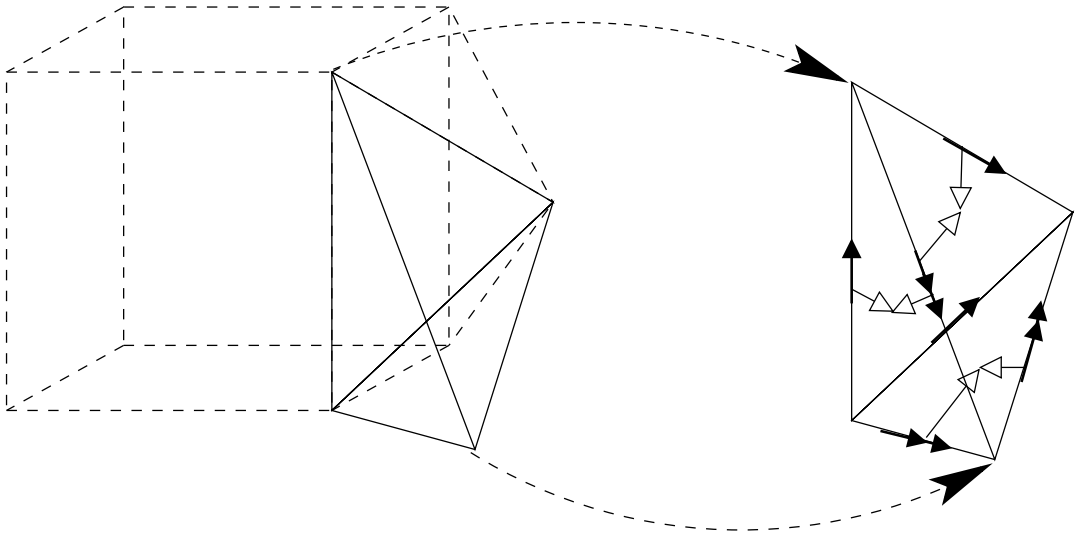

Figure 6.5: Illustration of basis functions on a tetrahedral element adjacent to a pyramidal and hexahedral element

typically used for antennas operating with the TEM mode of excitation. In the time-harmonic case, the total electric fields inside a transmission line exciting a TEM wave in the $+z$ direction is given by

$$\begin{aligned}\vec{E} &= \vec{E}^{inc} + \vec{E}^{ref} \\ &= E_o \vec{e}_{TEM} e^{-j\beta z} + \Gamma E_o \vec{e}_{TEM} e^{j\beta z}\end{aligned} \tag{6.5}$$

where $\vec{e}_{TEM}$ is the modal field distribution, E_o is the incident modal amplitude, Γ is the reflection coefficient of TEM mode and β is the propagation constant of the TEM mode inside the transmission line. For dielectric filled coaxial lines and striplines,

$$\beta = \sqrt{\varepsilon_r} k_0 = \sqrt{\varepsilon_r}\omega/c \tag{6.6}$$

where ε_r is the dielectric constant of the medium. From (6.5),

$$\hat{n} \times \nabla \times \vec{E} = j\beta\gamma_t(\vec{E}) - 2j\beta\gamma_t(\vec{E}^{inc}) \tag{6.7}$$

where $\hat{n} = -\hat{z}$ is the outward normal unit vector and $\gamma_t(\vec{u}) = \hat{n} \times \vec{u} \times \hat{n}$ is the tangential trace of $\vec{u}$. From (6.7), the time-dependent boundary condition for the electric field in a

port (filled with non-magnetic material) excited by TEM mode is obtained as

$$\hat{n} \times \nabla \times \vec{E}(t) = \frac{\sqrt{\varepsilon_r}}{c} \frac{\partial}{\partial t} \gamma_t \left(\vec{E}(t) \right) - \frac{2\sqrt{\varepsilon_r}}{c} \frac{\partial}{\partial t} \gamma_t \left(\vec{E}^{inc}(t) \right) \tag{6.8}$$

Due to the simple dispersion relationship between the propagation constant and the wavenumber for the TEM mode, it is straightforward to arrive at the time-domain equivalent of (6.7). For the case of higher order modes (TE and TM modes), it is possible to arrive at the time domain equivalent modal boundary condition [99], leading to temporal convolution operations involving the field solution. Time integration schemes then involve discretization of both derivative operators and the convolution integral operators. However, when modeling antennas designed with TEM mode of excitation, higher order modes (which are evanescent) can be neglected at the port boundary. However, the modeled transmission line should be sufficiently long for the evanescent higher order modes to attenuate significantly [31].

The initial value problem in the FETD region is then, the time-dependent vector Helmholtz's equation

$$\nabla \times \mu_r^{-1} \nabla \times \vec{E}(t) + \frac{\varepsilon_r}{c^2} \frac{\partial^2}{\partial t^2} \vec{E}(t) = 0, \quad \text{in}\, \Omega \tag{6.9}$$

with the boundary condition (6.8) on the port surface and the initial conditions $\vec{E}(0) = 0$ and $\frac{\partial}{\partial t} \vec{E}(t)|_{t=0} = 0$. Following the same procedure as in Sec. 2.3.6, we test (6.9) with suitable testing function resulting in the following weak form viz.,

seek $\vec{E}(t)$ such that

$$\begin{aligned} \int_\Omega \left[\nabla \times \vec{v}(t) \cdot \mu_r^{-1} \nabla \times \vec{E}(t) + \frac{\varepsilon_r}{c^2} \vec{v}(t) \cdot \frac{d^2}{dt^2} \vec{E}(t) \right] d\Omega \\ + \int_{\Gamma_p} \vec{v}(t) \cdot (\hat{n} \times \nabla \times \vec{E}(t)) ds = 0, \end{aligned} \tag{6.10}$$

$$\forall \vec{v}(t) \in \mathcal{H}(\text{curl}; \Omega).$$

Using (6.8) in (6.10) with $\vec{E}^{inc}(t) = E_o(t) \vec{e}_{TEM}$ and expanding the solution $\vec{E}(t)$ using vector basis functions defined over tetrahedral, pyramidal and hexahedral elements as

$\vec{E}(t) = \sum_{i=1}^{N} e_i(t)\vec{W}_i$ leads to the following system of ordinary differential equation viz.,

$$\mathbf{Se} + \frac{1}{c}\mathbf{R}\frac{d}{dt}\mathbf{e} + \frac{1}{c^2}\mathbf{T}\frac{d^2}{dt^2}\mathbf{e} = \frac{1}{c}\mathbf{f}\frac{d}{dt}E_o(t) \tag{6.11}$$

where

$$\mathbf{R}(i,j) = \int_{\Gamma_p} (\hat{n} \times \vec{W}_i) \cdot \sqrt{\varepsilon_r}(\hat{n} \times \vec{W}_j)\ ds$$
$$\mathbf{f}(i) = 2\int_{\Gamma_p} (\hat{n} \times \vec{W}_i) \cdot \sqrt{\varepsilon_r}(\hat{n} \times \vec{e}_{TEM})\ ds.$$

$E_o(t)$ is the excitation waveform with significant spectral contents in the frequency band of interest. In fact, $E_o(t)$ is the time domain modal amplitude of the TEM mode being excited at the port. The modal distribution $\vec{e}_{TEM}$ is obtained by a 2-D finite element eigenvalue solver. The eigenvector solution for the dominant mode gives the modal distribution of TEM mode and this eigenvector corresponds to a physical DC mode belonging to group 2 discussed in Sec. 3.2.1. It is noted that at least two non-touching conductors are needed for the TEM mode to exist. By applying a transformation of variables discussed in the classical paper [100], the 2-D eigenvalue problem is posed such that eigen-pairs are the propagation constant and the corresponding modal distribution, at a particular specified frequency. Alternatively, 2-D eigenvalue solver based on the A-V formulation with constrained Lanczos algorithm to suppress the spurious DC modes (proposed in [101]) can be employed. The operating frequency in the 2-D eigenvalue problem is chosen as the center frequency in the band of interest under the assumption that the modal distribution of the TEM mode remains unchanged within the band. This assumption is true for coaxial lines and stripline feed structures [102]. With the need for computing the TEM modal distribution alone, the eigenvalue solver need not model the longitudinal component of the electric field which, in the general case of inhomogeneous ports, is expanded using nodal finite elements [100]. For ports with homogeneous medium, only the transverse electric field needs to be expanded using

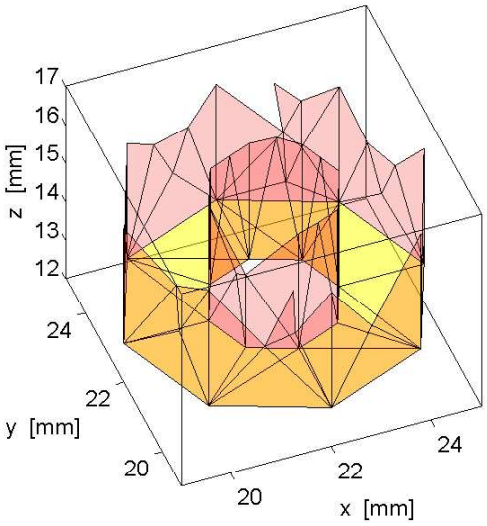

(a) 3-D Port Triangulation

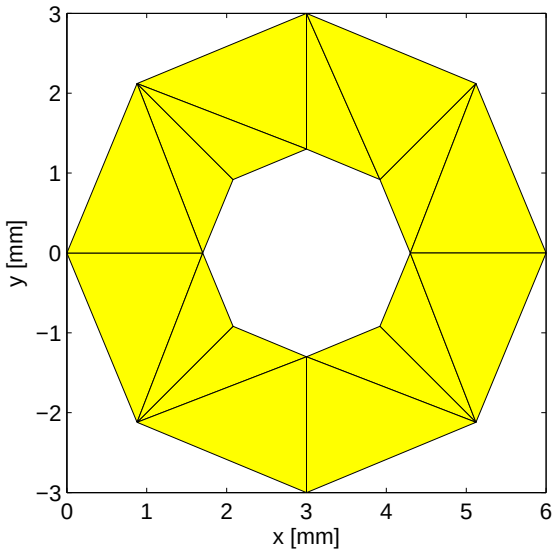

(b) 2-D Port Mesh

Figure 6.6: Illustration of the use of triangulation of the port from the 3-D finite element mesh for the 2-D mesh.

vector basis functions since only the transverse modes exist in this case. The triangulation of the port surface in the 3-D tetrahedral mesh is used as the finite element mesh for the 2-D eigenvalue problem. As an illustrative example, the coaxial line port shown in Fig. 6.6(a) is considered to be embedded in the unstructured 3-D finite element mesh. To obtain the modal field distribution, the corresponding 2-D triangulation of the port as shown in Fig. 6.6(b) is used. Similar to the 3-D case, the electric field can be expanded using either 2-D edge elements or higher order elements, consistent with the order of basis used in the 3-D case. In the case of $\mathcal{H}^1(\text{curl};\Omega)$ elements, the number of basis functions associated with a triangular element is 8 where 2 basis functions are associated with each of the three edges and 2 basis functions associated with the triangular face. The modal field distribution is obtained as

$$\vec{e}_{TEM} = \sum_{j=1}^{N_p} e_{TEM,j}\vec{W}_j \tag{6.12}$$

where vector $\mathbf{e}_{TEM}$ is the eigenvector solution of the TEM mode and N_p is number of unknowns for the 2-D eigenvalue problem. N_p is equal to the number of edges on the port triangulation if edge elements are used. If $\mathcal{H}^1(\text{curl};\Omega)$ elements are used, N_p is twice the number of edges and triangular faces in the port triangulation. The TEM modal field distribution for the case of a coaxial line, obtained numerically, is shown in Fig. 6.7. Indeed the numerical solution has a radial electric field as it is the case for the TEM mode in a coaxial line. Moreover, the variation of the intensity of the field along the radial distance is in accordance with the analytical solution which dictates the field solution to be inversely proportional to the radial distance.

The temporal discretization of (6.11) is performed using the Newmark-beta method as discussed in [10]. It is observed that $\mathbf{R}$ is similar to the case for the 1st order ABC discussed in Sec. 2.3.6. The boundary condition at the port given in (6.8) is the same as the 1st order ABC and boundary condition is exact in the current case of TEM mode with the wave propagation normal to the port boundary.

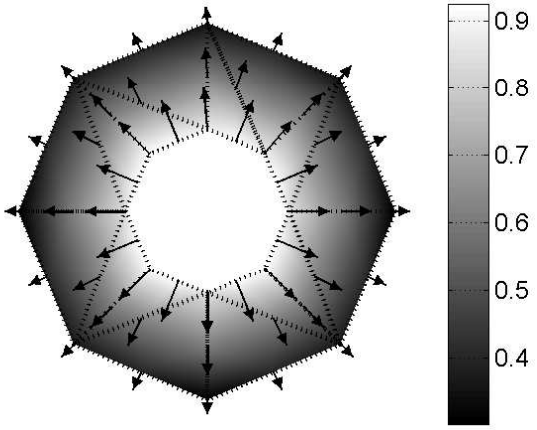

Figure 6.7: TEM modal distribution of the electric field in a coaxial line obtained from the 2-D eigenvalue solution

Using the orthogonality property of the modes, the reflection coefficient in (6.5) can be obtained as

$$\Gamma(\omega) = \frac{1}{\mathcal{F}\left(E_o(t)\right)} \mathcal{F}\left(\frac{1}{A_m}\int_{\Gamma_p} \vec{E}(t)\cdot\vec{e}_{TEM}\, ds\right) - 1 \tag{6.13}$$

where $\mathcal{F}\left(u(t)\right)$ is the Fourier transform of $u(t)$ and A_m is a constant given as

$$A_m = \int_{\Gamma_p} \vec{e}_{TEM}\cdot\vec{e}_{TEM}\, ds.$$

From the reflection coefficient, the frequency dependent input impedance of the antenna structure, at the port terminal is computed as

$$Z_{in}(\omega) = Z_c \frac{1+\Gamma(\omega)}{1-\Gamma(\omega)} \tag{6.14}$$

where Z_c is the characteristic impedance of the port which can be obtained from the eigenvector solution. Note that Z_c is different from the wave impedance Z_0, which for the TEM mode is simply $\sqrt{\frac{\mu_0}{\varepsilon_r\varepsilon_0}}$. From the eigenvector solution the characteristic

impedance is computed as

$$Z_c = \frac{|V_p|^2}{\int_{\Gamma_p} \vec{e}_{TEM} \times \vec{h}_{TEM} \cdot d\vec{s}} \tag{6.15}$$

where the magnetic field distribution on the port, $\vec{h}_{TEM} = \frac{1}{Z_0}\hat{n} \times \vec{e}_{TEM}$, and the voltage across the port terminals, V_p, is obtained as

$$V_p = \int_{l_p} \vec{e}_{TEM} \cdot d\vec{l}, \tag{6.16}$$

where l_p is any line connecting the inner and outer conductors of the port. For a coaxial line the characteristic impedance can be evaluated analytically as

$$Z_c = \frac{Z_0}{2\pi} \ln\left(\frac{b}{a}\right)$$

where a is the radius of the inner conductor and b is the radius of the outer conductor. For the port shown in Fig. 6.6(b) with $a = 0.95$ mm and $b = 3.28$ mm and the medium between the conductors having a dielectric constant, $\varepsilon_r = 2.2$, the analytical characteristic impedance is computed to be 50.13 Ω. The numerical solution for Z_c obtained using (6.15) on the modal solution of the mesh in Fig. 6.6(b) is computed to be 49.89 Ω having an acceptable degree of error with the analytical solution.

6.4 Numerical Examples

The 3-D hybrid FETD-FDTD code was implemented in C++ using object-oriented programming features. The FETD update matrices are stored in compressed column storage format for sparse matrices. For efficient implicit update of the FETD unknowns, PCG solver is used with incomplete Cholesky factorization as the preconditioner. To reduce the number of non-zero entries in the Cholesky factor, matrix reordering is applied [44]. In all the examples to be presented, anisotropic PML is used in the FDTD region. The maximum edge length in the finite element region is $1.5\Delta h$. All the simulations are carried out in 2.2 GHz, 64 bit Dual CPU Opteron Machine with an available RAM of

32 GB.

6.4.1 Coax-fed Square Patch Antenna

The first example is the modeling of a coaxial line fed square patch antenna. This antenna is the unit radiating element in a JINA 2004 Test Case [103]. The 16.2 mm$\times$16.2 mm square patch is embedded in a 19.6 mm$\times$19.6 mm substrate with $\varepsilon_r = 2.2$ and thickness 2.34 mm, as shown in Fig. 6.8(a). The square patch element is embedded inside the substrate at a depth of 0.76 mm from the top. The element is inserted in a perfectly conducting cavity and is fed by a coaxial line feed offset by 3.9 mm along the $y-$ axis from the center of the patch. The diameters of the inner and outer conductors are 1.9 mm and 6.56 mm, respectively. The region between the two conductors is filled with dielectric material of $\varepsilon_r = 2.2$. Δh is set as 1 mm and the cross section of the hybrid mesh is shown in Fig. 6.8(b). The finite element region has a 109,720 tetrahedra, 4,672 hexahedra and 17,280 pyramidal elements with a total of 162,913 degrees of freedom. This corresponds to the non-PEC edges in the finite element region, as only edge elements are used in this example. The characteristic impedance of the coaxial port structure was computed to be 48.17 Ω. Reflection coefficient obtained using the hybrid code is shown in Fig. 6.9, where excellent agreement is observed with results from Ansoft HFSS®, a commercial frequency domain finite element method based full-wave electromagnetic solver. The reflection coefficient shows a minimum at 5.2 GHz. Using NFFF transformation technique in the FDTD region, the far-zone electric field is computed as in (2.30). The antenna directivity pattern is then computed as

$$D_\theta(\omega,\theta,\phi) = \frac{2\pi}{\eta}\frac{|E_\theta(\omega,\theta,\phi)|^2}{P_{rad}(\omega)} \tag{6.17a}$$

$$D_\phi(\omega,\theta,\phi) = \frac{2\pi}{\eta}\frac{|E_\phi(\omega,\theta,\phi)|^2}{P_{rad}(\omega)} \tag{6.17b}$$

$$D(\omega,\theta,\phi) = D_\theta(\omega,\theta,\phi) + D_\phi(\omega,\theta,\phi) \tag{6.17c}$$

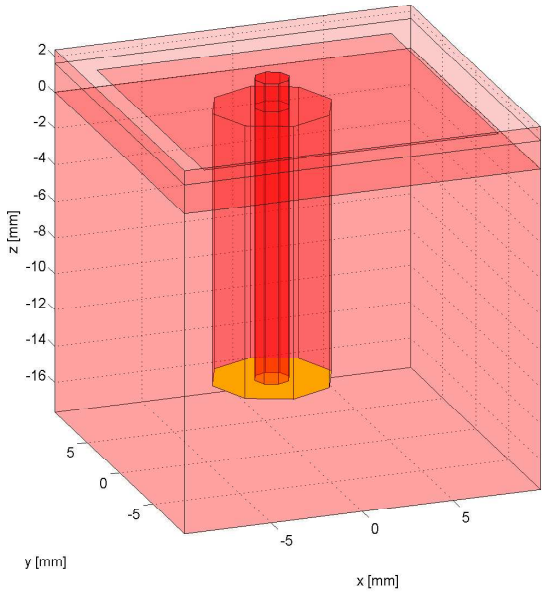

(a) Geometry

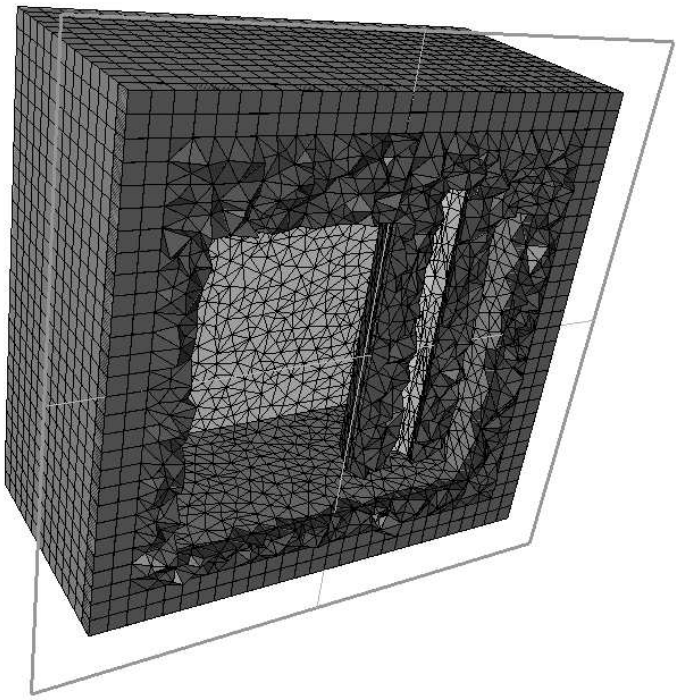

(b) Hybrid Mesh

Figure 6.8: Modeling of coaxial line fed square patch antenna.

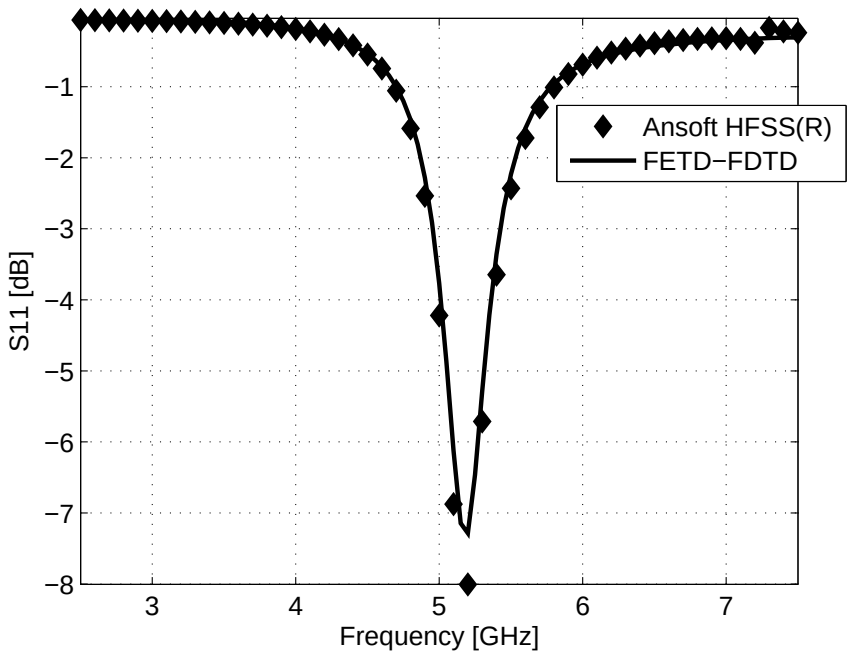

Figure 6.9: Reflection coefficient of patch antenna indicating the resonant frequency

where $\eta = 377\,\Omega$ is the intrinsic impedance of free space. $P_{rad}(\omega)$ is the total radiated power computed as

$$P_{rad}(\omega) = \frac{1}{2\eta}\int_0^{2\pi}\int_0^{\pi}\left[\,|E_\theta(\omega,\theta,\phi)|^2 + |E_\phi(\omega,\theta,\phi)|^2\,\right]\,\sin\theta\,d\theta\,d\phi$$

$$\approx \frac{\Delta\theta\Delta\phi}{2\eta}\sum_{i=0}^{N_\theta}\sum_{j=0}^{N_\phi}\left[\,|E_\theta(\omega,i\Delta\theta,j\Delta\phi)|^2 + |E_\phi(\omega,i\Delta\theta,j\Delta\phi)|^2\,\right]\,\sin i\Delta\theta. \tag{6.18}$$

Note that the accuracy of the computation of $P_{rad}(\omega)$ in the discrete case depends on the angular resolution $\Delta\theta$ and $\Delta\phi$ of the far-field observation points. The pattern results for all the examples are shown in this Chapter, where $\Delta\theta = 1^\circ$ with $N_\phi = 180$ and $\Delta\phi = 5^\circ$ with $N_\phi = 72$. The frequency domain NFFF transformation is used as it is more efficient when the number of far-field observation points are high, as in this case.

The directivity pattern in the principal planes at 5.2 GHz for the square patch antenna is shown in Figs. 6.10(a) and (b) where broad beam-widths in both the planes, the

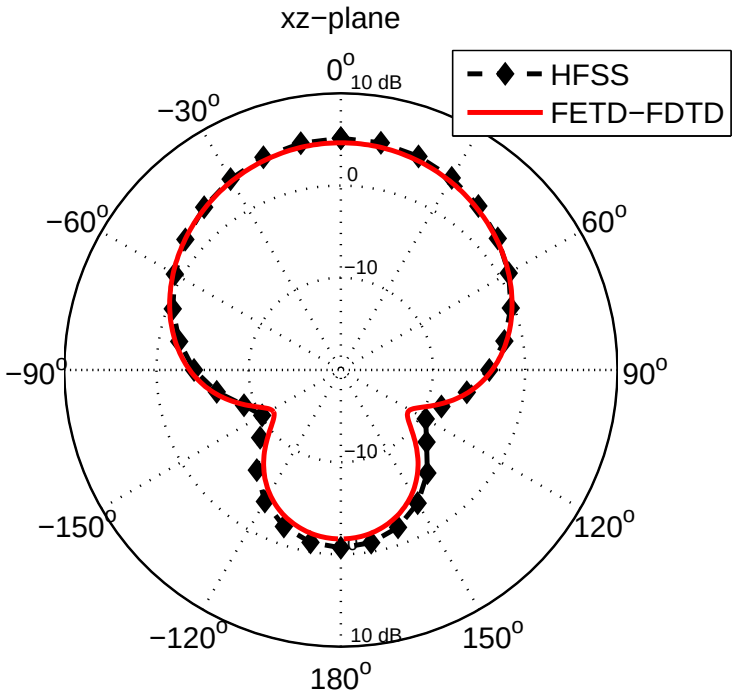

(a) H-plane pattern

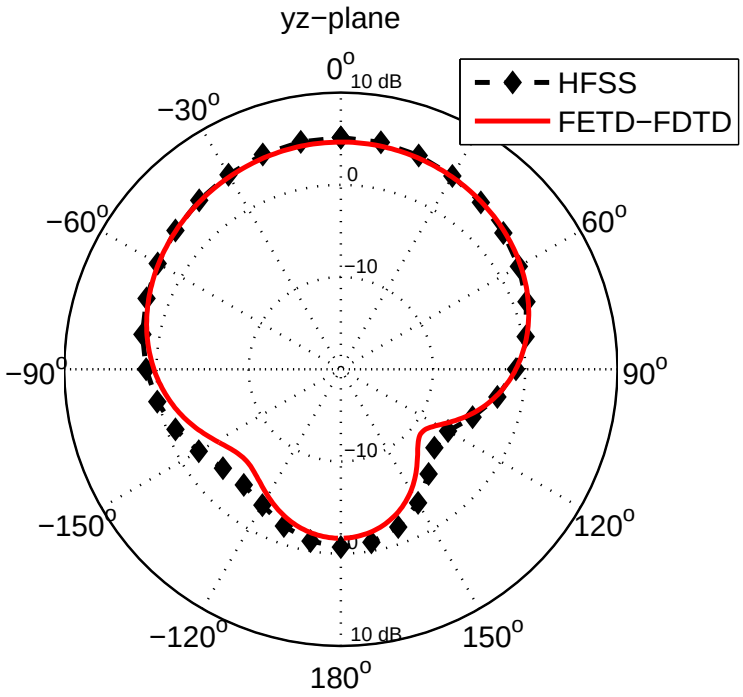

(b) E-plane pattern

Figure 6.10: Directivity pattern results for the modeling of coaxial line fed square patch antenna.

typical characteristic of patch antennas, are observed. The patterns are in a good agreement with HFSS results also shown in Fig. 6.10. With the offset in the feed along the $y-$ axis, the $E-$plane of the patch is the $yz-$ plane and the $H-$plane is the $xz-$plane. Note that the $E-$plane pattern has a broader beam-width than the $H-$plane pattern. While the $H-$plane pattern is symmetric about $\theta = 0°$, the $E-$plane pattern is asymmetric due to the offset in the coaxial feed along the $y-$axis. The computed maximum directivity, D_0, at 5.2 GHz is 4.64 dB.

6.4.2 Stripline-fed Vivaldi Antenna

Vivaldi antennas typically exhibit wide bandwidth characteristics, and with proper design, can potentially be used for UWB applications. The vivaldi antenna considered in this example is a stripline-fed tri-plate structure as shown in Fig. 6.11(a). Vivaldi patterns are etched out in the ground planes of the tri-plate structure. The substrate has a dielectric constant of $\varepsilon_r = 2.2$ and is assumed to be lossless. The thickness of the substrate is 1.5 mm and the feed is embedded in the middle of the substrate i.e., at a depth of 0.75 mm. The width of the stripline is 1 mm. The curvature of the vivaldi taper is defined as an exponential function of the form $y = c_1 e^{Rz} + c_2$ where

$$c_1 = \frac{y_2 - y_1}{e^{Rz_2} - e^{Rz_1}}$$
$$c_2 = \frac{y_1 e^{Rz_2} - y_2 e^{Rz_1}}{e^{Rz_2} - e^{Rz_1}}$$

and $R = 0.2$ are constants describing the profile of the tapering between the points P_1 and P_2 shown in Fig. 6.11(a).

The steps involved in the modeling of this antenna using the hybrid FETD-FDTD code is illustrated in Fig. 6.11. The first step is to generate the 3-D solid model of the antenna structure with clearly defined boundary conditions as shown in Fig. 6.11(b). The second step shown in Fig. 6.11(c) is to specify the boundary of the finite element region as a set of rectangular faces with edge length equal to the chosen FDTD cell size.

The finite element boundary encloses the antenna structure. To reduce the number of implicit unknowns and hence decrease the CPU time for the solution, it is necessary for the finite element boundary to closely enclose the radiating structure. The third step, shown in Fig. 6.11(d) is the tetrahedral mesh generation of the finite element region. Either a Delaunay tessellation or an advancing front algorithm can be utilized. However, it is to be taken care that on the boundary of the finite element region specified in step 2, no new nodes are inserted. This condition is not necessarily satisfied by a general Delaunay tessellation based mesh generator where as mesh generators based on advancing front algorithm can guarantee a mesh which respects the requirement on the finite element boundary. The final step in the mesh generation for the hybrid method, shown in Fig. 6.11(e), is to enclose the tetrahedral mesh with hexahedral, pyramidal and tetrahedral elements as discussed in Sec. 6.2.1. In the implementation, steps 2, 3 and 4 can be automated.

The FDTD cell size is 1 mm and maximum edge length allowable in the finite element mesh is set as 1.5 mm. The resulting finite element mesh has 73,962 tetrahedral elements, 4,844 hexahedral elements and 17,850 pyramidal elements. The total number of unknowns in the finite element region with mixed order basis functions is 450822. The FDTD domain size is $22\times43\times52$ cells enclosed by a 8 cell thick PML. While the matrix factorization takes 20 mins, the wall time for hybrid time stepping for 4000 time steps is 2hrs. The results of the reflection coefficient obtained in the band of 2 GHz-7 GHz, using the hybrid FETD-FDTD code and HFSS are shown in Fig. 6.12, where a good agreement between the two results are observed. The vivaldi antenna modeled in this example is an unoptimized test case and hence the impedance bandwidth is not appreciable.

The directivity pattern of the antenna for each polarization viz., D_θ and D_ϕ in the two principle planes at discrete frequencies of 2 GHz, 3 GHz, 5 GHz and 7 GHz are

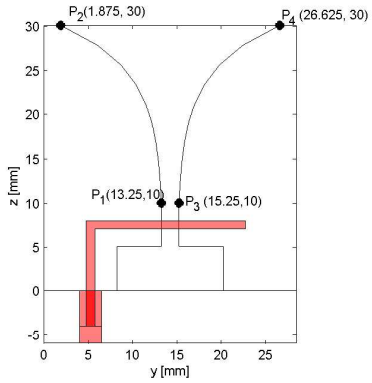

(a) Model

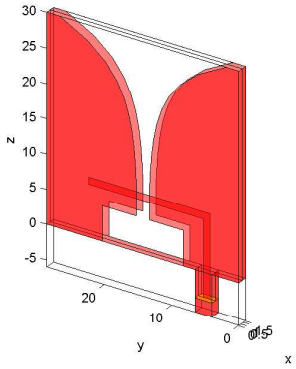

(b) Step 1

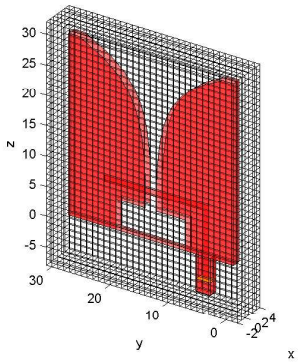

(c) Step 2

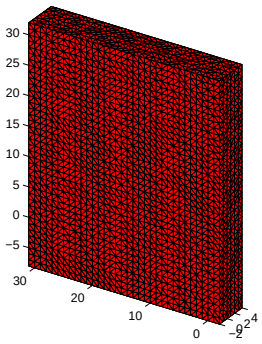

(d) Step 3

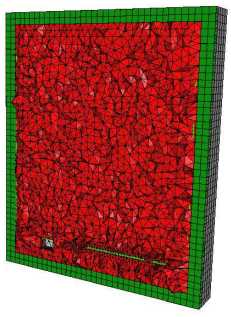

(e) Step 4

Figure 6.11: Step involved in the modeling of stripline fed Vivaldi antenna using the FETD-FDTD code.

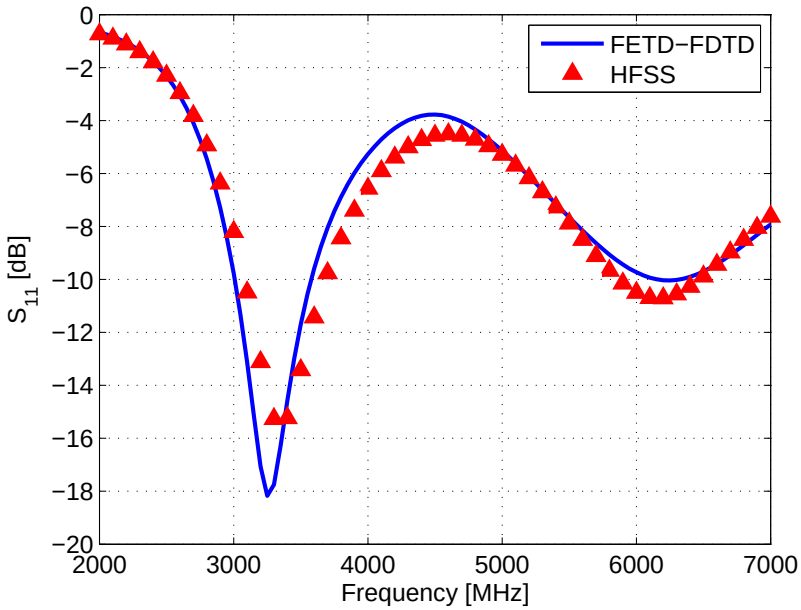

Figure 6.12: Comparison of reflection coefficient of stripline fed Vivaldi antenna.

shown in Fig. 6.13, Fig. 6.14, Fig. 6.15 and Fig. 6.16, respectively. A frequency domain NFFF transformation is applied in the FDTD region to obtain the far-field solution based on which the directivity is computed. At all frequencies, good agreements with HFSS results are observed. Since the tapered slot has wider aperture in the yz-plane, the beam-width in the yz-plane is narrower than the beam-width in the xz-plane. This fact is in agreement with the numerical results at all frequencies. At center of the aperture the electric field has a strong E_y component and hence the $E-$plane is the yz-plane. The xz-plane is the $H-$ plane. The cross-polar pattern in the $H-$plane is relatively stronger than the cross-polar pattern in the $E-$plane at all frequencies. This result is in agreement with the results for a similar vivaldi antenna configuration, obtained using analytical technique in [104]. It is also observed from the results that the asymmetry in the antenna geometry along the $E-$plane due to the stripline feed structure does not have significant impact on the symmetry of the pattern in that plane.

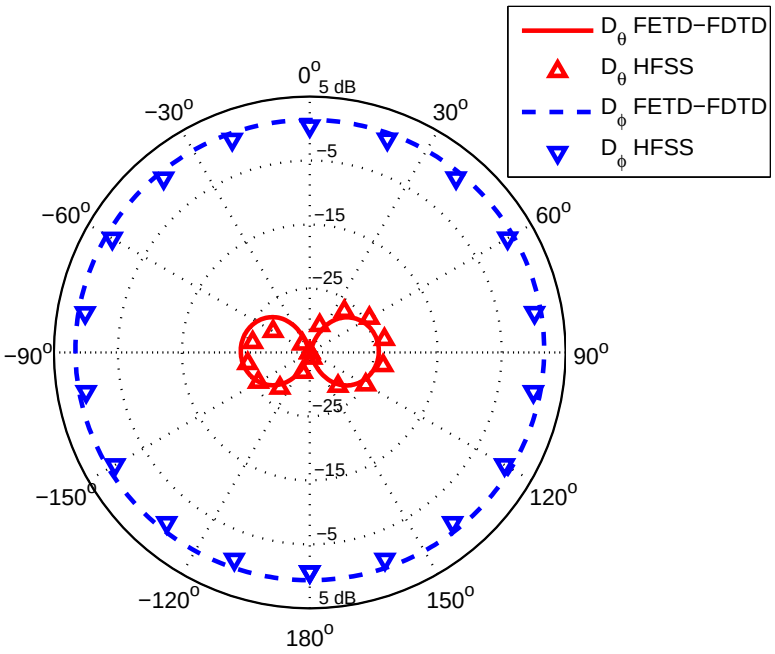

(a) xz-plane pattern

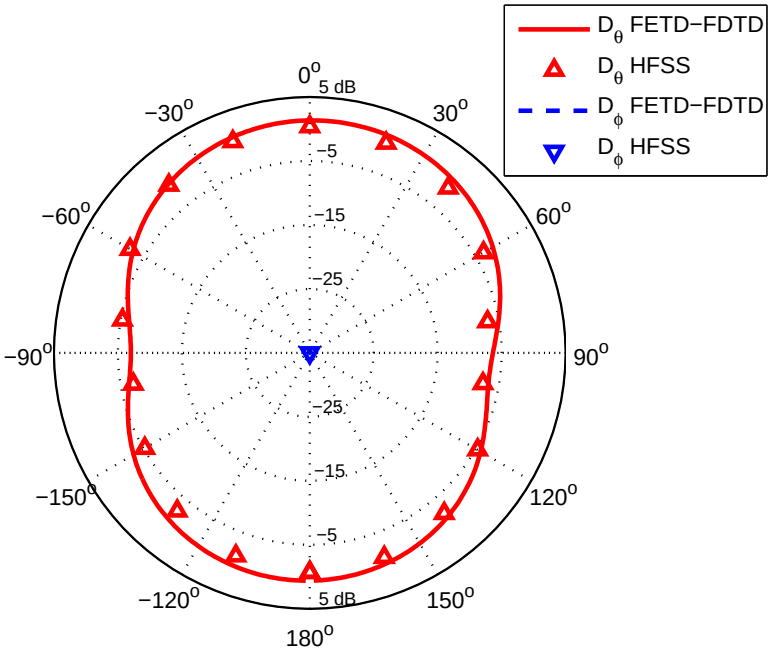

(b) yz-plane pattern

Figure 6.13: Results of directivity pattern at 2 GHz for the stripline fed Vivaldi antenna.

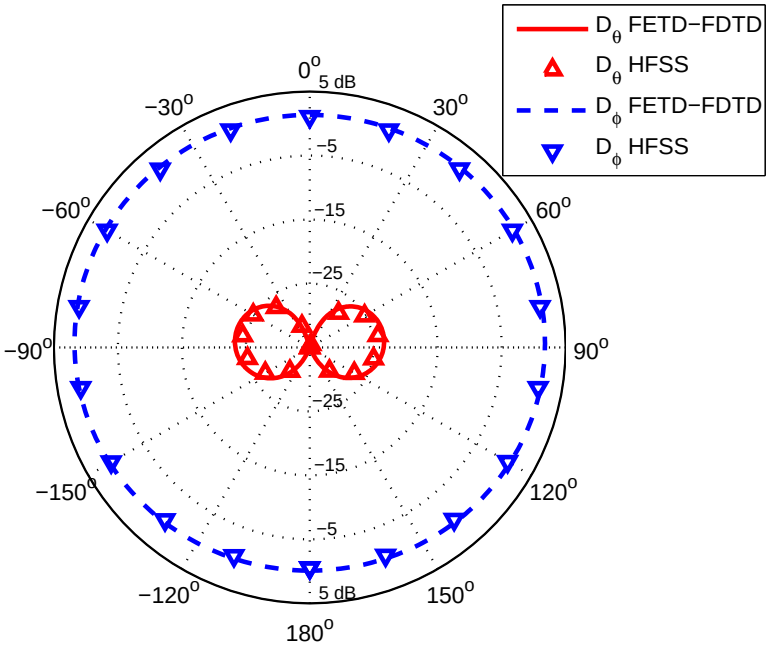

(a) xz-plane pattern

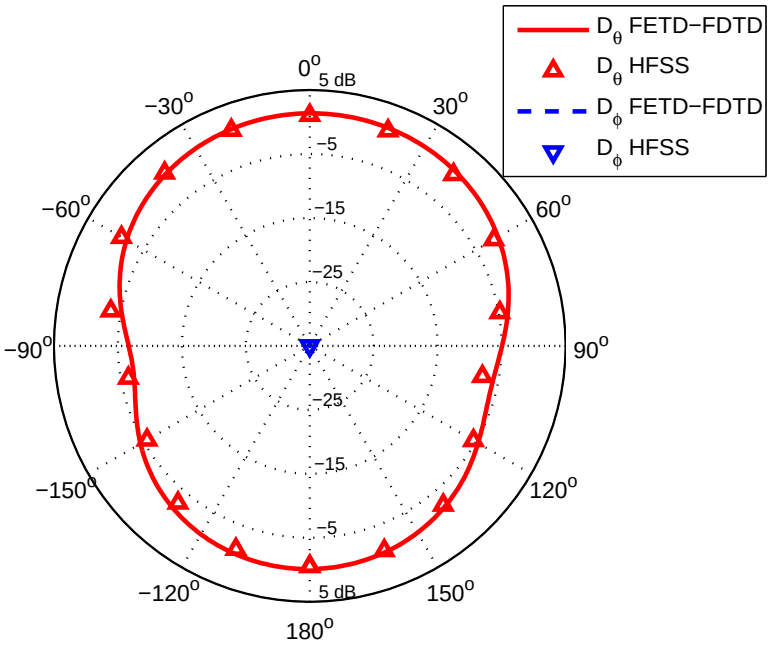

(b) yz-plane pattern

Figure 6.14: Results of directivity pattern at 3 GHz for the stripline fed Vivaldi antenna.

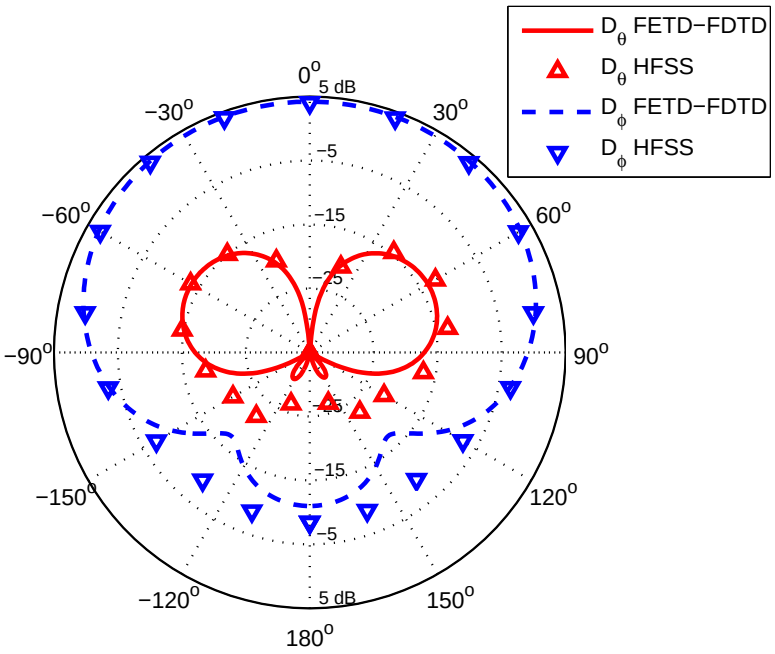

(a) xz-plane pattern

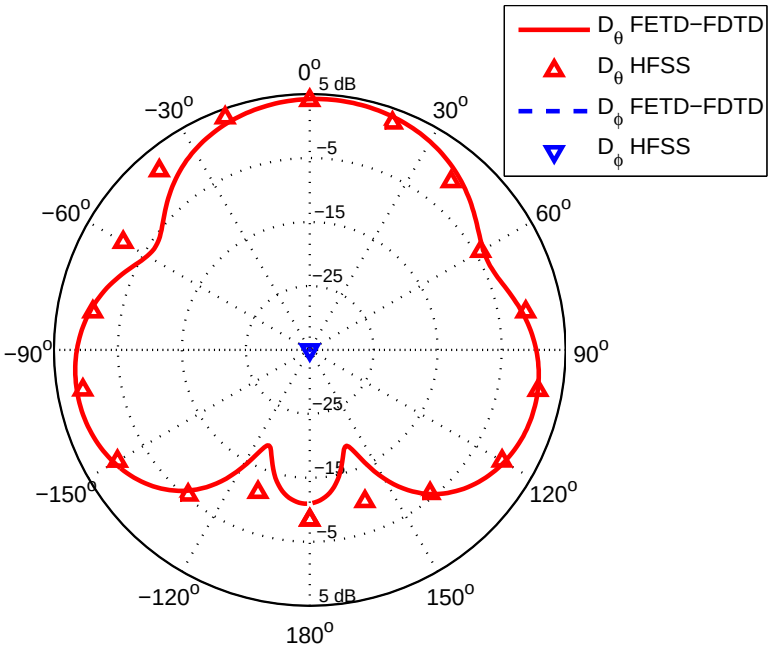

(b) yz-plane pattern

Figure 6.15: Results of directivity pattern at 5 GHz for the stripline fed Vivaldi antenna.

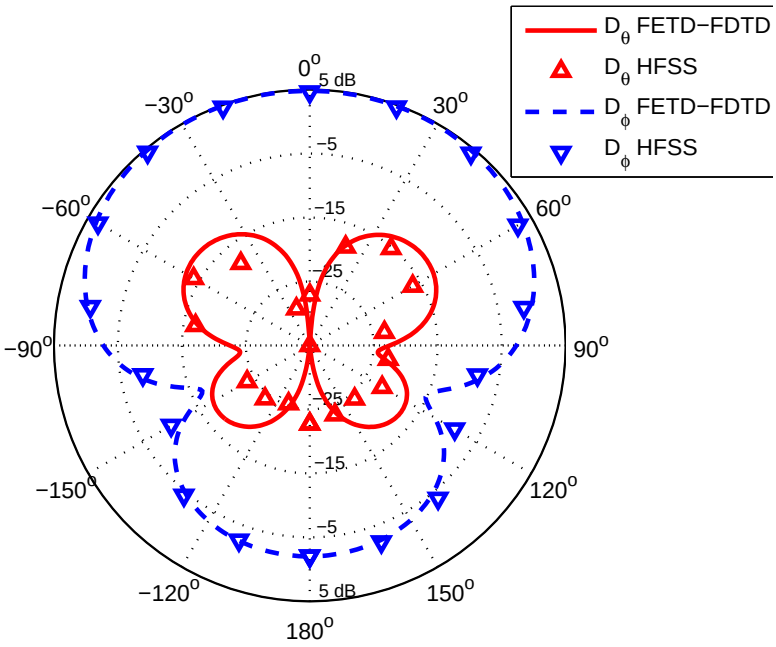

(a) xz-plane pattern

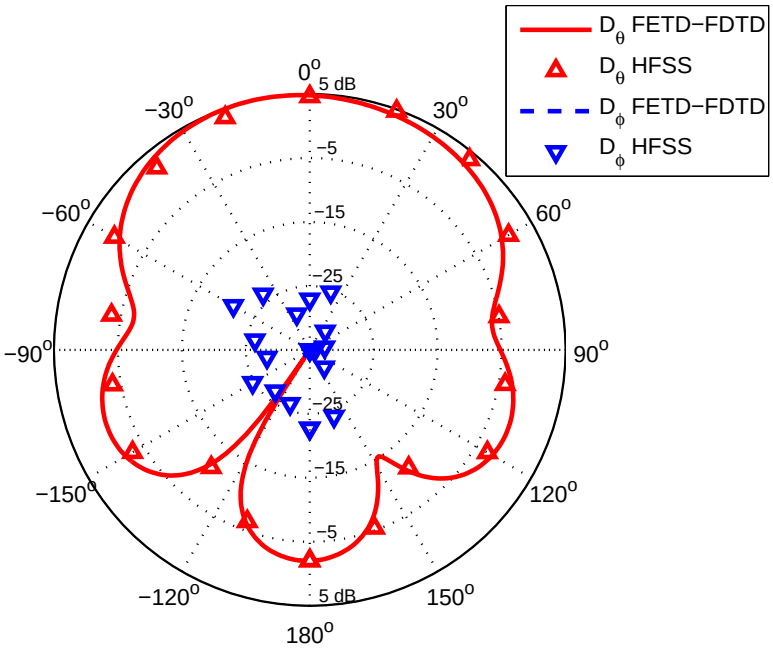

(b) yz-plane pattern

Figure 6.16: Results of directivity pattern at 7GHz for the stripline fed Vivaldi antenna.

6.4.3 Balanced Anti-podal Vivaldi Antenna

The next example is the modeling of a wideband anti-podal vivaldi antenna. The simulated problem was set as the 2000 CAD benchmark problem by Microwave Engineering Europe [105]. The requirement was to compute the reflection coefficient of the stripline fed antenna structure shown in Fig. 6.17 in the frequency band 0.5-10 GHz. From the geometry it is seen that both the microstrip line and ground plane gradually flare out. The antenna is a triplate structure with the substrate being 40 mm$\times$90b mm with a dielectric constant of $\varepsilon_r = 2.32$. The strip line track width is 3 mm. The combined thickness of the two sandwiched substrates is 3.15 mm and the antenna is fed by a stripline port of dimension 12 mm by 3.15 mm. The antenna geometry with elliptic output flares, details of which can be found in [105], is a typical example to highlight the advantage of the hybrid method with unstructured mesh to model the geometry accurately. Δh is set as 2 mm. Also shown in Fig. 6.17 is the triangulation of PEC surface of the antenna geometry in the final finite element mesh. Solution using both edge element and higher order basis functions are obtained using the same hybrid mesh. The number of unknowns in the FETD region is 119,898 in the case of the edge elements; and is 657,546 in the case of higher order basis functions for tetrahedral elements. For both the cases, the FDTD region has 38$\times$18$\times$62 cells surrounded by a 8 cell thick PML region. For the higher order solution, complete Cholesky factorization with re-ordering takes 48 mins and the time taken for time-stepping 5000 time steps is 4 hrs. The TEM modal distribution on the stripline feed is shown in Fig. 6.18. The reflection coefficient at the port obtained using both edge element and higher order basis functions is compared with the results obtained using HFSS in Fig. 6.19. As expected, the higher order solution has excellent agreement with HFSS than the lower order edge element solution. The S_{11} reported in Fig. 6.19(a) is the case with matched input impedance at the antenna feed terminal. It is observed that the 10 dB bandwidth is from 2.8-7.6 GHz. Though

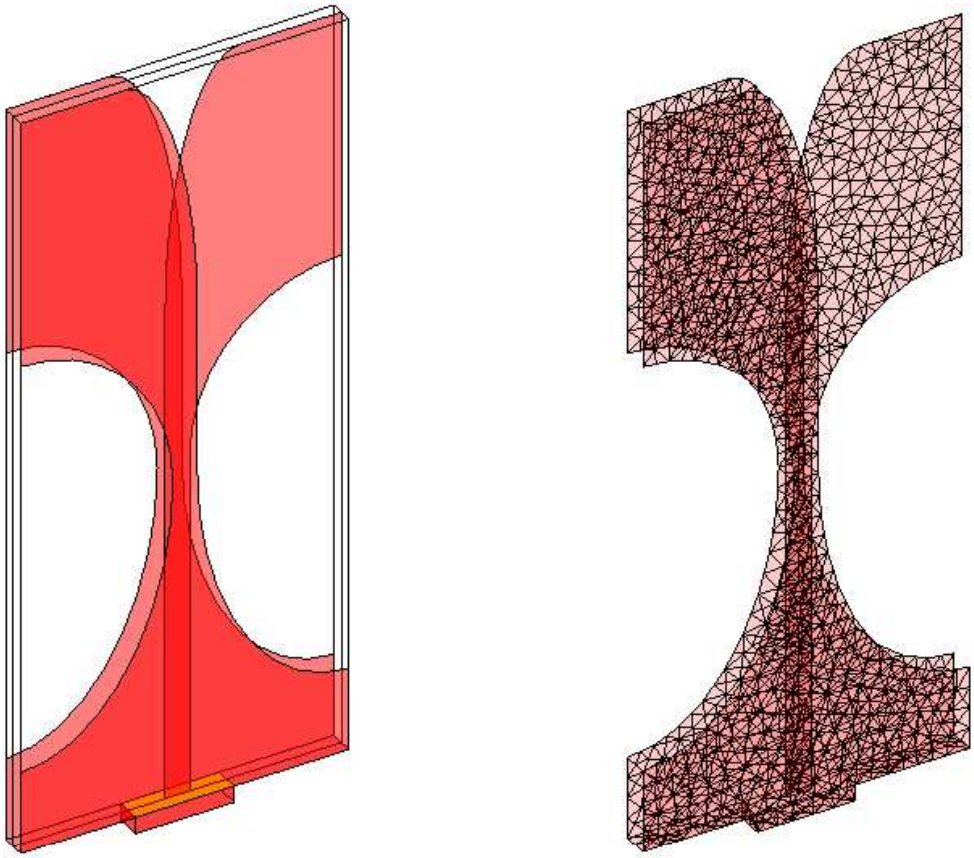

Figure 6.17: Geometry of balanced anti-podal Vivaldi antenna and triangulation of PEC surface in the finite element mesh.

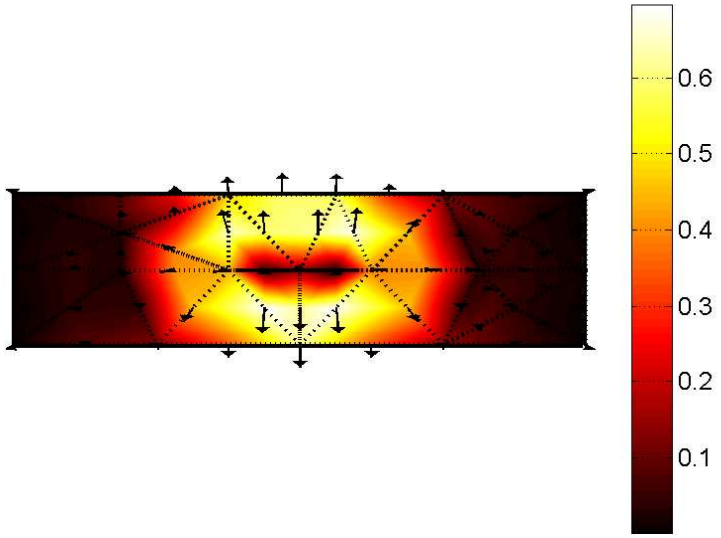

Figure 6.18: TEM modal solution on the stripline port feeding the balanced antipodal Vivaldi antenna.

not shown, the results are comparable to the results from other commercial codes involved in the benchmark exercise [105]. In Fig. 6.19(b), S_{11} after renormalization to a 50 Ω input impedance is shown, where again a good agreement with the results from HFSS can be observed. The time domain modal electric field amplitude of the reflected signal at the stripline port obtained with edge element and higher order basis functions is compared in Fig. 6.20. The input signal is a differentiated Guassian pulse. Though a similar trend is observed in the two waveforms the lower order solution in general lags behind the more accurate higher order solution. It is to be noted that the HFSS solution in the benchmark exercise was obtained using adaptive mesh refinement while the FETD-FDTD solution with higher order basis functions proposed in this thesis is obtained by a crude increase in the order of basis functions in the FETD region.

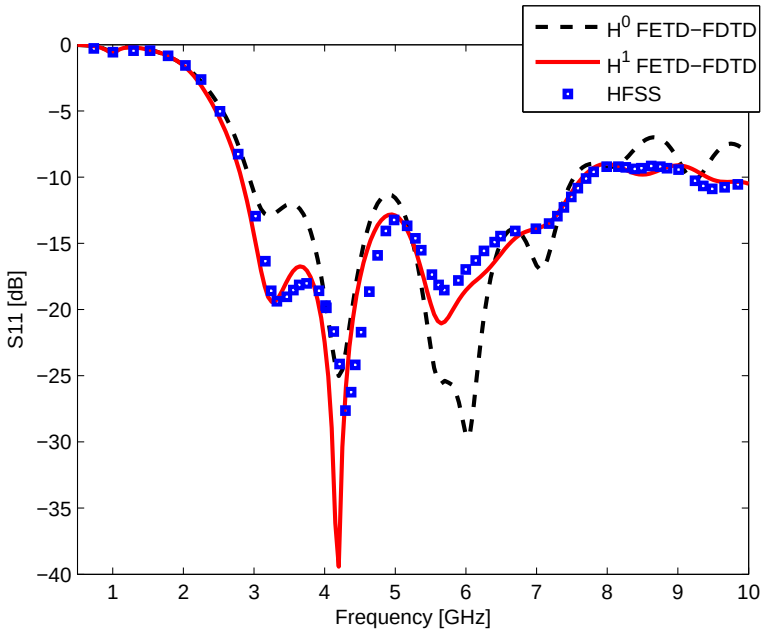

(a) Matched Load

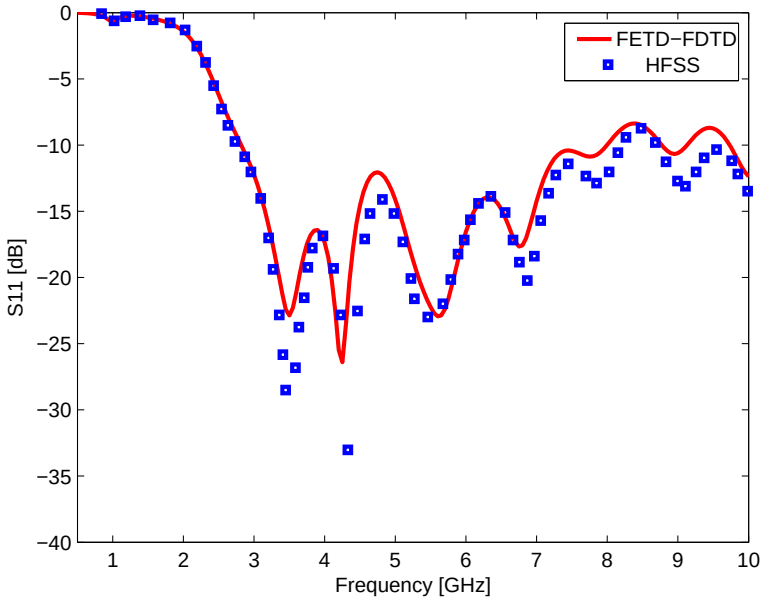

(b) Renormalized to 50Ω

Figure 6.19: Comparison of reflection coefficient of balanced anti-podal Vivaldi antenna.

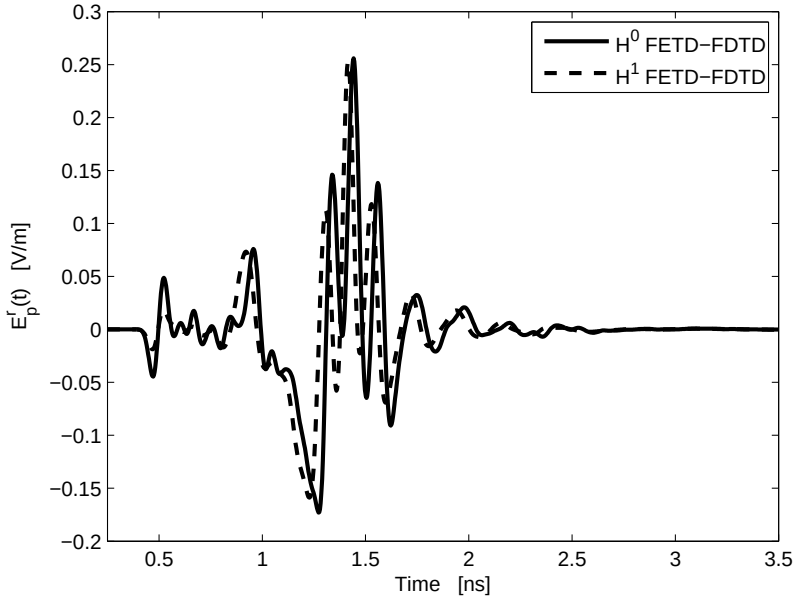

Figure 6.20: Modal amplitude of received signal at the stripline port feeding the balanced anti-podal Vivaldi antenna.

6.4.4 Printed Dipole Antenna

The next example is the modeling of a planar printed dipole antenna fed by a microstrip line. The antenna was originally designed as an unit cell of an antenna array developed at Temasek Laboratories, National University of Singapore. The top and the ground plane of the fabricated antenna prototype are shown in Figs. 6.21(a) and (b), respectively. The two dipole arms are 5 mm wide and flared out for better impedance bandwidth performance. The printed dipole arms are fed by a wideband balun structure transitioning from a 50 Ω microstrip line. The balun is etched in the ground plane of the substrate as shown in Fig. 6.21(b). The microstrip line is fed through a 50 Ω SMA connector. The numerical model of the geometry is shown in Fig. 6.21(c) with the detailed modeling of the coaxial line to microstrip line transition as shown in Fig. 6.21(d). The substrate has a dielectric constant of $\varepsilon_r = 2.2$ and a thickness of 0.787 mm. The

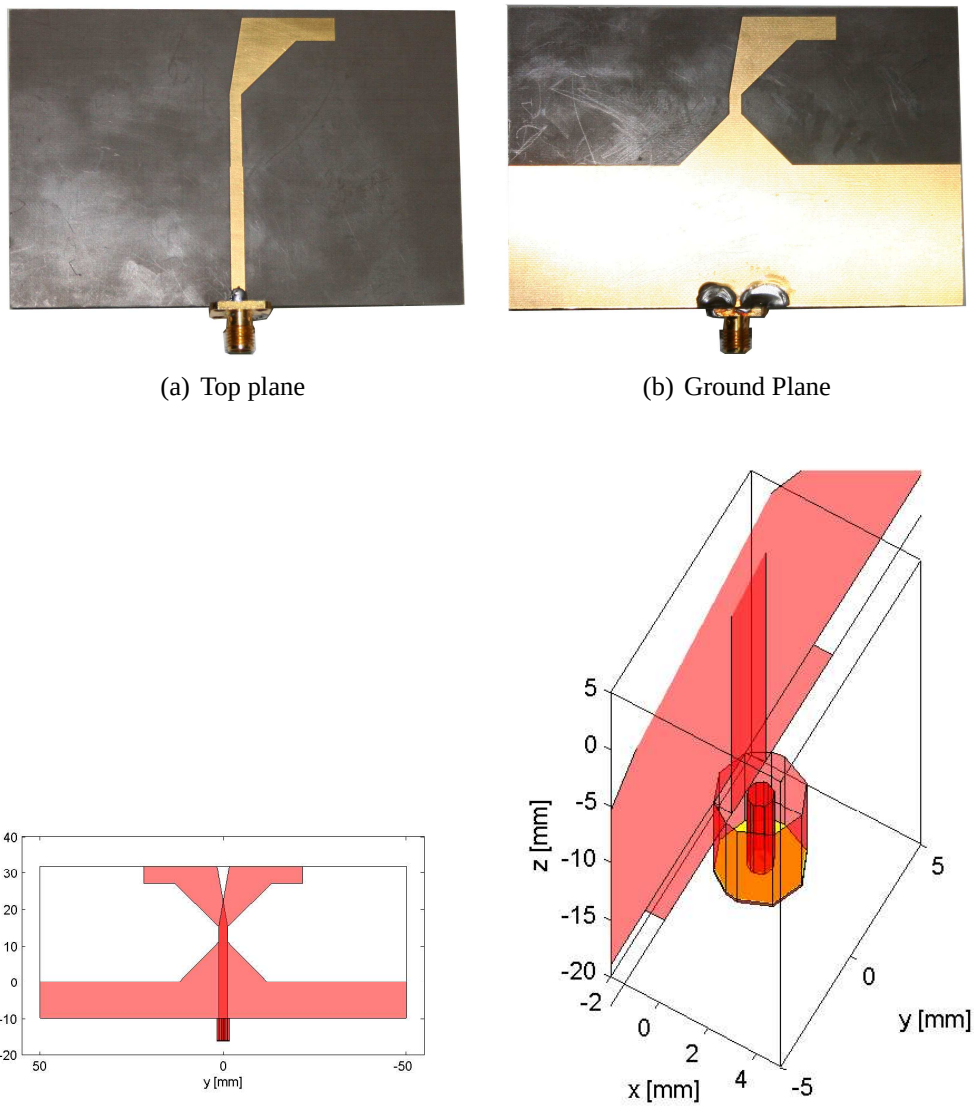

(a) Top plane (b) Ground Plane

(c) Model (d) Coax-to-Microstrip Port

Figure 6.21: Fabricated prototype and numerical model of printed dipole antenna.

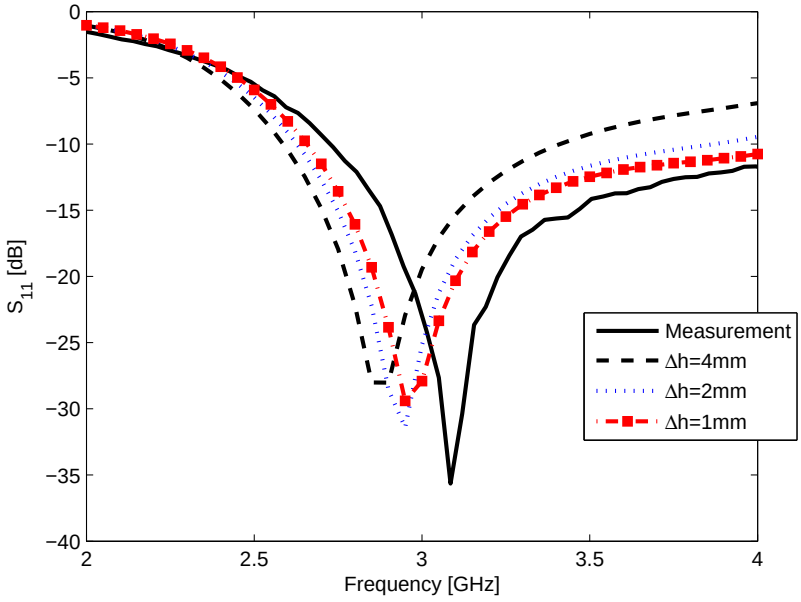

Figure 6.22: Comparison of reflection coefficient of planar printed dipole antenna.

input reflection coefficient was measured in the band 2-4 GHz. The S-parameter measurement was performed using HP8510C network analyser. The results of the reflection coefficient obtained using the hybrid code are compared with the measurement results in Fig. 6.22. The numerical solution using the hybrid code was obtained under three different FDTD grid sizes viz., $\Delta h = 4$ mm, 2 mm and 1 mm. The results for all the three cases are shown in Fig. 6.22 and compared with the measurement results to show the convergence behaviour of the numerical solution. It is observed that the agreement of the numerical results with the measurement results improves significantly as the grid size gets finer. This behaviour in the solution with different grid resolution suggests and substantiates the need for adaptive mesh refinement techniques for optimal performance of the hybrid method. Adaptive mesh refinement techniques have not been well explored in the FETD method unlike the frequency domain FEM case and is gaining interest fairly recently. One of the possible future directions to extend the current work would be to develop adaptive error estimation and reduction techniques within the

FETD method.

6.4.5 Square Planar Monopole Antenna

The final example is the modeling of square planar monopole antenna proposed in [106]. The antenna has ultra-wideband characteristics and is intended to be used in the frequency band of 2-11 GHz specifically for IEEE 802.11a applications. The antenna geometry is a simple square plate with notches on the lower corners, as shown in Fig. 6.23(a). In [106], it is shown that by properly selecting the dimensions of the notches good impedance bandwidth can be achieved. A particular dimension of notches was reported leading to a four-times larger impedance bandwidth compared to a simple square monopole antenna. The square plate is fed by a 50 Ω SMA connector through a via hole on the ground plane. The square plate has a dimension of 30 mm$\times$30 mm and the size of the ground plane is 100 mm$\times$100 mm. The input impedance of this antenna in the band of 2-13 GHz is computed using the hybrid code. The FDTD grid size is set as 2 mm. In Fig. 6.23(b), the cross section of the hybrid mesh along the $xz-$plane is shown. The number of implicit unknowns is reduced significantly by having the finite element region closely conforming to the square plate and the ground plane. In Fig. 6.24, the reflection coefficient at the port, computed using the hybrid method, is compared with the measured and HFSS simulation results reported in [106]. All three results exhibit similar trend in the return loss across the entire band. In Fig. 6.25, Fig. 6.26 and Fig. 6.27, the directivity patterns of the antenna at 2.5, 5 and 7.5 GHz in both the $xz-$ and $yz-$ planes are compared with the HFSS results reported in [106]. A good agreement in the overall pattern is observed and minor difference in the results from HFSS and the time domain hybrid method is attributed to the difference in modeling of the ground plane. In the hybrid code, the ground plane is modeled as a PEC box enclosing the coaxial conductor. At 2.5 GHz, being in the lower frequency of the band, the antenna

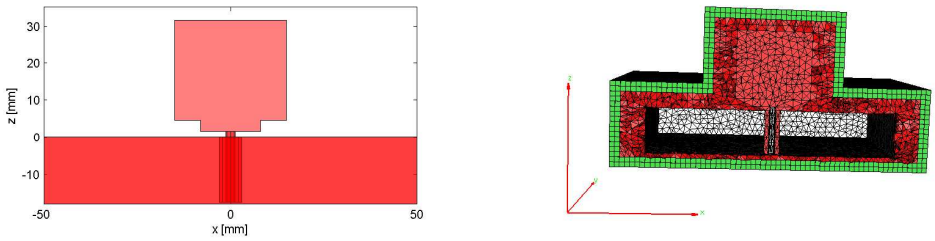

(a) xz-View (b) Hybrid Mesh

Figure 6.23: Numerical modeling of square planar monopole antenna

has similar butter-fly patterns in both $xz-$ and $yz-$ planes even though the geometry has an asymmetry along the two planes. As the frequency increases, the patterns in the two principal planes begin to differ.

6.5 Conclusion

The hybrid FETD-FDTD method offers an upper hand in the detailed and accurate modeling of complex structures with a marginal loss in the efficiency of regular FDTD method. By incorporating the antenna feed with TEM excitation in the FETD formulation to obtain the modal reflection coefficient, full-wave simulation of antenna structures with ports and transmission line feeds can be modeled. Successful application of the hybrid method on many real world antenna geometries demonstrates the potential use of the techniques for analysis and design of complex antenna structures and in particular, can be a vital tool in the characterisation of wideband and ultrawide band antennas. The application of the method is not restricted to antenna modeling alone and can be extended to problems in electromagnetic scattering and EMI-EMC related problems.

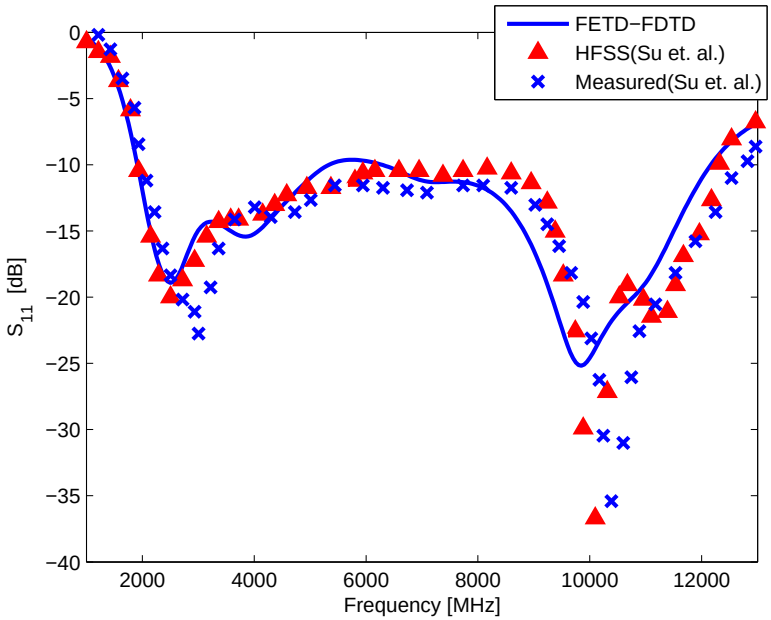

Figure 6.24: Comparison of reflection coefficient of square planar monopole antenna.

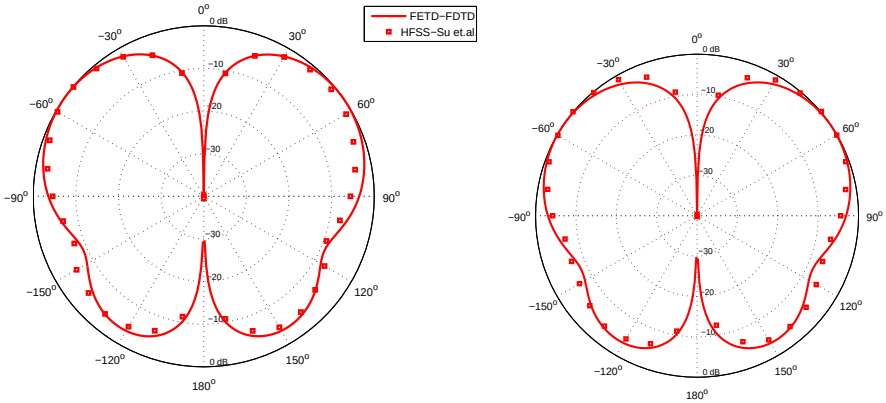

(a) xz-plane (b) yz-plane

Figure 6.25: Results of directivity pattern at 2.5 GHz for the square planar monopole antenna

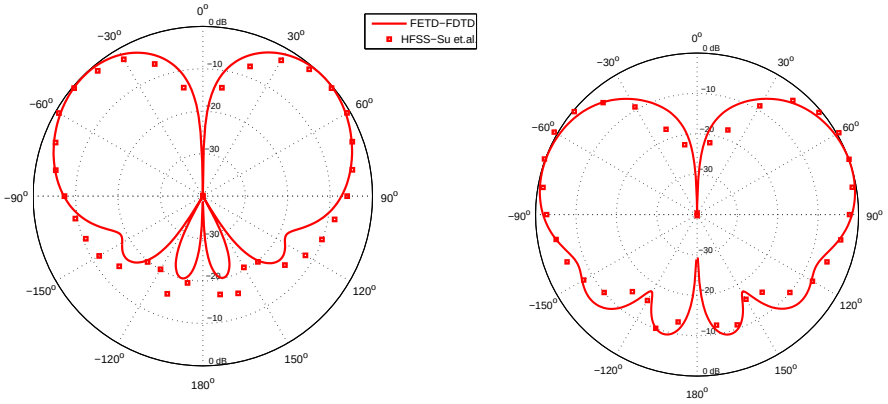

(a) xz-plane (b) yz-plane

Figure 6.26: Results of directivity pattern at 5 GHz for the square planar monopole antenna

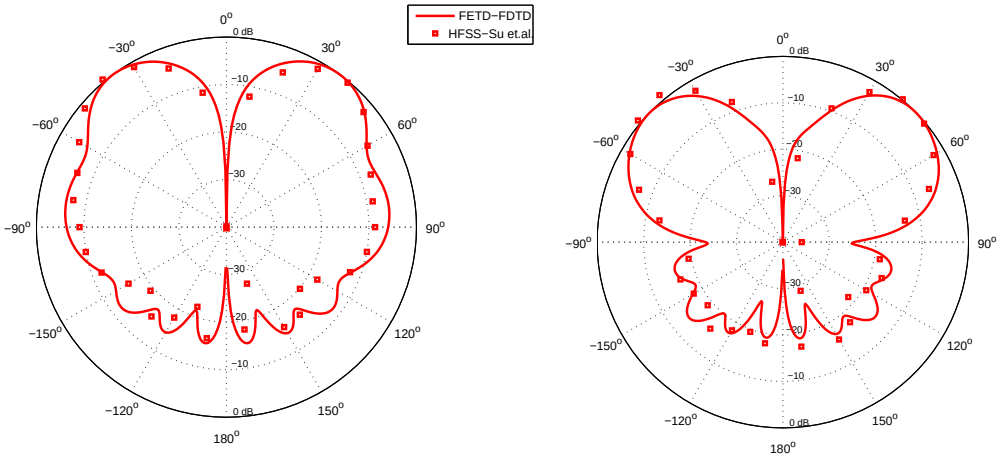

(a) xz-plane (b) yz-plane

Figure 6.27: Results of directivity pattern at 7.5 GHz for the square planar monopole antenna

CHAPTER 7

CONCLUSIONS AND FUTURE WORK

The finite element method, with its rigorous mathematical foundations, has been explored extensively in the frequency domain regime. However, its time domain counterpart, the FETD method has been gaining interests in the CEM community only fairly recently. The two basic finite methods viz., the FDTD method and the FETD method are reviewed in Chapter 2. Each of the two methods have certain advantages and disadvantages. Hybrid CEM methods are formulated such that they retain the advantages of a particular method, while overcoming disadvantages by hybridising the method with a different method which complements the disadvantage. The hybrid FETD-FDTD method is one such hybrid method which retains the efficiency of FDTD method in modeling simple homegeneous shapes and overcomes stair-casing errors using the FETD method which, in general, is based on unstructured grids. The basic idea of hybridising the two finite methods to have a robust method for time domain solution of Maxwell's equations is presented in Chapter 2. Elimination of errors due to stair-case approximations is evident in the numerical examples. The advantage in terms of efficiency of the hybrid method over regular FDTD method is also highlighted. However, the conditional numerical stability of FDTD method is lost. Two kinds of instabilities are observed viz., a) weak-instability where the solution grows linear with time and b) severe-instability where the solution grows exponentially with time. While the problem of linear time growth is inherent with FETD method, the severe-instability is an artifact which appears as a consequence of the hybridisation scheme.

In Chapter 3, the problem of linear time growth is thoroughly investigated. While solution of the vector Helmholtz's equation is obtained using edge element basis functions in the FETD method, the divergence-free condition of the electric flux is neither explicitly nor implicitly imposed. Since edge elements span a gradient vector function space, solution with non-zero divergence can exist in the FETD solution. A novel method of applying constraint equations for obtaining a divergence-free solution by suppressing or eliminating the gradient components in the solution is proposed. The constriant equations can be efficiently imposed using tree-cotree decomposition of the finite element mesh. The method is extended for eigenvalue problems in the modeling of electromagnetic resonators and is successfully applied to eliminate the appearance of non-physical DC modes.

With the weak-instability in the form of linear time growth observed in FETD method controlled using constraint equations, the problem of severe-instability encountered in the FETD-FDTD method is investigated in detail in Chapter 4. A framework for studying the stability of the hybrid FETD-FDTD method and an investigation of stability under different hybridisation schemes is presented. The equivalence between FDTD method and a special case of FETD method on hexahedral elements with trapezoidal integration and central differencing in time was shown. It is this fact that enables a stable hybrid FETD-FDTD method to be formulated. By treating the volumetric elements in the finite element mesh as either implicit or explicit instead of the unknowns, hybrid update eqautions with symmetric update coefficient matrices are obtained. Subsequently, condition on choice of time-step to have a stable time-marching scheme is derived.

Many concepts from the frequency domain FEM can be extended and explored in the time domain regime. Some of the concepts include error estimation and adaptive mesh refinement techniques. An example is the method of treatment of hanging variables dicussed in Chapter 5. It is shown that with successful treatment of hanging variables in hexahedral elements stable FDTD sub-gridding method can be achived. The method

proposed is based on single time-step scheme, with the update of unknowns in both the coarse and the fine regions having the same time step which statisfies the Courant criteria for the coarse grid. A research topic that needs further investigation is to extend the method for the multiple time-step case with the coarse and the fine regions having a different time step, dictated by the Courant criteria for the particular region. Following the lines of the proposed subgridding scheme and further research in the adaptive mesh refinement techniques for the time dependent case can lead to adaptive subgridding schemes.

In Chapter 6, the robustness of the 3-D hybrid FETD-FDTD method in the context of antenna modeling with examples of simulation of radiation from geometrically complex antennas is presented. With the accurate modeling of ports which excite the antenna element with the TEM mode, computation of modal reflection coefficient at the port terminal is presented. The use of higher order heirarchical basis functions in the tetrahedral elements of the FETD region allows the use of coarse mesh with better representation of the field solution. Agreement of the numerical results with the results obtained from other commericial CEM CAD tools such as Ansoft HFSS and measurement results demonstrate the potential application of the hybrid method in the design and analysis of broadband and ultrawideband antennas. There are two areas which could be improved. Firstly, increasing the order of accuarcy in the FDTD region using higher order FDTD schemes and deriving an equivalent FETD scheme could lead to a hybrid method which has low dispersion errors and is highly efficient with larger elements and needing fewer unknowns for the representation of the field solution. Secondly, exploring techniques for the relaxation of requirements in the hybrid mesh generation. In Chapter 5, an attempt to alleviate the need for pyramidal elements at the interface of tetrahedral and hexahedral elements using techniques similar to hanging variables is presented along with the pitfall of appearance of spurious modes which renders the technique infeasible. Future work would be to develop techniques which can support

non-matching interfaces. Investigation in the lines of the recently introduced domain decomposition techniques for FEM solution of time harmonic Maxwell's equations is necessary. Also in Chapter 6, improvement in the accuracy of the solution with higher order basis functions in the FETD region and mesh refinement were demonstrated. This clearly highlights the need for extending/developing the concepts of error estimation and adaptive refinement techniques to time domain methods and in particular to the FETD method.

BIBLIOGRAPHY

[1] K. S. Yee. Numerical solution of initial boundary value problems involving Maxwell's equations in isotropic media. *IEEE Transactions on Antennas and Propagation*, 14(3):302–307, March 1966.

[2] A. Taflove and S. Hagness. *Computational Electrodynamics: The Finite-Difference Time-Domain Method, 2 ed.* Artech House, Boston, MA, 2000.

[3] A. Taflove, editor. *Advances in Computational Electrodynamics: The Finite-Difference Time-Domain Method*. Artech House, Boston, MA, 1998.

[4] D. M. Sullivan. *Electromagnetic Simulation Using the FDTD Method*. IEEE Press, New York, 2000.

[5] A. Cangellaris, C.-C. Lin, and K. Mei. Point-matched time domain finite element methods for electromagnetic radiation and scattering. *IEEE Transactions on Antennas and Propagation*, 35(10):1160–1173, Oct 1987.

[6] G. Mur. A mixed finite element method for computing three-dimensional time-domain electromagnetic fields in strongly inhomogeneous media. *IEEE Transactions on Magnetics*, 26(2):674–677, Mar 1990.

[7] Man-Fai Wong, O. Picon, and V. Fouad Hanna. A finite element method based on whitney forms to solve maxwell equations in the time domain. *IEEE Transactions on Magnetics*, 31(3):1618–1621, May 1995.

[8] J.-F. Lee. WETD - a finite element time-domain approach for solving maxwell's equations. *IEEE Microwave Guided Wave Letters*, 4(1):11–13, Jan. 1994.

[9] Jin-Fa Lee and Z. Sacks. Whitney elements time domain (wetd) methods. *IEEE Transactions on Magnetics*, 31(3):1325–1329, May 1995.

[10] S. D. Gedney and U. Navsariwala. An unconditionally stable finite element time-domain solution of the vector wave equation. *IEEE Microwave Guided Wave Letters*, 5(10):332–334, Oct. 1995.

[11] K.S. Komisarek, N.N. Wang, A.K. Dominek, and R. Hann. An investigation of new FETD/ABC methods of computation of scattering from three-dimensional material objects. *IEEE Transactions on Antennas and Propagation*, 47(10):1579–1585, Oct. 1999.

[12] M. Feliziani and F. Maradei. Modeling of electromagnetic fields and electrical circuits with lumped and distributed elements by the WETD method. *IEEE Transactions on Magnetics*, 35(3):1666–1669, May 1999.

[13] Jin-Fa Lee, R. Lee, and A. Cangellaris. Time-domain finite-element methods. *IEEE Transactions on Antennas and Propagation*, 45(3):430–442, March 1997.

[14] Ruey-Beei Wu and T. Itoh. Hybridizing FD-TD analysis with unconditionally stable FEM for objects of curved boundary. In *IEEE MTT-S International Microwave Symposium Digest, 1995.*, pages 833–836vol.2, 16-20 May 1995.

[15] Ruey-Beei Wu and T. Itoh. Hybrid finite-difference time-domain modeling of curved surfaces using tetrahedral edge elements. *IEEE Transactions on Antennas and Propagation*, 45(8):1302–1309, Aug. 1997.

[16] M. Feliziani and F. Maradei. Mixed finite-difference/Whitney-elements time domain (FD/WE-TD) method. *IEEE Transactions on Magnetics*, 34(5):3222–3227, September 1998.

[17] M. Feliziani and F. Maradei. Hybrid finite element solutions of time dependent maxwell's curl equations. *IEEE Transactions on Magnetics*, 31(3):1330–1335, May 1995.

[18] T. Rylander and A. Bondeson. Stability of explicit-implicit hybrid time-stepping schemes for Maxwell's equations. *Journal of Computational Physics*, 179(2):426–438, July 2002.

[19] S Wang, R. Lee, Texeira F. L., and J. F. Lee. A hybrid finite element time domain/finite difference time domain approach for electromagnetic modeling. In *Progress in Electromagnetics Research Symposium, 2003.*, January 2003.

[20] R. F. Harrington. *Time-Harmonic Electromagnetic Fields*. Wiley-IEEE Press, New York, NY, 2001.

[21] R. E. Collin. *Foundations for Microwave Engineering*. Wiley-IEEE Press, New York, NY, 2000.

[22] B. Gustafsson, H.-O. Kreiss, and J. Oliger. *Time-Dependent Problems and Difference Methods*. Wiley, New York, 1995.

[23] J.-P. Berenger. Perfectly matched layer for the FDTD solution of wave-structure interaction problems. *IEEE Transactions on Antennas and Propagation*, 44(1):110–117, Jan. 1996.

[24] W. C. Chew and W. H. Weedon. A 3D perfectly matched medium from modified Maxwell's equations with stretched coordinates. *Microwave and Optical Technology Letters*, 7(13):599–604, September 1994.

[25] Z.S. Sacks, D.M. Kingsland, R. Lee, and Jin-Fa Lee. A perfectly matched anisotropic absorber for use as an absorbing boundary condition. *IEEE Transactions on Antennas and Propagation*, 43(12):1460–1463, Dec. 1995.

[26] S. D. Gedney. An anisotropic perfectly matched layer-absorbing medium for the truncation of FDTD lattices. *IEEE Transactions on Antennas and Propagation*, 44(12):1630–1639, Dec. 1996.

[27] Jo-Yu Wu, D.M. Kingsland, Jin-Fa Lee, and R. Lee. A comparison of anisotropic pml to berenger's pml and its application to the finite-element method for em scattering. *IEEE Transactions on Antennas and Propagation*, 45(1):40–50, Jan. 1997.

[28] R.J. Luebbers, K.S. Kunz, M. Schneider, and F. Hunsberger. A finite-difference time-domain near zone to far zone transformation [electromagnetic scattering]. *IEEE Transactions on Antennas and Propagation*, 39(4):429–433, April 1991.

[29] Z. C. Zienkiewicz and R. L. Taylor. *The Finite Element Method. Vol. 1: Basic Formulation and Linear Problems*. McGraw-Hill, New York, 1989.

[30] P. P. Silvester and R. L. Ferrari. *Finite Elements for Electrical Engineers*. Cambridge University Press, Cambridge, 1996.

[31] J. Jin. *The Finite Element Mehod in Electromagnetics, 2nd Edition*. Wiley, New York, 2002.

[32] J. C. Nedelec. Mixed finite elements in r3. *Numer. Math.*, 35:315–341, 1980.

[33] J.P. Webb. Edge elements and what they can do for you. *IEEE Transactions on Magnetics*, 29(2):1460–1465, Mar 1993.

[34] A. Bossavit. Whitney forms: A class of finite elements for three-dimensional computations in electromagnetism. In *IEE Proceedings A: Science, Measurement and Technology*, volume 135, pages 493–500, Nov 1988.

[35] A. Bossavit. *The Mathematics of finite elements and applications VI (Uxbridge, 1987)*, chapter Mixed Finite Elements and the Complex of Whitney forms, pages 137–144. Academic Press, London, 1988.

[36] Din Sun, J. Manges, Xingchao Yuan, and Z. Cendes. Spurious modes in finite-element methods. *IEEE Antennas and Propagation Magazine*, 37(5):12–24, Oct. 1995.

[37] J.P. Webb. Hierarchal vector basis functions of arbitrary order for triangular and tetrahedral finite elements. *IEEE Transactions on Antennas and Propagation*, 47(8):1244–1253, Aug. 1999.

[38] Z. J. Cendes. Vector finite elements for electromagnetic field computation. *IEEE Transactions on Magnetics*, 27(5):3958–3966, Sep 1991.

[39] D.-K. Sun, J.-F. Lee, and Z. Cendes. Construction of nearly orthogonal nedelec bases for rapid convergence with multilevel preconditioned solvers. *SIAM Journal on Scientific Computing*, 23(4):1053–1076, Apr. 2001.

[40] J.-H. Lee and Q. H.; Liu. A 3-D spectral-element time-domain method for electromagnetic simulation. *IEEE Transactions on Microwave Theory and Techniques*, 55(5):983–991, May. 2007.

[41] T. J. R. Hughes. *The Finite Element Method: Linear Static and Dynamic Finite Element Analysis*. Printice Hall, Englewood Cliffs, NJ, 1987.

[42] G. H. Golub and C. F. Van Loan. *Matrix Computations*. Johns Hopkins University Press,, 1997.

[43] S. Toledo. TAUCS - a library of sparse linear solvers. http://www.tau.ac.il/ stoledo/taucs/.

[44] G. Karypis and V. Kumar. METIS - serial graph partitioning and fill-reducing matrix ordering. http://glaros.dtc.umn.edu/gkhome/metis/metis/overview.

[45] T.V. Yioultsis, N.V. Kantartzis, C.S. Antonopoulos, and T.D. Tsiboukis. A fully explicit whitney element-time domain scheme with higher order vector finite elements for three-dimensional high frequency problems. *IEEE Transactions on Magnetics*, 34(5):3288–3291, Sept. 1998.

[46] J. Webb and V. Kanellopoulos. Absorbing boundary conditions for the finite element solution of the vector wave equation. *Microwave and Optical Technology Letters*, 2(10):370–372, Oct. 1989.

[47] S. Caorsi and G. Cevini. Assessment of the performance of First- and Second-order Time-Domain ABC's for the truncation of finite element grids. *Microwave and Optical Technology Letters*, 38(1):11–16, July 2003.

[48] V. Mathis. An anisotropic perfectly matched layer-absorbing medium in finite element time domain method for maxwell's equations. In *1997 IEEE Antennas and Propagation Society International Symposium Digest*, volume 2, pages 680–683vol.2, 13-18 July 1997.

[49] Hsiao-Ping Tsai, Yuanxun Wang, and T. Itoh. An unconditionally stable extended (use) finite-element time-domain solution of active nonlinear microwave circuits using perfectly matched layers. *IEEE Transactions on Microwave Theory and Techniques*, 50(10):2226–2232, Oct. 2002.

[50] D. Jiao, Jian-Ming Jin, E. Michielssen, and D.J. Riley. Time-domain finite-element simulation of three-dimensional scattering and radiation problems using perfectly matched layers. *IEEE Transactions on Antennas and Propagation*, 51(2):296–305, Feb. 2003.

[51] T. Rylander and Jian-Ming Jin. Perfectly matched layer in three dimensions for the time-domain finite element method applied to radiation problems. *IEEE Transactions on Antennas and Propagation*, 53(4):1489–1499, April 2005.

[52] Shumin Wang, R. Lee, and F.L. Teixeira. Anisotropic-medium PML for vector FETD with modified basis functions. *IEEE Transactions on Antennas and Propagation*, 54(1):20–27, Jan. 2006.

[53] D.J. Riley and C.D. Turner. Volmax: a solid-model-based, transient volumetric maxwell solver using hybrid grids. *IEEE Antennas and Propagation Magazine*, 39(1):20–33, Feb. 1997.

[54] S. Dey and R. Mittra. A locally conformal finite-difference time-domain (FDTD) algorithm for modeling three-dimensional perfectly conducting objects. *IEEE Microwave Guided Wave Letters*, 7(9):273–275, Sep. 1997.

[55] Tian Xiao and Q.H.; Liu. Enlarged cells for the conformal fdtd method to avoid the time step reduction. *IEEE Microwave and Wireless Components Letters*, 14(12):551–553, Dec. 2004.

[56] M. Chai, Tian Xiao, Gang Zhao, and Qing Huo Liu. A hybrid PSTD/ADI-CFDTD method for mixed-scale electromagnetic problems. *IEEE Transactions on Antennas and Propagation*, 55(5):1398–1406, May. 2007.

[57] C. A. Balanis. *Advanced Engineering Electromagnetics*. Wiley, New York, 1989.

[58] J. R. Shewchuk. Triangle - A Two-Dimensional Quality Mesh Generator and Delaunay Triangulator. http://www-2.cs.cmu.edu/ quake/triangle.html.

[59] R. Luebbers, D. Ryan, and J. Beggs. A two-dimensional time-domain near-zone to far-zone transformation. *IEEE Transactions on Antennas and Propagation*, 40(7):848–851, July 1992.

[60] C.-F. Wang and Y.-B. Gan. 2d cavity modeling using method of moments and iterative solvers. In *Progress In Electromagnetic Research, PIER 43*, 2003.

[61] E. Abenius, U. Andersson, L. Edlvik, and G. Ledfelt. Hybrid time domain solvers for the Maxwell equations in 2D. *International Journal for Numerical Methods in Engineering*, 53(9):2185–2199, March 2002.

[62] C-T Hwang and R-B Wu. Treating late-time instability of hybrid Finite-Element/Finite-Difference time-domain method. *IEEE Transactions on Antennas and Propagation*, 47:227–232, 1999.

[63] N.V. Venkatarayalu and Jin-Fa Lee. Removal of spurious dc modes in edge element solutions for modeling three-dimensional resonators. *IEEE Transactions on Microwave Theory and Techniques*, 54(7):3019–3025, July 2006.

[64] N.V. Venkatarayalu, M.N. Vouvakis, Yeow-Beng Gan, and Jin-Fa Lee. Suppressing linear time growth in edge element based finite element time domain solution using divergence free constraint equation. In *2005 IEEE Antennas and Propagation Society International Symposium*, volume 4B, pages 193–196 vol.4B, 3-8 July 2005.

[65] S.G. Perepelitsa, R. Dyczij-Edlinger, and Jin-Fa Lee. Finite-element analysis of arbitrarily shaped cavity resonators using H^1(curl) elements. *IEEE Transactions on Magnetics*, 33(2):1776–1779, March 1997.

[66] B. N. Parlett, editor. *The Symmetric Eigenvalue Problem*. Printice Hall, Englewood Cliffs, NJ, 1980.

[67] D.A. White and J.M. Koning. Computing solenoidal eigenmodes of the vector helmholtz equation: a novel approach. *IEEE Transactions on Magnetics*, 38(5):3420–3425, Sept. 2002.

[68] R. Lehoucq, D. Sorensen, and C. Yang. *ARPACK User's Guide: Solution of Large-Scale Eigenvalue Problems with implicitly Restarted Arnoldi Methods*. SIAM, Philadelphia, PA, 1998.

[69] C. W. Crowley, P. P. Silvester, and Jr. Hurwitz, H. Covariant projection elements for 3d vector field problems. *IEEE Transactions on Magnetics*, 24(1):397–400, Jan. 1988.

[70] Jin-Fa Lee and Din-Kow Sun. p-type multiplicative schwarz (pmus) method with vector finite elements for modeling three-dimensional waveguide discontinuities. *IEEE Transactions on Microwave Theory and Techniques*, 52(3):864–870, March 2004.

[71] P. Monk. A simple proof of convergence for an edge element discretization of maxwell's equations. *Computational Electromagnetics, Lecture Notes in Computational Science and Engineering*, 28:127–142, 2003.

[72] S. S. Skiena. *The Algorithm Design Manual*. Springer-Verlag New York, New York, USA, 1997.

[73] Seung-Cheol Lee, Jin-Fa Lee, and R. Lee. Hierarchical vector finite elements for analyzing waveguiding structures. *IEEE Transactions on Microwave Theory and Techniques*, 51(8):1897–1905, Aug. 2003.

[74] J.F. Lee, D.K. Sun, and Z.J. Cendes. Tangential vector finite elements for electromagnetic field computation. *IEEE Transactions on Magnetics*, 27(5):4032–4035, Sep 1991.

[75] R. Chilton and R. Lee. The discrete origin of fetd late time instability and a correction scheme. *Journal of Computational Physics*. To appear.

[76] R. D. Richtmeyer and K. Morton. *Difference Methods for initial value problems*. New York, John Wiley & Sons, 1967.

[77] M. A. Celia and W. G. Gray. *Numerical Methods for Differential Equations - Fundamental Concepts for Scientific and Engineering Applications*. Prentice Hall; United States, 1991.

[78] N. V. Venkatarayalu, Y.-B. Gan, and L.-W. Li. Investigation of numerical stability of 2D FE/FDTD hybrid algorithm for different hybridization schemes. *IEICE Transactions on Communications*, E88-B(6):2341–2345, June 2005.

[79] A. Monorchio and R. Mittra. Time-domain FE/FDTD technique for solving complex electromagnetic problems. *IEEE Microwave Guided Wave Letters*, 8(2):93–95, Feb. 1998.

[80] N.V. Venkatarayalu, G.Y. Beng, and L.-W. Li. On the numerical errors in the 2d FE/FDTD algorithm for different hybridization schemes. *IEEE Microwave Guided Wave Letters*, 14(4):168–170, April 2004.

[81] S.S. Zivanovic, K.S. Yee, and K.K. Mei. A subgridding method for the time-domain finite-difference method to solve maxwell's equations. *IEEE Transactions on Microwave Theory and Techniques,*, 39(3):471–479, March 1991.

[82] G. A. Baker. Error estimates for finite element methods for second order hyperbolic equations. *SIAM J. Numer. Anal.*, 13(4):564–576, 1976.

[83] N. V. Venkatarayalu, R. Lee, Y. B. Gan, and L.-W. Li. A Stable FDTD Subgridding Method based on Finite Element Formulation with Hanging Variables. *IEEE Transactions on Antennas and Propagation*, 55(3):907–915, Mar 2007.

[84] R. Lee. A note on mass lumping in the finite element time domain method. *IEEE Transactions on Antennas and Propagation*, 54(2):760–762, Feb 2006.

[85] S. Wang and F. L. Teixeira. Some remarks on the stability of time-domain electromagnetic simulations. *IEEE Transactions on Antennas and Propagation*, 52(3):895–898, March 2004.

[86] T. Rylander, A. Bondeson, and Yueqiang Liu. Stability, accuracy and application of an FDTD-TDFEM algorithm [patch antenna example]. In *2004 IEEE Antennas and Propagation Society International Symposium*, volume 2, pages 1676–1679, 20-25 June 2004.

[87] V. Hill, O. Farle, and R. Dyczij-Edlinger. Finite element basis functions for nested meshes of nonuniform refinement level. *IEEE Transactions on Magnetics*, 40(2):981–984, March 2004.

[88] V. Hill, O. Farle, and R. Dyczij-Edlinger. A stabilized multilevel vector finite-element solver for time-harmonic electromagnetic waves. *IEEE Transactions on Magnetics*, 39(3):1203–1206, May 2003.

[89] M. Okoniewski, E. Okoniewska, and M.A. Stuchly. Three-dimensional subgridding algorithm for FDTD. *IEEE Transactions on Antennas and Propagation*, 45(3):422–429, March 1997.

[90] M. W. Chevalier, R. J. Luebbers, and V. P. Cable. Fdtd local grid with material traverse. *IEEE Transactions on Antennas and Propagation*, 45(3):411–421, March 1997.

[91] Shumin Wang, F.L. Teixeira, R. Lee, and Jin-Fa Lee. Optimization of subgridding schemes for FDTD. *IEEE Microwave and Wireless Components Letters*, 12(6):223–225, June 2002.

[92] P. Monk. Sub-gridding FDTD schemes. *ACES Journal*, 11:37–46, 1996.

[93] N. V. Venkatarayalu, Y. B. Gan, R. Lee, and L.-W. Li. Application of hybrid FETD-FDTD method in the modeling and analysis of antennas. *IEEE Transactions on Antennas and Propagation,Submitted and under Review.*

[94] Zheng Lou and Jian-Ming Jin. Modeling and simulation of broad-band antennas using the time-domain finite element method. *IEEE Transactions on Antennas and Propagation*, 53(12):4099–4110, Dec. 2005.

[95] J.-L. Coulomb, F.-X Zgainski, and Y. Marechal. A pyramidal element to link hexahedral, prismatic and tetrahedral edge finite elements. *IEEE Transactions on Magnetics*, 33(2):1362–1365, March 1997.

[96] J.P. Webb and B. Forghani. Heirarchal scalar and vector tetrahedra. *IEEE Transactions on Magnetics*, 29(2):1495–1498, Mar 1993.

[97] R. Dyczij-Edlinger, G. Peng, and J.-F. Lee. Efficient finite element solvers for the maxwell equations in the frequency domain. *Comput. Methods Appl. Mech. Engrg.*, 169(3–4):297–309, Feb 1999.

[98] J.F. Lee. Conforming hierarchical vector elements. In *2002 IEEE Antennas and Propagation Society International Symposium*, volume 1, pages 66–69vol.1, 16-21 June 2002.

[99] Zheng Lou and Jian-Ming Jin. An accurate waveguide port boundary condition for the time-domain finite-element method. *IEEE Transactions on Microwave Theory and Techniques*, 53(9):3014–3023, Oct. 2005.

[100] J.-F Lee, D. K Sun, and Z. J. Cendes. Full-wave analysis of dielectric waveguide using tangential vector finite elements. *IEEE Transactions on Microwave Theory and Techniques*, 39(8):1262–1271, Aug 1991.

[101] S.V. Polstyanko, R. Dyczij-Edlinger, and Jin-Fa Lee. Fast frequency sweep technique for the efficient analysis of dielectric waveguides. *IEEE Transactions on Microwave Theory and Techniques*, 45(7):1118–1126, July 1997.

[102] Din-Kow Sun, Jin-Fa Lee, and Z. Cendes. The transfinite-element time-domain method. *IEEE Transactions on Microwave Theory and Techniques*, 51(10):2097–2105, Oct. 2003.

[103] A. Barka and G. Salin. Jina 2004 test case 8: 20x20 patch array antenna. http://www.elec.unice.fr/pages/congres/jina2004/workshop/test8.pdf.

[104] Benoit Stockbroeckx and Andre Vander Vorst. Copolar and cross-polar radiation of vivaldi antenna on dielectric substrate. *IEEE Transactions on Antennas and Propagation*, 48(1):19–25, Jan. 2000.

[105] Microwave Engineering Europe Magazine. The 2000 cad benchmark unveiled. http://www.mwee.com/magazine/2000/cad_benchmark.html.

[106] Saou-Wen Su, Kin-Lu Wong, and Chia-Lun Tang. Ultra-wideband square planar monopole antenna for IEEE 802.16a operation in the 2-11-GHz band. *Microwave and Optical Technology Letters*, 42(6):463–466, Sept. 2004.